Operational Experience and Control Strategies for a Stand-Alone Power System based on Renewable Energy and Hydrogen

Harald Miland

February 2005

Thesis submitted for the degree of
Doktor ingeniør

NTNU

Norwegian University of Science and Technology
Faculty of Natural Sciences and Technology
Department of Materials Technology

IMT-report 2004:66

Operational Experience and Control Strategies for a Stand-Alone Power System based on Renewable Energy and Hydrogen

Harald Miland
Department of Materials Technology
Norwegian University of Science and Technology
Trondheim, Norway

ISBN-nummer: 82-471-6919-3 (elektronisk)
ISBN-nummer: 82-471-6920-7 (trykt)

Doktor ingeniøravhandling 2005:28

Preface

The work presented in this thesis has been carried out at Department of Energy Systems (ENSYS) at Institute for Energy Technology (IFE), Kjeller in the period 2001 – 2004. Parts of the work were also performed at NTNU - Norwegian University of Science and Technology in Trondheim, and at Econnect ltd in Hexham, UK.

When building the HSAPS test-facility, it was difficult to find manufacturers who could deliver PEM (or any) fuel cells in the range > 1 kW late 2001. However, it was encouraging that many of the fuel cell manufacturers at this time were shifting from making custom fuel cells to production of complete fuel cell systems ready for automatic operation, thus a step towards a commercial product. In early 2004 several small-scale fuel cells have become available on the market. Also some small-scale electrolysers in the range > 5 kW have also become available on the market within the last two years, which are designed for running on fluctuating power from new renewable resources (wind and solar energy).

Acknowledgement

My supervisor was late Georg Hagen who sadly past away too early, in autumn 2004. Professor Hagen was employed at Department of Materials Technology, NTNU in Trondheim. My gratitude goes to Dr. Børre Børresen, Department of Materials Technology, NTNU, who kindly took over the responsibility for helping me finalise this work.

Also, my gratitude goes to supervisor Dr. Rolf Jarle Aaberg, an extremely efficient and dedicated person who helped me defining the key milestones throughout my PhD work, he also gave the initial idea for an alternative high-level energy controller. No less, supervisor Dr. Ronny Glöckner is acknowledged for introducing me to the world of modelling and computer simulations, in addition to his contributions and knowledge regarding hydrogen systems in general. They both worked as research fellows at ENSYS, IFE. At present Rolf Jarle works at Statkraft Energi AS, while Ronny works at Høgskolen i Agder (HiA). During my stay at Econnect ltd, UK, October 2003, Dr. Phil Taylor introduced me to the fundamentals of power electronics and fuzzy control, something that became essential in this PhD work. Furthermore, Prof. Sigurd Skogestad, Prof. Heinz A. Preisig, and PhD student Federico Zenith, all from Department of Chemical Engineering, NTNU, deserve gratitude's for proofreading my thesis and giving me valuable inputs, helping Professor Hagen when he was sick. Others who kindly have shown their interest in proofreading my thesis is Dr. Preben Vie and Dr. Øystein Ulleberg, both research fellows at ENSYS, IFE. A very special thanks goes to Dr. Jon Eriksen, IFE, for helping me building IFE's 2nd generation hydrogen system based on his experience from the 1st generation hydrogen system, which he struggled with in his PhD study. Jon has also contributed with experimental data and many fruitful discussions, especially regarding Chapter 3 and Chapter 5, not to mention discussions on less scientific matters and the lovely "plastic" coffee he served in the laboratory. Thomas Førde and Yngve Tranøy have also contributed a lot with labview programming, thoughts about control strategies, and data acquisition in addition to valuable coffee breaks, when they wrote their diploma thesis here at IFE in 2002. I also want to thank Dipl.-Ing. Ursula Wittstadt, Fraunhofer Institute for Solar Energy Systems ISE in Freiburg, Germany, for letting me stay a whole week for training on how to operate the electrolyser. The Norwegian Research Council (NFR) is acknowledged for financing this PhD study.

Of course, I appreciate the support I have got from my parents, brother, and sister throughout the years, when I played with my lego, even when I played in a hard rock band occupying the barn on our little farm at Miland. But, the greatest patience has been shown by my dear Åshild, a nurse who has been more concerned about my health than the computer models I have been struggling with late nights. This autumn we got our first child, a little boy who has turned our lives upside down, and of course to the better. It must be mentioned that Åshild's parents offered me an "office" with a beautiful view over the lake Tinnsjøen in Tinn Austbygd, and that large parts of this thesis were written there.

Finally, I would like to dedicate this work to my late father, Olav Harald Miland

Kjeller, December 2004

Harald Miland

Summary

The topic of this thesis is investigation of a small-scale stand-alone power system, based on both experimental work and computer simulations. The power system in this study uses solar energy as energy input, lead-acid batteries as short-term energy storage, and hydrogen as long-term energy storage. The main focus is upon operation and control of the hydrogen subsystem, as a robust controller is needed in order to prevent excessive use of the components in this subsystem. The laboratory power system comprises of: Hydrogen subsystem (PEM electrolyser, metal hydride, and PEM fuel cell), a lead-acid battery, programmable power supply for emulation of PV arrays, wind turbines, and controlled characterisation of the individual system components, and a programmable electronic load.

The intention was to build the laboratory power system as simple and energy efficient as possible. The components were connected directly in parallel on a common 48 V DC bus bar, no power electronics were applied between the components. Furthermore, the metal hydride and the fuel cell were air-cooled, avoiding auxiliaries required for water-cooling. The electrolyser, however, needed water-cooling. But with the electrolyser delivering hydrogen at 16 bars to a low pressure metal hydride, no use of compressor was required. On the other hand, metal hydrides needs purified hydrogen gas, > 99.999 %, in order to maintain its capacity as specified by the manufacturer.

The actual work in this thesis is divided in *three* main parts:

1. Design, construction, and operation of a laboratory hydrogen power system

2. Establishment of a computer model of the laboratory hydrogen power system, which interpolates and extrapolates its outputs based on experimental data collected from the laboratory system

3. Establishment of control algorithms for high-level energy management of the laboratory hydrogen power system based on the developed computer model. It is a goal to make the implementation and maintenance of these control algorithms as simple as possible. Furthermore, the control algorithms must enable efficient usage of the system components and secure energy supply to the end user

The results of this thesis are divided in *two* main parts:

The first part of the main results relates to the proposal and development of two types of *control algorithms* for high-level energy management, which will be denoted as the *Control Matrix* and the *Fuzzy controller* in the thesis. These control algorithms are suggested as opposed to the more traditional *battery five-step charge controller*. Identification of important *system parameters* and choosing proper settings for *control parameters* must be implemented into the control algorithms in order to finalise a complete *control strategy*. It will be shown that the electrolyser annual runtime decreases while the electrolyser annual hydrogen production remains the same by using the proposed control strategies, thus running the electrolyser more efficient.

Furthermore, with a reduction in the total number of electrolyser start-ups, a more stable system operation is achieved.

The second part of the main results relates to the operational experience of the small-scale laboratory hydrogen power system. Due to the amount of power required by the local control system integrated into the fuel cell and the electrolyser, the energy efficiency of the fuel cell and the electrolyser is lower at partial loads. Thus, with the additional energy needed for hydrogen purification, the round-trip efficiency of the hydrogen subsystem is found to be rather low (< 30 %), when the fuel cell and the electrolyser runs at low partial loads. However, it is encouraging that the hydrogen subsystem can reach 35 – 40 % when the fuel cell and the electrolyser are allowed to run at nominal power levels, in addition to optimal arrangement of the hydrogen purification unit. These energy efficiencies are higher than efficiencies achieved with diesel-fuelled generators. Besides, stand-alone power systems often resides in remote areas where transportation of diesel is costly, thus local production of the fuel by means of electrolyser and excess renewable energy can be profitable.

Regarding the difficulty of measuring the true amount of hydrogen present in the metal hydride, and because this system parameter is important in the control strategy, a pressurised vessel is recommended instead of the air-cooled metal hydride. Furthermore, it is recommended to use DC/DC converters in the hydrogen power system in order to ensure power quality within specifications and robust operation.

Abbreviations

BAT	= Battery
DACS	= Data acquisition and data control system
DAQ	= Data acquisition
DI	= Deionised
DSC	= Data supervisory control
ELY	= Electrolyser
FC	= Fuel cell
GPIB	= General purpose industrial interface
HHV	= Higher heating value
HSAPS	= Hydrogen stand-alone power system
LHV	= Lower heating value
MH	= Metal hydride
MPPT	= Maximum power point tracker
PAFC	= Phosphoric acid fuel cell
PCT	= Pressure concentration temperature
PEM	= Proton exchange membrane
PID	= Proportional integral derivative
PV	= Photovoltaic
RES	= Renewable energy resources
SAPS	= Stand-alone power system
SOC	= State-of-charge

Contents

1. Introduction and background

Several stand-alone power systems (SAPS) are installed around in Europe, usually located in small communities or at technical installations that are not connected to a main electricity grid. The majority of these power systems are based on fossil fuel power generation. The European Union and Norway account for only 6.4 % of the world's total use of Renewable Energy Sources (RES). Despite this low figure the European expertise in terms of RES technology is high [1], and lately there has been a growing initiative to include renewable energy technologies, particularly wind and solar power, into SAPS. When included in SAPS, wind and solar power often operate in combination with diesel generators and/or batteries, reducing the fossil fuel consumption. Replacement of diesel generators and batteries by fuel cells running on hydrogen, produced locally with renewable energy, offers a great opportunity to improve environmental standards, and reduce operation and maintenance costs.

The work described in this thesis is concerned with small to medium size SAPS, which is in the range of a few ten's of kW. Other terms for non-interconnected power systems exist in the literature such as *autonomous electrical power systems*, *isolated/islanded power systems* and *mini-grids*. These types of electrical power systems are not interconnected to large transmission systems, thus, their stability characteristics are quite different and therefore require different approaches for control/regulation.

1.1 Motivation

More than 30 % of the world's population that has access to electricity does not have access to reliable electricity supply. Only 10 % of the urban households in Africa are estimated to have an electricity supply and the fraction of the rural households is much less. Even in Europe there are about 300.000 households located in remote areas such as islands and mountainous regions without access to the grid. In Norway, there are approximately 660 inhabited islands with a total of about 140.000 inhabitants (3 % of the population). Most of these islands have access to the main grid, but many of them are far from shore with long transmission lines that are costly to upgrade and maintain. Replacement of these transmission lines with SAPS using renewable energy as an input and hydrogen as an energy buffer might be an attractive option in the future. Most of the remote installations in rural areas around the world use SAPS running on diesel. Diesel systems are reliable and have relatively low initial costs, but the fuel is polluting and expensive when the additional transportation costs are taken into account. The market potential for introduction of hydrogen in SAPS, as defined in this thesis, and the hydrogen society in general are closely linked to the market for renewable energy [2, 3]. The favourable economy of renewable energy compared to diesel generation has already been documented, and an example of island and mainland diesel costs compared to small-scale wind power is given in Table 1.1.

Table 1.1 Relative costs of electricity in Euros [4, 5]

Island diesel	0.34 € / kWh
Mainland diesel	0.074 € / kWh
Small-scale wind power	0.060 € / kWh

Integration of renewable energy into SAPS introduces some technical challenges. The SAPS will experience fluctuating or intermittent power generation from the renewable energy sources in addition to unpredictable load profiles. Fluctuations in combination with relatively low system inertia may cause system instability and decrease in system efficiency. The technical challenges are listed below:

- Frequency/voltage control – power quality
- Difference in response time for integrated components requires careful control for stable operation, e.g. interplay between wind turbine and fuel cell
- Fluctuating generation and load
- Long-term energy storage
- Security of supply
- Low renewable energy penetration
- Energy dumping
- Load growth

For small SAPS of a few 100's of watts based on solar energy (photovoltaic arrays), only DC loads should be selected because an inverter, and hence its losses, can be eliminated. Low-power DC loads tolerate a wide range of input voltage, but care must be taken into identification of the acceptable voltage range for each load in order to select an appropriate voltage control technique. But, because of low availability of DC appliances, most SAPS will be based on AC bus in the power range > 1 kW. For power levels exceeding 5 kW the AC system will be suited for three-phase loads. AC systems have to maintain their frequency within a certain limit (about ± 2%). Mismatch between power generated and power consumed causes the system frequency to drift: overload pulls the frequency down while less load spins the frequency up. This is not the case in large national grids where mismatch easily gets absorbed due to the size and inertia of the grid. Voltage level within limit (about ± 10 %) is of course an issue in AC systems as it is in DC systems, even though DC systems can tolerate larger voltage fluctuations. Wind power fluctuates within minutes whilst solar and river-hydro power fluctuates on longer terms, hours and days respectively. This leads to a system where it is difficult to provide a stable power supply. Typically penetration of wind power in a wind-diesel SAPS without any other energy storage than the diesel, is limited to approximately 30 %. There might also be some fluctuations on the demand side, when additional load is added and the renewable power input is low the system may have a shutdown. Excess energy has to be dumped when the renewable power input is high and the load demand is low. Possible solutions to these challenges:

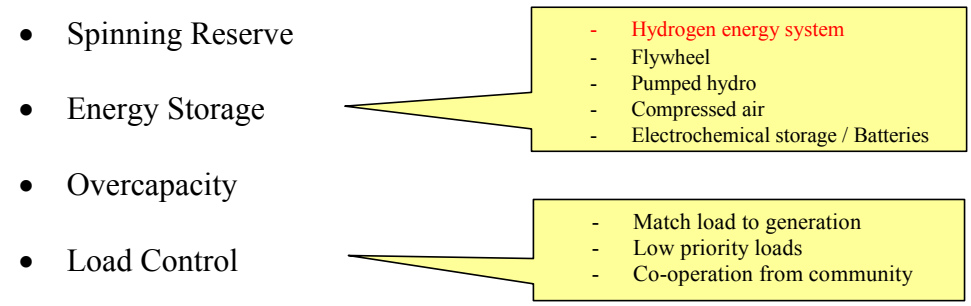

Usage of spinning reserves or oversized storage capacities in order to cover the load would not be economically justifiable for SAPS, but both load control and energy storage are viable solutions. Hydrogen technology has the potential to offer compact design, low operation and maintenance costs and a sustainable solution for energy storage aiming for 100 % penetration of renewable energy. Hydrogen technology implemented in a SAPS is in the forthcoming denoted as HSAPS.

1.2 The role of hydrogen in SAPS (HSAPS) and its market

A HSAPS is a stand-alone power system that converts excess electricity from renewable energy in the system into hydrogen for chemical energy storage. This chemical energy can be re-electrified in the system during deficit energy supply from the renewable energy sources. The hydrogen subsystem, also called a hydrogen-loop, comprises an electrolyser for conversion of water and electricity to hydrogen, a hydrogen storage unit, and a fuel cell for re-electrification of hydrogen with water as a by-product. The excess heat may also be of value for the user. Figure 1.1 shows a schematic where the hydrogen-loop enables an energy storage option for the renewable energy sources in order to secure the energy supply and power quality to the end user.

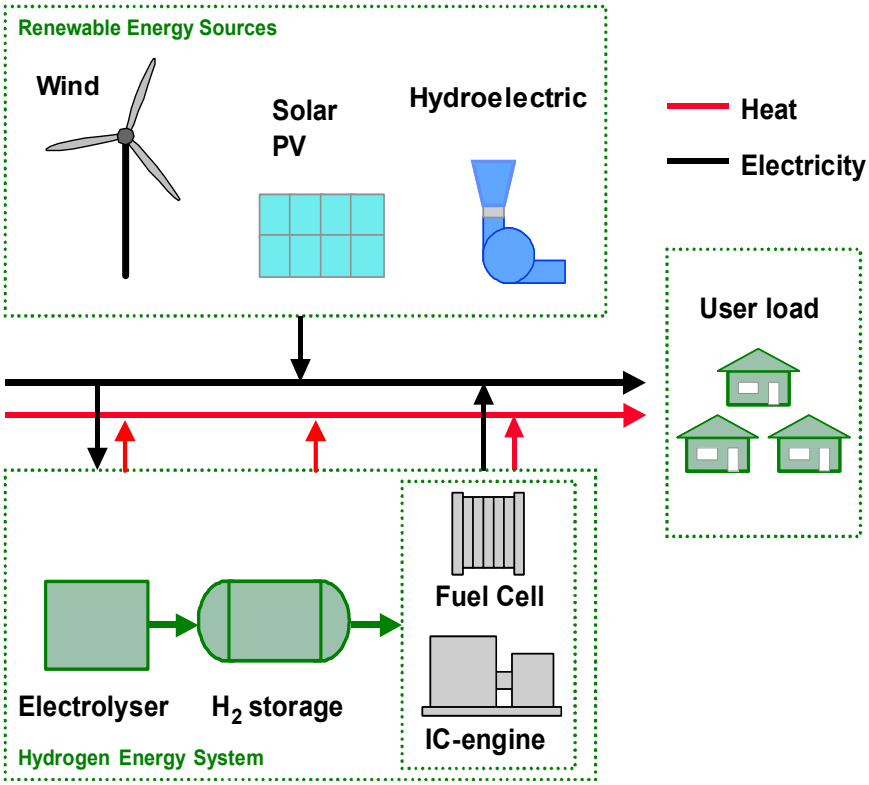

Figure 1.1 Schematic of a HSAPS, the hydrogen energy system enables an energy storage option for the renewable energy resources.

A preliminary market study from the literature indicates a market potential in Europe of 450 – 600 million euro for SAPS sizes up to about 300 kW in the midterm 2005, and some 20 billion euro in the long term [6]. However, this study was based on counting the number of actual areas in Europe where an implementation of a HSAPS based on wind energy could be appropriate. No other external factors were included.

In order to asses the European market potential for introduction of hydrogen into SAPS, a market analysis has been performed by [2]. A categorisation of the market segments was done and the three main segments are shown in Figure 1.2.

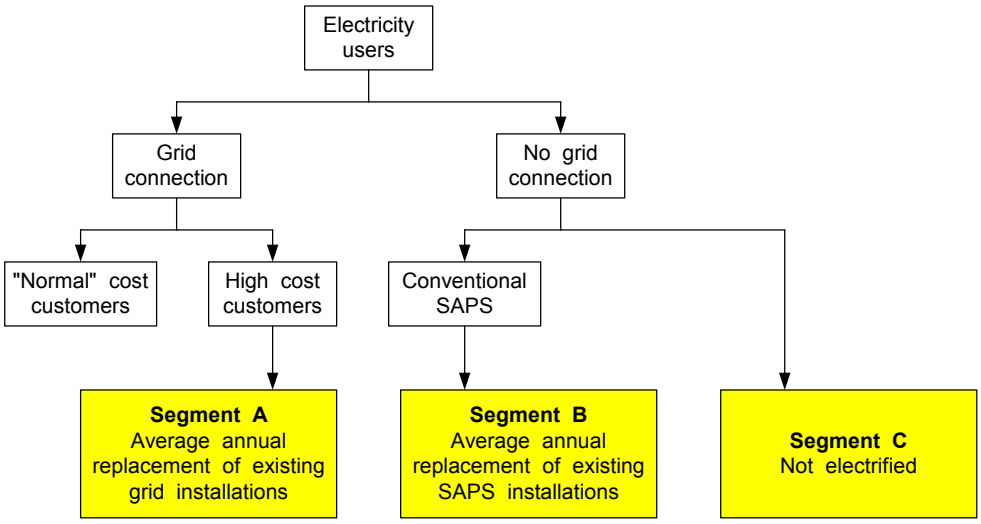

Figure 1.2 Market segments for HSAPS.

These segments can again be divided into four end-user categories:

1. Residential
2. Agricultural
3. Commercial
4. Public services

The actual market analysis for Europe was performed by directing questionnaires to energy authorities, statistical agencies, users and operators of existing SAPS and other interested parties. For evaluation of hydrogen technology and costs, two questions were raised: "Is hydrogen technology ready for SAPS?" and "What steps should be taken in order to get it ready?" In order to answer these questions, techno-economic modelling of hydrogen in existing SAPS along with evaluation of external factors such as general public and political opinions were conducted. The results from the evaluation were given in a highly qualitative manner where technology maturity, cost reduction and demonstration were given the highest priority. The other factors were environment, information dissemination and regulation/legislation. More information about this HSAPS project is found at www.hsaps.ife.no.

1.3 Literature study

Several experimental studies of hydrogen systems based on renewable energy have been carried out during the last decade. Many of these projects investigate(d) the hydrogen production performance. However, only projects concerned with a stand-alone application on both the electrolyser and the fuel cell implemented into the hydrogen subsystem will be considered in this literature survey. Eight experimental projects that investigate a complete HSAPS based on renewable energy are presented in Table 1.2. Common for these projects was a focus on energy efficiencies and the interplay between the electrolyser and the photovoltaic array. To date, very few HSAPS projects have been based on wind energy; only one wind-HSAPS project is

presented in this literature study. Many of the electrolysers were alkaline and operated at low pressure. Storage of the hydrogen was restricted to gaseous or metal hydride solutions. The fuel cells were often based on proton exchange membrane (PEM) technology. Comparison of the different projects indicates that the auxiliary equipment (switches, valves, compressors etc.) often was the main reason for plant shutdown and low energy efficiencies. Academic communities initiated some of the projects, other by private persons or industry. Many of the projects have also been carried out by governmental research organisations.

Table 1.2 Important HSAPS projects. In this table; PEM = proton exchange membrane, PAFC = phosphoric acid (fuel cell), and η_{H2} = hydrogen round-trip efficiency, which includes the electrolyser efficiency, the H_2 storage efficiency, and the fuel cell efficiency

Project name [Ref.]	Electrolyser		Storage			Fuel Cell		η_{H_2} [%]
	Type	Size [kW]	Type	Compression work by:	Capacity [Nm^3 H_2]	Type	Size [kW]	
NEMO (-98) [7]	alkaline	0.8	Pressurised vessel, 25 bar	compressor	200	PAFC	0.5	18-25
Self-sufficient Solar House (-96) [8]	PEM	2.0	Pressurised vessel, 28 bar	electrolyser	400	PEM	3.5	~34*
SAPHYS (-97) [9]	alkaline	5.0	Pressurised vessel, 200 bar	compressor	120	PEM	3.0	~23*
Trois Riviéres [10]	alkaline	5.0	Pressurised vessel, 10 bar	compressor	40	PEM	5.0	~28
INTA (-93) [11]	alkaline	5.2	Metal Hydride and Pressurised vessel, 200 bar	compressor	24 / 9	PAFC	10.0	(28-35)**
SCHATZ (-93) [11]	alkaline	6.0	Pressurised vessel, 8 bar	electrolyser	60	PEM	1.5	~34*
PHOEBUS (-99) [12]	alkaline	26.0	Pressurised vessel, 120 bar	compressor	3000	PEM	5.6	(33-36)**
SWB (-98) [13]	alkaline	100.0	Pressurised vessel, 30 bar	electrolyser	5000	PAFC	80.0	~35**

*The efficiency does not include the auxiliary power used by the electrolyser control system.
**The energy needed for hydrogen gas treatment (drying and/or compression work) not included in the hydrogen round-trip efficiency calculation. Inclusion of this energy loss parameter lowers the efficiency with about 5 – 8 %.

NEMO (Finland)[7]

The Solar Hydrogen Pilot Plant (1-2 kWh/day load) project in Finland was divided in two phases. The objective of the first phase (1990 – 92) was to demonstrate the technical feasibility of the components and the integrated system. The objective of the second phase was to improve the round-trip efficiency of the seasonal storage (electrolyser, hydrogen storage and fuel cell) and the reliability by computational and experimental methods. The system consisted of:

- Photovoltaic array with peak power 1.3 kW_{peak}.
- A 0.8 kW alkaline electrolyser.
- A pressurised steel vessel at 25 bars with hydrogen capacity of 200 Nm^3.
- A 0.5 kW phosphoric acid fuel cell.
- Lead-acid batteries with a capacity of 12 kWh.

The ON/OFF control of the electrolyser and the fuel cell (the main system control action) is based on the battery state-of-charge. The state-of-charge is calculated by

integration of the charge/discharge current. The objective of the system control is to maximise the direct energy flow from the photovoltaic array to the electrolyser whenever the electrolyser is ON. The battery is used only to level the current variations from the photovoltaic array and the load at night. Time of day limit was also used to increase the average direct current input from the photovoltaic array to the electrolyser. In order to achieve better overall efficiency and avoid extra cost for converters, the system components were connected directly in parallel. But direct coupling calls for careful matching of the different components. The voltage of the photovoltaic array and the fuel cell were both high enough to charge the battery, and the voltage required by the electrolyser was low enough to be powered by the battery.

A test-run during August-September (33 days) 1991 revealed that the system auxiliaries (valves, switches etc.) demanded an average of 63 % out of the total energy balance of 143 kWh. Thus the optimisation of the system auxiliaries was as important as optimising the components itself, especially for this small-scale system. The photovoltaic array was on the other hand reported to operate close to the maximum power point and no maximum power point tracker was needed. To operate 100 % self-sufficient in Helsinki, the photovoltaic array output power had to be sized 3 times as large as the load. The fuel cell reached a voltage efficiency of 60 %, but hydrogen losses due to open-end stack construction and the electric losses due to the pre-heating decreased the operational efficiency, thus the low temperature polymer electrolyte membrane fuel cell was considered as a better solution for a fluctuating system as the solar hydrogen system.

The NEMO project indicates that the most important loss mechanisms in the storage system are the conversion losses in the electrochemical components. Thus the voltage and current efficiencies is of great importance to optimise the hydrogen storage subsystem. The power consumption of the process control units may be significant, especially in small applications. Therefore one of the main tasks in optimising small-scale system would be minimising the power consumption of this units.

Reported component degradation:
After about 2000 hours of operation during three years, the voltage efficiency of the 0.8 kW alkaline electrolyser was reported to decrease from 75 % to 73 %. The 0.5 kW phosphoric acid fuel cell had a conversion efficiency decrease from 38 % to 31 %. The decrease was suspected to be due to leakages in the fuel cell stack.

Self-Sufficient House in Freiburg (Germany)[8]
An energy self-sufficient solar house in Freiburg, Germany was build by The Fraunhofer Institute for Solar Energy Systems. The households total energy demand is entirely supplied by solar energy. The system consisted of:

- Photovoltaic array with peak power 4.2 kW_{peak}.
- A 2.0 kW PEM electrolyser.
- A pressurised steel vessel at 28 bars with hydrogen capacity of 400 Nm^3.
- A 3.5 kW PEM fuel cell.
- Lead acid batteries with capacity of 20 kWh.

The system control was based on battery state-of-charge. All peripheral parts of the system, like valves, sensors and gas analysis, were energy optimised to be about 75 %

efficient. Due to problems with an alkaline electrolyser, the institute developed its own polymer exchange membrane electrolyser.

The loss of battery capacity over three years of operation underlines the need for an advanced state-of-charge control algorithm. Except for a short breakdown of the fuel cell, all the energy was delivered by the stand-alone power system. The author expects further optimisation during PV, battery and electrolyser operation by using a DC/DC converter between the electrolyser and system bus, even though Vanhanen [7], amongst others, suggests that use of direct coupling is suited for these small-scale power systems. The fuel cell was connected to the system with a DC/DC to match 48 V system of the house. The total energy usage of the solar house is about 13 times less than the total energy usage in a normal house in Germany.

Reported component degradation:
No information about any component degradation was given.

SAPHYS (Italy, Norway, Germany)[9]
The two main objectives of the SAPHYS project were to assess the efficiency of hydrogen used as storage medium of solar electric energy and to design a HSAPS for unattended operation. The SAPHYS plant configuration consisted of:

- Photovoltaic array with peak power of 5.6 kW_{peak}.
- A 5.0 kW alkaline electrolyser.
- A pressurised steel vessel at 200 bars with hydrogen capacity of 120 Nm^3.
- A 3.0 kW PEM fuel cell.
- Lead-acid batteries with capacity of 51 kWh.

The photovoltaic array supplied energy to a common DC bus bar interconnecting an electrolyser, a battery, a fuel cell and the load. The electrolyser and the fuel cell were connected to the DC bus bar with a step-down and a step-up converter respectively.

The battery state-of-charge was used as a system control parameter. It was pointed out that the determination of battery state-of-charge is sensitive to errors in current measurement. It is also difficult to base the battery state-of-charge on the battery voltage due to its dynamic fluctuation during charge and discharge. It was suggested to implement a battery state-of-charge correction procedure into the energy management system.

In general, both electrolyser and plant efficiencies were encouraging and compared well with other experimental studies. The electrolyser was demonstrated to be a mature technology and reliable enough for operation via a photovoltaic array. However, faults in the auxiliary equipment required for system operation such as water demineralisation unit, compressed air treatment unit and inert gas were the main reason for plant shutdowns. The PEM fuel cell appeared to be suitable for small-scale systems. However, the PEM fuel cell did suffer from some long shutdown periods and freezing temperatures. It was stated that maintenance had to be done at least once before wintertime.

Reported component degradation:
No information about any component degradation was given.

Trois Riviéres (Canada)[14]
A stand-alone renewable energy system based on hydrogen production from wind and solar energy was developed and installed at the Hydrogen Research Institute (HRI) in Canada. The system consisted of:

- Wind turbine with peak power of 10.0 kW_{peak}.
- Photovoltaic array with peak power of 1.0 kW_{peak}.
- A 5.0 kW alkaline electrolyser with compressor.
- A pressurised steel vessel at 10 bars with hydrogen capacity of 40 Nm^3.
- A 5.0 kW PEM fuel cell.
- Lead-acid battery with capacity of 42 kWh.

The goal of the system was to demonstrate that an autonomous energy system may be realised with long-term storage of energy in the form of hydrogen, and that operation of such a system was safe and reliable. The system was mounted on a DC-bus bar with DC/AC-inverters installed in order to cover an AC load. Successful automatic operation and performance of the energy system laboratory showed that an autonomous RE system based on electrolytic hydrogen can be used for stand-alone power applications. The developed power conditioning devices gave proper matching among the components. The performance analysis was undertaken by changing the load profile, the programmed output pattern (programmable power source) and the energy levels in the control algorithm. The developed control system and the power conditioning devices were tested successfully for autonomous operation. Furthermore, storage, purification, drying, and re-utilization of O_2 as oxidant for the PEM fuel cell system were also successfully demonstrated.

Reported component degradation:
No specific information about any component degradation was given.

INTA (Spain)[11]
The INTA program on hydrogen technology defined in 1989, consisted of two main objectives: the use of hydrogen as a storage medium for solar electricity; the use of integrated systems for manned space missions. Since 1994 the activities have been concentrated on the utilization of hydrogen in fuel cells as well as a clean fuel for transportation. The system consisted of:

- Photovoltaic array with peak power 8.5 kW_{peak}.
- A 5.2 kW alkaline electrolyser.
- A pressurised steel vessel at 200 bars with hydrogen capacity of 9 Nm^3.
- A metal hydride unit with hydrogen capacity of 24 Nm^3 (maximum 10 bars).
- A 10 kW phosphoric acid fuel cell.

The system components were integrated on a DC mini-grid. The electrolyser could be powered in three different ways: direct connection to the photovoltaic array (with constant or variable number of active cells), through a Maximum Power Point tracker (a DC/DC converter that allows the photovoltaic array to work at its maximum power), or by means of a power supply. Part of the fuel cell generation covers an AC grid load through a DC/AC - inverter.

The most critical component of the system was the pneumatic feed water pump of the electrolyser. No solution was found to the periodic malfunction of the pump. It was stated that it was difficult to find components of optimum size for small-scale integrated systems (1994) operated on a DC mini-grid. Operation of electrochemical components like fuel cells and electrolysers on a DC mini-grid requires careful design of components in terms of number of cells to be installed.

Reported component degradation:
No degradation in the electrolyser performance was reported after 600 operation hours.

SCHATZ (USA)[11]
The goal of the project was to demonstrate that hydrogen can operate as a practical energy storage medium for solar energy and convert the chemical energy back to electric energy via a fuel cell. An air compressor (600 W) for aeration of an aquarium operated as the load. The load was connected to the HSAPS via a DC/AC inverter. The system consisted of:

- Photovoltaic array with peak power of 9.2 kW_{peak}.
- A 6.0 kW alkaline electrolyser.
- A pressurised steel vessel at 8 bars with hydrogen capacity of 60 Nm^3.
- A 1.5 kW PEM fuel cell.
- Lead-acid batteries with capacity of 5.3 kWh.

The photovoltaic array and the electrolyser were directly coupled. At nominal operating conditions, the photovoltaic array voltage and electrolyser voltage matched well. However, an increase in voltage mismatch was found, especially with an old cold electrolyser and a warm photovoltaic array.

A charging flag indicated whether the battery was recently charged or discharged. If the battery had been recently discharged, the control system determined the minimum number of sub-arrays to switch to the load that would provide enough PV current to exceed the current drawn by the inverter. Excess current from these sub-arrays was used to charge the battery. The rest of the sub-arrays were switched to the electrolyser. When the battery had been recently charged, the control system allocated the maximum number of sub arrays, which would not cause the PV current to exceed the inverter current. The battery provided the deficit. The rest of the PV sub arrays were switched to the electrolyser. When there was insufficient insolation to provide PV power to the load, the control system started up the fuel cell.

The most frequent cause of shutdowns was a hood exhaust error caused by a defective switch. In addition to the unscheduled shutdowns, the electrolyser required extensive inspections and maintenance.

Reported component degradation:
According to the manufacturer (Teledyne) of the 6.0 kW alkaline electrolyser, the stack voltage is expected to increase 3.3 V over an operation life of about 25.000 hours. After a total hydrogen production of 4556 Nm^3 (about 4000 operation hours) from 1992 to 1998, no noticeable degradation was reported. After 5 months of operation, the PEM fuel cell showed signs of serious degradation. After further

problems with the fuel cell, it was in 1996 decided to remove the stack from the system.

PHOEBUS Jülich (Germany)[12]
The PHOEBUS demonstration plant supplied energy to part of the Central Library in Forschungszentrum Jülich, Germany, for 10 years. The technical feasibility of a self-sufficient energy supply system based on solar energy, battery, and hydrogen storage was demonstrated. The system consisted of:

- Photovoltaic array with peak power of 43 kW_{peak}.
- A 26.0 kW alkaline electrolyser.
- A pressurised steel vessel at 120 bars with hydrogen capacity of 3000 Nm^3.
- A 5.6 kW PEM fuel cell.
- A system of 110 lead acid batteries with total capacity of 304 kWh.

The electrolyser and the fuel cell were connected to the 200 V – 260 V DC bus bar by DC/DC converters. The DC/DC converter between the photovoltaic array and the DC bus bar was omitted for nine months in 1997. Because of that, the photovoltaic output was reduced by 3 %. At the same time, the loss in the DC/DC converter, which was around 10 %, was also reduced and the overall efficiency of the system increased.

The energy required to compress hydrogen by air-driven pneumatic compressor was more than 100 % of the total energy stored. Thus, a metal membrane compressor replaced the pneumatic compressor and the energy demanded for compression was reduced to 9 %. It was learned that it is possible to eliminate the compressor by producing high pressure via the electrolyser (~120 bars) and reduce the compression work to only 3 %. However, due to poor flange construction the PHOEBUS project experienced high hydrogen leakage rate (about 1 m^3/day) in the high-pressure vessel. A total of 19 % of the annual production was thus lost.

PHOEBUS Jülich demonstrates that an electrical energy supply with purely renewable energy without connection to the public grid is basically possible. Plant operation is fully automated. Plant costs can be further decreased with standardized system-engineering solutions and with market introduction of electrochemical energy converters (electrolysers and fuel cells).

Reported component degradation:
The electrolyser operated without any major problems for 10 years. The electrolyser energy efficiency (according to the 1st law of thermodynamics) was reported to decrease from about 87 % down to about 83 % during the last five years, but still the electrolyser energy efficiency was above 80 % after ten years of operation, which is quite encouraging.

In the first phase of operation, a 6.5 kW alkaline fuel cell (Siemens BZA 4-2 type) was introduced into the system. During operation, it was found that the alkaline fuel cell was not reliable. Afterwards an effort was made to develop a 5 kW PEM fuel cell, but the targeted power level was not achieved. Finally, by the end of 1999 a PEM fuel cell was introduced, which functioned in the system until the end of the PHOEBUS operations without any problems. Because the fuel cell operation was not regular (three different fuel cells) no information about fuel cell-degradation was given.

Solar-Wasserstoff-Bayern Hydrogen demonstration project at Neunberg Vorm Wald (Germany)[13]

The aim of the Solar-Wasserstoff-Bayern (SWB) hydrogen project was to test, on an industrial demonstration scale, major technologies of the hydrogen cycle utilising electric power generated without releasing carbon dioxide. The system consisted of:

- Photovoltaic array with a maximum field capacity of 370 kW_{peak}.
- An alkaline pressure-type electrolyser, 100 kW, with a working pressure of 32 bars.
- A pressurised steel vessel at 30 bars with a hydrogen capacity of 5000 Nm^3.
- A 80 kW phosphoric acid fuel cell.

The large photovoltaic arrays feed power through maximum power point controlled DC/DC converters (also referred to as Maximum Power Point Trackers, MPPT, in the literature) to a common DC bus bar interconnecting the photovoltaic arrays, the electrolyser (connected by a DC/DC converter), and the AC grid, which was the load. The fuel cell was connected to the AC grid by a DC/AC inverter. Operation of the DC/DC converters and the DC/AC inverters was not immediately satisfactory, which was only partly to be explained by the prototype nature of these units (1997). Subsequent improvements, some of appreciable magnitude, proved necessary. Some improvements in the electrolyser stack design had to be done because of an increased O_2 in H_2 content. A total of three electrolyser stacks had to be replaced because of a number of problems, the reason for the last shutdown in 1998 was because of deficiencies in the cell voltage measuring lines. No battery is implemented into this HSAPS. The overall control strategy is to convert as much excess electric energy in system as possible into hydrogen for uninterrupted power supply. Load profile for small hospital on an island-site was emulated.

It was decided to decommission the alkaline fuel cell in 1994 because of several replacements of the stack. Experience with the alkaline fuel cell proved it to be too sensitive due to its complexity. Regarding the phosphoric acid fuel cell, major problems occurred that required extensive repairs and changes. Most of the difficulties originated in the associate peripheral systems, with very few in the fuel cell stack itself.

It was stated that several of the subsystems installed at the solar hydrogen facility failed to work at the start. Throughout the operation period, SWB was however able to solve the almost all the problems that occurred.

Reported component degradation:

Valuable knowledge to long-term operation of the phosphoric acid fuel cell was acquired. The approximately 450 starts and stops over a cumulative total of about 2600 operation hours resulted in a fuel cell decrease output of about 15 kW_{el}, i.e. 19 % reduction. In the period 1990 – 96, a 100 kW PEM electrolyser was tested by SWB solar electricity input [15]. This unit had to be shutdown after a total operating time of 2300 h only due to H_2 level in O_2 > 3 vol %. It must be stressed, however, that the electrolyser plant had been on stand-by for 50 000 h with a small protective polarisation current of about 150 mA in order to prevent corrosion on the cathode current collectors. Furthermore, an identical 100 kW PEM electrolyser was tested by Stellram SA, a metallurgical speciality company in Switzerland, some years earlier in

the period 1987 – 90 with a total operating time of 15 000 h with nominal operation at 400 A [15]. Also in this case the reason for shutdown was H_2 level in O_2 > 3 vol %. In both cases, post mortem analysis revealed that the Nafion® 117 was the weakest part in a PEM electrolyser regarding long-term performance.

1.4 Scope of work

The results of this thesis are divided in *two* main parts:

- Experimental part
  Report on the energy round-trip efficiency for a state-of-the-art hydrogen storage subsystem, in addition to gain more practical operation experience within hydrogen systems (transients, availability and controllability). Implement a control strategy for autonomous operation of the laboratory HSAPS.

- Computational part
  Utilise experimental data from the hydrogen system laboratory for development of detailed empirical computer models. The empirical models will be used for development and tuning of HSAPS control strategy algorithms.

A schematic of the general tools utilised and the structure of the work performed in order to accomplish the main goal of autonomous operation of a laboratory HSAPS is shown in Figure 1.3.

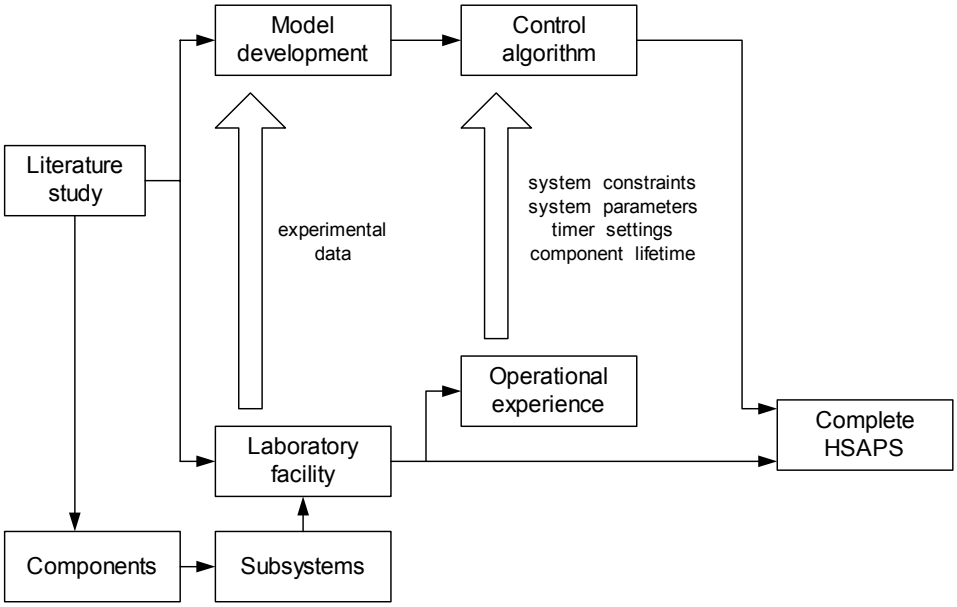

Figure 1.3 Schematic of the experimental- and computational work towards autonomous operation of the laboratory HSAPS.

A brief outline of the content in this thesis:

- Collection of experimental characteristics and hands-on experience from manual and autonomous operation of the laboratory HSAPS test-facility (Chapter 3 and Chapter 6)

- Simulations of annual HSAPS-performance in order to evaluate different control strategies for high-level energy management, using computer models calibrated with the experimental data collected in the laboratory (Chapter 4 and Chapter 5)

- Comparison of the metal hydride used in the laboratory with a pressurised steel vessel as two viable solutions for H_2-storage in small-scale HSAPS (Chapter 7)

- Use of electrolyser as a load control for a wind-HSAPS (Chapter 8)

References

1. European Commission, *Best Practice Projects Yearbook 1997-2000*. 2002: Brussels.
2. R.Glöckner, et al., *Market Potential Analysis for Introduction of Hydrogen Energy Technology in Stand-Alone Power Systems. Final report, EU/ALTENER Programme. Contract No. 4.1030/Z/01-101/200*. 2004, Institute for Energy Technology, Kjeller, NO-2027, 2004.
3. European Wind Energy Association EWEA, in *Windpower Monthly*. May 2003.
4. A report produced by ETSU for the DTI, *New and renewable energy prospects in the UK for the 21st century*. 1999. p. 164.
5. J.H.Bass, *The potential of combined heat and power generation, wind power generation and load management techniques for cost reduction in small electricity supply systems"*. 1987, University of Strathclyde. p. pp11-23.
6. M.Altmann, et al. *WhySE Wind-Hydrogen Supply of Electricity Markets-Technology-Economics*. in *Wind Power for the 21st Century conference*. 2000. Kassel, Germany.
7. J.P.Vanhanen, *On the performance of improvements of small-scale photovoltaic hydrogen energy systems*. 1996, PhD Thesis, Espoo, Finland.
8. K.Voss, et al., *The Self-sufficient Solar House in Freiburg- Results of 3 years of operation.* Solar Energy, 1996. **58**: p. 17-23.
9. S.Galli, et al., *Stand Alone Photovoltaic Hydrogen Energy System, SAPHYS.* 1997, ENEA, IFE, KFA.
10. K.Agbossou, et al., *Renewable systems based on hydrogen for remote applications.* Journal of Power Sources, 2001. **96**: p. 168-172.
11. T.Schucan, *Case studies of integrated Hydrogen Energy Systems*. 2001, IEA.
12. H.Barthels, et al., *Phoebus-Jülich:an Autonomous energy supply system comprising Photovoltaics, Electrolytic Hydrogen, Fuel Cell.* J. Hydrogen Energy, 1997. **23**(4): p. 295-301.
13. A.Szyszka, *Ten years of solar hydrogen demonstration project at Neunberg vorm Wald, Germany.* Int.J.Hydrogen Energy, 1997. **23**(10): p. 849-860.

14. K.Agbossou, et al., *Electrolytic hydrogen based renewable energy system with oxygen recovery and re-utilization.* Renewable energy, 2004. **29**: p. 1305-1318.
15. S.Stucki, et al., *PEM water electrolysers:evidence for membrane failure in 100kW demonstration plants.* J.Appl.Electrochem, 1998. **28**: p. 1041.

2. Concepts of HSAPS

2.1 Elements of a general system

The elements of a system comprises of *components*, *attributes* and *relationships*, described as follows [1]:

1. *Components* are the operating parts of a system consisting of input, process and output. Each system component may assume a variety of values to describe a system state as set by control action and one or more constraints.
2. *Attributes* are the properties of the components of a system. These attributes characterize the system.
3. *Relationships* are the links between the components and attributes.

A system is a set of interrelated components working together toward some common objective. The set of components has the following properties:

1. The properties and behaviour of each component of the system have an effect on the properties and behaviour of the system as a whole.
2. The properties and behaviour of each component of the system depends upon the properties and behaviour of at least one other component in the system.
3. Each possible subset of components has the two properties listed above; the components cannot be divided into independent subsets.

As every system is made up of components, any component can be broken down into smaller components. If two hierarchical levels are involved in a given system, the lower is conveniently called a *subsystem*. It is important to define the system under consideration by specifying its limits or boundaries. Everything that remains outside the system is considered to be the *environment*. Flow components like material, energy and/or information must often pass through the boundaries as *inputs* and *outputs* to and from the system. Flow components that enter the system in one form and leave in another are usually called *throughputs*. Constraints placed on the system will limit its operation and define the boundary within which the system is intended to operate. Similarly the system puts constraints and boundaries on its subsystems. The viewpoint of the systems looks at a system from top down rather than from the bottom up. Attention is first directed towards the system as a black box that interacts with its environment. Next, the attention is focused on how the smaller black boxes (subsystems) combine to achieve the system objective. The lowest level of concern is then the individual components.

2.2 Elements of the HSAPS

The main objective of a SAPS is, as already mentioned in Chapter 1, to supply a certain load requirement at a remote location where connection to a main grid seems costly and/or difficult. It is very important to define the consumer load and expected deviations from this load profile, in addition to obtain realistic time data series for the renewable energy profiles when designing a HSAPS. A system configuration describes how the involved components (subsystems) are placed and interconnected; this system configuration is first of all a function of the load profile and the renewable energy profile. From the system configuration it is possible to define the different

modes of operation for the system. Based upon the system configuration and modes of operation it is further possible to determine the sizes of the components and the control strategy through simulations of the system. Thus the renewable energy- and load profiles set the overall system boundaries.

Figure 2.1 shows an example of a HSAPS based on solar energy. This system configuration is a function of solar radiation data and the load profile for a single household. Solar radiation data has predictable periods within days and seasons, but from the viewpoint of the earth's surface lesser predictable radiation within the hours due to expected disturbance from clouds. The load profile for a typical household is characterised by both energy requirements and power requirements. The load profile is energy determined by the requirements of rather constant loads such as space- and water heating and illuminating purposes, which is easy to predict, and power requirements because of the inhabitants' more unpredictable use of electric articles like e.g. microwave ovens, laundry- and dishwashers. The system configuration in Figure 2.1 illustrates three main components; PV arrays, batteries and the hydrogen subsystem. Depending on the amount of actual excess solar power and amount of excess solar energy already stored in the system, the solar power has the options to flow through three different pathways as indicated.

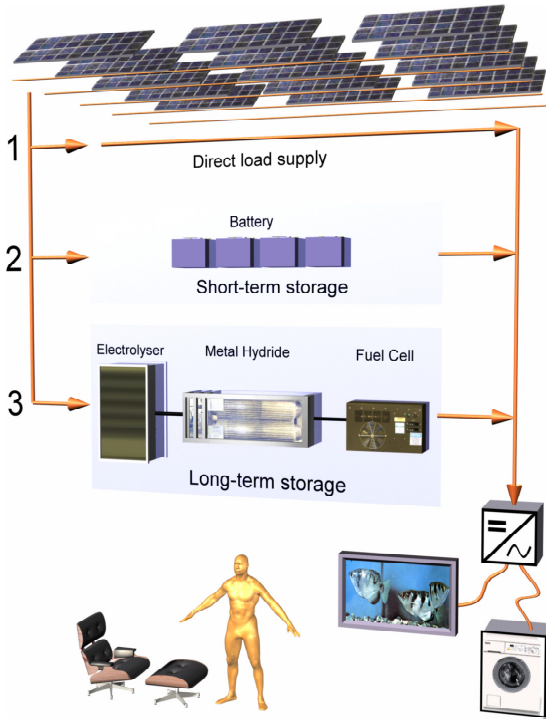

Figure 2.1 HSAPS system configuration where the batteries are installed as short-term energy storage, basically supplying power-requiring loads. The hydrogen subsystem is installed as long-term energy storage basically supplying energy-requiring loads. (Figure made by Bård A. *Melk Design*)

2.2.1 Scaling of components

The solar energy can flow directly to the load (1), and/or through the batteries, which are scaled for power requiring loads and short-term operation of any type of load (2), and/or through the hydrogen storage, which is basically scaled for energy requiring loads on seasonal/long-term basis (3). Scaling of the batteries for power requirements can though be a problem because also the energy capacity will be altered. If the load

calls for a high power peak and the battery is scaled to manage this, the battery energy capacity might be unreasonable large and to costly. This is not the case for the hydrogen subsystem, because the energy storage size (the hydrogen) and the power source size (fuel cell) are rather physically independent of each other. A thorough analysis on altering the fuel cell and electrolyser sizes is not performed in this thesis as the main focus is on the actual components installed in the HSAPS laboratory, which will be presented in detail in Chapter 3. However, with an attempt to express the life cycle cost of a HSAPS, a simulation study is performed in Appendix F in order to find the specific combination of battery- and hydrogen storage (metal hydride) size giving the minimum life cycle cost. The criterion for all combinations of battery- and metal hydride sizes is that an annual load requirement of 650 kWh/year must be balanced.

2.2.2 Modes of operation and control strategy

The hydrogen subsystem comprises an electrolyser and a fuel cell as processing units and a hydrogen storage as a static unit. While the PV array, the batteries and the load are always connected, the components of the hydrogen subsystem are closely related to three modes of operation that have been identified, where the following individual components are involved;

1. Hydrogen charging → PV array, electrolyser, batteries and load
2. Hydrogen balancing → PV array, batteries and load
3. Hydrogen discharging → PV array, fuel cell, batteries and load

With the modes of operation defined, a control strategy must be implemented in order to switch between the proper modes at any time to optimize the total system. The control strategy must ensure stable system operation towards highest energy efficiency possible with minimal wear on the individual components. This is a matter of compromise that often only can be solved by trial and error. In order to optimize the control strategy it is important for the controller to know the *state of system*. The state of system for the HSAPS is closely related to the energy available in both the battery and the hydrogen storage. Other important parameters for determining state of system are the actual balance of the power flow through the system and if possible, load and weather prediction. The general control scheme with the different modes of operation is given in Figure 2.2.

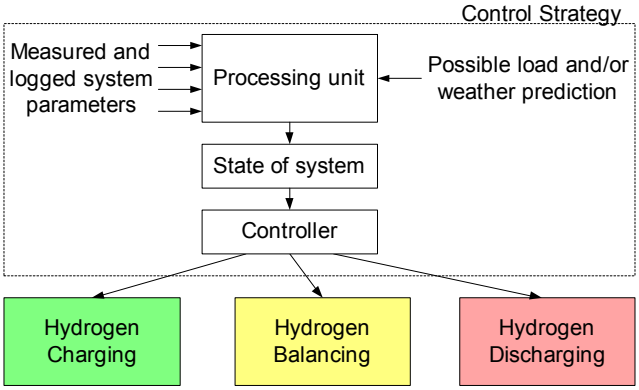

Figure 2.2 The control scheme of an HSAPS with the different modes of operation.

Two different methods for high-level control of an HSAPS are proposed in this thesis. The proposed control strategies are compared through computer simulations with a conventional control algorithm that is exclusively based on the energy content in the battery. This comparison study is the subject of Chapter 5. In order do develop a robust controller it is important to identify and classify the key parameters that influence the system. For each of the control strategies, these key parameters are classified and listed in Appendix D, which is related to Chapter 5.

2.2.3 Component characteristics in a power system based on hydrogen

Two types of characteristics are important for comparison and scaling of the components in a hydrogen system. These have also been identified in a larger hydrogen system project [2]:

-Specific component characteristics

- Component efficiency
- Component cost
- Reliability
- Acceptance
- Safety

-Component input/output characteristics

- Current, voltage, and power flow
- Hydrogen flow
- Heat transfer

2.2.4 System attributes and relationships

The attributes of the HSAPS are the electric energy capacitive properties of both the battery and the hydrogen subsystem, in addition to high power density related to the battery and high energy density related to the hydrogen subsystem. The electric energy capacitive property of the hydrogen subsystem is further related to the fluid capacitive property of the hydrogen storage unit.

2.2.5 Measures of performance

Some critical parameters must be identified in order to measure and evaluate the system performance. Parameters relevant to the HSAPS on annual basis are:

- Total system energy efficiency
- Comparison of initial and final hydrogen content
- Wear on components given in operation hours and on/off switching
- Reliability and stability
- System cost

While the four last parameters are self-explanatory, the first parameter will be explained in detail; the total system efficiency is dependent on fractions of the solar energy flowing through the three different paths indicated in Figure 2.1. Typically energy efficiencies for the components involved in the HSAPS are given in Table 2.1.

Table 2.1 Typical component energy efficiency

Photovoltaic arrays	η_p	0.13
Battery	η_b	0.80
DC/DC Converter	η_c	0.95
Electrolyser	η_e	0.75
Fuel Cell	η_f	0.50

The energy efficiency (E_X) for each of the three different paths is simply defined as:

$$E_x = \frac{\text{output power}}{\text{input power}} \tag{2.1}$$

Highest efficiency is accomplished in situations where the photovoltaic arrays directly serve the load. If a DC/DC converter or a DC/AC inverter is coupled between the HSAPS and the load, the efficiency for this energy vector is given by:

$$E_{Direct} = \eta_p \cdot \eta_c \approx 0.12 \tag{2.2}$$

Intermediate energy storage and electrochemical energy conversion in the battery will decrease the efficiency of the energy flow from source to load:

$$E_{Battery} = \eta_p \cdot \eta_b \cdot \eta_c \approx 0.1 \tag{2.3}$$

The hydrogen subsystem energy path yields the lowest energy efficiency:

$$E_{Hydrogen} = \eta_p \cdot \eta_e \cdot \eta_f \cdot \eta_c \approx 0.05 \tag{2.4}$$

The total system efficiency (E_T) is then expressed by:

$$E_T = \frac{SE_T(aE_{Direct} + bE_{Battery} + cE_{Hydrogen})}{SE_T} \tag{2.5}$$

Where a, b and c are the fractions of the total solar energy (SE_T) flowing through each of the pathways. Equation 2.5 underlines the importance of a smart control strategy, which optimizes the solar energy flow through the *Direct* energy path between the photovoltaic arrays and the load, thus minimizing the need for energy storage.

References

1. B.S.Blanchard and W.J.Fabrycky, *System Engineering and Analysis*. 1990, New Jersey: Prentince-Hall, Inc.
2. A.de Groot and M.Bracht, *Design Evaluation and System Comparison Guidelines*. 2001, IEA.

3. The HSAPS test-facility

The motivation for the construction of the HSAPS laboratory was to develop a flexible test-facility for investigations of the properties of the different components and different configurations within a HSAPS. The experimental data obtained from the characterisation of the components were applied for development of detailed empirical component models. The computer model of the HSAPS was used for development and optimisation of control strategies. The component models for the HSAPS laboratory will be presented in Chapter 4. Along with the valuable information concerning practical operation of a small-scale HSAPS, the test-facility has also a great value as a demonstration site for the industry, politicians, educational institution, and research communities.

3.1 System overview

The HSAPS laboratory test-facility has a modular structure in order to achieve a high degree of flexibility with respect to type of components and system to be investigated. Future expansion of the test-facility is taken into consideration by using solutions with wide working ranges. The test-facility is designed for testing of individual components, for subsystems or for complete HSAPS operation. The complete HSAPS in this study comprises of a programmable power supply, electrolyser, H_2 purification unit (99.999 % H_2 quality), a metal hydride storage (MH-storage), a lead-acid battery, a fuel cell, and a programmable load, Table 3.1.

The test-facility is equipped with $H_{2(g)}$, $N_{2(g)}$, and $Ar_{(g)}$, cooling water, deionised water supply and utility power (230 V_{AC}, 400 V_{AC}, 24 V_{DC}, 12 V_{DC} and 5 V_{DC}). Control and data acquisition system is based on a PC with modular distributed I/O modules (NI, Fieldpoint), GPIB interface, mass flow readers/controllers, relays and valves for automatic and manual operation of the complete system or the individual components. The software for the control and data acquisition system is developed in LabVIEW. A multifunctional DAQ-card (200 000 samples/s, 16 bit) is also installed in the PC for investigations of voltage and current transients with 5 μs resolution.

Table 3.1 An overview of the HSAPS test-facility components (details of the components will be given in Section 3.2 and in Appendix A)

Component	Type	Manufacturer	Power [W]
PV array	Emulated by a power supply	Agilent, USA	max 4800
Electrolyser	PEM	Fraunhofer ISE, Germany	1500
Oxygen remover	Catalytic	Aquagas, Sweden	200
Hydrogen dryer	Molecular sieve	Aquagas, Sweden	1800
Fuel Cell	PEM	H-power, USA	500
Electrical load	Programmable load	Kikusui, Japan	Max 600
			Capacity [kWh]
Battery	Lead-acid (4X12 V)	MicroKiel, Japan	2.1
Hydrogen storage	Metal hydride	GfE/HERA, Germany/Canada	42 (LHV)

All the components are commercially available, and less attention is paid to individual component optimisation since the main focus of this work has been the study of the

system as a whole. The reason for simulating the photovoltaic array and the user load is to avoid uncertainty and possible failure that can divert the attention away from the hydrogen subsystem, which is the main feature of this study. A H_2 subsystem comprising of an electrolyser, H_2-storage, and a fuel cell is in the literature also referred to as the hydrogen-loop.

The system in this study will be based on solar energy as input and designed to supply a load varying between 0 – 500 W. Typical applications of such power systems could be for mountain cabins, telecommunication stations, signal beacons, among others. The basic idea is to connect the components in parallel without DC/DC converters in order to avoid the extra cost and loss of efficiency caused by this component [1]. Connecting the components in parallel without DC/DC converters gives however no degrees of freedom regarding the ability to regulate the actual power level of the different components. The only action possible in the HSAPS in this study is to switch the components either ON or OFF. The power levels are more or less predefined by the voltage levels chosen for the different components. Power to the hydrogen purification unit is currently supplied by the main grid, but is taken into account in the annual simulation runs to show the overall energy balance. A detailed study of energy consumed by the H_2 purification unit is given in Chapter 7. A schematic of the laboratory system is shown in Figure 3.1. The shaded area in Figure 3.1 named "Control unit/Switch" symbols the interface between software and hardware.

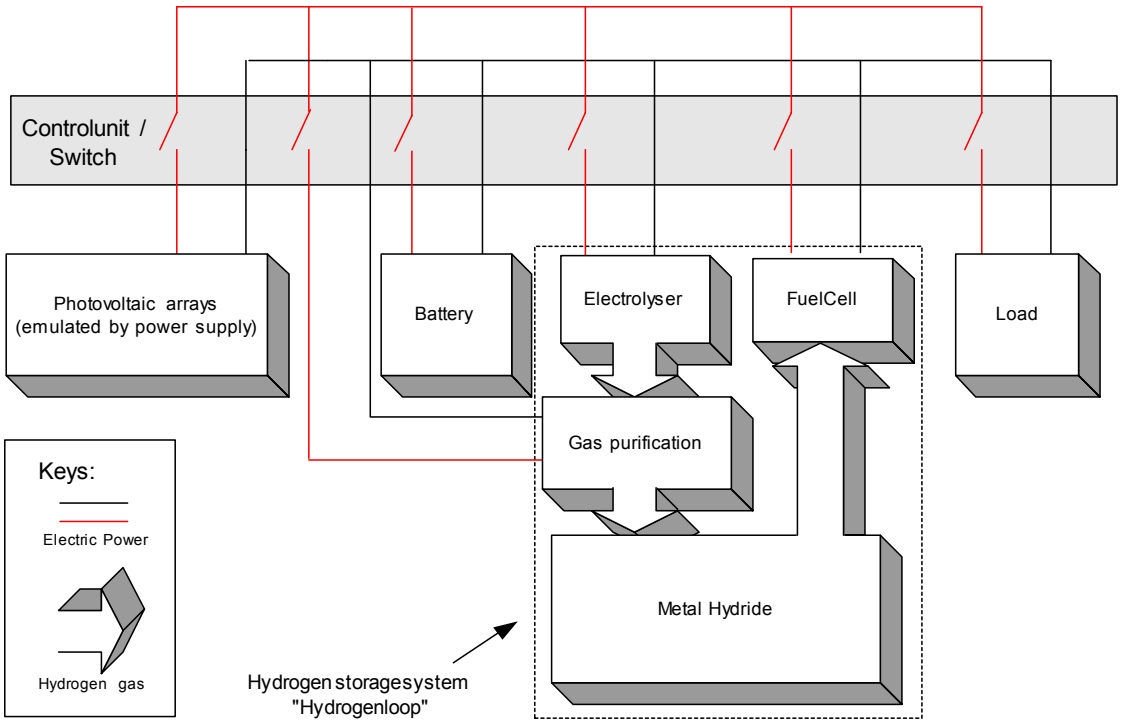

Figure 3.1a Schematic of the laboratory HSAPS test-facility.

A more detailed diagram of the hydrogen-loop, which represents the H_2 infrastructure in the HSAPS test-facility, is given in Figure 3.1b. The detailed diagram shows all the measuring points, the automatic controllers, and the manually controlled equipment.

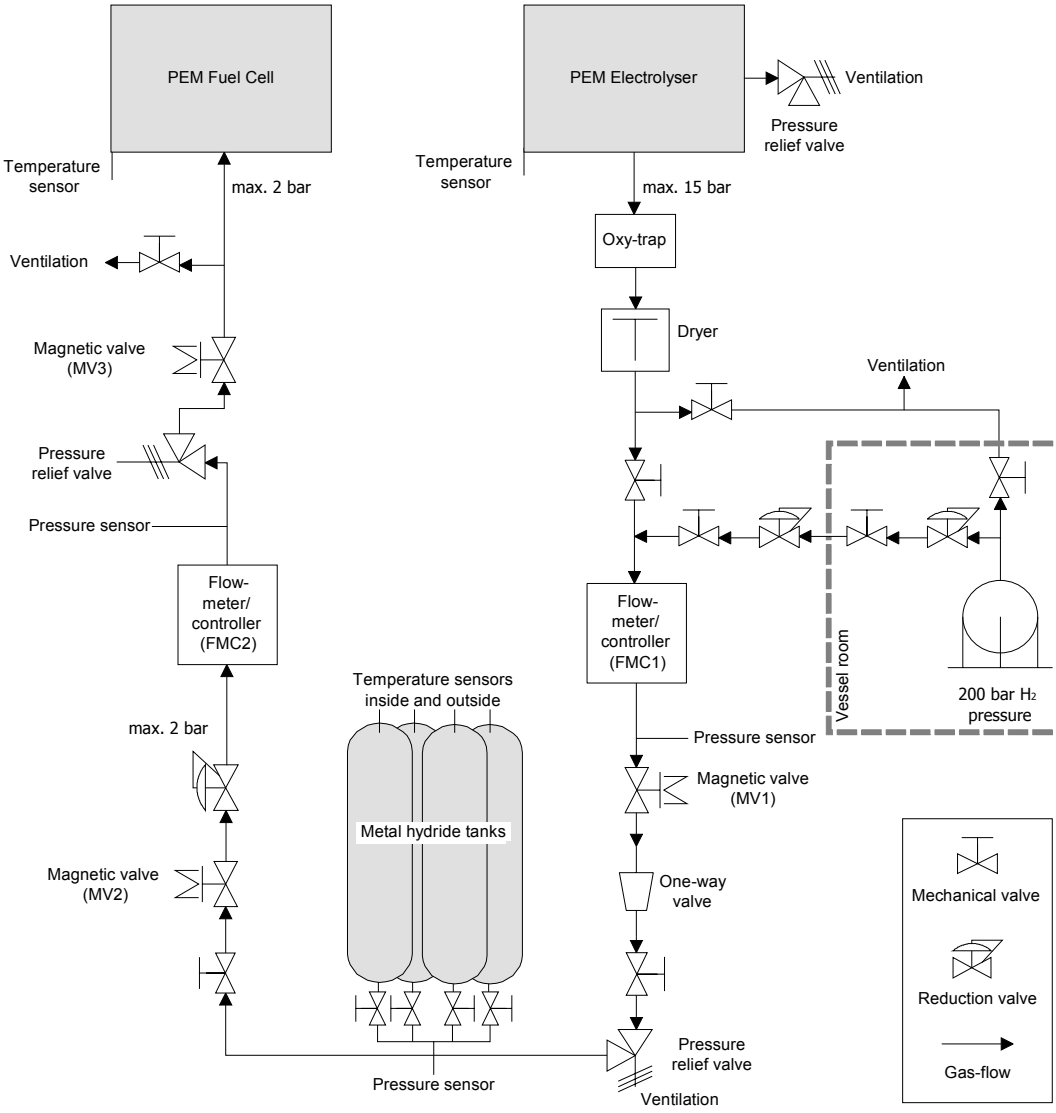

Figure 3.1b Schematic of the hydrogen-loop, showing the measuring points, the automatic controllers, and the manually controlled equipment.

The first task identified was to design the system with regard to parameters such as; type of components (choice of technology), capacity, and lifetime. In the following the reasoning for the selection of the main components in the hydrogen-loop is given.

Electrolyser

PEM electrolysers have some advantages compared to alkaline systems, especially when installed in a small-scale HSAPS:

- *Current density*: PEM electrolysers can operate at far higher current densities compared to alkaline systems. A PEM electrolyser can operate in the current-density range of about 1 – 2 A/cm^2 [2]. The PEM electrolyser used in this work operates at 0.6 A/cm^2 under nominal conditions. Alkaline electrolysers typically operate at maximum 0.2 – 0.6 A/cm^2. Higher current densities give more compact systems regarding both volume and mass.

- *Energy efficiency*: The energy efficiency for PEM electrolysers is often reported to be higher than in conventional alkaline systems and approximately the same for advanced alkaline electrolysers.
- *Maintenance*: The solid polymer electrolyte requires much less maintenance than the alkaline electrolyte.
- *Corrosion*: PEM electrolysers are in general subjected to corrosion to a much lesser degree than alkaline systems. Thus, a PEM electrolyser may be operated with much less or even without additional protective current, which the alkaline electrolysers require in order to reduce the corrosion problems during stand-by.

Disadvantages with PEM technology compared to alkaline electrolysers:

- At present expensive technology
- Requirement of ultra-pure water (about 1 μS/cm)

A PEM electrolyser rated at 1.5 kW (nominal) and a peak power of 1.7 kW was selected, manufactured by Institute for Solar Energy (ISE), Fraunhofer Gesselschaft (Germany). This electrolyser is capable of producing 7 NL/min at peak power, which is sufficient for supplying a 0.5 kW fuel cell operated at maximum power. The two main reasons for choosing this prototype PEM electrolyser were i) that it was intended for connection to a fluctuating renewable energy source and ii) could deliver hydrogen at a pressure of 15 bars, reducing the need for additional pressurisation. The electrolyser was delivered with its own control system. Because the PEM electrolyser was a prototype, no warranty could be expected from the manufacturer.

Fuel cell
A similar reasoning was used as a motivation for choosing a PEM fuel cell to be installed in the laboratory HSAPS. The advantages of PEM fuel cells can be summarised as follows:

- Low temperature of operation (80°C maximum)
- High energy density (even for small systems)
- Compact solutions
- Low need for maintenance
- Modular and flexible design

Disadvantages with PEM technology compared to alkaline fuel cells:

- At present expensive technology
- Requirement of humidification of membrane
- Low energy efficiency

A 0.5 kW PEM air-cooled fuel cell was selected for the system, manufactured by H-Power (USA). This fuel cell was available on a semi-commercial basis at a relatively low price and short delivery time. The PEM fuel cell was delivered with a lifetime warranty of 1,500 operation hours. The fuel cell unit was delivered with its own control system that made it attractive for the laboratory HSAPS where the main focus was on the overall system control and the integration of the MH-storage.

Hydrogen storage
In order to keep the HSAPS test-facility as simple as possible, a MH-storage with heat management during charging and discharging using heat exchanging with the ambient air was selected. The MH-storage was manufactured by GfE (Germany) and HERA (Canada). The design criteria for the MH-storage were set in accordance with pressure and flow-rates of the electrolyser and fuel cell and the expected ambient temperature. Since the fuel cell may be operated at a pressure down to 1.35 bars (0.35 barg), a design criterium was that the MH-storage should be able to deliver H_2 at pressure levels above this lower fuel cell operating limit at room temperature (~20°C).

Maximum electrolyser pressure is 16 bars. Thus, the next criterion for the MH-storage was that charging should be possible within the electrolyser pressure range at room temperature (~20°C). The hydrogen-loop was regarded as the long-term energy storage of the HSAPS. Hence, the choice of the total capacity of the MH-storage became a compromise between price and long-term storage capability. It was decided that the MH-storage should have an H_2-capacity sufficient for 3 – 4 days of continuous fuel cell operation at 50 % of rated power (250 W). This required a storage capacity of some 12 – 15 Nm^3 of hydrogen.

3.2 Description of the system components

3.2.1 Power supply
With focus on H_2 energy system, it was seen advantageous to be able to precisely control the PV array output power. Thus, the fluctuating PV array characteristic was emulated using a programmable power supply. Measured solar radiation data was used to program the power supply. The specifications for the power supply with peak power of 4.8 kW is given in Table A.1.

3.2.2 Electronic Load
A programmable electronic load, PLZ-603W from Kikusui Electronics, was implemented to emulate different consumption patterns, at maximum 600 W. It comprises four different modes of constant operation: current, voltage, resistance, and power. Details are given in Table A.2.

3.2.3 Electrolyser
The 1.5 kW PEM Pressure Electrolyser is composed of 26 cells each with an active area of 57 cm^2. The electrolyser is designed for nominal operation with approximately 30 A at a stack voltage of 48 V, stack operating temperature at 70°C – 75°C, and a working pressure of 16 bars. The nominal hydrogen production is equivalent to approximately 0.36 Nm^3/hour (~0.03 kg/hr). The maximum pressure is 18 bars and the peak power is 1.7 kW (49 V, 35 A). Detailed specifications are given in Table A.3. Water droplets in the product gases are removed in a filter in the electrolyser. However, the hydrogen is still saturated with water at 40°C when it leaves the electrolyser and needs further drying, especially due to the MH-storage specification of > 99.999 % H_2. The O_2 content in H_2 out from the electrolyser is in the range 0.01 % – 0.3 %. In order to prevent possible O_2 accumulation and to avoid degradation of the metal hydride alloy, the O_2 must be removed by combination over a catalyst. The deionised water supplied to the electrolyser should have a maximum electric conductivity of < 1 μS/cm. The proper quality of the water for electrolysis is maintained by passing through two containers filled with ion exchanging resin.

Figure 3.2 shows the electrolyser stack and a schematic explaining how the stack interacts with the peripheral electrolyser system. The electrolyser is equipped with a control system that is divided into two levels of operation, namely supervising of critical parameters (highest level of priority) and supervising and control of normal operating parameters.

Critical parameters: maximum stack-temperature (80°C); maximum electrolyser pressure (18 bars); H_2 and/or O_2 gas-bubbles accumulation in the deionised water circulating in the electrolyser; lower deionised water level, and manual shutdown button. If any of these parameters are violated or engaged, the electrolyser will deflate pressure and shut down.

Normal operating parameters: electrolyser pressure (< 16 bars) regulated by opening and closing a magnetic valve; stack-temperature (< 75°C) cooled with a water based heat exchanger controlled by a proportional and integral (PI) regulator; and deionised water level (between high and medium level) controlled by upper and lower magnetic sensors which switch the deionised water pump ON and OFF.

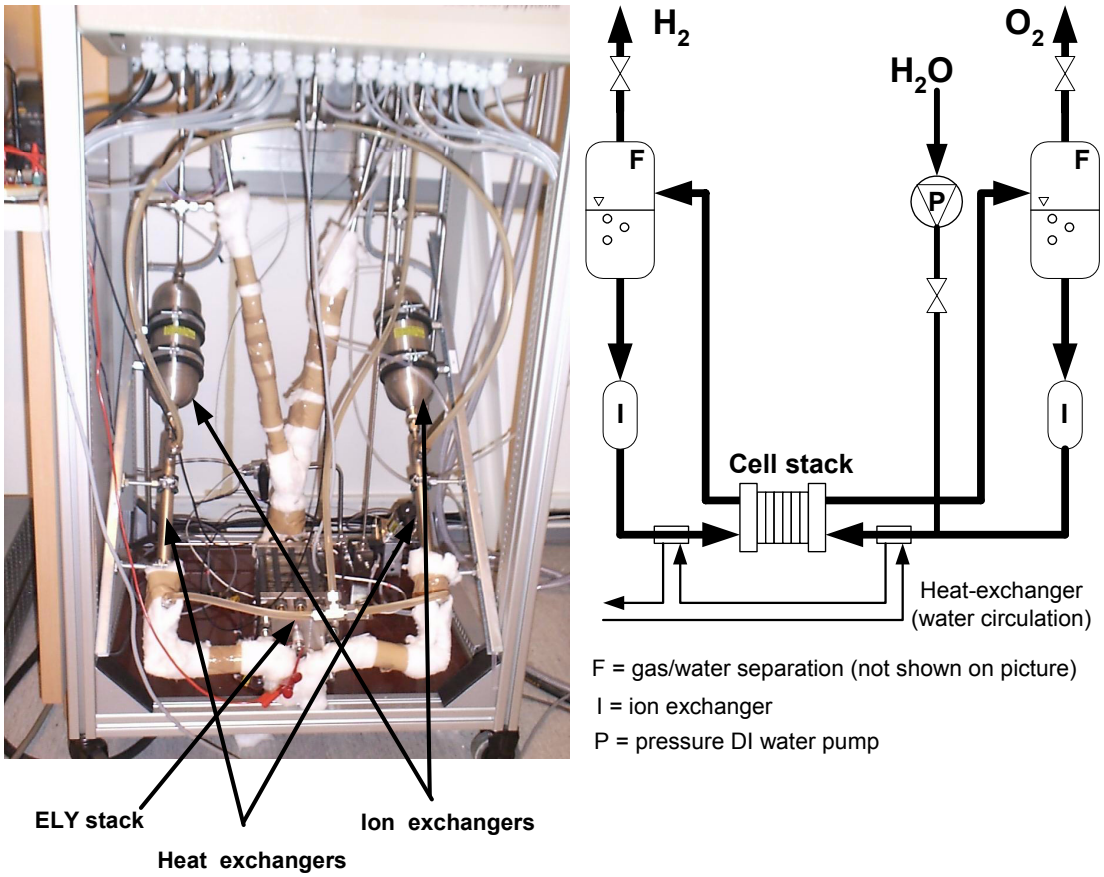

Figure 3.2 Picture of the 16 bars PEM laboratory electrolyser and a schematic of the interaction between the electrolyser stack and the peripheral system consisting of gas/water separators (flash), ion exchangers, heat exchangers, and deionised water pump. The construction of the U-connection tube ensures pressure equalisation between the cathode and the anode.

3.2.4 The H_2 purification unit (oxygen remover and hydrogen dryer)

The H_2 purification unit consists of an oxygen trap and a dryer. The oxygen trap contains a catalytic noble metal that combines traces of oxygen with hydrogen to formation of water ($H_2 + ½O_2 = H_2O$). The water content in the hydrogen from the electrolyser and the water produced over the catalyst in the oxygen trap are removed downstream in the dryer. The dryer consists of two filters, each containing 6 kg desiccant, that are used in alternation to ensure continuous operation, i.e., when the first filter is to be regenerated the second filter is put into operation and so on. The dryer is designed to run with maximum H_2 flow rate at 0.5 Nm^3/h. Each of the filters is capable of treating about 84 Nm^3 electrolytic hydrogen (corresponding to an amount of 115 kWh electrical energy from a fuel cell operating with electrical efficiency of 50 %). The desiccant in the filters has to be regenerated by heated (150 – 200°C) nitrogen gas (10 Nm^3/h) for 6 hours. The power required by the H_2 purification unit is approximately 1.8 kW for the dryer and about 0.15 kW for the oxygen trap. This H_2 purification unit is not optimised for stand-alone application, it was integrated into the HSAPS laboratory for fast regeneration of the desiccant. Optimisation of the H_2 purification unit was not in focus in this work, however, it was suggested to be an issue for further work. The H_2 purification unit including the dryer with heater and oxygen remover is shown in Figure 3.3. Details are given in Table A.4a and A.4b for the oxygen trap and the dryer, respectively.

Measurement of humidity in hydrogen at the dryer output was performed before the hydrogen was directed to the MH-storage. The measurement was conducted using a flow-through electrolytic moisture analyser. After the moisture in the new tubing was driven out, the water content decreased down to 2.5 ppm, which was specified by the manufacturer of the gas purification system. That is, the quality of the purified electrolytic hydrogen is comparable to that of hydrogen 5.0 (99.999 %). No O_2 in H_2 measurements were though performed.

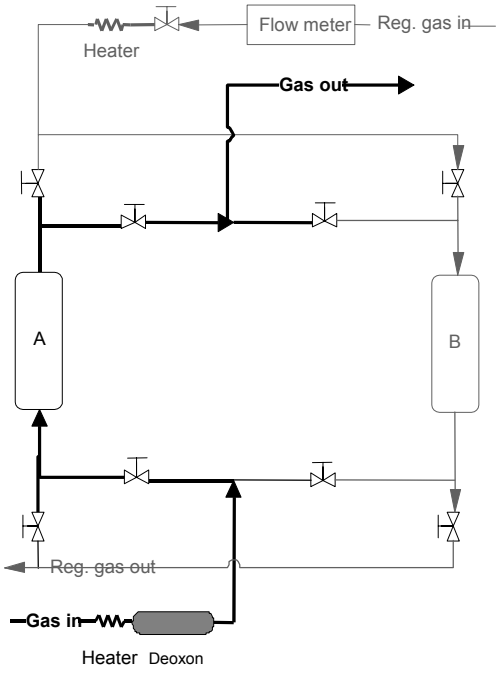

Figure 3.3 The gas purification unit with oxygen trap (deoxon) and dryer columns. Due to regeneration of desiccant two columns are installed to ensure continuous operation.

3.2.5 Fuel Cell

The PEM fuel cell (model name: PS-P-500-1), shown in Figure 3.4, is a self-humidified hydrogen-air operating fuel cell system rated at 500 W. The stack consists of 64 individual cells with an active area of 78 cm^2 each. The technical specification of the PEM fuel cell system is summarised in Table A.5.

Figure 3.4 Picture of the PEM fuel cell.

The FC system includes all the ancillary hardware for monitoring of the stack temperature, terminal voltage, and output current. The local control system also controls the air pump speed, hydrogen purging, cooling fan operation, and low voltage disconnect function. The power requirements during start-up are supplied using eight AA batteries, while during normal operation the ancillary hardware is powered by the stack. The fuel cell has though no output voltage regulation.

Supply of reactants is of key importance for optimal fuel cell performance. A single stage pressure regulator adjusts the incoming hydrogen pressure to a slight overpressure (0.35 barg). An air pump is used in order to feed the fuel cell with oxidant. The continuous supply of the oxidant is controlled in proportion to the amount of current drawn from the fuel cell stack. As H_2 and O_2 are consumed, water accumulates at the cathode, blocking for reaction sites. Thus, the fuel cell control system periodically purges the stack (removes water from the cathode), by means of the air pump. The fuel cell control system purges H_2 at the anode every 2^{nd} minute and O_2 (air) at the cathode every 15^{th} minute.

Another important operating variable is the stack-temperature. To avoid overheating of the fuel cell stack (and thus, the possibility for membrane dehydration), the fuel cell control system operates the cooling fans according to a pre-programmed control scheme that increases the fan speed with increasing stack-temperature. The temperature range for the stack is 0 – 55°C. However, freezing of the fuel cell may cause permanently damage in the stack. Thus, an operating temperature in the range of 2 – 55°C is recommended.

3.2.6 Metal hydride

The metal hydride storage (MH-storage) 4-SL 14 AR shown in Figure 3.5 is based on an AB_2-type hydride (Hydralloy C10) that absorbs and desorbs hydrogen at near-ambient temperatures.

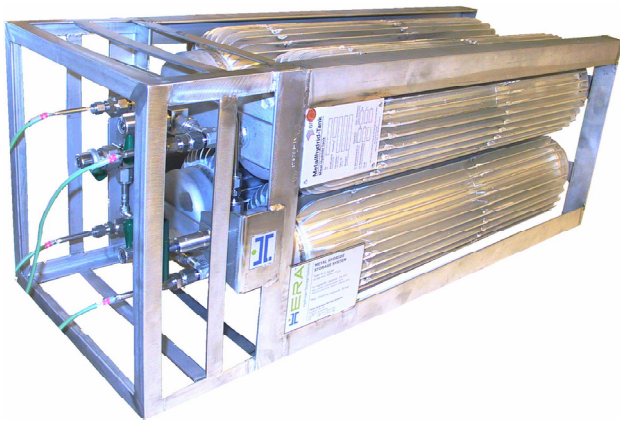

Figure 3.5 Picture of the MH-storage 4-SL 14 AR.

The MH-storage consists of four similar MH-tanks adding up to a nominal H_2 storage capacity of 14 Nm^3. In the forthcoming, the four tanks will be denoted Tank #1, Tank #2, Tank #3, and Tank #4 counting from the H_2 inlet valve. The MH-storage was designed for operation with heat transfer through air convection at room temperature (~20°C). Aluminium cooling-fins were used in order to improve the natural heat transfer. The technical specification of the MH-storage is summarised in Table A.6, while the PCT-diagram (pressure-concentration-isotherm) for the hydride alloy at 25°C is given in Figure 3.6 (provided by the manufacturer).

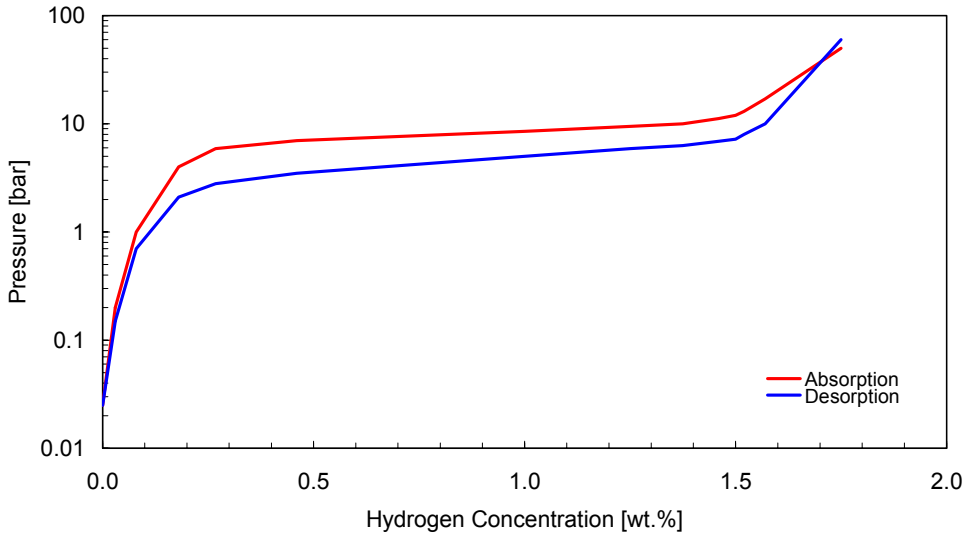

Figure 3.6 PCT-diagram for Hydralloy C10, with both the absorption and desorption curve at 25°C shown (provided by the manufacturer).

Charging of the MH-storage (absorption of hydrogen) is an exothermic process while discharging (desorption of hydrogen) is an endothermic process. Thus, the MH-temperature will rise during charging (maximum operating temperature is ~60°C). The MH-storage can be charged with a H_2 flow rate of 15 NL/min (equivalent to an electrolyser power of about 3 kW) at room temperature (~20°C).

Charging should be terminated at maximum MH-pressure of 30 bars, and the operation is completed when the MH-temperature has returned to initial conditions.

During discharge the MH-temperature will decrease. Since the H_2 pressure in the MH-storage (MH-pressure) in the tanks is related to the MH-temperature, the H_2 desorption flow is dependent on the heat transfer of the MH-storage. At a pressure above 1.2 bar, a H_2 flow greater than 8 NL/min (equivalent to a fuel cell power of 650 W with an energy efficiency of about 50 %) can be maintained if enough heat is available from the surroundings.

The durability of the storage capacity is highly depended on the H_2 quality. Experiments (Bonhoff, Forschungszentrum Jülich) have shown that the MH-storage capacity decreases to 93 % of the nominal capacity after 2100 cycles with H_2 quality of 5.0 (99.999 %). For electrolytic H_2 and H_2 quality 3.0 (99.9 %), the MH-storage capacity is reduced to 40 % and 35 % after 250 cycles, respectively. Thus, purification of electrolytic H_2 is of key importance to maintain high MH-storage capacity upon repeated cycling. During testing of the MH-storage, H_2 was supplied from standard 200 bars pressure flasks with H_2 of quality grade 5.0. A summary of the main substances causing the various H_2 qualities is given in Table A.5.

3.2.7 Lead-acid battery

For short-time energy storage, four secondary lead-acid batteries were connected in series to fit the 48 V DC bus bar in the HSAPS. However, one of the 12 V batteries can be removed in order to investigate a 36 V configuration. The electrical storage capacity is 44 Ah, which gives 48 V · 44 Ah = 2.1 kWh. The specification of a single battery is given in Table A.8. The measured *IU*-curves for different battery state-of-charge levels (in percent) are given in Figure 3.7.

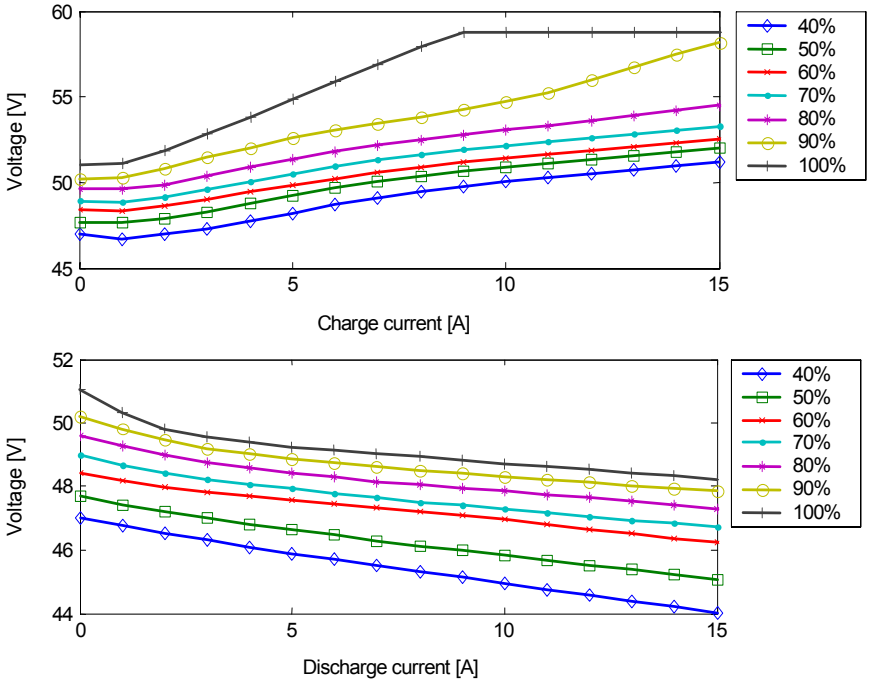

Figure 3.7 *IU*-curves for different battery state-of-charge levels. The values for charging current above 13 A are extrapolated due to the upper charging current limit.

3.3 Testing of the components

3.3.1 Electrolyser testing

IU-characterisation

Several experiments were conducted in order to measure the current-voltage (*IU*) curves at different stack-temperatures for the 1.5 kW PEM electrolyser. *IU*-curves for four different stack-temperatures are shown in Figure 3.8. The average cell voltage in Figure 3.8 is calculated by dividing the measured stack-voltage with the 26 cells in the stack. An average cell voltage of 1.86 V was obtained at 72°C and 0.53 A/cm^2 which was at the nominal current-density given by the manufacturer. Figure 3.9 shows the single cell voltages in the stack measured by the manufacturer at two different temperature/current-density combinations [3]. The average cell voltage is 1.85 V/cell for both of the temperature/current-density combinations, with a voltage deviation of ± 3.68 % and ± 5.41 % for the cells in the stack at 30°C / 0.40 A/cm^2 and 70°C / 0.62 A/cm^2, respectively. The measured cell voltages are generally higher than the results found in the literature in the same current-density range for PEM cells, where the cell voltages are typically varying between 1.65 V and 1.75 V at about 80°C and approximately at 1 A/cm^2 [4-8]. However, the results referred to from the literature are usually based on single cell measurements and at cell temperatures of about 80°C and above, and often at 1 atm.

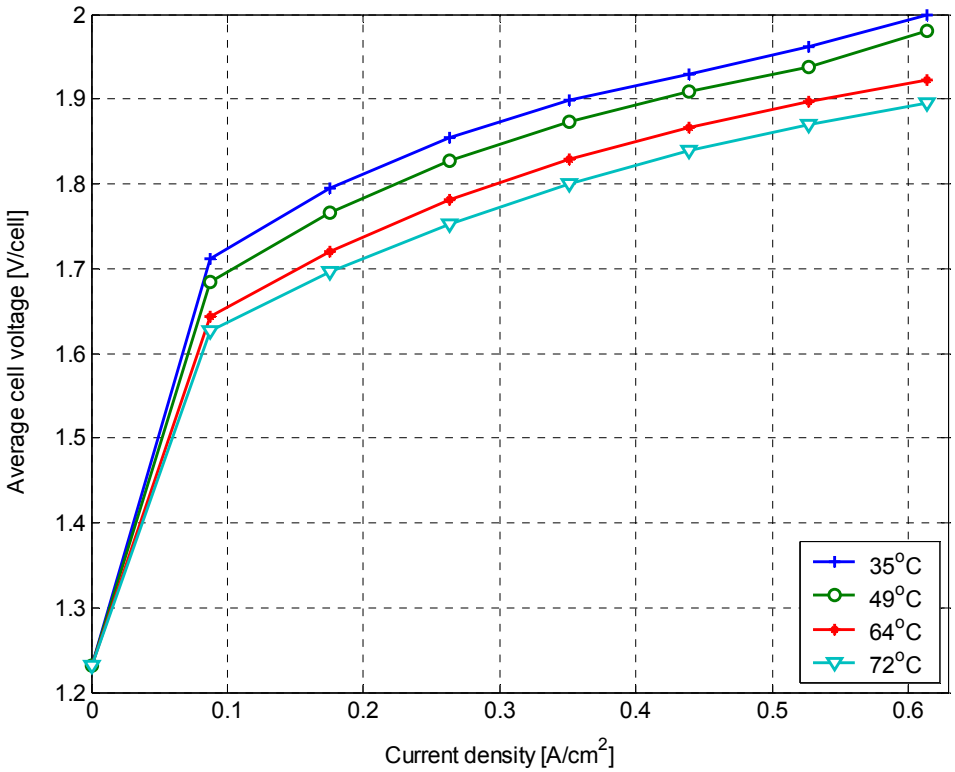

Figure 3.8 Measured current-voltage characteristic at four different electrolyser stack-temperatures.

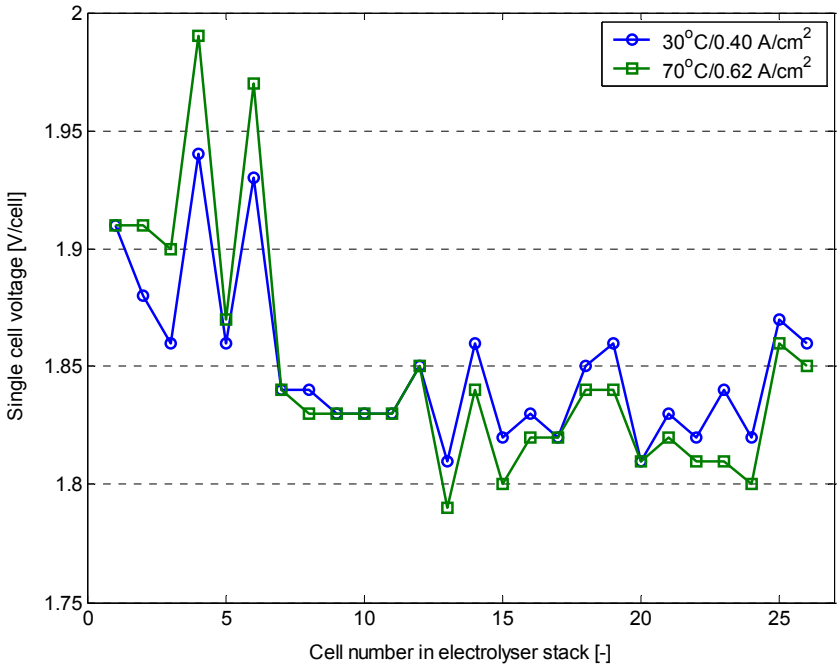

Figure 3.9 Single cell voltages measured by the manufacturer [3].

The measured cell voltages for cell number 4 and 6 in Figure 3.9 are approximately 150 mV higher than the average cell voltage for the 26 cells. The higher over-voltage for cell number 4 and 6 are also indicated in Figure 3.10, where the ohmic resistances for each of the cells have been measured by the manufacturer [3].

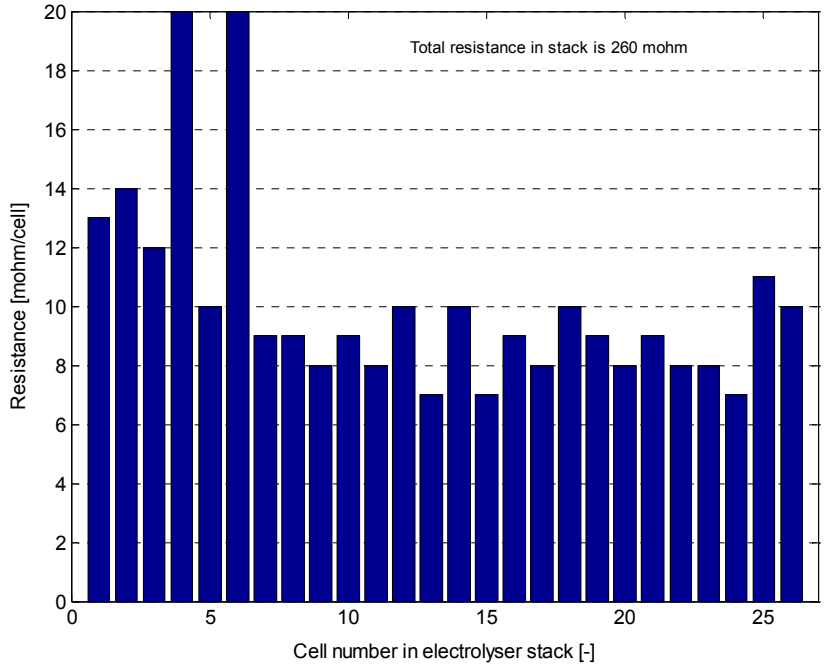

Figure 3.10 Single cell ohmic resistances measured by the manufacturer [3].

Electrolyser Efficiency

The efficiencies are defined as:

$$Faraday\ efficiency = \frac{measured\ \ production\ of\ \ hydrogen}{theoretic\ \ production\ of\ \ hydrogen} \tag{3.1}$$

The theoretic production of hydrogen is related to Faraday's law:

$$\dot{n}_{H_2} = n_c \frac{I}{nF} \tag{3.2}$$

where

$\dot{n}_{H_2}$	hydrogen production rate [mol/s]
I	current through each of the cells connected in series [A]
n_c	number of cells connected in series, $n_c = 26$
n	number of moles of electrons per moles of water, $n = 2$
F	Faraday constant, $F = 96485$ [C/mol]

$$Voltage\ efficiency = \frac{thermoneutral\ voltage\ \ (U_{tn})}{measured\ voltage\ during\ hydrogen\ \ production} \tag{3.3}$$

The thermoneutral voltage (U_{tn}) is the theoretical voltage for hydrogen production and is related to the total change in enthalpy (ΔH) for splitting water by the expression:

$$U_{tn} = n_c \frac{\Delta H}{nF} \tag{3.4}$$

where n_c, n, and F are the same as in Equation 3.2. The thermoneutral voltage for a single cell is 1.482 V at standard conditions (1 atm., 25°C) . The exact thermoneutral voltage for water splitting at elevated temperature and pressure may be calculated from thermodynamic data or approximated by [9]:

$$\begin{aligned} U_{tn}(T_{ely,stack}, P_{ely,stack}) &= 1.4989 - 6.4568 \cdot 10^{-5} T_{ely,stack} + 3.0202 \cdot 10^{-8} {T_{ely,stack}}^2 \\ &- 4.8158 \cdot 10^{-12} {T_{ely,stack}}^3 + 5.7158 \cdot 10^{-16} {T_{ely,stack}}^4 - 9.3360 \cdot 10^{-11} (P_{ely,stack} - P_{ref}) \end{aligned} \tag{3.5}$$

where

$T_{ely,stack}$	electrolyser stack-temperature [K]
$P_{ely,stack}$	electrolyser stack-pressure [Pa]
P_{ref}	reference pressure [Pa]

The voltage measured during hydrogen production is higher than the theoretic voltage because of overvoltage due to the required activation potential and ohmic resistance in the cells.

The total electrical efficiency is simply the Faraday efficiency multiplied by voltage efficiency:

$$\textit{Electrical efficiency} = \text{Faraday efficiency x Voltage efficiency} \qquad (3.6)$$

The total electrical efficiency corresponds to the electrolyser's energy efficiency defined by:

$$\textit{Energy efficiency} = \frac{\textit{hydrogen produced in watts}}{\textit{electrical power supplied to the electrolyser stack}} \qquad (3.7)$$

Figure 3.11 shows the Faraday efficiency, the voltage efficiency, and the corresponding electrical efficiency measured at a stack-temperature of 71°C ± 2°C.

The energy efficiency based on Equation 3.7 is not shown in Figure 3.11. However, the calculated result for this equation is consistently about 1 % higher than the result for the electrical efficiency from Equation 3.6. The calculated result from Equation 3.7 was based on hydrogen higher heating value (HHV) = 3.54 kWh/Nm^3 H_2 [10].

The Faraday efficiency can be seen to level out at 92 % – 93 % at current densities above 0.15 A/cm^2, corresponding to a stack-current of about 8 A and above. The voltage efficiency is higher at lower current densities where the over-potential is lower. Multiplication of the Faraday efficiency and the voltage efficiency results in a maximum electrical efficiency of about 80 % in the region 0.09 – 0.2 A/cm^2 (5 – 11 A). The voltage efficiency decays to 79 % at 0.53 A/cm^2 (30 A) where the Faraday efficiency is 93 %, resulting in an electrical efficiency of 73 % at the nominal operation point.

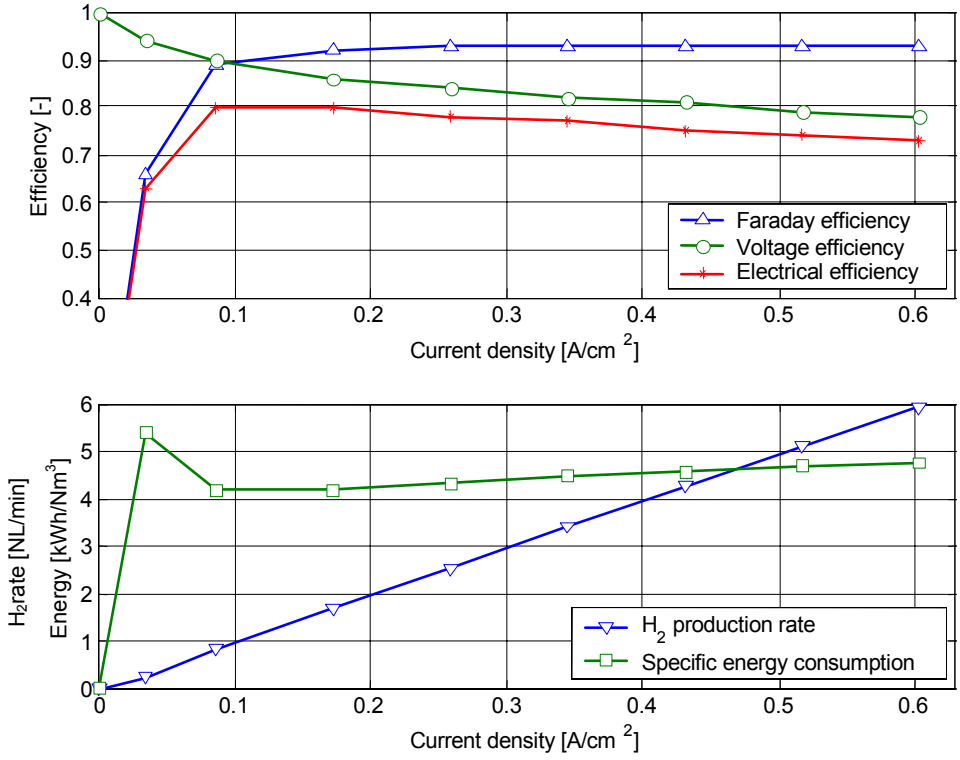

Figure 3.11 The Faraday efficiency, voltage efficiency, and the corresponding electrical efficiency measured at a stack-temperature of 71°C (above). The calculated specific electrolyser energy consumption and the measured hydrogen production rate at a stack-temperature of 71°C (below).

Start-up and nominal operation

During initialisation of the electrolyser, the electrolyser control system evaluates the level of the deionised water and checks the U-connecting tube for gas bubbles. The initialisation safety limit is set to three minutes. After initialisation, the electrolyser stack is connected to the common DC bus bar. The electrolyser stack-temperature, current, voltage, and peripheral system temperature as a function of time in the start-up period are given in Figure 3.12. As a result of a higher reaction rate and lesser ohmic resistance at increased stack-temperature, the stack-current increases throughout the start-up period. With a constant stack-voltage of about 48.6 – 48.2 V, the stack-temperature can be seen to reach the nominal temperature region, 70°C < $T_{ely,stack}$ < 75°C, approximately 1.5 hours after start-up from room temperature (~20°C). At nominal stack-voltage (48 V), hydrogen at a pressure of 16 bars, is available from the stack after four minutes of operation. Initially, the stack-temperature increases rapidly with 1.5°C/min. However, after about 20 minutes the increase in stack-temperature suddenly lowers to 0.3°C/min because the shear forces from the product gases starts dragging the deionised water from the stack and round in the peripheral system. Thus, some of the heat generated due to the ohmic resistance is transported out of the stack, slowing down the heatup of the stack. This is also indicated by the measured peripheral system temperature, which starts to increase at the same time the stack-temperature changes to a slower heating rate.

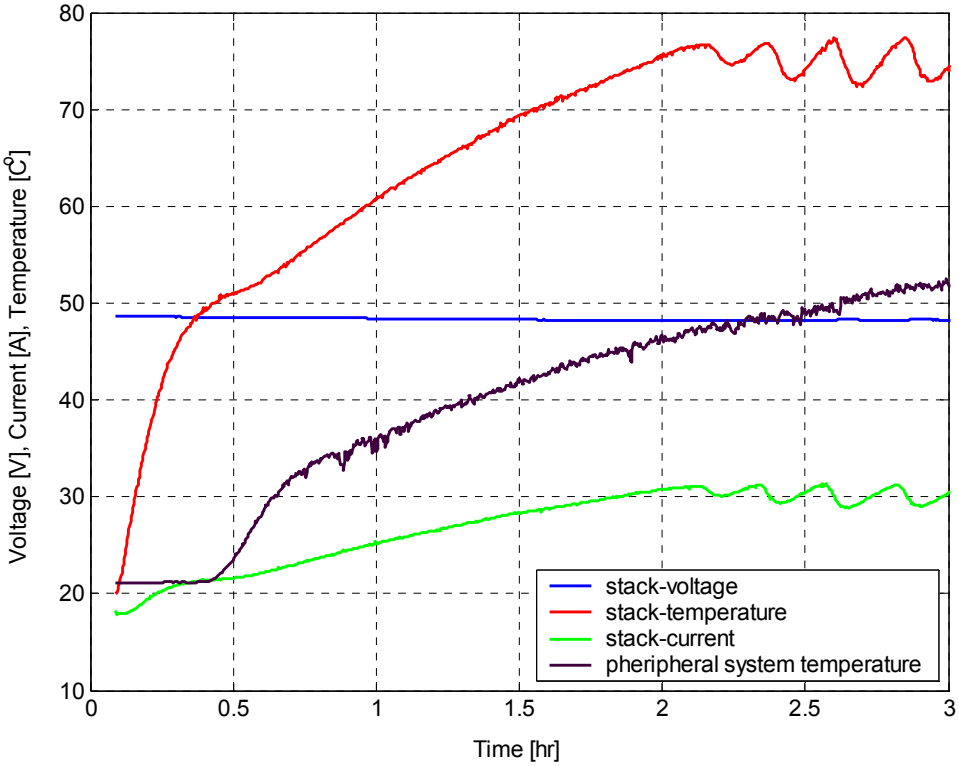

Figure 3.12 Electrolyser stack-temperature, current, voltage, and peripheral system temperature during a start-up. The peripheral system temperature is measured at the gas/water separator.

During normal operation, the electrolyser control system monitors the stack-temperature, O_2 pressure, level of the electrolysis water, and checks the pressure equalising U-connecting tube for gas bubbles. The level of the electrolysis water is automatically refilled and the stack-temperature is indirectly controlled by heat

exchangers between cold water and the deionised water, where a PI regulator regulates the amount of cooling water. The cooled deionised water will then enter the stack and remove heat. Note how the electrolyser current consumption (ΔI_{ely} = 2.6 A), and thus, the power consumption (ΔP_{ely} = 125 W) vary as a result of the stack-temperature regulation during normal electrolyser operation after about 2 hours. Of course, the stack-voltage would vary in the same manner if the electrolyser were to be controlled at constant current.

IU-transients

The current and voltage transients of the electrolyser stack at about 64°C were investigated using a high-speed data acquisition I/O-board. The sampling rate was 10 kHz in all experiments. Transients were measured between condition close to stand-by position and 64 % of rated capacity, and between 64 % and 100 % of rated capacity. Both current and voltage were used as input-parameters for these electrolyser stack step-tests.

Figure 3.13 shows the measured stack-current and stack-voltage transients when the input current was stepped from 2.5 A to 20 A and back to 2.5 A. The stack-voltage changed from 38 V to 48 V in the step-up test, and down to 38 V when the input current was stepped back to 2.5 A ($\Delta V_{2.5\text{-}20\ A,\ 64°C}$ = 10 V). If the power source disconnects, the stack-voltage depends on the amount of H_2 and O_2 present in the cathode and anode, respectively, thus a function of time since last shutdown of the electrolyser. The open-circuit potential is also dependent on the hydrated conditions of the electrode catalysts. However, even though the start- and end-voltages differed at stand-by position, the stack-voltage transients stabilised within 0.2 s in both the step-up and the step-down tests. The measured stack-current transients also stabilised within 0.2 s.

Figure 3.14 shows the measured stack-current and stack-voltage transients when the input current was stepped from 30 A to 20 A and back to 30 A. The stack-voltage changed from 49 V to 47 V in the step-down test, and back to 49 V when the input current was stepped back to 30 A ($\Delta V_{20\text{-}30\ A,\ 64°C}$ = 2.5 V). The stack-current and stack-voltage transients stabilised within 0.2 s in both the step-down and the step-up tests.

Figure 3.15 shows the measured stack-current and stack-voltage transients when the input voltage was stepped from 49.0 V down to 45.5 V and back to 49.0 V. The stack-current decreased from 30 A to 16 A when the input voltage was stepped from 49 V down to 45.5 V, and back to 30 A when the input voltage was stepped from 45.5 V back to 49 V ($\Delta A_{45.5\text{-}49\ V,\ 64°C}$ = 14 A). The stack-current and stack-voltage transients stabilised within 0.1 s in both the step-down and the step-up tests, thus the stack stabilises faster due to perturbations in the input voltage compared to perturbations in the input-current. Furthermore, the stack-current and stack-voltage can be seen to follow quite well. Care must though be taken as the transients may be influenced by the power supply, however the current and voltage transients were reported to stabilise within 900 μs by the power supply manufacturer.

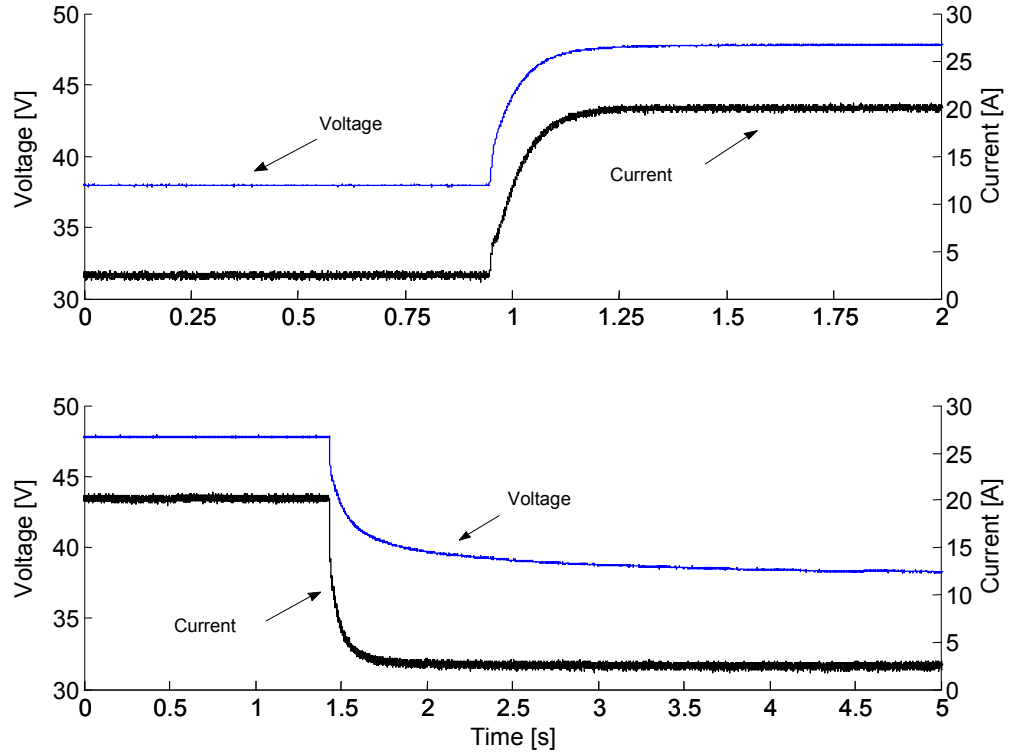

Figure 3.13 Measured electrolyser stack-current and stack-voltage transients when stepping the input current from 2.5 A to 20 A (above) and back to 2.5 A (below).

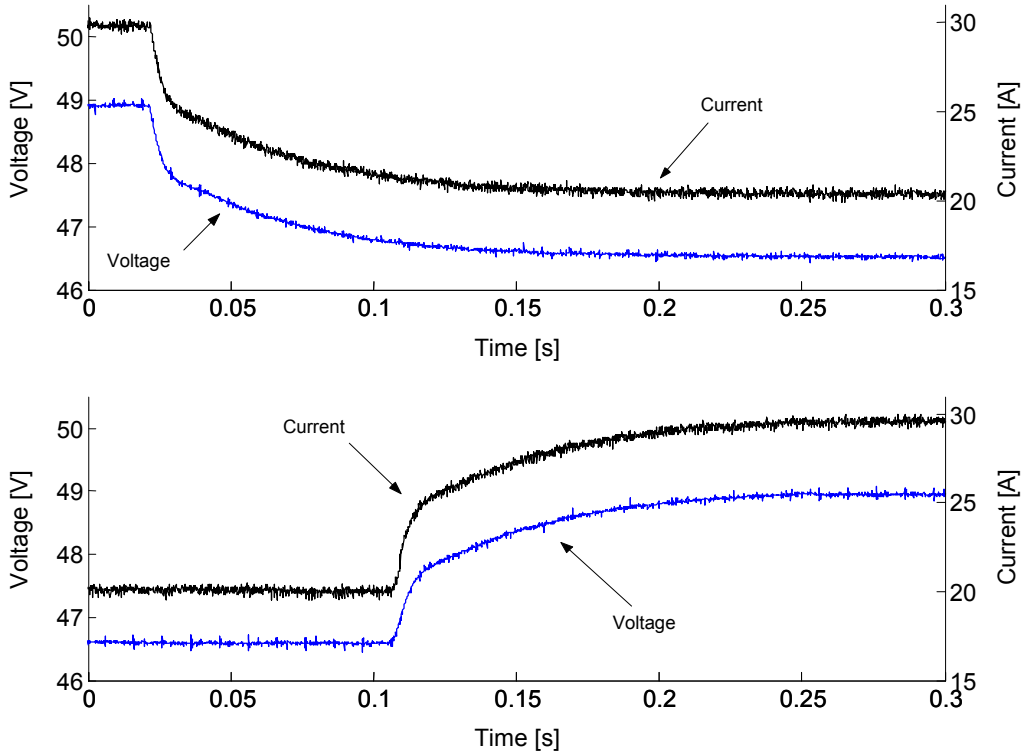

Figure 3.14 Measured electrolyser stack-current and stack-voltage transients when stepping the input current from 30 A to 20 A (above) and back to 30 A (below).

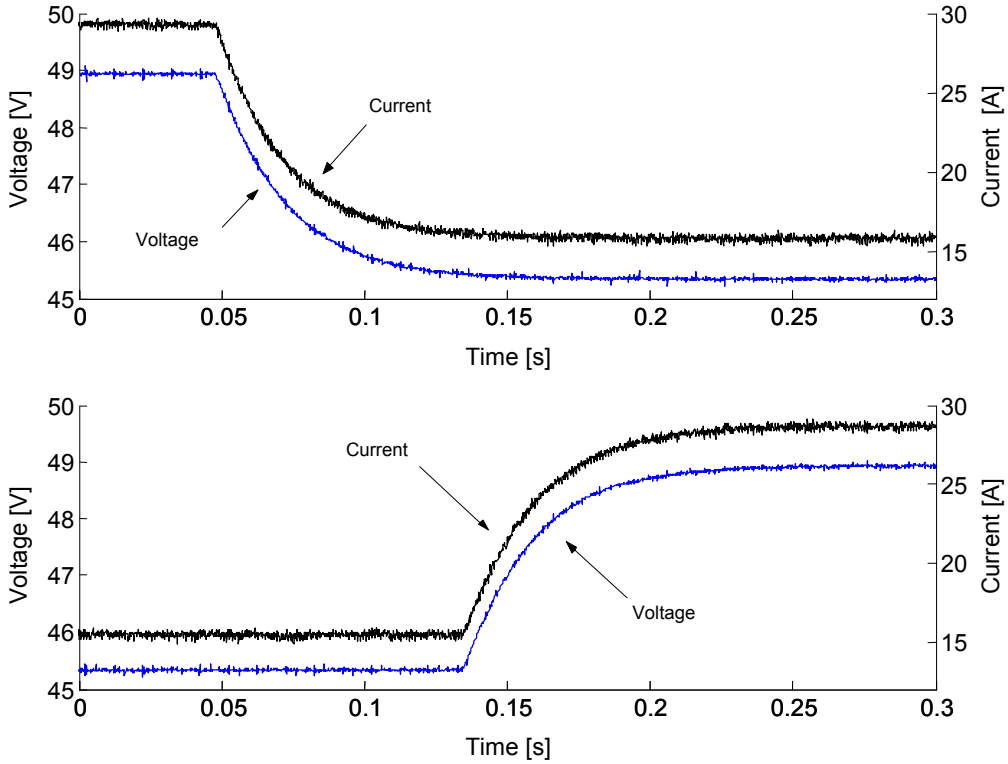

Figure 3.15 Measured electrolyser stack-current and stack-voltage transients when stepping the input voltage from 49.0 V to 45.5 V (above) and back to 49.0 V (below).

3.3.2 Fuel cell testing

IU-characterisation

Several experiments were performed to determine the current-voltage (*IU*) characteristic of the fuel cell stack. One important conclusion from these experiments is that the stack-voltage is very sensitive to the O_2-purging, particularly at lower current densities. In order to investigate the *IU*-characteristic for different time lags with respect to the O_2-purging, the required current was increased by 0.5 A immediately after each O_2-purging while the stack-voltage and stack-current were measured with 10-second intervals. The *IU*-curves for each of the three time lags are shown in Figure 3.16a. The *IU*-curves in Figure 3.16a are measured at an average operating temperature of about 50°C.

Time lag 1 corresponds to an average of the measurements taken 1.5 – 2.5 minutes after last O_2-purging, while time lag 2 and time lag 3 are averages of the measurements taken in the time periods 7 – 8 minutes and 13.5 – 14.5 minutes after purging, respectively.

From Figure 3.16a, three different *IU*-curves are given for the fuel cell dependent on the time lag selected. However, at higher current densities, where the throughput rate of air is constantly high, the *IU*-curves are almost identical for all the three time lags. This might indicate that the system could be further improved with respect to the oxygen/water management. E.g., [11] showed that sequential exhausting of each cell in a PEM fuel cell stack improved the reactant gas and liquid water management. More specifically, only one cell at a time is allowed to exhaust, thereby insuring that

the cell is receiving gas flow. This insures that no cell will be starved of fuel. With sequential exhausting, the momentary gas flow rate is much higher, so there is more water removal by shear force, thus in addition to better control, the amount of power to the air blower can be reduced.

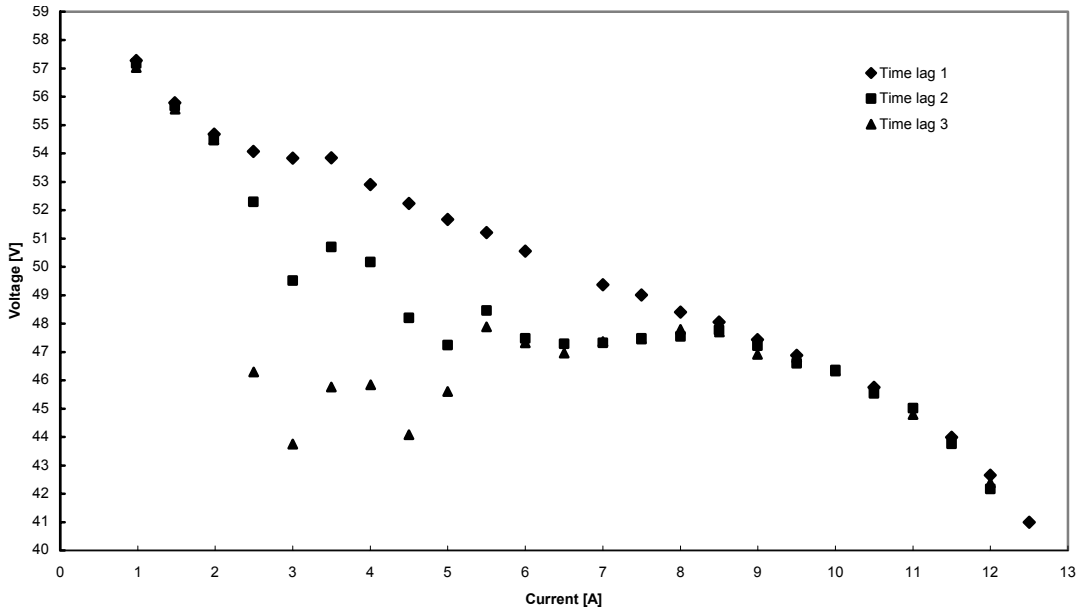

Figure 3.16a Measured *IU*-pairs for the PEM fuel cell system.

The voltage transient of the fuel cell stack during an O_2-purging was investigated by using the high-speed data acquisition I/O-board. The sampling rate was 10 kHz and the transient was measured at constant fuel cell stack-current of 5 A. The transient is shown in Figure 3.16b. The voltage transient during H_2-purging (not shown in figure) at stack-current of 5 A was measured to be lowered by only 0.35 V for about 1 second regardless of when the last O_2-purging occurred.

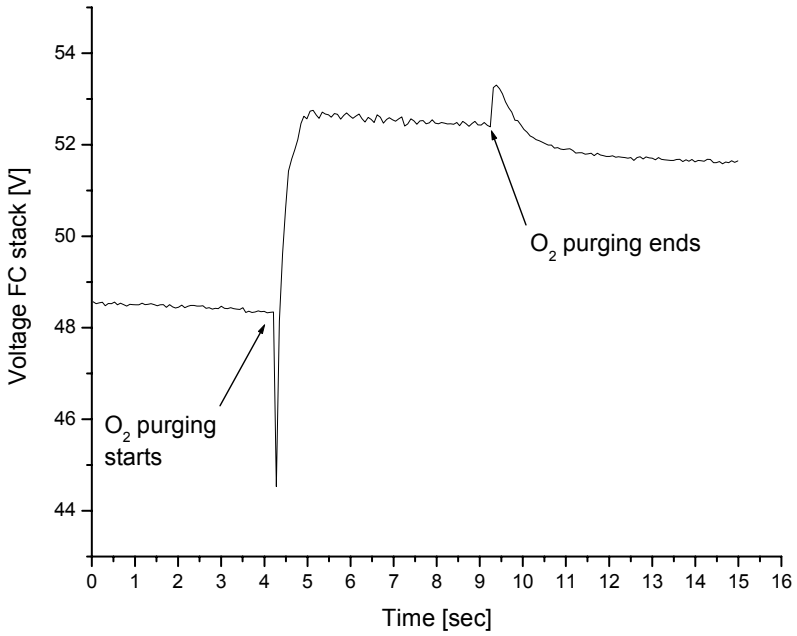

Figure 3.16b Voltage transient measured during O_2-purging at a constant stack-current of 5 A.

The *IU*-curves for three different fuel cell temperatures are given in Figure 3.17. The measurements are performed between each O_2-purging, according to time lag 2 in Figure 3.16. The reason for using time lag 2 is to represent the average performance of the 0.5 kW PEM FC. The *IU*-curves at 45°C and 55°C in Figure 3.17 agrees with the *IU*-curve measured at about 50°C with time lag 2 in Figure 3.16.

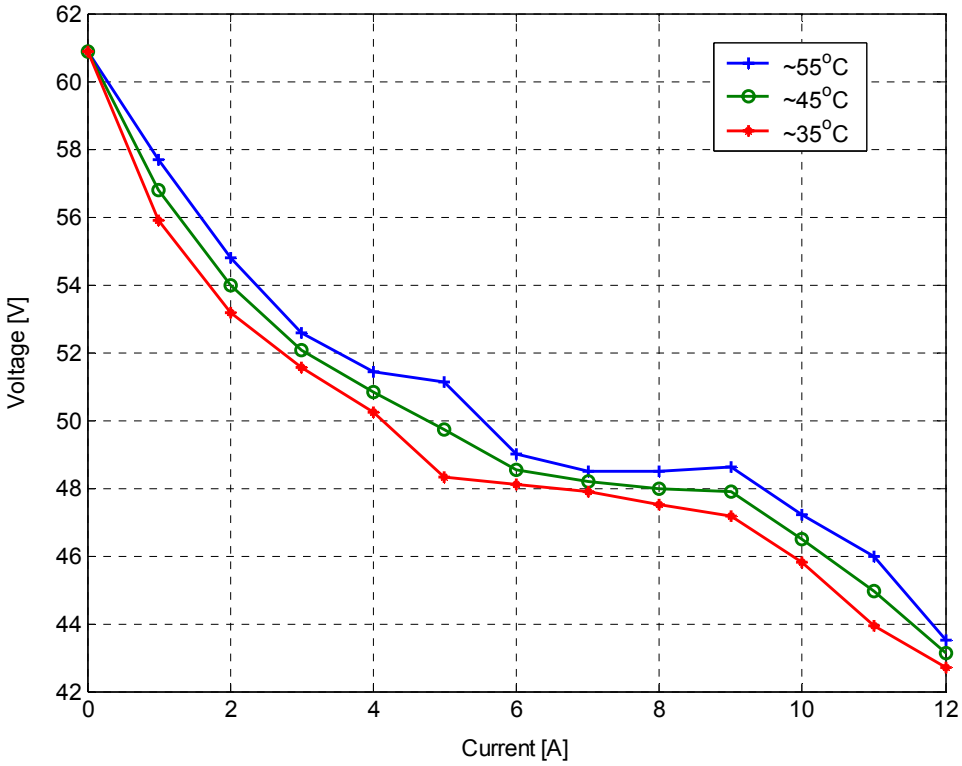

Figure 3.17 The 0.5 kW PEM fuel cell current-voltage (*IU*) curves measured at three different fuel cell stack-temperatures.

Fuel Cell Efficiency

The energy efficiency η_e of the FC-system can be calculated from:

$$\eta_e = \frac{\text{Energy out}}{\text{Energy in}} = \frac{P_{FC}}{\dot{V}_{H_2}\rho_{H_2}} \tag{3.8}$$

where

P_{FC} Fuel Cell power output, W

$\dot{V}_{H_2}$ H_2 consumption flow rate, kg/s

ρ_{H_2} Energy density of hydrogen (LHV), 120 MJ/kg

The calculated fuel cell energy efficiency is presented in Figure 3.18. The power output used in the efficiency calculation is based on the *IU*-curves in Figure 3.16a. Note that the sensitivity with respect to flushing of oxygen was affecting the electrical efficiency of the FC-system in the same manner as described for the *IU*-curves in Figure 3.16a.

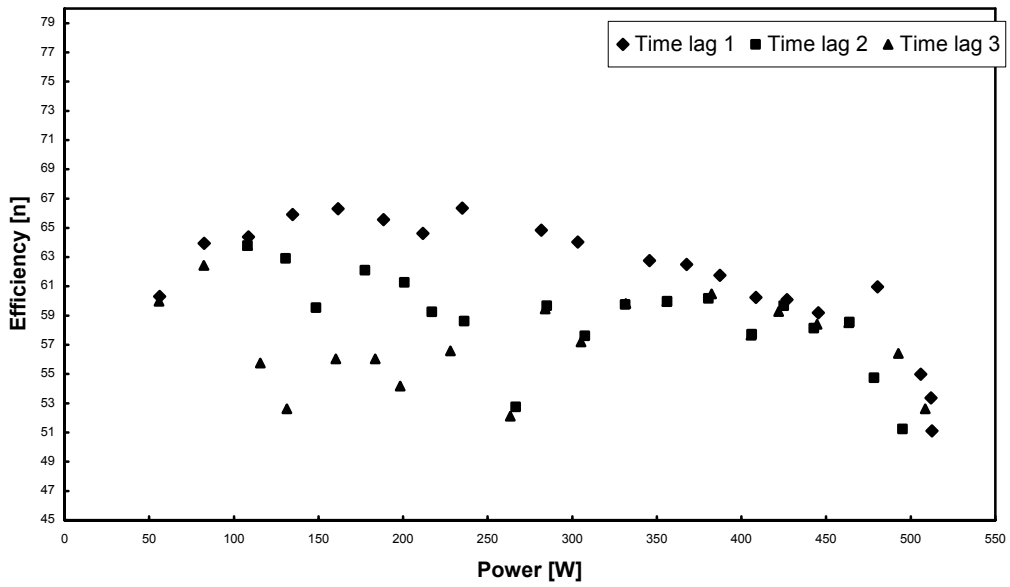

Figure 3.18 Calculated electrical efficiency (LHV) as a function of fuel cell power for each time lag. This energy efficiency includes the energy required by the fuel cell control system.

Start-up and nominal operation

During fuel cell start-up, the fuel cell control system measures the open circuit stack-voltage. If the open circuit stack-voltage is stable at minimum 60 V within 2–5 minutes, depending on the stack-temperature, electrical connection to the output terminal is made. If the stack-voltage does not stabilise within the start-up time, the fuel cell control system shuts down the fuel cell. An automatic shutdown is also triggered if the stack-voltage drops below 38 V during normal operation. If the fuel cell has been out of duty for more than two days, usually 2–3 restarts are required before the output terminal is connected. If the fuel cell has not been used for about 2–3 months and the output terminal is connected, the stack should be allowed to operate at low/moderate power output for about 3 minutes for the membranes to gain proper humidity (recommended by the manufacturer).

Figure 3.19 shows a start-up of the fuel cell, with an initial stack-temperature at room temperature (~20°C). When the fuel cell was switched ON, the fuel cell control system preheated the stack to ~27°C in about 4 minutes with the aid of the start-up batteries. Then the stack was allowed to be connected to the output terminal when the stack-voltage was found to be stable and above the minimum stack-voltage. The fuel cell was let idling for about 20 min before load was applied to the fuel cell. The stack-temperature decreased some during the idling period, but started to increase immediately after 3 A was required. The stack-temperature increased with a rather constant rate, even though the amount of current required from the stack was stepped from 3 A to 4 A after about 10 minutes. When the stack-temperature reached about 45°C, the fuel cell control system started the cooling fans. The sudden levelling of the stack-temperature about 20 minutes after the load was applied to the fuel cell indicates this. Thus, the fuel cell needed about 20 minutes to reach nominal stack-temperature.

The regular peaks in the fuel cell stack-voltage profile in Figure 3.19 was due to O_2-purging, while the peaks in the H_2 flow rate is due to H_2-purging.

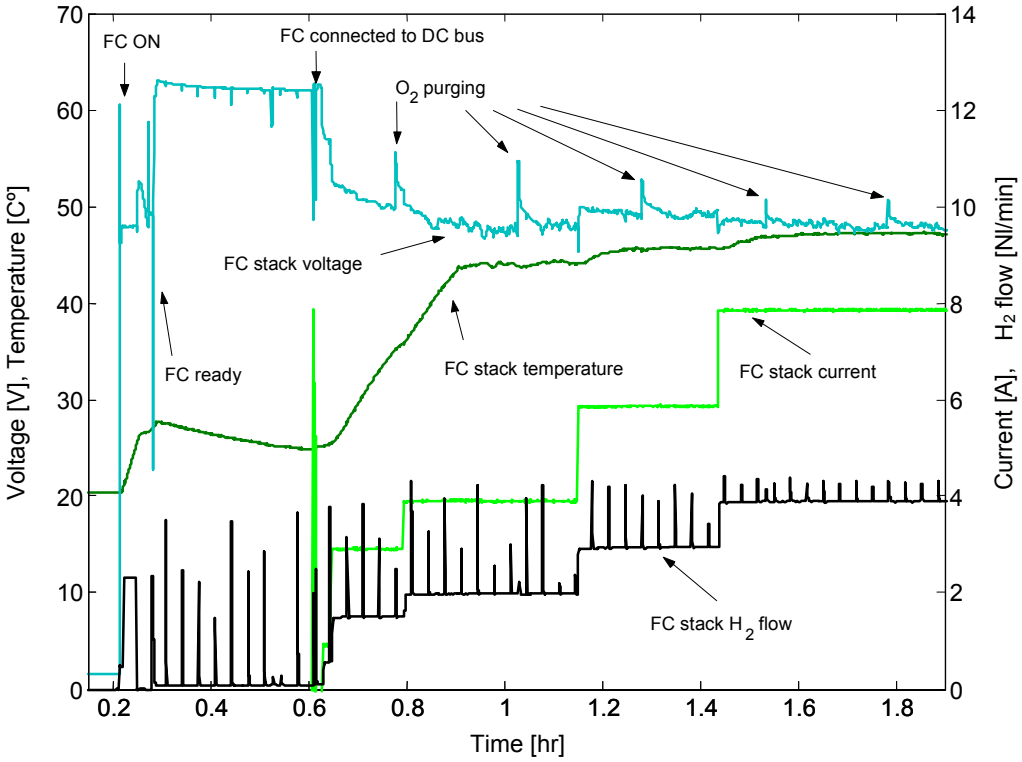

Figure 3.19 Measured stack-voltage, stack-current, stack-temperature, and H_2 flow during a fuel cell start-up. The regulation is done by stepping the required current from the fuel cell stack. The peak in the fuel cell stack-current at 0.6 hours occurred when the switch between the fuel cell and the electronic load was closed.

IU-transient

The current and voltage transients of the fuel cell stack were investigated at 50°C by using the high-speed data acquisition I/O-board. The sampling rate was 10 kHz in all experiments. Transients were measured from stand-by position to 50 % of rated capacity, and from 10 % to 100 % of rated capacity. Only the current was used as input-parameter for these fuel cell step tests.

Figure 3.20 shows the measured stack-current and stack-voltage transients when the required current was stepped from 0 A to 5 A and back to 0 A. The voltage transient stabilised after about 0.2 s when stepping from 0 A to 5 A. When removing the load current requirement, the voltage needed about 1.5 s to stabilise back to the open circuit stack-voltage, the voltage difference was $\Delta V_{0\text{-}5\ A,\ 50°C} = 12$ V.

Figure 3.21 shows the measured stack-current and stack-voltage transients when the required current was stepped from 1 A to 11 A and back to 1 A. The voltage stabilised at the new level after about 0.1 s, thus faster than when going from zero current, even with twice the size of the current step. The voltage stabilised within about 0.5 s after the current had been stepped down to 1 A again, still faster than the corresponding step-down test in Figure 3.20 which involved stand-by position. The voltage difference was $\Delta V_{1\text{-}11\ A,\ 50°C} = 14$ V.

However, in all cases the measured current transients were shorter than the 0.1 ms sampling rate resolution used in these transient investigations, which is excellent.

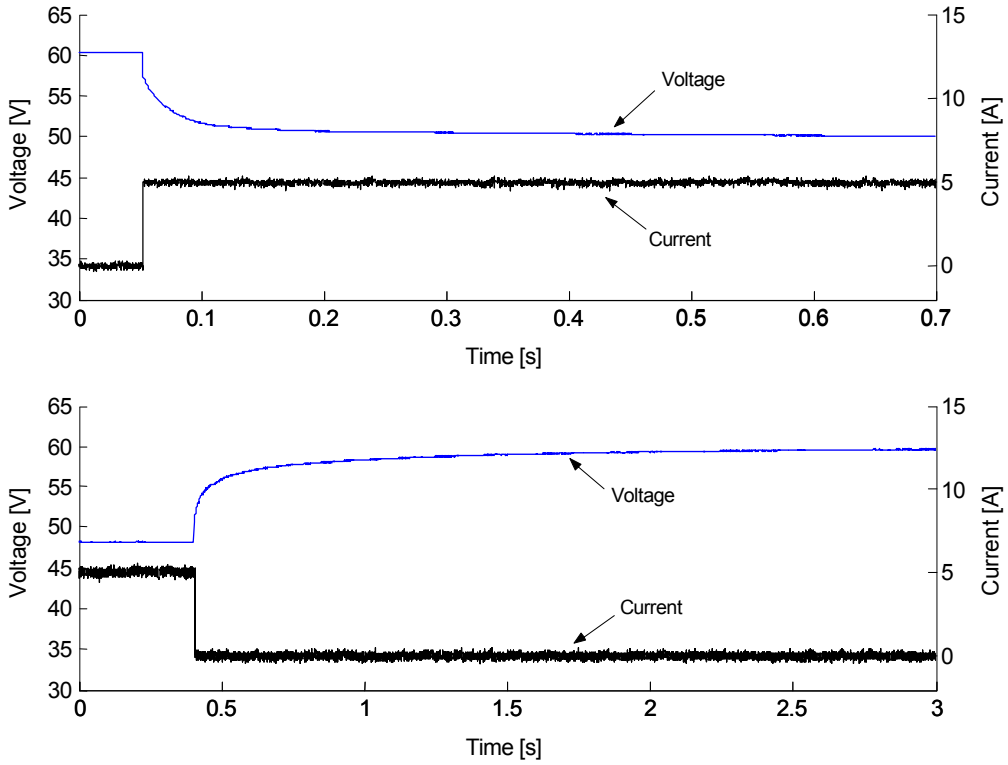

Figure 3.20 Measured stack-voltage and stack-current transients when stepping the required fuel cell current from 0 A to 5 A (above) and from 5 A back to 0 A (below).

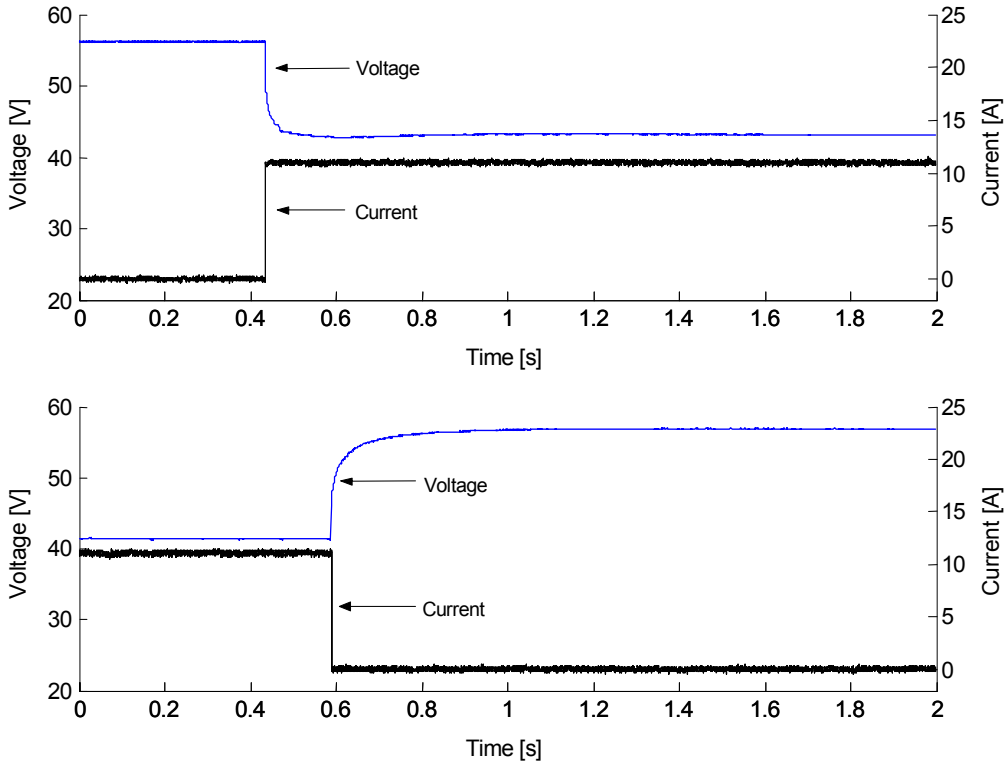

Figure 3.21 Measured stack-voltage and stack-current transients when stepping the required fuel cell current from 1 A to 11 A (above) and back to 1 A (below).

3.3.3 Metal hydride testing

In order to characterise the MH-storage unit, several charging and discharging experiments where the storage was isolated from the rest of the system were performed. Furthermore, the MH-storage interface with the electrolyser and the fuel cell were also investigated as subsystems.

Charging

The nominal capacity of the MH-storage unit is 14 Nm^3 H_2. In order to verify this capacity and to investigate the relation between the MH-pressure/temperature and the H_2 content (i.e., large-scale PCT-analysis), several experiments were performed by using standard 200 bars, 50 L H_2 bottles.

During charging of the MH-storage, the H_2 absorption flow rate, MH-pressure, H_2 input pressure, and nine different temperatures (in the middle of each of the four cylindrical tanks, on the surface of each tank, and on one of the cooling fins in the cavity between the four tanks) were measured. However, in the forthcoming the MH-temperature will be presented as the average of the measured internal temperature in each of the four MH-tanks.

Generally, the internal temperatures of the MH-tanks increased faster than the surface temperatures, indicating poor heat transfer between the hydride and the container. Furthermore, during the first phase of the charging process the internal temperature of Tank #4 was found to increase faster than that of Tank #2 and Tank #3, while Tank #1 was found to have a lower temperature increase, leading to a constant temperature difference between Tank #1 and Tank #4 of typically 2–4°C. The same trend was observed among the surface temperatures, but here the temperature difference was in the order of 1–2°C. Note also that the cavity temperature could get 4–6°C higher than the other surface temperatures. This is due to the compact storage design combined with horizontal cooling fins and no forced air convection.

In the charging experiment given in Figure 3.22, the MH-storage was charged at a constant H_2 flow rate of 7 NL/min and the ambient temperature was kept at 23 ± 1°C. The MH-storage was charged under these conditions until the MH-pressure balanced the H_2 input pressure. This pressure-balance occurred 22 hours and 40 minutes after charging was activated. Charging of the MH-storage was fulfilled in a second "peak-charging" experiment (indicated by the blue arrow in Figure 3.22) after switching to a new H_2 bottle. Again, the H_2 flow rate was set to 7 NL/min, while the ambient temperature was kept at 21 ± 1 °C. In this "peak-charging" experiment, the pressure-balance occurred after 2 hours and 30 minutes. The amount of absorbed H_2 for different pressure intervals during charging is given in Table 3.2.

When the first pressure-balance occurred, the MH-temperature had increased by 23°C (from 23°C to 46°C) and the MH-pressure had reached 16.7 bars. At the beginning of the "peak-charging" experiment the MH-pressure had decreased to only 7.2 bars at 21°C for the very same H_2 concentration. Note also that the total amount of H_2 absorbed by the MH-storage during the 4-day period corresponds to about 80 % (11.4 Nm^3) of the nominal capacity (specified by manufacturer), and that most of the capacity is available at lower pressure levels.

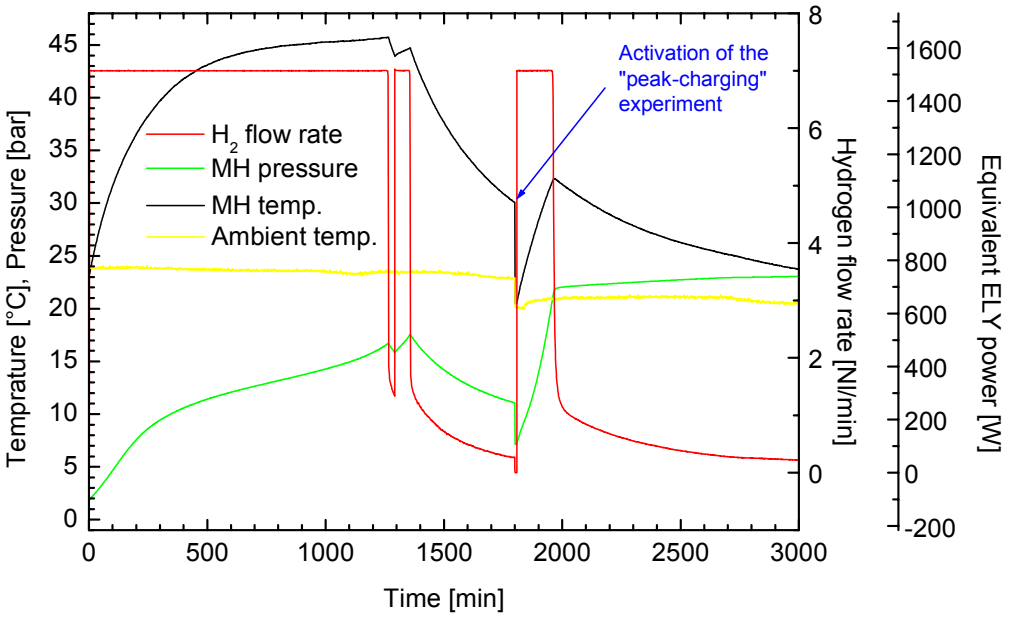

Figure 3.22 Measurement of MH-pressure, MH-temperature, and H_2 flow rate during a 4-day period, while charging the MH-storage. The equivalent electrolyser power input was based on an energy efficiency of 75 %.

Table 3.2 Amount of absorbed H_2 for different MH-pressure intervals during charging of the MH-storage at a constant hydrogen flow rate of 7 NL/min

Pressure interval [bar]	1.7–12	12–16	16–21	21–23	Total
Amount of hydrogen [NL]	4108	4381	2194	732	11417

Charging MH-storage with the electrolyser

Figure 3.23a and 3.23b show a start-up and about 1.5 hours of operation with the electrolyser/MH-storage subsystem. The MH-storage was charged with ~1.1 Nm^3 H_2, increasing the MH-pressure from 5.5 bars at 19°C to 10 bars at 30°C. Note that even if a pressure of 15 bars is available from the electrolyser after only four minutes of operation, additional time is needed to pressurise the H_2 purification unit. In the experiment shown in Figure 3.23b, where the electrolyser/H_2 purification unit output pressure had to be increased by 5.2 bars, charging of the MH-storage started 15 min after electrolyser start-up.

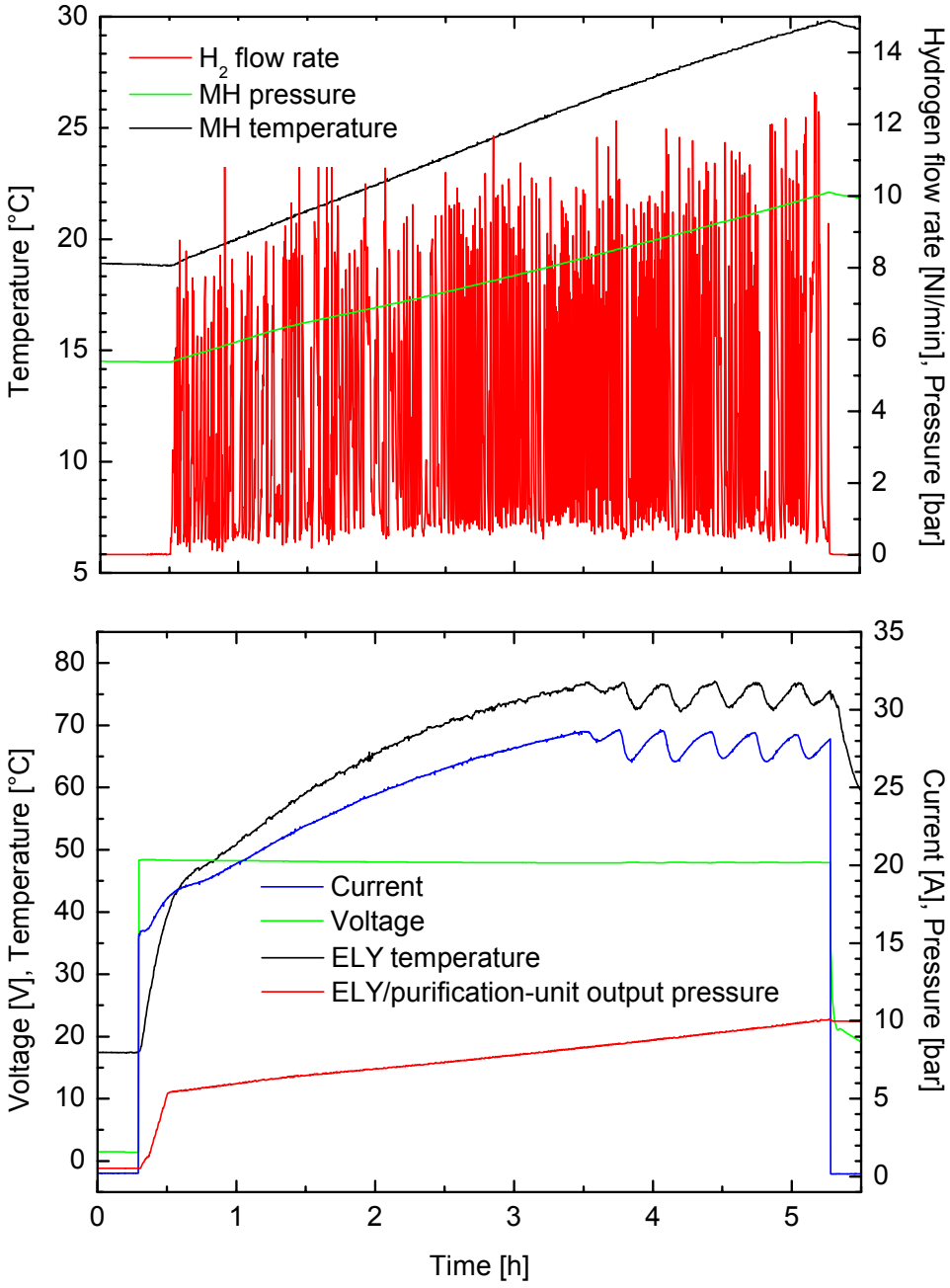

Figure 3.23a (above) Electrolyser/MH-storage subsystem start-up experiment. Measurements of the MH-pressure, MH-temperature, and H_2 flow rate.

Figure 3.23b (below) Electrolyser/MH-storage subsystem start-up experiment. Measurements of the electrolyser stack-current, stack-voltage, stack-temperature, and the electrolyser /H_2 purification unit output pressure.

A three-days experiment shown in Figure 3.24 was also conducted in order to observe the MH-pressure and the internal MH-temperature during daily operation when the MH-storage was close to be fully charged (~75 %). After the electrolyser had reached nominal operation conditions, it was operated at constant 30 A. Because this was one of the very first experiments where the electrolyser was used to fill the MH-storage, the electrolyser was allowed to purge the tubing between the electrolyser and the MH-storage for 8 hours. When the H_2 flow was directed into the MH-storage after 8 hours

with H_2 flushing, the MH-temperature increased from room temperature (~20°C) to ~30°C in 3 hours, which agree well with the MH-temperature in Figure 3.22, even though the H_2 flow from the electrolyser was "chopped" ON/OFF by a magnetic valve compared to the continuous H_2 flow from the pressurised bottles. The elevated MH-temperature and the specific H_2 concentration in the MH-storage forced the MH-pressure to increase from 4 bars to 8 bars. The MH-storage was charged with 898 NL H_2 during the first charging period. The electrolyser was switched OFF and the elevated MH-temperature and MH-pressure was allowed to recover within a period of 14 hours, which in a real-world HSAPS typically would be from sunset at about 6 pm to sunrise at about 8 am. The internal MH-temperature decreased to room temperature while the MH-pressure decreased to about 5 bars during this period. The MH-storage was then charged for another 5 hours in a second charging period the day after, adding 1172 NL H_2 to the storage. Again, the MH-temperature increased to about 30°C while the MH-pressure increased to 10 bars. During a recovering period of about 18 hours the MH-temperature decreased to room temperature and the MH-pressure decreased to 7 bars. However, during the third charging period where 1009 NL H_2 was added to the storage in about 6 hours, the MH-pressure increased rapidly towards the nominal electrolyser pressure of 16 bars. Therefore, unless there exists a robust measurement of the actual H_2 concentration in the MH-storage, there is no clear indication during the last couple of days that the MH-storage is close to be fully charged the next day. E.g., the pressure in a conventional pressurised tank would give a better indication of the exact H_2 content in the storage.

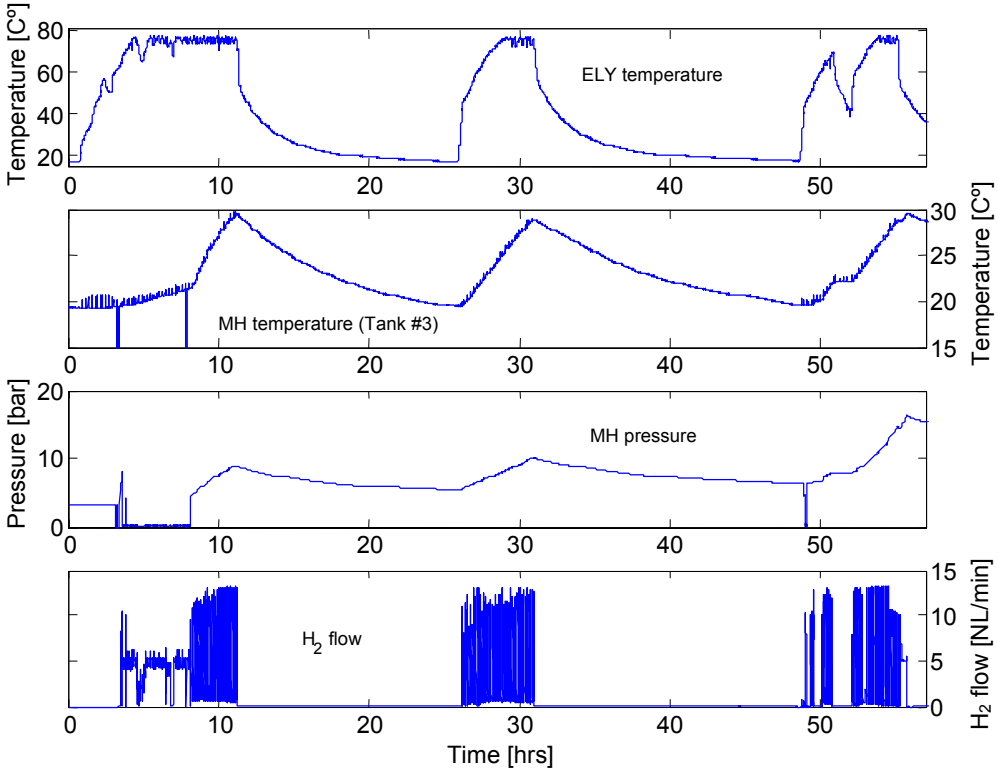

Figure 3.24 A three-days experiment investigating the MH-pressure and internal MH-temperature. The electrolyser stack-temperature and H_2 production rate is also shown.

Discharging

Several MH-storage discharging experiments were performed in order to investigate the H_2-capacity and the relation between the MH-pressure/temperature and the H_2

concentration. Particular attention was paid to the characteristics at the H_2 flow rate of 7 NL/min specified in the design criteria. During discharging of the MH-storage, the H_2 desorption flow rate in addition to the MH-pressure and the nine different MH-temperatures were measured during the charging experiments.

Generally, the internal temperatures of the MH-tanks decreased faster than the surface temperatures. Furthermore, during the first phase of the discharging process, the internal temperature of Tank #4 was found to decrease faster than that of Tank #2 and Tank #3, while Tank #1 was found to have a lower temperature decrease, leading to a constant temperature difference between Tank #1 and Tank #4 of typically 2–3 °C. The same trend was observed among the surface temperatures, but here the temperature difference was in the order of 1°C.

In the discharging experiment given in Figure 3.25, the MH-storage was discharged at a constant H_2 flow rate of 7 NL/min at ambient temperature of 24 ± 1°C. The MH-storage was discharged under these conditions until the MH-pressure reached the lower pressure limit of 1.7 bar (corresponding to the lower fuel cell input pressure). The minimum pressure limit was reached 7 hours and 36 minutes after discharging was activated. At this point, the MH-temperature had decreased by 19°C (from 24°C to 5°C) and the amount of H_2 desorbed from the MH-storage corresponded to 23 % (3.2 Nm^3) of the nominal capacity, Table 3.3.

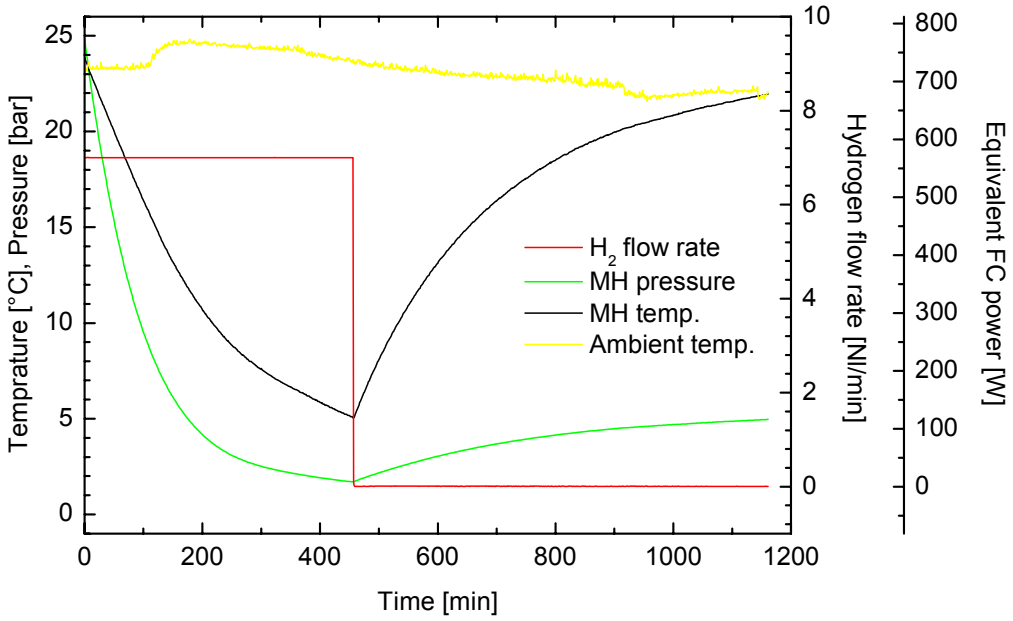

Figure 3.25 MH-storage discharge experiment at 7 NL/min. Measurement of MH-pressure, MH-temperature, and H_2 flow rate during a 20-hour period. The equivalent fuel cell power was based on energy efficiency of 50 %.

Table 3.3 Amount of desorbed H_2 for different pressure intervals during discharging of the MH-storage unit at a constant H_2 flow rate of 7 Nl/min

Pressure interval [bar]	24.8–16	16–6	6–4	4–3	3–2	2–1.7	Total
Amount of hydrogen [NL]	322	749	377	307	924	518	3204

In a second experiment the H_2 flow rate was reduced to 5.4 NL/min that corresponds to a fuel cell power output of 500 W, Figure 3.26. However, the 1.7 bar limit was reached 11 hours after activation, and similar results were found with respect to

MH-temperature decrease (17°C, from 23°C to 6°C) and amount of desorbed H_2 (3.4 Nm^3, or 25 % of the nominal capacity), Table 3.4.

Based on the results of the discharging experiments, it was concluded that the MH-storage did not meet the design criteria for the H_2 flow rate. Furthermore, the MH-temperature was found to decrease faster than expected, resulting in a low plateau MH-pressure regarding fuel cell operation.

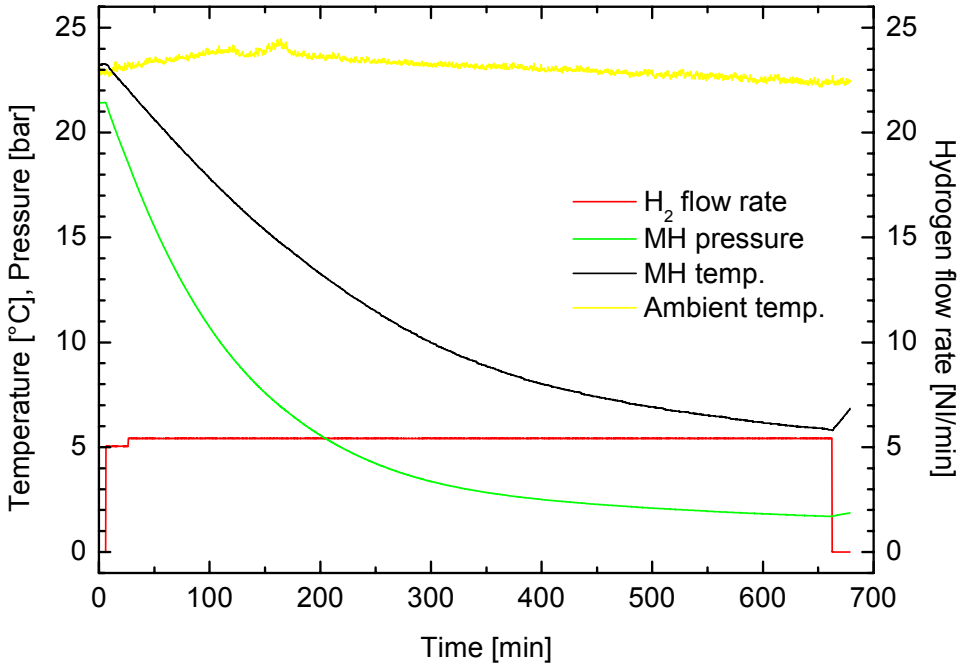

Figure 3.26 MH-storage discharge experiment at 5.4 NL/min corresponding to a fuel cell power output of 500 W. Measurement of MH-pressure, MH-temperature, and H_2 flow rate during an 11.5-hour period.

Table 3.4 Amount of desorbed H_2 for different pressure intervals during discharging of the MH-storage at a constant H_2 flow rate of 5.4 NL/min

Pressure interval [bar]	21.4–4	4–3	3–2	2–1.7	Total
Amount of hydrogen [Nl]	1373	388	1083	705	3548

Discharging MH-storage with FC

Generally, a MH-storage can benefit from heat wasted by other components to increase the system efficiency. Thus, to obtain an internal heat transfer between the fuel cell and the MH-storage, these components were situated next to each other in such a way that part of the fanned air from the fuel cell was directed into the cavity of the MH-storage. That is, the fuel cell was heating the MH-storage unit during operation. Prior to these discharge tests with the fuel cell, the MH-storage was charged with standard 200 bars, 50 L bottles.

In Figure 3.27a and Figure 3.27b, the MH-storage/fuel cell interface was operated at a constant load of 450 W (corresponding to a H_2 flow rate of 5.1 Nl/min) and an ambient temperature of 25 ± 1°C. The flow controller was set to 100 % (i.e. 10 Nl/min H_2). Thus, the H_2 flow rate was determined by the consumption rate of the fuel cell. The subsystem was operated under these conditions until the MH-pressure reached the lower limit of 1.7 bars (as for the individual MH-storage experiments). The lower

limit pressure was reached after 36 hours. At this point, the MH-temperature had decreased by only 4°C (from 23°C to 19°C) and the amount of H_2 desorbed from the MH-storage corresponded to about 80 % (11.1 Nm^3) of the nominal capacity (14 Nm^3). Compared to the individual MH-storage experiments, the heated air from the fuel cell system contributed to a considerable improvement in the MH-storage performance. Note also that 60 % (6.5 Nm^3) of the H_2 was delivered at a pressure below 4 bars and at a temperature of 24°C. This clearly indicates that the poor MH-storage thermal performance under normal operating conditions (without forced air convection) could be considerably improved with a better thermal system design.

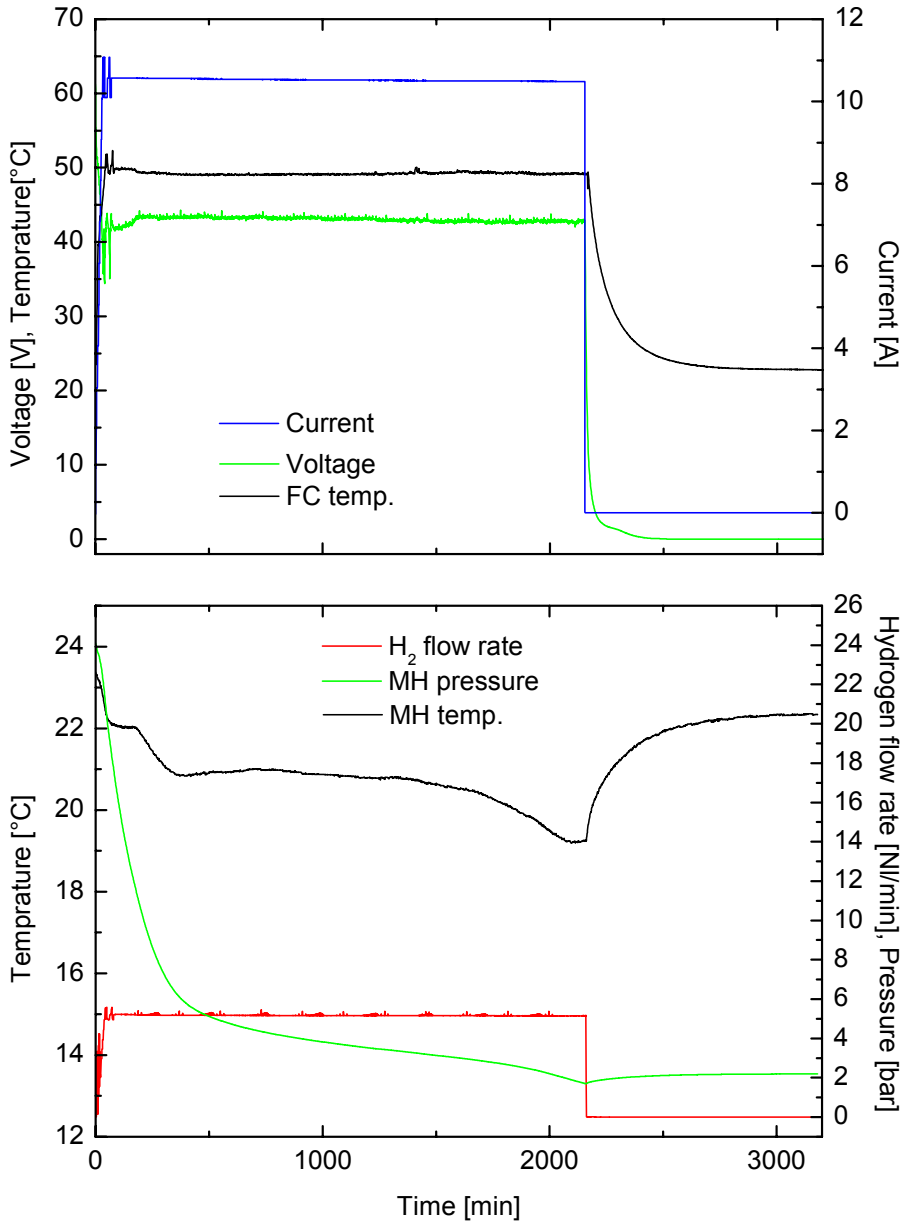

Figure 3.27a (above) MH-storage/fuel cell subsystem experiment for a power load of 450 W. Measurements of the fuel cell stack-current, stack-voltage, and stack-temperature.

Figure 3.27b (below) MH-storage/fuel cell subsystem experiment with a load requirement of 450 W. Measurements of the MH-pressure, MH-temperature, and H_2 flow rate.

Table 3.5 Amount of desorbed H_2 for different pressure intervals during operation of the MH-storage/fuel cell interface at a constant H_2 flow rate of 5.1 Nl/min

Pressure interval [bar]	27–16	16–12	12–6	6–4	4–3	3–2	2–1.7	Total
Amount of hydrogen [Nl]	430	349	1096	2666	3673	2372	495	11080

In order to investigate the influence of the internal heat transfer from the fuel cell to the MH-storage at low power outputs another experiment with the MH-storage/fuel cell subsystem was performed, shown in Figure 3.28a and 3.28b. Here, the MH-storage/fuel cell subsystem was operated at a load requirement of maximum 100 W (corresponding to a H_2 flow rate of 1.1 Nl/min) and the ambient temperature fluctuated from day-time to night-time (22 ± 4°C).

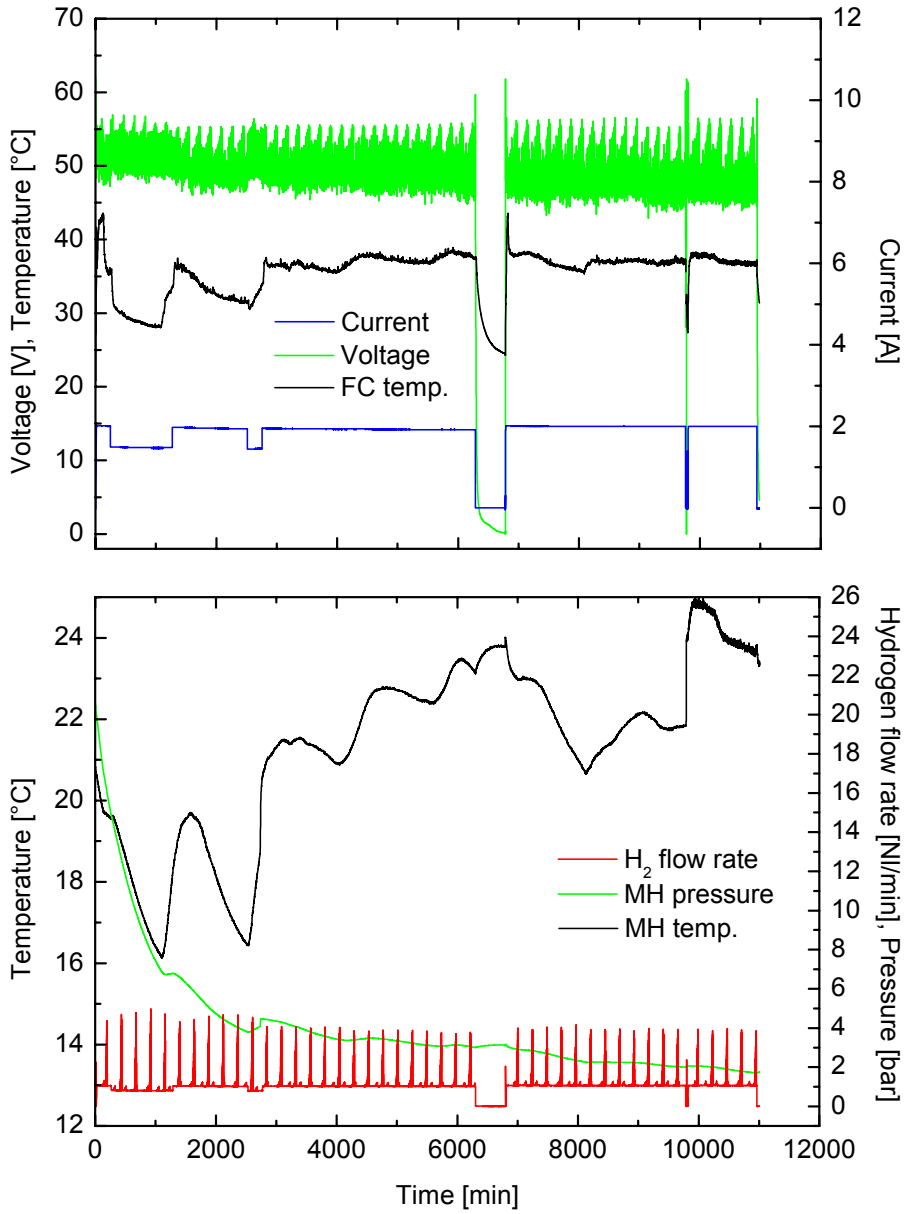

Figure 3.28a (above) MH-storage/fuel cell subsystem with maximum load 100 W. The fuel cell stack-current, stack-voltage, and stack-temperature are given.

Figure 3.28b (below) MH-storage/fuel cell subsystem with maximum load 100 W. The MH-pressure, MH-temperature, and H_2 flow rate are given.

Again, the flow controller was set to 100 % and the experiment was automatically terminated after a little more than one week when the MH-pressure reached the lower pressure limit of 1.7 bars.

As for the high power output experiment, the amount of H_2 desorbed from the MH-storage shown in Table 3.6 corresponded to about 80 % (11.6 Nm^3) of the nominal capacity (14 Nm^3). However, while the internal heat transfer dominated the MH-temperature in the high power output experiment, the MH-temperature in the low power output experiment was mainly dominated by natural air convection. This is clearly seen from the variation in the MH-temperature with the day-/night-time temperature fluctuations in the laboratory. Note also that 79 % (9.1 Nm^3) of the H_2 was delivered at a pressure below 4 bars and a temperature of 23 ± 2°C, which is comparable with the result of the high power output experiment.

Table 3.6 Amount of desorbed H_2 for different pressure intervals during operation of the MH-storage subsystem at a H_2 flow rate of 1.1 NL/min (100 W power output)

Pressure interval [bar]	20–4	4–3	3–2	2–1.7	Total
Amount of hydrogen [Nl]	2469	4333	3450	1329	11581

3.3.4 Testing the interplay between Battery/Fuel cell and Battery/Electrolyser

Battery/fuel cell

The battery and the fuel cell were directly connected, but a power diode had to be installed between the two components in order to prevent cell current reversal in the fuel cell stack. The main operating variables for a battery/fuel cell subsystem experiment are given in Figure 3.29.

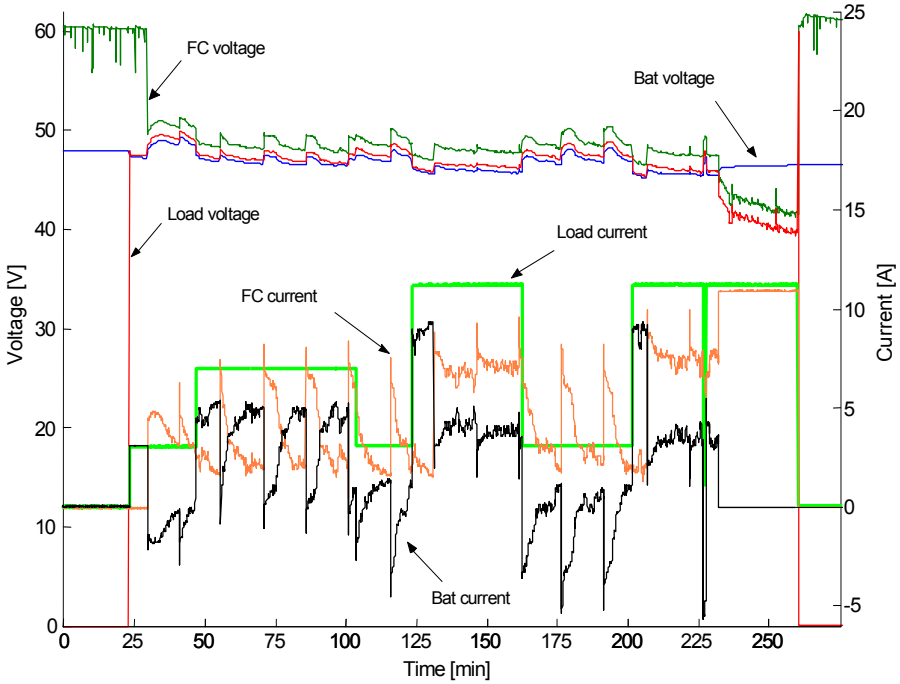

Figure 3.29 Interaction between the fuel cell and battery. Measurements of the fuel cell stack-current and stack-voltage in addition to the battery current and voltage. The corresponding current required by the load is also measured. Notice how the power-balance between the fuel cell and the battery fluctuates due to the O_2-purging. The voltage supplied to the load is varying between 47 V – 50 V.

From Figure 3.29 at 50 minutes, when the battery charge current had dropped down to zero again after the last O_2-purging (45 minutes), the load current was stepped up to 7 A. This increase in load requirement did not affect the fuel cell operation, but caused the battery to start discharge to the load with a rate of 5 A (71 % of the load). This continued until a new O_2-purging (60 minutes) increased the fuel cell stack-voltage, and thus the fuel cell stack-current to above 7 A, but the fuel cell stack-voltage and stack-current decreased down to about 2 A (29 % of the load). This sequence was repeated within each of the O_2-purging intervals with load current at 7 A. The same behaviour was observed when the load current requirement was stepped from 3 A to 11 A. However, the O_2-purging at about 130 minutes caused the air pump in the fuel cell to run at higher speed (due to higher stack-current) which continuously flushed the product water out of the stack. This allowed better fuel cell operation because the stack-current stabilised at 7 A (64 % of the load). The same behaviour is shown in the next period with load current requirement of 11 A, starting at 200 minutes. The battery/fuel cell behaviour within the periods with load current requirement of 3 A were reproducible in all the three periods. After 230 minutes at a load current requirement of 11 A, the battery was switched out of the subsystem. This caused the fuel cell stack-voltage to decrease from 48 V to 43 V, demonstrating that the DC bus bar voltage was more stable with the battery connected to the HSAPS.

A nominal battery-configuration of 42 V giving a charging-voltage range of 42 V – 51.5 V (maximum charging voltage per cell is 2.5 V) would be suitable compared to the fuel cell voltage operation range of about 43 V–50 V. Then the fuel cell could offer a continuous charging process, compared to the charging-current in Figure 3.29. However, a DC/DC converter would ensure stable voltage output from the fuel cell.

Battery/electrolyser

Figure 3.30 shows a 36 V battery-configuration initially being charged. When the battery state-of-charge reaches 70 %, the electrolyser is switched ON and runs in parallel with the battery charging process. No user load was applied, thus, all power available from the emulated photovoltaic array was regarded as excess renewable energy. The reason for using a 36 V instead of the 48 V battery in this experiment was to avoid battery-discharge to the 48 V electrolyser. The PEM electrolyser used in this work handles fluctuating power input. Thus, battery-discharging to the electrolyser in order to ensure constant power level was not necessary, and energy conversion from the battery (short-term storage) to the hydrogen-loop (long-term storage) was avoided. Furthermore, the point with this experiment was to illustrate that the electrolyser could be switched ON at lower battery state-of-charge, e.g., at 70 % as in this case, compared to 90 % which is a typical setting used in earlier works, e.g. [1, 12, 13] (earlier works and battery state-of-charge settings will be discussed in Section 5.5).

From Figure 3.30, the battery voltage flattened out at about 44.5 V. Due to charging, the increase in over-potential caused the charging current to decrease from 10 A to 2.5 A (charging current is negative in Figure 3.30). This decrease in battery charging current corresponded to the observed decrease in the current drawn from the power supply. The electrolyser stack-current of about 5 A was too small to notice any rise in stack-temperature, thus, the stack-current was rather constant throughout the experiment. However, the battery was charged from 70 % state-of-charge to 90 % state-of-charge in 2 hours, about the same time the electrolyser would have needed to reach nominal operation according to Figure 3.12 if the stack-voltage had been 48 V.

Furthermore, the battery charging current decreased with 6 A during the first hour after electrolyser start-up, which corresponds well with the electrolyser stack-current increase of 7 A during the first hour of operation as shown in Figure 3.12.

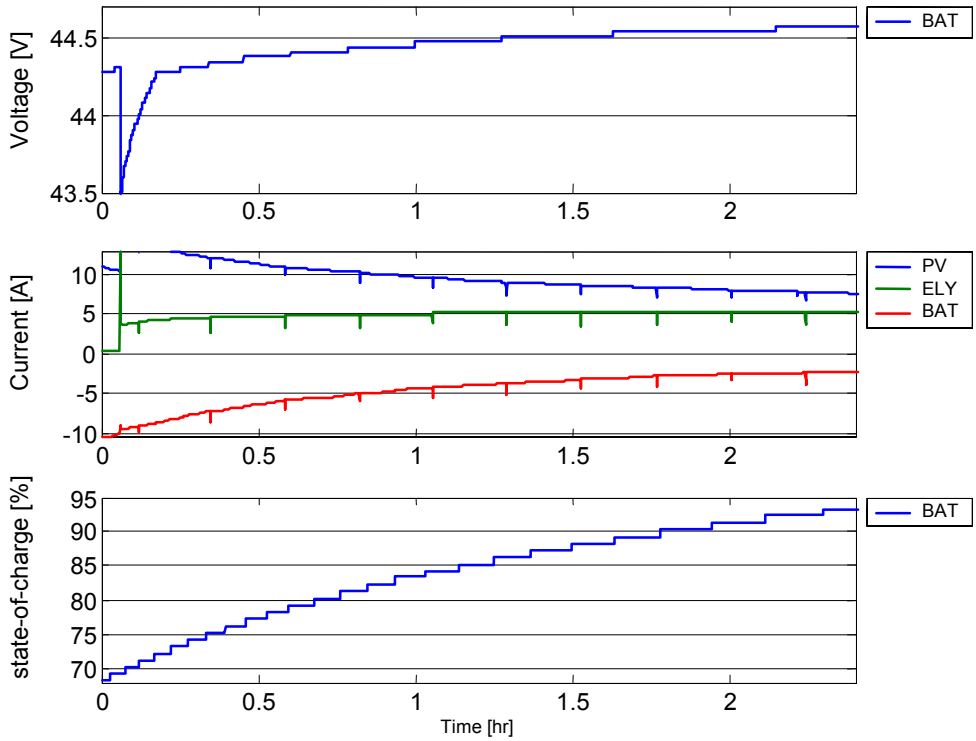

Figure 3.30 Voltages and currents measured during an electrolyser start-up in parallel with a battery charging process. The battery state-of-charge was also estimated. A 36 V battery configuration is used in this experiment in order to avoid discharge to the 48 V electrolyser.

The maximum allowable charging voltage is 45 V for the three 12 V batteries connected in series. This is a rather low electrolyser stack-voltage resulting in 5 A with a cold stack and 10 A with a warm stack. Still, Figure 3.30 illustrates the idea with this experiment; the current available from the power supply was set at constant 13 A (maximum battery charging current), but the current drawn from the power supply slowly decreased as the battery over-potential increased due to charging. This indicated a decrease in conversion of available energy from the power supply (excess renewable energy in a real-world HSAPS) into chemical energy for storage. The available energy conversion efficiency would have been closer to 100 % if the electrolyser stack were allowed to operate at nominal stack-voltage, which would be the case if the nominal battery voltage had been at 42 V, resulting in a maximum charging voltage of 51.5 V. In this case, the electrolyser would accept higher stack-current and thus the stack-temperature could rise and allow even more current to pass through the stack until nominal operation conditions had been reach within about 1.5 hours. At the same time, the battery state-of-charge would reach the upper levels where no more current could pass into the battery, not even at maximum charging voltage. In other words, the electrolyser does not have to “wait” until the battery is fully charged in order to be switched ON. Parallel operation of the electrolyser during start-up and the battery in charging mode is then able to share the excess renewable

energy. This start-up sequence can be tuned by altering both the battery size and the state-of-charge control limit, which signals the electrolyser ON.

3.4 Data acquisition and control system (DACS)

Figure 3.31 shows the architecture of the data acquisition and control system (DACS) for the HSAPS. The intentions for choosing this type of solution was the need for a modular and flexible design as the purpose of the test facility was to both demonstrate a hydrogen energy system in operation, but also to be able to expand the system and exchange components in a rational and efficient way.

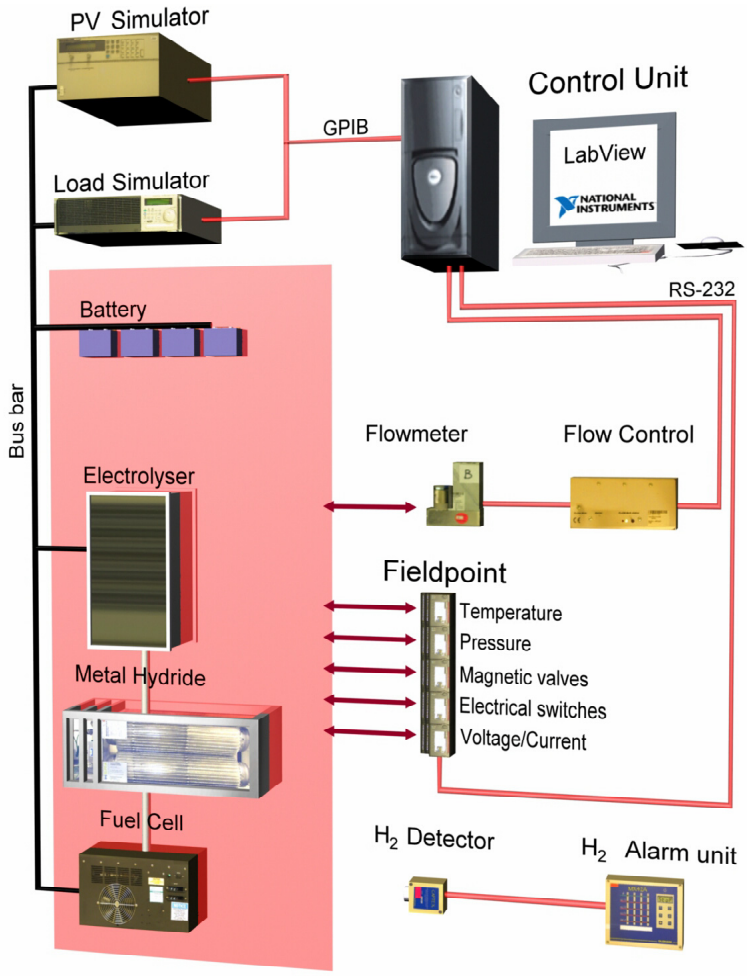

Figure 3.31 The overall data acquisition and control system (DACS) for the HSAPS test-facility. (Figure made by Bård A. *Melk Design*)

The DACS developed for the HSAPS test-facility consists of both hardware and software components.

Hardware

An overview of the DACS hardware is given in Figure 3.32. Once switched ON, the fuel cell and the electrolyser were controlled by their own control system developed by the manufacturer, while high-level energy management were performed by the DACS. For distributed monitoring and control, a modular I/O system (Fieldpoint, National Instruments) and mass flow meter/controllers were used, as also indicated in

Figure 3.31. The implementation of the multi I/O-board used for high-speed data acquisition is also shown in Figure 3.32. The I/O-modules handles voltage and temperature measurements as well as transmitter and transducer signals (for pressure and current measurements) and relay operations (for valve operations and ON/OFF-switching of components). The I/O-capacity of the DACS is summarised in Table A.9.

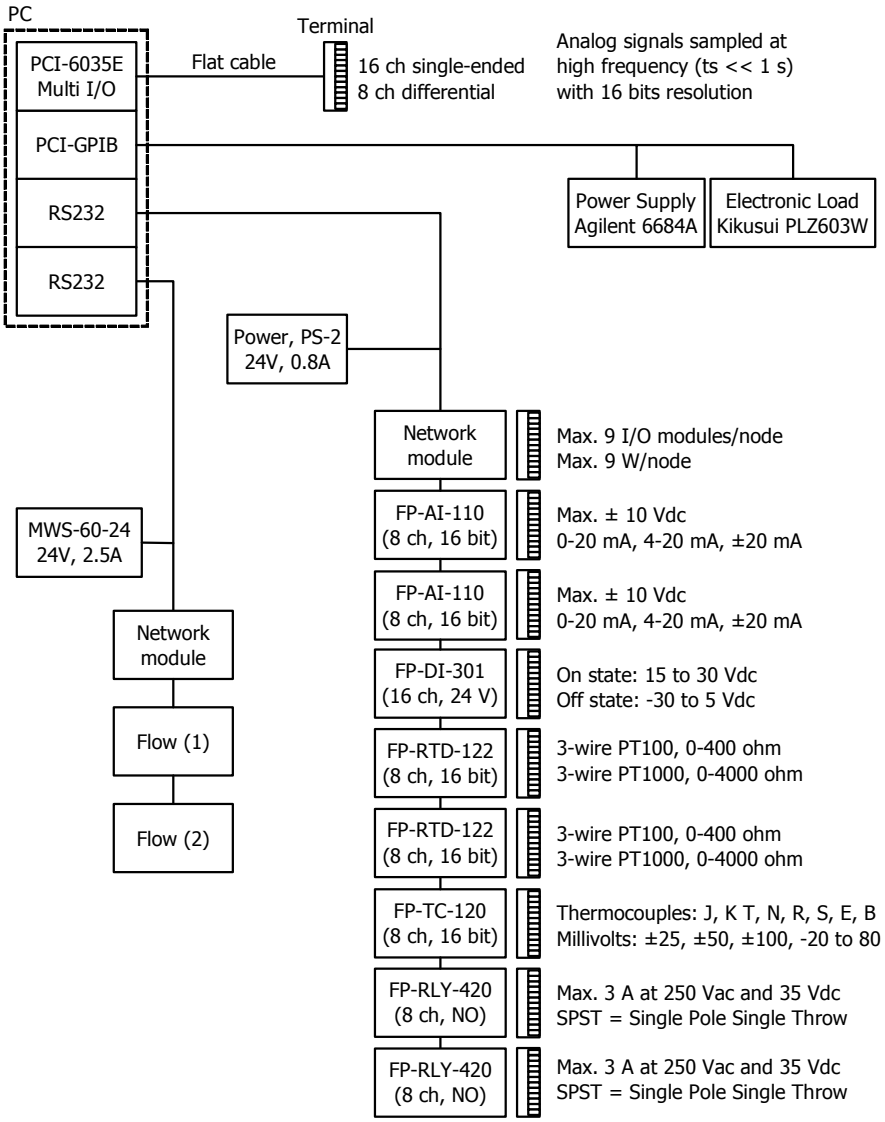

Figure 3.32 Overview of the DACS hardware.

Software

The DACS software was based on a PC running LabVIEW 6.1 with the data logging and supervisory control (DSC) add-on module. The DSC add-on module provides I/O-management, event logging, alarm management, distributed logging, tagged historical data base and trending, built-in security, configurable networking features, and OLE for process control (OPC) device connectivity. Finally, drivers for hardware from National Instruments and many third party manufacturers do exist. For communication with the flow meter/controllers a flow-bus DDE server, FlowDDE32 from Bronkhorst, was used. Communication with hardware was illustrated in Figure 3.32.

References

1. J.P.Vanhanen, *On the performance of improvements of small-scale photovoltaic hydrogen energy systems*. 1996: PhD.Thesis, Espoo, Finland.
2. E.Rasten, *Electrocatalysis in Water Electrolysis with Solid Polymer Electrolyte*, in *Department of Materials Technology*. 2001, PhD.Thesis, Norwegian University of Science and Technology (NTNU): Trondheim, Norway.
3. Institute for Solar Energy (ISE) Fraunhofer. 2002: Freiburg, Germany.
4. P.Millet, R.Durand, and M.Pineri, *Preparation of new solid polymer electrolyte composites for water electrolysis.* J. Hydrogen Energy, 1990. **15**: p. 245.
5. H.Mori, et al., *Development of membrane-electrode composites for polymer water electrolysis using new chemical plating method.* Hydrogen Energy progress XI, 1996. **1**: p. 579.
6. M.Kondoh, et al., *Development of polymer-electrolyte water electrolyser.* J.New.Mat.for Electroanal. Chem, 2000. **12**: p. 3777.
7. K.Ledjeff, et al., *Development of pressure electrolyser and fuel cell with polymer electrolyte.* Int.J.Hydrogen Energy, 1993. **19**: p. 453.
8. S.Stucki, et al., *PEM water electrolysers:evidence for membrane failure in 100kW demonstration plants.* J.Appl.Electrochem, 1998. **28**: p. 1041.
9. K.Tømmerberg, *Vannelektrolyse*, in *Institutt for Informatikk*. 1995, Universitet i Oslo.
10. Bronkhorst High-Tech B.V, T.N., *FLUIDAT on the net*. 2004.
11. T.Nguyen and M.W.Knobbe, *A liquid water management strategy for PEM fuel cell stacks.* Journal of Power Sources, 2002. **114**: p. 70-79.
12. Ø.Ulleberg, *Stand-Alone power systems for the future: Optimal design, operation & control of solar-hydrogen energy system*. 1998, NTNU, Norges teknisk-naturvitenskapelige universitet: Trondheim. p. 210.
13. H.Barthels, et al., *Phoebus-Jülich:an Autonomous energy supply system comprising Photovoltaics, Electrolytic Hydrogen, Fuel Cell.* J. Hydrogen Energy, 1997. **23**(4): p. 295-301.

4. Modelling the test-facility

The core of this thesis is based on the laboratory HSAPS test-facility. However, computer models of this laboratory system were developed. The motivation for the modelling work was to verify proposed control strategies for high-level HSAPS energy management. The HSAPS in this work is based on solar energy, thus, it is of key importance to let the system run throughout the complete solar cycle of 365 days in order to fully evaluate the control strategies. With a time resolution of one hour, a year is simulated within minutes in with the semi empirical computer model used in this work. The energy storage capacity for the battery and the hydrogen storage in the laboratory are mainly limited due to cost, thus they are better suited for investigation of daily and weekly operations rather than annual behaviour. As will be shown in Chapter 5, Chapter 7, and Appendix F, the hydrogen storage size should be about 250 kWh in a real-world system with the given 0.5 kW fuel cell and the 1.5 kW electrolyser. Thus, in addition to verify the proposed control strategies, a detailed computer model of the laboratory HSAPS is advantageous with the ability to swiftly alter the storage capacity for both the hydrogen storage and the battery. The HSAPS computer model is developed in SIMULINK [1]. SIMULINK is an interactive tool for modelling, simulating and analysing dynamic multidomain systems. One can build a block diagram, simulate its performance and refine the design. SIMULINK integrates seamlessly with MATLAB, providing immediate access to an extensive range of analysis and design tools.

4.1 HSAPS Component models

4.1.1 Photovoltaic array

A simple model of a PV array proposed by [2] is used in this modelling work. In this study, the PV array efficiency is excluded from the system efficiency for the HSAPS, thus the detailed dynamics of a PV array is not in focus in this case. The PV array model uses the intensity of the solar radiation to calculate the power output. Starting point is the relation between the cell voltage and current density (fitted curve):

$$i = \frac{b_1 \Psi}{n_s} - \frac{b_2}{(V_{OC} - V_C) \cdot n_s} \tag{4.1}$$

where

i = current density [A/cm^2]
Ψ = solar intensity [W/cm^2]
b_1 = constants in current [V^{-1}]
b_2 = density correlation [W/cm^2]
V_{OC} = open cell voltage [V]
V_C = cell voltage [V]
n_S = number of cells in series [-]

The voltage per cell depends on the total voltage and on the number of cells in series:

$$V_C = \frac{V}{n_S} \tag{4.2}$$

where

V = total voltage [V]

The total current from the PV array is given by:

$$I = i \cdot A \tag{4.3}$$

where

I = current [A]
A = total PV array area [m^2]

The electrical power generated by the PV array is given by:

$$E = I \cdot V = V_C b_1 \Psi A - \frac{V_C b_2 A}{V_{OC} - V_C} \tag{4.4}$$

where

E = electrical power [W]

The following data were used in order to estimate b_1 and b_2 [2]:

Ψ_{max} = 1000 [W/m^2]
Energy efficiency of PV array = 0.12 [-]
V_{OC} = 0.6 [V]

Subsequently, using $b_2 = 0.01 \cdot b_1$ as a form factor and Equations 4.1 – 4.4, [2] estimated the coefficients b_1 and b_2 to be 0.57 and 0.0057, respectively.

4.1.2 Maximum Power Point Tracker (MPPT)

A Maximum Power Point Tracker (MPPT) is an advanced DC/DC converter locating the maximum PV array power output. The MPPT in this model calculates the optimal voltage based on the maximum power for the PV array [2]. The input for the model is the solar radiation intensity and the characteristics (b_1, b_2, n_S, and V_{OC}) of the PV array. The electrical power generated in the PV array is given in Equation 4.4, the maximum power point is found when:

$$\frac{dE}{dV_C} = b_1 \Psi - \left(\frac{V_{OC} b_2}{(V_{OC} - V_C)^2} \right) = 0 \tag{4.5}$$

Correspondingly the MPPT sets the voltage to:

$$V = \left(V_{OC} - \sqrt{\frac{V_{OC} b_2}{b_1 \Psi}} \right) n_S \tag{4.6}$$

Figure 4.1 and Figure 4.2 show the current-voltage characteristic (*IU*-curve) and the power-voltage characteristic (*PU*-curve) for the PV model scaled with 130 cells in series and an area of 20 m^2 at four different solar radiation flux densities. The characteristics for the PV array in Figure 4.1 and Figure 4.2 are generated without the MPPT. When enabled, the MPPT will ensure a PV array power output corresponding to the maximum power at the actual solar insolation, corresponding to the highest points on the *PU*-curves in Figure 4.2. Figure 4.2 also includes *PU*-curves for the 1.5 kW PEM laboratory electrolyser presented in Chapter 3, measured at two different stack temperatures. The *PU*-curves in Figure 4.2 indicates that the PV array size in the

model is matched with respect to the PEM electrolyser because the *PU*-curve at 75°C follows quite well the PV array maximum power points. It should be noted that the *PU*-curves for the electrolyser are extrapolated above 1.7 kW. A 2.5 kW_{peak} PV array model is chosen due to the ability to serve a load at about 0.3 – 0.5 kW in addition to parallel operation of the electrolyser.

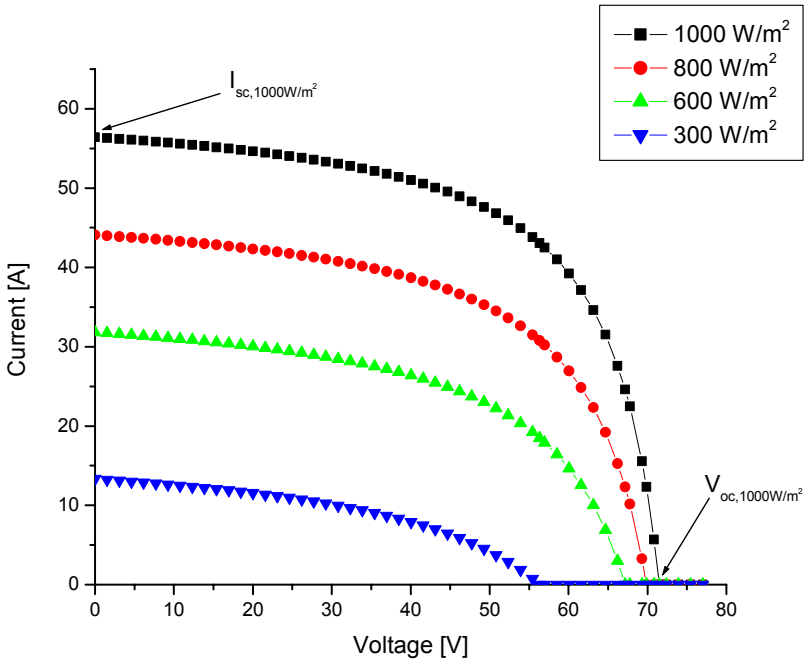

Figure 4.1 Current-voltage characteristics for the PV array model at four different solar radiation flux densities. At zero current, the open cell (circuit) voltage (V_{OC}) is reached, and at zero voltage, the short circuit current (I_{SC}) is reached.

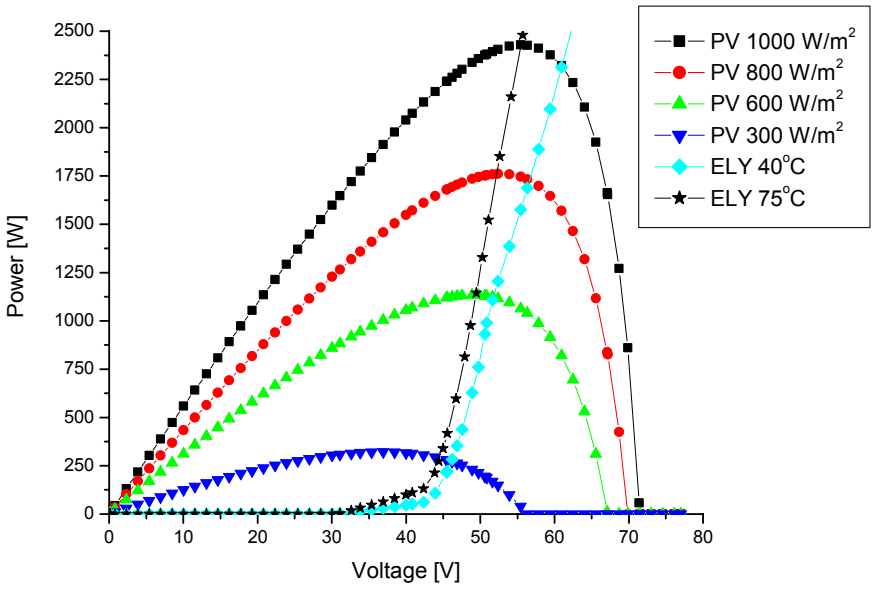

Figure 4.2 Power-voltage characteristics for the PV array model at four different solar radiation flux densities. The measured *PU*-curves for the electrolyser are extrapolated above 1.7 kW.

4.1.3 Electrolyser

The component model of the 1.5 kW PEM laboratory electrolyser is semi empirical. The non-linear *IU*-curves are measured at four different stack-temperatures ($T_{stack,ely}$) and implemented in two 3-dimensional look-up tables. One look-up table for interpolation of the stack-current ($I_{stack,ely}$) with PV array voltage (V_{PV}) and $T_{stack,ely}$ as inputs, and one look-up table for the interpolation of the stack-voltage ($V_{stack,ely}$) with PV array current (I_{PV}) and $T_{stack,ely}$ as inputs. A schematic of the look-up procedures are shown in Figure 4.3. The look-up table routine was available from the standard SIMULINK block sets. The measured *IU*-curves applied for calibration of the computer model were shown in Figure 3.3 in Section 3.2.3. Estimation of both $I_{stack,ely}$ and $V_{stack,ely}$ ensures correct electrical operation point for the electrolyser stack. E.g., if I_{PV} = 30 A, the electrolyser model checks the required $V_{stack,ely}$ (at the actual $T_{stack,ely}$). If $V_{stack,ely}$ resulting from the interpolation requires a higher voltage than available from the PV array, 30 A cannot flow through the stack. In this case the current flowing through the stack will be interpolated based on $T_{stack,ely}$ and V_{PV}. This means that the final simulated electrolyser stack-current and stack-voltage can be written:

$I_{stack,ely}$ final output = MIN{I_{PV}, $I_{stack,ely}$ interpolated based on V_{PV} and $T_{stack,ely}$ }
$V_{stack,ely}$ final output = MIN{V_{PV}, $V_{stack,ely}$ interpolated based on I_{PV} and $T_{stack,ely}$ }

In other words, $I_{stack,ely}$ cannot operate above I_{PV} and $V_{stack,ely}$ cannot operate above V_{PV}. The data in the look-up table is extrapolated if the values are outside the measurement range.

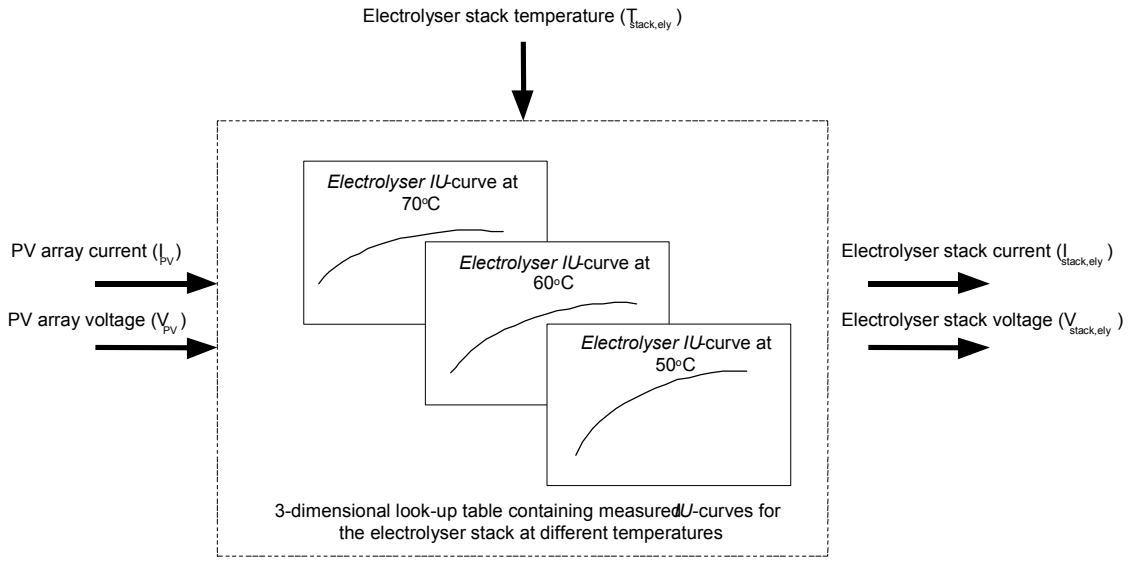

Figure 4.3 Schematic of the three-dimensional look-up table for the electrolyser stack where the inputs and the resulting output are inter-/extrapolated. If the electrolyser stack is current-controlled by the PV array, the output from the look-up table is $V_{stack,ely}$. If the electrolyser stack is voltage-controlled by the PV array, the output from the look-up table is $I_{stack,ely}$. The stack-temperatures in this figure are only used as examples.

Calculation of $T_{stack,ely}$ is based on a quasi-static, lumped capacitance thermal model where heat accumulated equals heat generated minus heat losses to the ambient and heat transported out of the electrolyser system by cooling facilities (Equation 4.7), one of the approaches also used by [3].

$$\dot{Q}_{store} = \dot{Q}_{gen} - \dot{Q}_{loss} - \dot{Q}_{cool} \tag{4.7}$$

However, simulation of thermal properties and finding $T_{stack,ely}$ for this specific electrolyser calls for another electrolyser system temperature, namely $T_{peripheral,ely}$. $T_{peripheral,ely}$ represents the average temperature of the deionised water flowing through the stack and peripheral system, presented in Section 3.2.3. The use of $T_{peripheral,ely}$ is necessary in order to simulate the correct electrolyser thermal transient, which is dominated by the rather abrupt change in the rate of increase of $T_{stack,ely}$. After 10 – 15 minutes during a normal start-up (nominal power from the PV array is available), $T_{stack,ely}$ starts flatten out at about 40 – 50 °C on its way up to nominal temperature at 70 – 75°C. The reason for this is related to the initial pressure build-up (4-10 minutes), meaning no release of product gases before reaching elevated pressures (10-15 bars). When the electrolyser starts releasing product gases (also containing vapour) the temperature gradient lowers because the escaping gas and vapour contain some of the generated heat in addition to that the shear forces of the product gases starts dragging deionised water from the stack and round in the electrolyser peripheral system (cooling effect on the stack). Figure 3.7 in Section 3.2.3 showed the interaction between the measured $T_{stack,ely}$ and the measured $T_{peripheral,ely}$.

The model takes care of the specific thermal behaviour by correlating the flow of deionised water circulating in the electrolyser system to the current allowed through the stack, shown in Figure 4.4. The correlation in Figure 4.4 was based on trial and error because it was not possible to measure the deionised water flow experimentally. This information was neither available from the manufacturer.

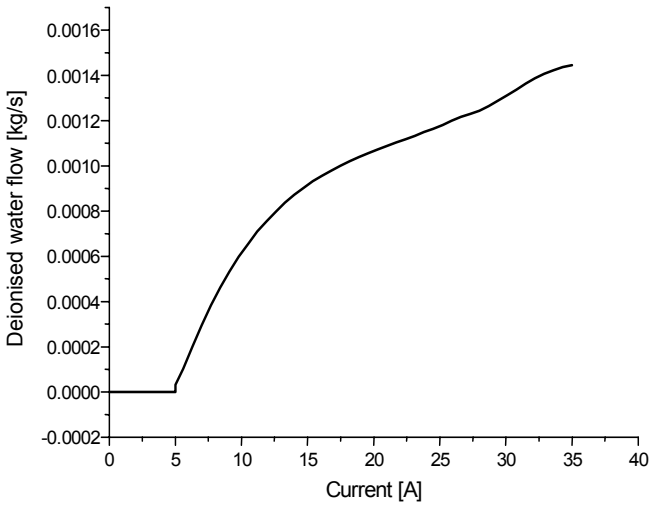

Figure 4.4 Deionised water flow in the electrolyser occurs due to the shear forces of the product gases H_2 and O_2. The production rates of the product gases are then again proportional to the stack-current, $I_{stack,ely}$.

The following sets of equations are proposed for finding $T_{stack,ely}$ through the use of $T_{peripheral,ely}$. In the following equations, the footnote-names *peripheral,ely* and *stack,ely* will be shortened to *periph* and *stack*, respectively. Deionised will be denoted *DI*.

Energy balance in the electrolyser stack:

$$\dot{Q}_{store,stack} = \dot{Q}_{gen} - \dot{Q}_{loss,stack} - \dot{Q}_{cool,periph} \quad \text{(Energy balance in stack)} \qquad (4.8)$$

Where

$$\dot{Q}_{store,stack} = C_{stack} \frac{dT_{stack}}{dt} \quad \text{(Thermal energy storage)} \qquad (4.9)$$

$$\dot{Q}_{gen} = n_c (U - U_{tn}) I_{stack} \quad \text{(Internal heat generation)} \qquad (4.10)$$

$$\dot{Q}_{loss,stack} = \frac{1}{R_{stack}} (T_{stack} - T_{amb}) \quad \text{(Heat losses to ambient)} \qquad (4.11)$$

$$\dot{Q}_{cool,periph} = \dot{m}_{DI}\, C_w (T_{stack} - T_{periph}) \quad \text{(Heat loss to DI water loop)} \qquad (4.12)$$

Insertion of Equation 4.9 – 4.12 into Equation 4.8 and solving for dT_{stack}/dt gives a first order non-linear differential equation (4.13):

$$\frac{dT_{stack}}{dt} = \frac{n_c (U - U_{tn}) I_{stack}}{C_{stack}} - \frac{(T_{stack} - T_{amb})}{C_{stack} R_{stack}} - \frac{\dot{m}_{DI}\, C_w (T_{stack} - T_{periph})}{C_{stack}} \qquad (4.13)$$

Energy balance peripheral system

$$\dot{Q}_{store,periph.} = \dot{Q}_{from\_stack} - \dot{Q}_{loss,periph.} - \dot{Q}_{cool,aux} \quad \text{(Heat balance periph.)} \qquad (4.14)$$

Where

$$\dot{Q}_{store,periph} = C_{periph} \frac{dT_{periph}}{dt} \quad \text{(Thermal energy storage)} \qquad (4.15)$$

$$\dot{Q}_{from\_stack} = \dot{Q}_{cool,periph} = \dot{m}_{DI}\, C_w (T_{stack} - T_{periph}) \quad \text{(Heat from stack)} \qquad (4.12)$$

$$\dot{Q}_{loss,periph} = \frac{1}{R_{periph}} (T_{periph} - T_{amb}) \quad \text{(Heat losses to ambient)} \qquad (4.16)$$

$$\dot{Q}_{cool,aux} = \dot{m}_{cool}\, C_w (T_{cw,i} - T_{cw,o}) \quad \text{(Auxiliary cooling)} \qquad (4.17)$$

Insertion of Equation 4.12 and 4.15 – 4.17 into Equation 4.14 and solving for $dT_{peripheral,ely}/dt$ gives a first order non-linear differential equation (4.18):

$$\frac{dT_{periph}}{dt} = \frac{\dot{m}_{DI}\, C_w (T_{stack} - T_{periph})}{C_{periph}} - \frac{(T_{periph} - T_{amb})}{C_{periph} R_{periph}} - \frac{\dot{m}_{cool}\, C_w (T_{cw,i} - T_{cw,o})}{C_{periph}} \qquad (4.18)$$

When solving Equation 4.18 for $T_{peripheral,ely}$, $T_{stack,ely}$ can finally be calculated from Eq. 4.13 and utilised in the look-up table along with either I_{PV} and V_{PV} for interpolation/extrapolation of the exact electrical and thermal operation point of the electrolyser.

The cooling system model was initially regulated with a PI controller, equal to the controller used in the laboratory electrolyser. The settings for the modelled PI controller were taken from the laboratory PI controller, which was tuned by the manufacturer. However, no significant difference in the annual simulation results were observed by replacing the PI controller with a simple relay function (ON/OFF-switching) that activated and allowed cooling water into the electrolyser model when $T_{stack,ely} > 77°C$. When $T_{stack,ely} < 73°C$, the relay function prevented simulated cooling water to enter the electrolyser model.

The constants and variables used in Equations 4.9 – 4.18 are:

n_c = number of cells in electrolyser stack [26]
U = cell voltage [V]
U_{tn} = thermo neutral cell voltage [V]
I_{stack} = stack-current [A]
C_{stack} = heat capacity in electrolyser stack [7400 J/K]
T_{stack} = temperature in electrolyser stack [K]
R_{stack} = thermal resistance in electrolyser stack [0.68 K/W]
C_{periph} = heat capacity in peripheral system [25000 J/K]
T_{periph} = temperature in peripheral system [K]
R_{periph} = thermal resistance in peripheral electrolyser system [0.43 K/W]
T_{amb} = ambient temperature [K]
C_w = specific heat capacity of water [4.18 kJ/kg K]
$\dot{m}_{DI}$ = mass flow deionised water [kg/s]
$\dot{m}_{cool}$ = mass flow cooling water [kg/s]
$T_{cw,i}, T_{cw,o}$ = temperature cooling water, in/out of heat exchanger respectively [K]

The heat capacities for the electrolyser stack (C_{stack}) and the peripheral electrolyser system (C_{periph}) were calculated based on measured geometry and tabulated (SI Chemical Data 3rd edition) specific heat capacity found for the specific materials used in the electrolyser. The thermal resistances for the electrolyser stack (R_{stack}) and the peripheral electrolyser system (R_{periph}) were calculated based on the respectively calculated heat capacities and the respectively measured thermal time constants (τ). The calculation of the thermal resistance will be shown later by using:

$$thermal\ resistance\ (R) = \frac{thermal\ time\ constant\ (\tau)}{heat\ capacity\ (C)} \tag{4.19}$$

Figure 4.5 shows both measured ($\Delta t_{measure} = 1$ s) and simulated ($\Delta t_{sim} = 1$ s) electrolyser start-up, about 4 hours nominal operation and eventually shutdown. $V_{stack,ely}$ constant at 48 V was applied to the laboratory electrolyser and to the electrolyser model (voltage not shown in Figure 4.5). Maximum current allowed to the electrolyser was 35 A. However, $I_{stack,ely}$ never reached 35 A because the current was limited by the voltage, thus, the electrolyser was voltage controlled at all time.

After about 2 hrs, the simulated $T_{stack,ely}$ reached 75°C and became regulated by the cooling water relay, which was in good agreement with the measured $T_{stack,ely}$ and the PI controller integrated in the laboratory electrolyser control system. The simulated $I_{stack,ely}$ evolved according to the simulated $T_{stack,ely}$ during start-up, which also agreed well with the measurements in the laboratory.

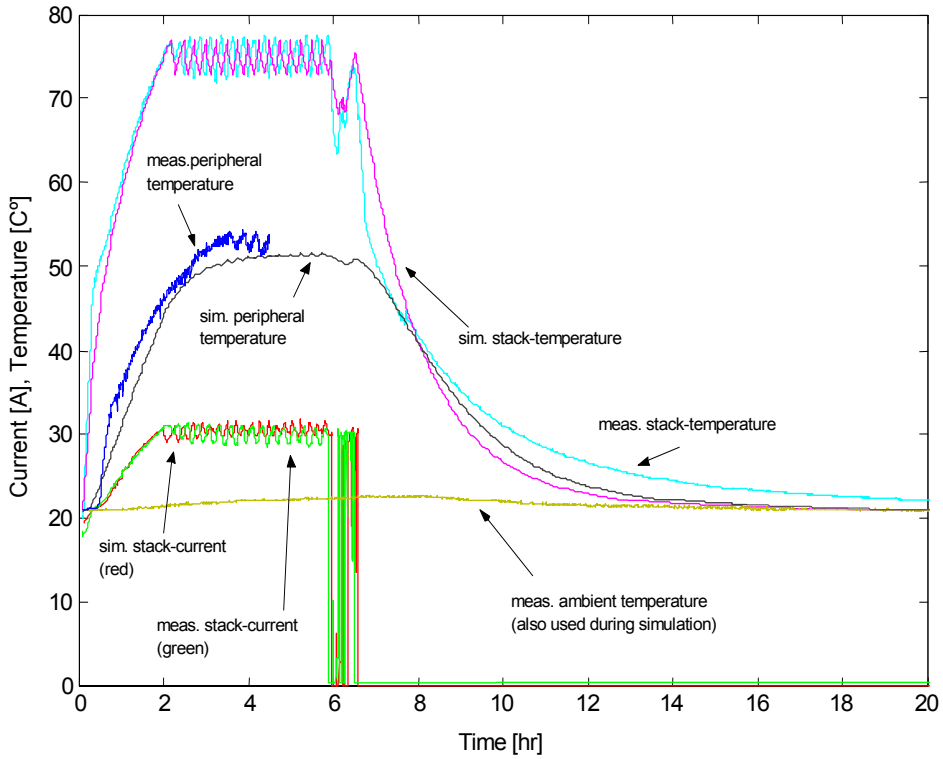

Figure 4.5 Verification of the semi empirical electrolyser model.

The simulated $T_{peripheral,ely}$ was to some extent underpredicted compared to the measured. However, the simulated $T_{peripheral,ely}$ ensured the special thermal behaviour of the electrolyser stack. The measured $T_{peripheral,ely}$ is only shown for the first 4 hrs of operation in Figure 4.5.

If $T_{periheral,ely}$ were to be excluded from the electrolyser model, meaning that the thermal calculation had only been based on the characteristics of the electrolyser stack, the simulated $T_{stack,ely}$ would reach nominal temperature about an hour earlier than the laboratory electrolyser. This would over-estimate the electrolyser performance.

The measured thermal time constant implemented in the electrolyser model was taken as an average of five different cool-down experiments. The average thermal time constant for the stack was found to be $\tau_{stack,ely} = 5034$ s. This is verified in the cool-down regime after shutdown of the electrolyser at 6.5 hrs. The thermal resistance for the electrolyser stack was calculated from Equation 4.19 and found to be 5034 s / 7400 J/K = 0.68 K/W. It should be noticed that the measured $T_{stack,ely}$ got influenced by a switch that was closed at 7.5 hrs in order to charge a battery, an action that was independent of this electrolyser experiment. However, $T_{stack,ely}$ was wrongly measured about 1°C above the true $T_{stack,ely}$ during the battery charging process.

With the same procedure, the thermal time constant for the electrolyser peripheral system was found to be $\tau_{peripheral,ely}$ = 10800 s. With Equation 4.19 the peripheral thermal resistance was calculated: 10800 s / 25000 J/K = 0.43 K/W.

The electrolyser start-up shown in Figure 4.6 indicates that the simulated $T_{stack,ely}$ is underpredicted to some extent. The reason for this deviation is mainly the complexity of simulating the special thermal start-up behaviour. However, the overall simulated current was in good agreement with the measured. Integration of $I_{stack,ely}$ for the period in Figure 4.6 resulted in 165.7 Ah for the measured and 165.1 Ah for the simulated, which was an error less than 1%.

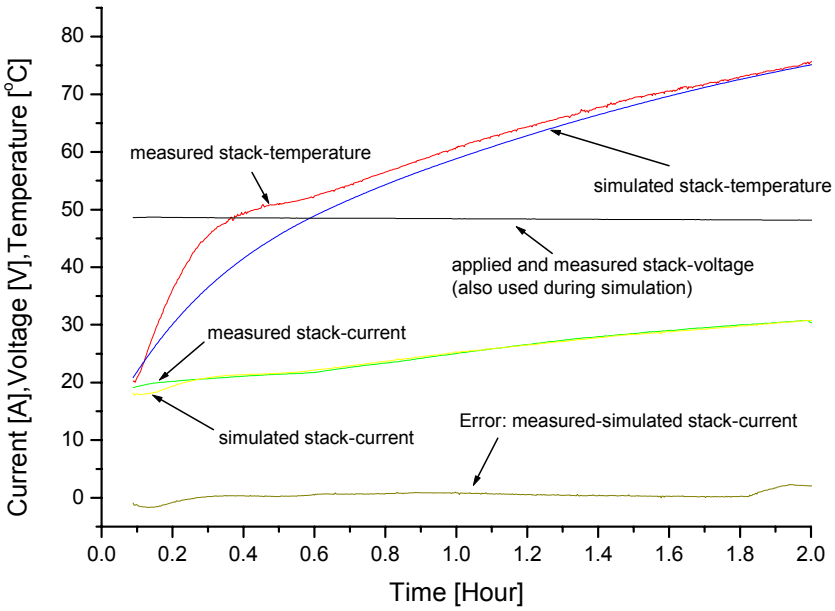

Figure 4.6 Measured/simulated stack-temperature and stack-current shown for an electrolyser start-up.

4.1.4 Fuel Cell

The procedure for finding the component model for the fuel cell unit is basically the same as for the electrolyser, except only one look-up table is used. The inputs to this look-up table is the load current requirement (also defined as the fuel cell stack-current, $I_{stack,FC}$) and the fuel cell stack-temperature ($T_{stack,FC}$). The output is the fuel cell stack-voltage, $V_{stack,FC}$. No checks on $V_{stack,FC}$ is performed because the load in this thesis is defined as a low power DC load which accepts a wide voltage range applied by the HSAPS. $T_{stack,FC}$ is found by using the general heat balance given in Equation 4.1 in terms of the fuel cell:

$$\dot{Q}_{store,FC} = \dot{Q}_{gen,FC} - \dot{Q}_{loss,FC} - \dot{Q}_{cool,FC} \quad \text{(Heat balance in fuel cell)} \qquad (4.20)$$

Where

$$\dot{Q}_{store,FC} = C_{stack,FC} \frac{dT_{stack,FC}}{dt} \quad \text{(Thermal energy storage)} \qquad (4.21)$$

$$\dot{Q}_{gen,FC} = n_c (U_{tn} - U) I_{stack,FC} \quad \text{(Internal heat generation)} \qquad (4.22)$$

$$\dot{Q}_{loss,FC} = \frac{(T_{stack,FC} - T_{amb})}{R_{stack,FC}} \quad \text{(Heat losses to ambient)} \qquad (4.23)$$

The cooling fans have a correlation: $\dot{Q}_{cool,FC} = P_{cool,fans}(T_{stack,FC}, I_{stack,FC})$ where $P_{cool,fans}$ is the required power input to the cooling fans, which is a function of $T_{stack,FC}$ and $I_{stack,FC}$. But the cooling model for the fuel cell is simplified by simply removing excess heat from the stack whenever $T_{stack,FC} > 50°C$, which is the fuel cell stack operating temperature.

The constants and variables used in Equations 4.21 – 4.23 are:

n_c	= number of cells in fuel cell stack [64]
U	= cell voltage [V]
U_{tn}	= thermo neutral cell voltage [V]
$I_{stack,FC}$	= stack-current [A]
$C_{stack,FC}$	= heat capacity in fuel cell stack [5700 J/K]
$T_{stack,FC}$	= temperature in fuel cell stack [K]
$R_{stack,FC}$	= thermal resistance [0.84 K/W]

Figure 4.7 shows start-up and nominal operation of the fuel cell unit. The measured $T_{stack,FC}$ started rising even though no load was connected to the fuel cell, while the simulated $T_{stack,FC}$ stayed at room temperature until current was drawn from the stack. This indicates that the model does not include the fact that the internal fuel cell control system requires energy from the stack, which causes a small increase in $T_{stack,FC}$. Apart from this, the measured and simulated $T_{stack,FC}$ followed quite well. The measured stack-voltage behaviour fluctuates caused by O_2-purging (Section 3.2.6). The simulated $V_{stack,FC}$ is somewhat lower than the average of the measured $V_{stack,FC}$.

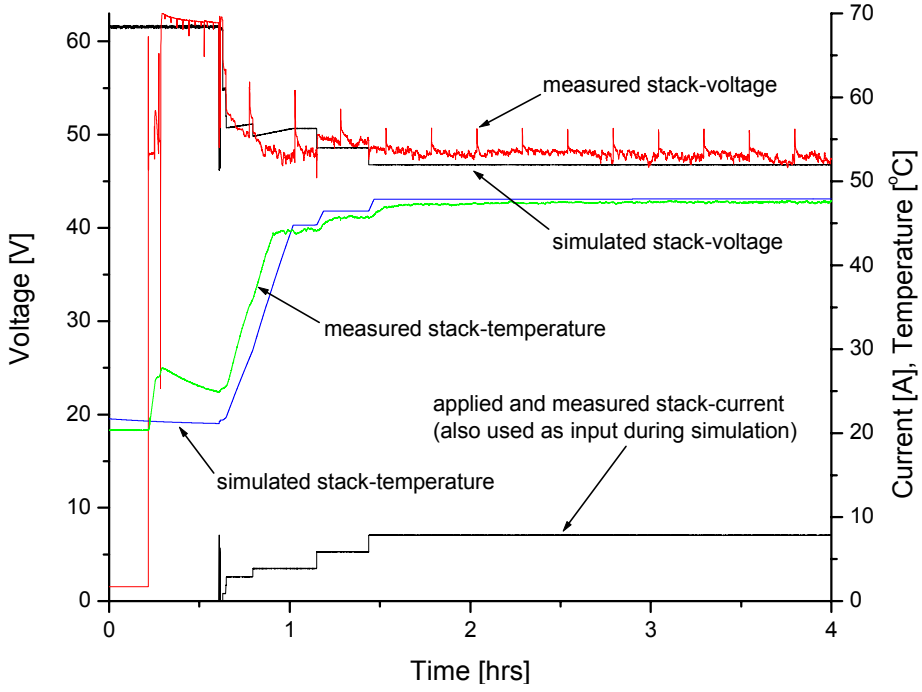

Figure 4.7 Measured and simulated fuel cell performance.

Figure 4.8 represents a measured and simulated FC cool-down experiment, which shows good agreement. The thermal time constant (τ_{FC}) was found to be 4763 s (average of five cool-down experiments) and $C_{stack,FC}$ was calculated to be 5700 kJ/K

based on measured geometry and tabulated (SI Chemical Data 3rd edition) specific heat capacities. Thermal resistance was then found to be $R_{stack,FC} = \tau_{FC}/C_{FC}$ = 4763 s / 5700 J/K = 0.84 K/W.

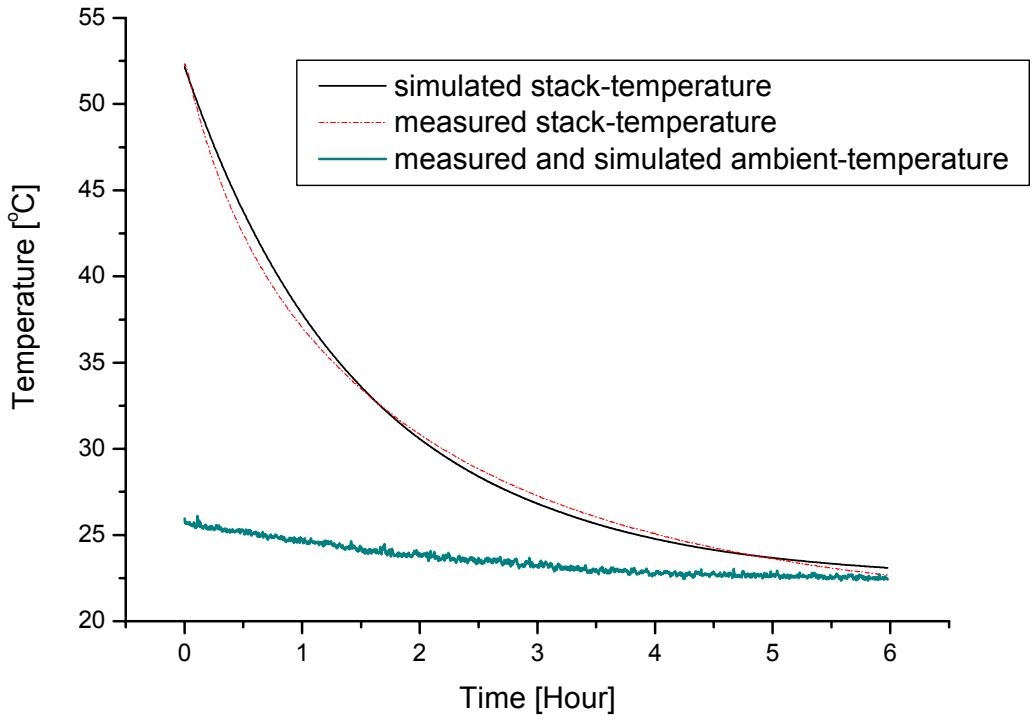

Figure 4.8 Measured and simulated cool-down experiment with the fuel cell.

4.1.5 Battery

The current-voltage characteristic of the battery is also implemented in a look-up table. The inputs to the battery look-up table model are the charge/discharge current and the battery state-of-charge (BAT_{SOC} [%]), the output is battery voltage. Because the battery is placed indoors, the battery model contains no thermal model since the temperature is relatively constant. Positive current is defined as charge current while negative current is defined as discharge current. BAT_{SOC} is found by simply integrate the charge/discharge current, as shown in Equation 4.24. Equation 4.24 is corrected for a battery self-discharge rate of 1 mA/100 Ah corresponding to about 1 % loss of nominal capacity per month.

$$BAT_{SOC} = \frac{Q_{bat,start} + \int I_{bat}dt + \int I_{bat,sd}dt}{Q_{bat,nom.capacity}} \qquad (4.24)$$

Where

$Q_{bat,start}$ = battery capacity at start time [Ah]
$Q_{bat,nom.capacity}$ = battery nominal capacity [Ah]
I_{bat} = battery charge/discharge current [±A]
$I_{bat,sd}$ = battery self discharge current [-A] (gassing current)

4.1.6 Metal hydride

Hydrogen stored in metal hydrides is chemically bonded. Hydrogen molecules are catalytically split to hydrogen atoms that dissolve and locate at interstitial sites of the metal hydride matrix. When storing hydrogen in metal hydrides, hydrogen absorption (charging) generates heat, while hydrogen desorption (discharge) consumes heat:

$$M_{(s)} + \frac{x}{2} H_{2,(g)} \leftrightarrow MH_{x,(s)} + Q \tag{4.25}$$

Experimental studies indicated that the laboratory MH-storage had insufficient heat transfer at high hydrogen discharge flow. However, when heat produced in the fuel cell was transferred to the surface of the MH-storage, the hydrogen discharge flow rate and MH-pressure could supply the fuel cell continuously until no hydrogen was left in the MH-storage. The MH-storage worked properly without any external heat management during hydrogen charging within the specified hydrogen flow rate range.

Ideally, the hydrogen state-of-charge of a metal hydride container can be obtained from a *pressure-concentration-temperature* (PCT) diagram at steady state. However, transients during hydrogen charge/discharge calls for detailed mathematical modelling of the mass and heat transfer in metal hydrides. This is quite complex and out of scope in this thesis. In order to simplify, the heat transfer in the MH-storage model was defined to be adequate at all hydrogen flow rates used in this study. Thus, no restrictions on the hydrogen flow rate were implemented in the model and the MH-storage was modelled as a simple hydrogen summation unit as shown in Equation 4.26:

$$MH_{SOC} = \frac{N_{MH,start} + \int \dot{V}_{H_2,ELY}\, dt - \int \dot{V}_{H_2,FC}\, dt}{N_{MH,nom.capacity}} \tag{4.26}$$

where

MH_{SOC} = total H_2 capacity in the MH-storage [NL]
$N_{MH,start}$ = H_2 content in MH at start time [NL]
$N_{MH,nom.capacity}$ = total H_2 capacity in MH [NL]
$\dot{V}_{H_2,ELY}$ = H_2 produced by the electrolyser [NL/min]
$\dot{V}_{H_2,FC}$ = H_2 consumed by the fuel cell [NL/min]

A purification unit is necessary in order to achieve a hydrogen gas quality (> 99.999 %), which will preserve maximal metal hydride unit capacity and lifetime.

4.1.7 Purification unit

<u>*Uniform heater element*</u>

Each of the two dryer columns had capacity of absorbing 84 Nm^3. The dryer unit was implemented in the HSAPS model as a sinus function with a period of 2·84 Nm^3, where the function input was the amount of hydrogen produced by the electrolyser with units [Nm^3]:

$$\sin\left(\left[\frac{V_{H_2,ely}}{2\cdot V_{capacity}}\right]2\pi\right)=[-1,1] \tag{4.27}$$

where

$V_{H_2,ely}$ = the amount of H_2 produced by the electrolyser [Nm^3]

$V_{capacity}$ = single column H_2 absorption capacity [84 Nm^3]

When 84 Nm^3 of hydrogen is produced, the sinus function outputs zero, which indicates that the desiccant in the first dryer column must be regenerated. The zero output initializes a 6 hrs 1.8 kW regeneration procedure of the desiccant. This power consumption is finally added to the total energy balance in the complete HSAPS model.

Segmented heater elements

As an option to the static dryer model, the dryer is also modelled with the heater segmented into 9 elements in series, each rated at 200 W. This model is only to be used in Chapter 7. The reason for scaling the heater power range is to make the regeneration more flexible with respect to usable excess power in system. The carrier gas for regeneration used in the model is dry hydrogen from the MH-storage. At least 200 W must be available for about 30 minutes before the heating element has high enough temperature to start the regeneration process, i.e. letting the regeneration gas flow through the heater elements and then through the dryer column where water is vaporised and transported out of the system.

A linear interpolation is made between power supplied to the heater and the amount of water removed from the dryer unit. The interpolation is made on the basis of the 1.8 kW laboratory dryer unit and a 200 W dryer described by Hollmuller et.al. [4]. The linear relation used in the model is:

$$\dot{H_2O}_{evaporate}=0.23\cdot P_{dryer} \tag{4.28}$$

where

$\dot{H_2O}_{evaporate}$ = amount of water evaporated in the dryer column [g/hr]

P_{dryer} = electric power supplied to the heater in the dryer [W]

The hydrogen leaves the electrolyser at about 40°C saturated with water. The water content in the hydrogen produced by the electrolyser per unit time is based on data measured by the electrolyser manufacturer [5] and given by a linear relationship, presuming a constant electrolyser pressure of 15 bars:

$$\dot{H_2O}_{ely}=370.37\cdot\dot{m}_{H_2,ely} \tag{4.29}$$

where

$\dot{H_2O}_{ely}$ = water content in produced hydrogen per unit time [g/hr]

$\dot{m}_{H_2,ely}$ = H_2 produced by the electrolyser [g/hr]

The amount of water accumulated in the dryer column ($H_2O_{accumulated}$) is then calculated by:

$$H_2O_{accumulated} = \int \dot{H_2O}_{ely}\, dt - \int \dot{H_2O}_{evaporate}\, dt \tag{4.30}$$

4.1.8 Compressor

The compressor model is used only in Chapter 7, where the suction and discharge pressures are 16 bars and 110 bars respectively, giving a compression ratio of 6.9 which requires a two stage compressor [6]. A model of an intercooled two-stage compressor is given in Equation 4.31:

$$W_{comp} = \dot{n}_{gas} \frac{w_1 + w_2}{\eta_{comp}} \tag{4.31}$$

where

$$w_1 = \frac{nRT_{inlet}}{n-1}\left[1 - \left(\frac{p_{1-2}}{p_1}\right)^{\left(\frac{n-1}{n}\right)}\right] \quad , \quad w_2 = \frac{nRT_{inlet}}{n-1}\left[1 - \left(\frac{p_2}{p_{1-2}}\right)^{\left(\frac{n-1}{n}\right)}\right]$$

where

W_{comp} = total compression work [W]

$\dot{n}_{gas}$ = Hydrogen gas flow [mol/s]

w_1, w_2 = polytrophic work, stage 1 and 2 respectively [W]

η_{comp} = compressor efficiency [-]

n = polytrophic efficiency [-]

p_1, p_{1-2}, p_2 = inlet, intermediate and final pressure respectively [bar]

4.1.9 Pressure vessel

To store hydrogen in a pressurized vessel is a physical method of making the gas more compact, where the molecules have weakly interactions with the environment. For pressures above about 150 – 200 bars one should use the available compressibility factors to avoid miscalculations for large storage systems. No compressibility factor is necessary in this study because the simulated pressure vessel has maximum pressure 110 bars. The component model for the pressurized vessel is basically the same as the accumulation model for the MH-storage - a simple summation of hydrogen produced subtracted by the hydrogen consumed:

$$\mathrm{H}_{2,\mathrm{SOC,pressurised\ vessel}} = \frac{\mathrm{N}_{\mathrm{H_2,pressurisedvessel,start}} + \int \dot{\mathrm{V}}_{\mathrm{H_2},ELY}\, \mathrm{dt} - \int \dot{\mathrm{V}}_{\mathrm{H_2},FC}\, \mathrm{dt}}{\mathrm{N}_{\mathrm{H_2,\ pressurised\ vessel,nominal\ capacity}}} \tag{4.32}$$

where

$\mathrm{H}_{2,\mathrm{SOC,pressurised\ vessel}}$ = calculated H_2 content in pressurised vessel [NL]

$N_{H_2,\,pressurised\ vessel,start}$ = initial H_2 content in pressurized steel vessel [NL]

$N_{H_2,\,pressurisd\ vessel,\,nominal\ capacity}$ = total capacity of H_2 in MH-storage [NL]

$\dot{V}_{H_2,ELY}$ = H_2 produced by the electrolyser [NL/min]

$\dot{V}_{H_2,FC}$ = H_2 consumed by the fuel cell [NL/min]

4.1.10 High-level control algorithms

Three types of high-level control strategies will be compared in Chapter 5. The three types of control strategies will be denoted as:

(1) *Battery five-step charge controller, described in Section 5.3.1*
(2) *Control Matrix, described in Section 5.3.2*
(3) *Fuzzy controller, described in Section 5.3.3*

The algorithms developed in SIMULINK for the different strategies are shown in Figure 4.9, Figure 4.10, and Figure 4.11, respectively.

(1) *Battery five-step charge controller*

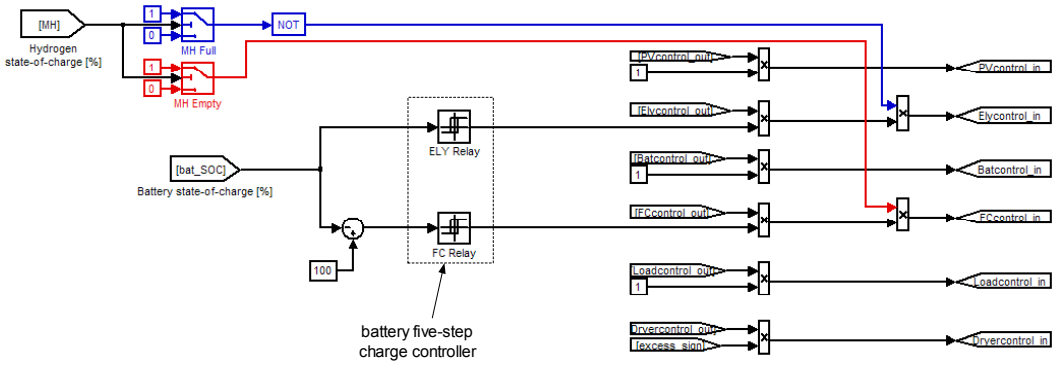

Figure 4.9 SIMULINK diagram of the battery five-step controller.

(2) *Control Matrix*

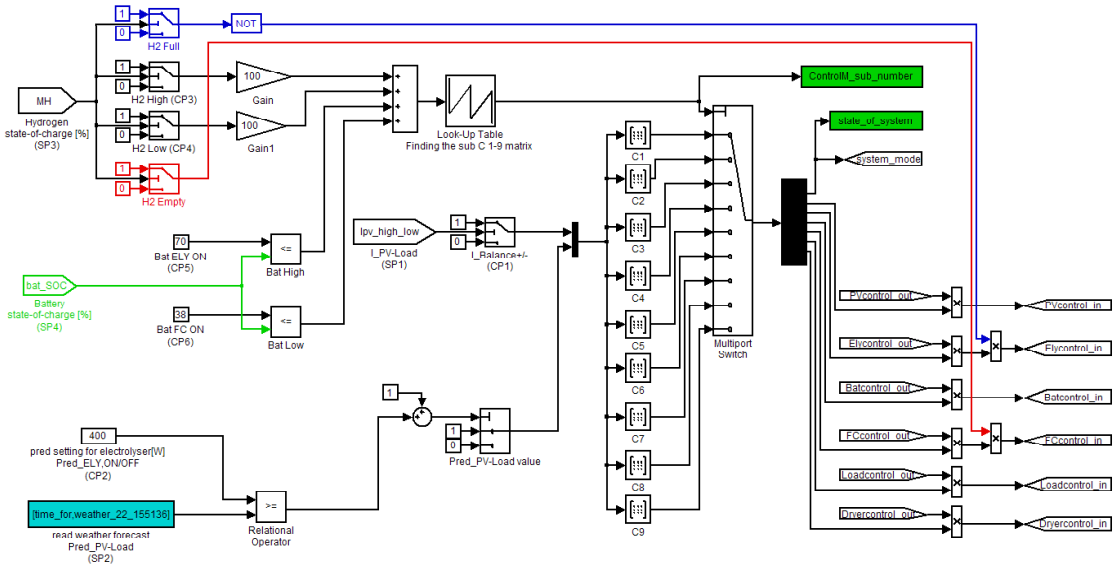

Figure 4.10 SIMULINK diagram of the Control Matrix.

(3) *Fuzzy controller*

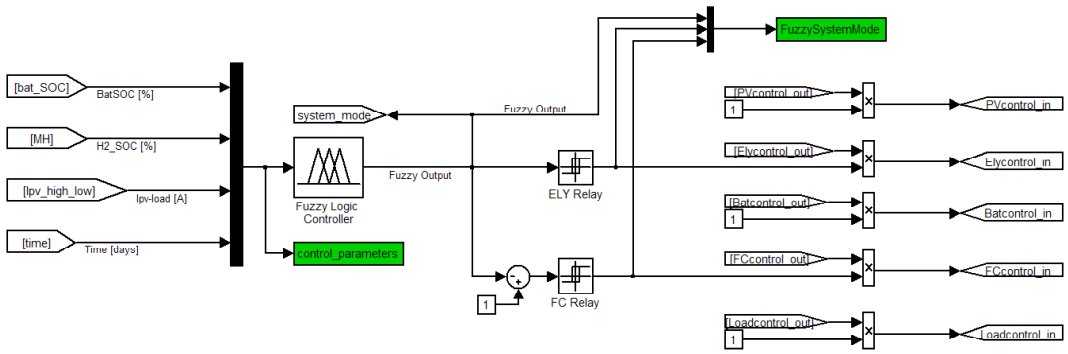

Figure 4.11 SIMULINK diagram of the Fuzzy controller.

The Fuzzy Logic Controller shown in Figure 4.11 belongs to the MATLAB Fuzzy Logic toolbox sold separable from the standard MATLAB and SIMULINK packages. All the membership functions and the fuzzy rules are generated and stored in a single *.FIS file that is called from the Fuzzy Logic Controller block in SIMULINK or from the command line in MATLAB. All the simulations concerning the high-level fuzzy controller that will be presented in Chapter 5 were done at Econnect ltd's office, Hexham, UK.

References

1. www.mathworks.com.
2. A.de Groot, *Topics (Simulation environment developed in MATLAB/SIMULINK)*. 2000: ECN, Netherlands.
3. Ø.Ulleberg, *Stand-Alone power systems for the future: Optimal design, operation & control of solar-hydrogen energy system*. 1998, PhD Thesis, NTNU, Norges teknisk-naturvitenskapelige universitet: Trondheim. p. 210.
4. P. Hollmuller, et al., *Evaluation of a 5 kW photovoltaic hydrogen production and storage installation for a residential home in Switzerland.* Int.J.Hydrogen Energy, 2000. **25**: p. 97-109.
5. Fraunhofer ISE. 2002: Freiburg, Germany.
6. P.C.Hanlon, *Compressor Handbook*. 2001, New York: McGraw-Hill.

5. Control strategy

Most systems operate in environments that change over time. Here, dedicated control at component level, subsystem level and/or system level can help maintain system performance within specified tolerances, or to increase the worth of a general system output. Every feedback control system has four basic elements [1]. These elements always occur in the same sequence and have the same relationship to each other:

1. A controlled output characteristic or condition.
2. A sensory device or a method for measuring the characteristic or condition.
3. A control device that will compare measured performance with planned performance.
4. An activating device that will alter the system according to the planned output characteristic or condition.

The control variables must be closely related to the state variables that characterise the system that is to be regulated. A general sequence for a feedback control system is shown in Figure 5.1. A feed forward control system would have the *Sensory device* mounted to the input and/or to possible disturbances (not shown).

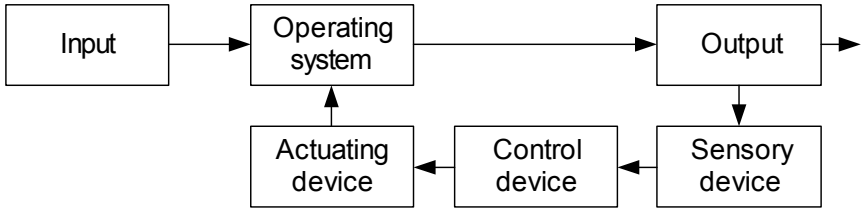

Figure 5.1 Schematic of a general feedback control sequence.

Furthermore, there are two basic types of control systems, the open-loop and the closed-loop. The open-loop does not have the control system as an integral part of the system, the control action is uniquely specified initially. The closed-loop, where the control system is an integral part of the system, has the possibility to alter the control variables during system operation.

5.1 Control of linear and approximated linear systems

A control problem may arise from the needs such as to regulate temperature, speed of a machine, quality/quantity of a product, or determine the trajectory of an aircraft. These are typically dynamic control problems where either a stable output according to some nominal conditions is required, or the output should be safely and swiftly changed from one stable reference setting to another. In order to solve these problems *classical linear control theory* is commonly used, where PID-type controllers are tuned based on differential equations related to the specific system or process.

There are a wide variety of processes for which the dynamic behaviour depends on the process variables in a nonlinear fashion. A typical example is the exponential dependence of reaction rate on temperature in a chemical reactor. Classical control theory has, however, been developed for linear processes. Thus, its use is restricted to linear approximations of the actual nonlinear control problem.

5.2 Continuous and discontinuous systems

According to [2], a general system or a machine can be defined by:

$$\Sigma = (\Gamma, X, U, \varphi) \tag{5.1}$$

where Γ is a time set, X is a nonempty set called the state space of Σ, U is a nonempty set input-value space of Σ, and φ called the transition map of Σ, $D_\varphi \rightarrow X$, which is defined on a subset D_φ of:

$$\{(\tau, \sigma, x, \omega) \mid \sigma, \tau \in \Gamma, \sigma \leq \tau, x \in X, \omega \in U^{[\sigma,\tau)}\} \tag{5.2}$$

such that the *nontriviality, restriction, semi group* and *identity properties* hold. The transition map φ can be read as the state at time τ resulting from the use of input ω, starting at time σ with state x.

5.2.1 Continuous systems

From Equation 5.1, a continuous system can have the following properties:

$$\Gamma = R\,,\ X \subseteq R^n\,,\ U \subseteq R^m \qquad (R = \text{all real numbers}) \tag{5.3}$$

and the transition map, φ, is induced by a differential equation on the form:

$$\frac{\partial x(t)}{\partial t} = f(x(t), u(t))\,, \qquad x(t_0) = x_0 \tag{5.4}$$

where f is a continuous function with the arguments $x(t) \in R^n$ and $u(t) \in R^m$.

5.2.2 Discrete-event systems

A discrete-event system is a system where the dynamics are event-driven (as opposed to time-driven) and for which at least one of the parameters that describes the dynamics is discrete [3]. The basic behaviour of these discontinuous systems is thus governed by the occurrence of events and not by the fact that time evolves. Thus, high-level control systems are almost always event-driven. From Equation 5.1, a discrete-event system can have the following properties:

> $\Gamma = Z$ which is a set of discrete numbers representing time, X is a finite set of discrete states, U is a finite set of inputs, and the transition map, φ, is defined as the next-state or transition map $\varphi(t+1,t,x,u)$.

5.2.3 Hybrid systems

Many objects surrounding us are of hybrid nature meaning that they possess continuous dynamics (e.g. described by differential equations) as well as discrete characteristic (e.g. logic switching), thus the system contains both continuous and discrete variables. Various descriptions for modelling hybrid systems are given by [4]. An example is a system that requires a hybrid model in order to characterise hysteresis. Another general example of a hybrid system is a continuous plant that is observed by discrete sensors (emitting signals when certain levels in the state space are reaching predefined control limits). Lately, there has been interest for studying systems observed by discrete sensors, and the motivation has been two fold [5]: The

first reason is the frequent occurrence of these types of sensors in practical situations, such as level sensors and encoders. The second reason is that control on the basis of discretised information can be used for hierarchical control. The discretised information can serve as coarse representation of the plant for high-level control, while possible continuous low-level controllers can be used for fine-tuning.

Because the high-level controller is based on discrete-events, the continuous state space representation of the system must be discretised, either with software or hardware. An interface containing analog-to-digital (A/D) conversion and digital-to-analog (D/A) conversion is shown in Figure 5.2.

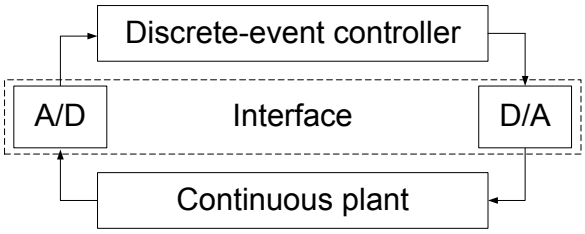

Figure 5.2 Hybrid system with a digital ↔ analog converter interface between the continuous plant and the discrete-event controller.

5.3 Control strategies for a HSAPS

In the PV-HSAPS configuration chosen in this work, classical linear control theory is used for marginal temperature regulation of the fuel cell stack and electrolyser stack. Due to the absence of DC/DC converters, the system configuration has no degree of freedom regarding the operation level for the electrolyser, the battery, and the fuel cell. The only regulation available for the components is ON or OFF. Thus, the laboratory HSAPS control is not a continuous linear problem based on a specific mathematical equation, but a problem where the decisions are discrete choices between the different modes of operation. These decisions are based on the individual components constraints and the energy balance of the HSAPS. The decisions made for changing between the different modes of operation are implemented in a control algorithm that comprises the system control strategy. In the literature, the control strategy of an energy system is often reported as the *energy management*. As explained in Chapter 2, the control strategy is dependent on measured and/or predicted system parameters and inputs, which together define the state of the system.

The HSAPS investigated in this work is closely related to the hybrid system described in Section 5.2.3. The system parameters are sampled and estimated at a fixed sampling rate, but their actual input to the control system is dependent on whether a certain level or condition is reached or not. Thus, the level sensor has an A/D-converter between the continuous energy system and its discrete-event controller as indicated in Figure 5.2. Likewise, the output from the HSAPS discrete-event controller to the energy system is a set of logic values that switches certain components ON/OFF. This means that the HSAPS investigated in this case only accepts discrete inputs from the controller and no D/A-converter is needed between the discrete-event controller and the continuous system. It is important to notice that even though the three modes of operation in the system are operating continuously, the change from one mode to another is a discrete action. This is comparable to a car

where the motor operates continuously, while shifting the gears introduces discrete "jumps" in the overall operation of the car as in a hybrid system.

In the following, three different control algorithms for the overall high-level energy management are discussed and compared. The first two control strategies are based on a discrete-event type controller, while the last is based on fuzzy logic. For each of the control schemes the terms *system parameters* and *control parameters* are used. The terms are defined as:

System parameters: Measured, derived, and predicted parameters

Control parameters: System parameters and/or system parameter thresholds for control of components

5.3.1 Battery five-step charge controller

In previous works on HSAPS containing a secondary battery as a short-term energy storage [6-12], the basic control strategy for ON/OFF-switching of the electrolyser and the fuel cell was mainly based on the state-of-charge of the battery (BAT_{SOC}). This control scheme might be regarded as a *five-step charge controller* where the electrolyser and the fuel cell never operate simultaneously. Figure 5.3 shows the ON/OFF-switching set points (or thresholds) for the electrolyser and the fuel cell with regard to BAT_{SOC}. When BAT_{SOC} reaches the "Electrolyser ON" threshold, the electrolyser is switched ON and kept on until BAT_{SOC} falls below the "Electrolyser OFF" threshold. By carefully selecting the threshold settings, a hysteresis band is formed for smooth electrolyser operation as opposed to a high frequency of ON/OFF-switching. The same procedure is valid for a fuel cell, except for the fact that the ON/OFF-sequence is reversed. In this control scheme the electrolyser and fuel cell ON/OFF thresholds function as control parameters that is dependent on the system parameter BAT_{SOC}, which is derived from the measured battery charge/discharge current (Section 4.1.5).

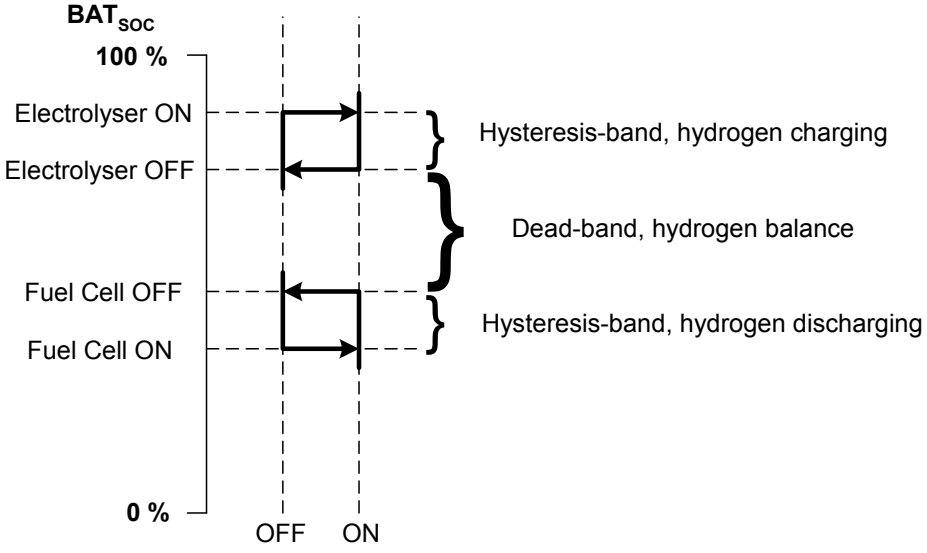

Figure 5.3 Electrolyser and fuel cell ON/OFF-switching based on BAT_{SOC}, a so-called *five-step charge controller*. Hysteresis bands are introduced in order to ensure smooth operation and avoid frequent ON/OFF-switching of the electrolyser and the fuel cell.

Furthermore, the fuel cell cannot operate if the hydrogen storage is empty and the electrolyser cannot operate if the hydrogen storage is full, thus the hydrogen state-of-charge parameter has to be implemented into the battery five-step charge controller. Figure 4.9 in Section 4.1.10 shows the implementation of the hydrogen state-of-charge parameter into the battery five-step charge controller algorithm developed in SIMULINK. From the literature [13, 14], improvement of the five-step controller by implementing some additional *smart* controller settings by changing the BAT_{SOC} ON/OFF-settings for the electrolyser and the fuel cell between the summer and winter seasons. Timer settings were also introduced where the electrolyser was only allowed to operate within a certain period during the day. However, the main problem with using the BAT_{SOC} as a controller signal is that it is difficult to measure the true battery state-of-charge. It would be intuitive to just measure the battery voltage, but the battery voltage is highly dynamic, both during charging and discharging. The best method to keep track of the BAT_{SOC} is to accumulate the battery charge/discharge current and thus estimate the state-of-charge, preferably with a continuous gassing correction factor. If no continuous gassing correction factor is implemented, the state-of-charge estimator should at least be calibrated within certain time-periods.

5.3.2 Control Matrix with load and weather prediction

The Control Matrix with load and weather prediction, which is the first of the two proposed control strategies in this study, enables an HSAPS energy management based on six vital *control parameters* that are dependent on four *system parameters*. The four system parameters are listed in Table 5.1a and the six control parameters are listed in Table 5.1b, respectively. Figure 4.10 in Section 4.1.10 shows the Control Matrix algorithm developed in SIMULINK.

The number of *system states* within the Control Matrix is defined as the number of combinations of the control parameters given by:

$$number\ of\ states = 2^{number\ of\ control\ parameters} \tag{5.5}$$

The digit 2 represents a digital system where the control parameters (Table 5.1b) are giving either 0 or 1 (ON/OFF) as outputs depending on their input values represented by the system parameters (Table 5.1a). Thus, the control parameters act as event driven functions. The definition of the control parameter outputs based on the system parameters are given in Table 5.2.

Table 5.1a The six system parameters used in the Control Matrix with load and weather prediction for HSAPS energy management strategy

System Parameter	Name	Description
SP1	$I_{PV\text{-}Load}$	Measured PV output current subtracted by measured current drawn by the load
SP2	$Pred_{PV\text{-}Load}$	Predicted average power from the PV array subtracted by predicted average power required by the load within the next two hours, i.e., weather forecast and load prediction
SP3	$H_{2,SOC}$	Accumulation of measured H_2 produced subtracted by measured H_2 consumed
SP4	BAT_{SOC}	Accumulation of measured battery charge current subtracted by measured battery discharge current

Table 5.1b The six system parameters used in the Control Matrix with load and weather prediction for HSAPS energy management strategy

Control Parameter	Name	Dependent on system parameter	Description
CP1	$I_{Balance,+/-}$	SP1	The value represented by $I_{PV\text{-}Load}$ is defined as positive or negative based on the threshold value $I_{Balance,+/-}$
CP2	$Pred_{ELY,ON/OFF}$	SP2	The value represented by $Pred_{PV\text{-}Load}$ is defined as high or low based on the threshold value $Pred_{ELY,ON/OFF}$
CP3	$H_{2,High}$	SP3	Hydrogen storage state-of-charge ($H_{2,SOC}$) is defined as high based on the threshold value $H_{2,High}$
CP4	$H_{2,Low}$	SP3	Hydrogen storage state-of-charge ($H_{2,SOC}$) is defined as low based on the threshold value $H_{2,Low}$
CP5	$BAT_{ELY,ON}$	SP4	Battery state-of-charge (BAT_{SOC}) threshold. Indicating that the electrolyser is allowed to be switched ON when $BAT_{SOC} > BAT_{ELY,ON}$
CP6	$BAT_{FC,ON}$	SP4	Battery state-of-charge (BAT_{SOC}) threshold. Indicating that the fuel cell is allowed to be switched ON when $BAT_{SOC} < BAT_{FC,ON}$

Table 5.2 Definitions of the control parameter values in the Control Matrix based on the system parameters

control parameter		dependent on system parameter	control parameter value*
number	name		
CP1	$I_{Balance,+/-}$	$I_{PV\text{-}Load}$	1 if $I_{PV\text{-}Load} > 0$ A, else 0
CP2	$Pred_{ELY,ON/OFF}$	$Pred_{PV\text{-}Load}$	1 if $Pred_{PV\text{-}Load} \geq 300$ W, else 0
CP3	$H_{2,High}$	$H_{2,SOC}$	1 if $H_{2,SOC} \geq 90$ %, else 0
CP4	$H_{2,Low}$	$H_{2,SOC}$	1 if $H_{2,SOC} \leq 10$ %, else 0
CP5	$BAT_{ELY,ON}$	BAT_{SOC}	1 if $BAT_{SOC} \geq 90$ %, else 0
CP6	$BAT_{FC,ON}$	BAT_{SOC}	1 if $BAT_{SOC} \leq 40$ %, else 0

*Values used as typical examples, except for the current threshold used for $I_{Balance,+/-}$ and the power threshold used for $Pred_{ELY,ON/OFF}$

The possible number of system states forms the system's *Control Matrix* (**C**). Actually, **C** constitutes two parts, one Input Matrix and one Output Matrix. The graphical representation in Figure 5.4 shows the data flow between the Input and Output Matrix, with the data processing of the system parameters indicated in Table 5.2.

The Input Matrix receives information from the system's data acquisition hardware/software utility (Section 3.4). Based on the measured data, the Input Matrix assigns the control parameters either 0 or 1, which again gives a unique combination that represents a unique system state. Next, this unique system state is fed to the Output Matrix where predefined rules describing the system operation within each of the possible states resulting from the system developer's know-how.

From Equation 5.5, the theoretic total number of system states for the Control Matrix method is $2^6 = 64$. However, $BAT_{ELY,ON}$ and $BAT_{FC,ON}$ represent dependent control parameters that must be treated with care to exclude non-existing system states. From Figure 5.5, e.g., if $BAT_{ELY,ON}$ is set to 1, $BAT_{FC,ON}$ must be 0. The same applies for the

control parameters $H_{2,High}$ and $H_{2,Low}$. The nine possible combinations for control parameters CP3 – CP6 are shown in Figure 5.5.

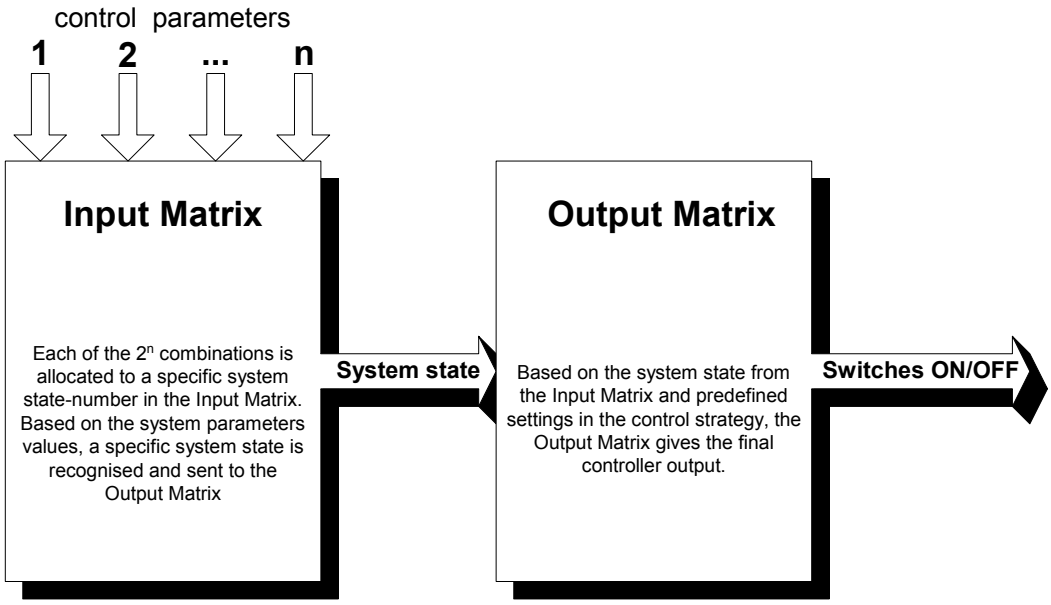

Figure 5.4 The Input Matrix and the Output Matrix implemented in the proposed Control Matrix, a method for the high-level energy management in a HSAPS.

Because of the dependent control parameters, it is convenient to divide **C** into smaller clusters, $\mathbf{C_1}$, $\mathbf{C_2}$, …, $\mathbf{C_9}$ according to the number of combinations shown in Figure 5.5. Each of the nine combinations related to the control parameters CP3 – CP6 will then have control parameters CP1 and CP2 as inputs, giving a total of $9 \cdot 2^2 = 36$ possible system states.

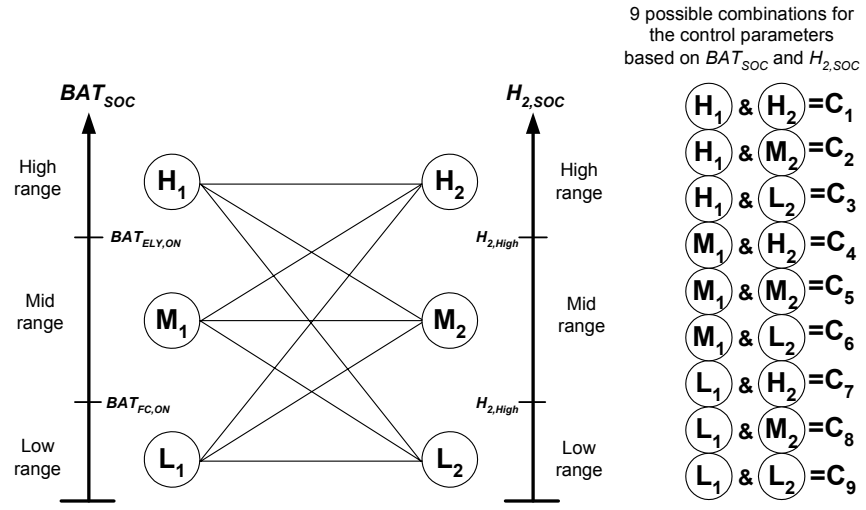

Figure 5.5 Schematic showing the nine possible combinations for the control parameters based on BAT_{SOC} and $H_{2,\,SOC}$.

Figure 5.6 shows the complete Control Matrix **C** used in this work based on the nine sub-matrixes shown on the right-hand side in Figure 5.5. Figure 5.6 also indicates the Input/Output matrixes in **C** jointed by the numbers that represent each of the possible system state. Thus, processing of the control parameters CP3 – CP6 finds the momentary sub-matrix, $\mathbf{C_{1\text{-}9}}$, and then the actual sub-matrix is further evaluated with

the control parameters CP1 and CP2, which eventually results in the HSAPS's momentary unique system state. The 1's and 0's in the Output Matrix indicates whether the respective components should be switched ON or OFF, respectively. These sets of 1's and 0's must be set for each of the state based on the system developer's expertise.

C_n	Input Matrix		system state	Output Matrix	
	$I_{Balance,+/-}$	$Pred_{ELY,ON/OFF}$		ELY	FC
C_1	0	0	1, B	0	0
	0	1	2, B	0	0
	1	0	3, B	0	0
	1	1	4, C	1	0
C_2	0	0	5, B	0	0
	0	1	6, B	0	0
	1	0	7, B	0	0
	1	1	8, C	1	0
C_3	0	0	9, B	0	0
	0	1	10, B	0	0
	1	0	11, B	0	0
	1	1	12, C	1	0
C_4	0	0	13, B	0	0
	0	1	14, B	0	0
	1	0	15, B	0	0
	1	1	16, B	0	0
C_5	0	0	17, B	0	0
	0	1	18, B	0	0
	1	0	19, B	0	0
	1	1	20, B	0	0
C_6	0	0	21, B	0	0
	0	1	22, B	0	0
	1	0	23, B	0	0
	1	1	24, B	0	0
C_7	0	0	25, D	0	1
	0	1	26, B	0	0
	1	0	27, B	0	0
	1	1	28, B	0	0
C_8	0	0	29, D	0	1
	0	1	30, B	0	0
	1	0	31, B	0	0
	1	1	32, B	0	0
C_9	0	0	33, D	0	1
	0	1	34, B	0	0
	1	0	35, B	0	0
	1	1	36, B	0	0

Figure 5.6 The Control Matrix (**C**) containing the Input/Output matrixes implemented in the HSAPS energy management. In the system state column, C stands for hydrogen charging, B stands for hydrogen balance, and D stands for hydrogen discharge. ELY = electrolyser, and FC = fuel cell.

In this study the photovoltaic array, the battery, and the load are always connected, i.e., the value is 1 in all defined system states for these components in the Output Matrix. Thus, they are not shown in the Output Matrix in Figure 5.6. The settings in the Output Matrix can easily be altered as the HSAPS is further developed and tuned for optimal operation. Additional control parameters may be added to the Input Matrix and additional components can be added to the Output Matrix for strict operational control in parallel with the main HSAPS components. E.g., control of the hydrogen purification operation could be implemented in the Control Matrix based on a parameter that indicates whether there is excess energy available or not. This feature is further investigated in Chapter 7. However, care should be taken as a large matrix might be hard to maintain and tune.

As opposed to the battery *five-step charge controller* described in Section 5.3.1, the Control Matrix utilises a *three-step charge controller*, both for the battery state-of-charge (BAT_{SOC}) and the hydrogen state-of-charge ($H_{2,SOC}$), Figure 5.7. In order to prove the robustness of the *three-step charge controller* for operation of the electrolyser and the fuel cell within the Control Matrix algorithm, the six control parameters will be further explained in the following.

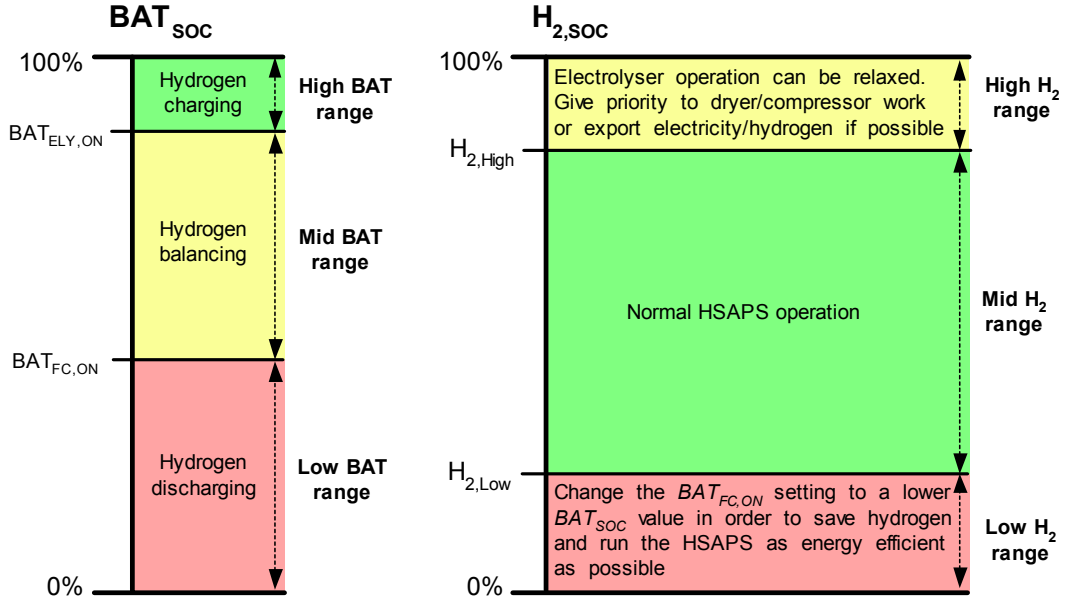

Figure 5.7 Three-step-charge controllers based on both long- and short-term energy storages.

Control Parameters CP1 and CP2: $I_{Balance,+/-}$ and $Pred_{ELY,ON/OFF}$

The control parameter $I_{Balance,+/-}$ should be negative for the fuel cell to operate, while it should be positive for the electrolyser to operate. The control parameter $Pred_{ELY,ON/OFF}$ predicts if there will be enough energy available to start the electrolyser. $Pred_{ELY,ON/OFF}$ could also use time-of-day information in the ON/OFF-switching of the electrolyser, e.g., even if there should be good conditions for hydrogen production one hour before sunset, it would not be favourable to start the electrolyser since it needs at about 1.5 hours to reach nominal operation conditions. In this work, the control parameter $Pred_{ELY,ON/OFF}$ will be based on weather forecast and load prediction with a time resolution of two hours. E.g., if $Pred_{ELY,ON/OFF}$ is set to 300 W, the electrolyser is switched ON if the average output from the photovoltaic arrays is predicted to be equal to or above the threshold setting of 300 W during the next two hours. If $Pred_{ELY,ON/OFF}$ reports a negative value for the next two hours, the fuel cell is set to idling if $I_{Balance,+/-}$ is positive only for some minutes.

Control Parameters CP3 and CP4: $H_{2,High}$ and $H_{2,Low}$

As shown on the right side of Figure 5.4, three regions are defined within the hydrogen state-of-charge scale. When the system parameter $H_{2,SOC}$ is above the control parameter $H_{2,High}$-threshold, hydrogen treatment tasks such as compression work and/or regeneration of the desiccant used to absorb water from the hydrogen, can be prioritised at the expense of hydrogen production. If the hydrogen system is

grid-connected, the strategy could be to export electricity instead of producing hydrogen if the electricity price is high. If the hydrogen system is connected through a common hydrogen network, the hydrogen produced when $H_{2,SOC}$ is above $H_{2,High}$ could also be exported if the hydrogen price is high enough. If $H_{2,SOC}$ is below $H_{2,Low}$, it can be decided to allow deeper discharge of the battery even though it may decrease battery lifetime. But deep discharge of the battery can be justified because switching from fuel cell- to battery operation increases the system energy efficiency during the critical period with low $H_{2,SOC}$.

Control Parameters CP5 and CP6: $BAT_{ELY,ON}$ and $BAT_{FC,ON}$

In addition to prevent the electrolyser and the fuel cell from operating simultaneously, hysteresis bands were implemented into the battery five-step charge controller in order to prevent frequent ON/OFF-switching of the electrolyser and the fuel cell, Section 5.3.1. From Figure 5.7 (left side), when the system parameter BAT_{SOC} reaches the control parameter $BAT_{ELY,ON}$-threshold, the electrolyser is allowed to be switched ON. This ON-signal is not set to OFF-position if BAT_{SOC} should drop below $BAT_{ELY,ON}$ during electrolyser operation. But, if $I_{Balance,+/-}$, $Pred_{ELY,ON/OFF}$, or $H_{2,High}$ signals the electrolyser OFF while BAT_{SOC} is below $BAT_{ELY,ON}$, only then the ON-signal triggered by $BAT_{ELY,ON}$ is reset to OFF-position. This means that the *hydrogen charging mode*-range of BAT_{SOC} can merge into the *hydrogen balance mode*-range if the battery should happened to be discharged during electrolyser operation. A hysteresis range on the BAT_{SOC} parameter for electrolyser operation is thus possible without a specific electrolyser BAT_{SOC} OFF-setting.

The control parameter $I_{Balance,+/-}$ does not include the battery current, it only senses a positive or negative current balance between the photovoltaic array and the load. Thus, the HSAPS high-level energy management controller receives no information about whether the battery is discharging to the electrolyser or not. This is however taken care of by means of a battery voltage control limit. Battery voltage that is lower than the nominal electrolyser voltage prevents the battery to be deeply discharged to the electrolyser. With this voltage configuration, the battery will only discharge to the electrolyser during electrolyser start-up. E.g., if BAT_{SOC} is initially below $BAT_{ELY,ON}$ (electrolyser is OFF) and both $I_{Balance,+/-}$ and $Pred_{ELY,ON/OFF}$ favours electrolyser start-up, and the battery is being charged with a high current which causes the battery voltage to be above the electrolyser nominal voltage, the battery will be discharged to the electrolyser for only a short instance when BAT_{SOC} reach $BAT_{ELY,ON}$ (electrolyser ON) and the battery voltage remains above the electrolyser nominal voltage.

The procedure for the control parameter $BAT_{FC,ON}$ is the same as for the procedure for the control parameter $BAT_{ELY,ON}$, except for the fact that it is activated in the opposite BAT_{SOC} direction. However, regarding the fuel cell voltage and the battery voltage in a direct coupled system; it will be shown in Section 6.2 that it can be advantageous to charge the battery with the fuel cell in a small- scale HSAPS in order to avoid the fuel cell running at partial loads where its efficiency decreases due to the constant power required by the fuel cell control system. The general fuel cell voltage can vary with a magnitude of about 2:1, where the voltage is high at low current output, and is low at high current output. Because of this, the nominal fuel cell voltage chosen for a small-scale HSAPS without converters should be about the same as the nominal battery voltage. In this case, the fuel cell will charge the battery with a higher power output than would be the case when running at partial loads.

5.3.3 Fuzzy control

Historical Background

Fuzzy control is a method first introduced by L.A. Zadeh in 1965 [15]. The first practical use of fuzzy control occurred in the mid 70's. During the last decades the use of fuzzy control has increased strongly, especially by Japanese scientists and companies. Today, commercial equipment using fuzzy control is quite common, e.g., self-focusing cameras, water quality in washing machines, anti-locking brakes, and elevator control.

A fuzzy controller can offer robust non-linear control. Conventional PID controllers can be very effective for a given application but their performance can suffer and become unstable when subjected to external disturbances or substantial parameter changes. Fuzzy control systems, on the other hand, can be developed to cope with these disturbances and changes [16]. Fuzzy control can be suitable when the process is based on human experience that forms a set of rules that express how the system should be operated. This means that fuzzy control might be advantageous when no exact mathematic presentation of the system exists, which is the case for the overall high-level energy flow control of the HSAPS. For a general description of fuzzy control theory, the reader is referred to Appendix B.

Fuzzy Logic Controller for the HSAPS

Four system parameters are used as inputs to the suggested fuzzy logic controller for the high-level energy management of the HSAPS. The four system parameters chosen are the battery state-of-charge (BAT_{SOC}), hydrogen state-of-charge ($H_{2,SOC}$), the actual electric current balance ($I_{PV\text{-}Load}$) in the HSAPS, and the time of the year (*Season*). The three modes of HSAPS-operation; hydrogen charging (electrolyser operation), hydrogen balance (hydrogen subsystem idling or not in use, only the battery is available as an energy storage), and hydrogen discharging (fuel cell operation), form the basis of three general fuzzy sets. These three modes of operation were introduced in Section 2.2, they were also used for the battery five-step charge controller and the Control Matrix control algorithm. The three general fuzzy sets are simply denoted *ELY*, *BAT,* and *FC* with respect to the modes of operation given above.

The four fuzzy controller input parameters, BAT_{SOC}, $H_{2,SOC}$, $I_{PV\text{-}Load}$, and *Season*, are arguments to the membership functions existing within each of the general fuzzy subsets. These membership functions can be thought of as the *control parameters* in the fuzzy logic controller. In the forthcoming, the arguments will be denoted as superscripts and the general fuzzy sets will be denoted in subscripts in the expressions for the membership functions, $\mu_{fuzzy\ set}^{argument}$, where μ is a symbol for a membership function. In this work, a total of ten input membership functions are chosen with the four arguments and the three general fuzzy sets given, Table 5.3. In addition there are three output membership functions that intuitively reflect the three modes of HSAPS operation, Table 5.3. These three output functions form the basis for the aggregation routine and the final de-fuzzification. Figure 4.11 in Section 4.1.10 shows the Fuzzy controller algorithm developed in SIMULINK.

Table 5.3 Overview showing the relation between the ten input membership functions (based on the four arguments and the three general fuzzy sets) and the three output membership functions

	BAT_{SOC} [Fig 5.8]	$H_{2,SOC}$ [Fig 5.9]	$I_{PV\text{-}Load}$ [Fig 5.10]	*Season* [Fig 5.11]	*Output* [Fig 5.12]
ELY	$\mu_{ely}^{bat_{soc}}$	$\mu_{ely}^{H_{2,soc}}$	$\mu_{ely}^{I_{pv-load}}$	μ_{ely}^{season}	μ_{ely}^{output}
BAT	$\mu_{bat}^{bat_{soc}}$	-	$\mu_{bat}^{I_{pv-load}}$	-	μ_{bat}^{output}
FC	$\mu_{fc}^{bat_{soc}}$	$\mu_{fc}^{H_{2,soc}}$	$\mu_{fc}^{I_{pv-load}}$	μ_{fc}^{season}	μ_{fc}^{output}

The membership functions are presented in Figures 5.8 – 5.12. As indicated in Table 5.3, the input membership functions that use the same argument are plotted in the same figure. There are no membership functions for the *BAT* fuzzy set with the arguments $H_{2,SOC}$ and *Season* as inputs because these inputs are mostly related to either hydrogen charging or hydrogen discharging. As seen from Figures 5.8 – 5.12, the membership functions are given as regions where the output is either 0 or 1, or a transition region given by a simple linear relationship. For the mathematical expressions for the thirteen membership functions the reader is referred to Appendix C.

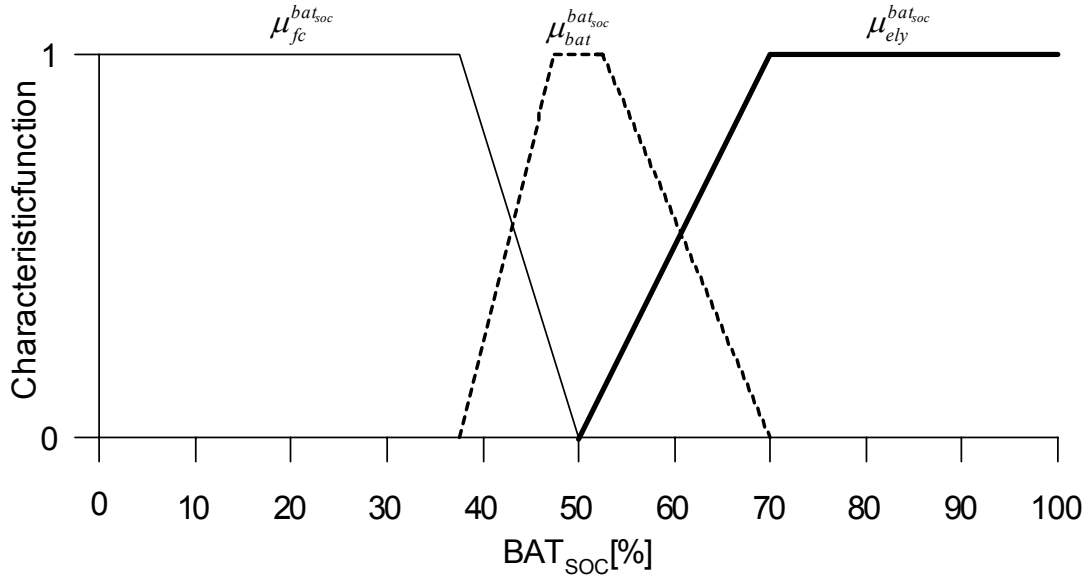

Figure 5.8 Input membership functions with BAT_{SOC} as argument.

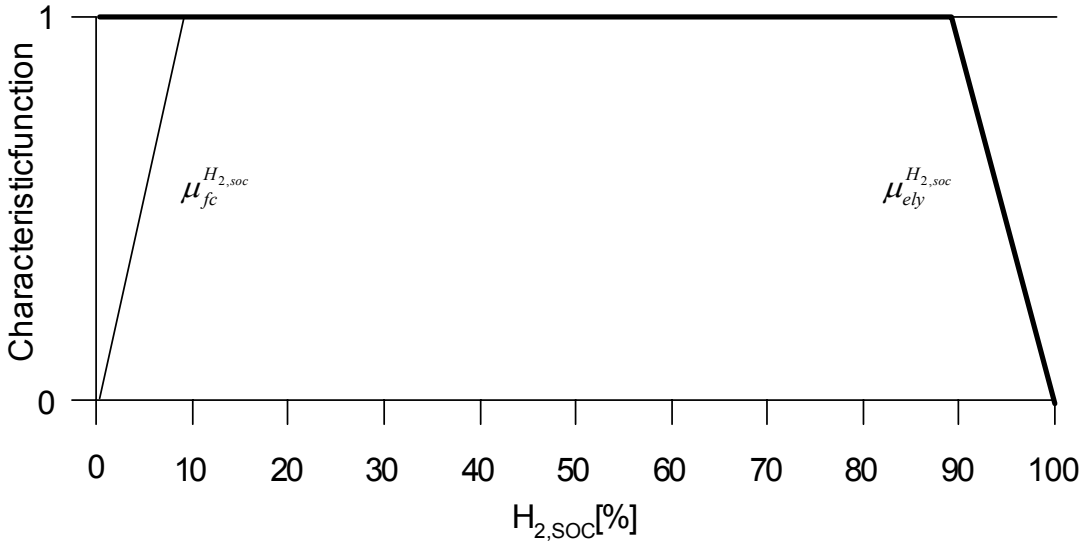

Figure 5.9 Input membership functions with $H_{2,SOC}$ as argument.

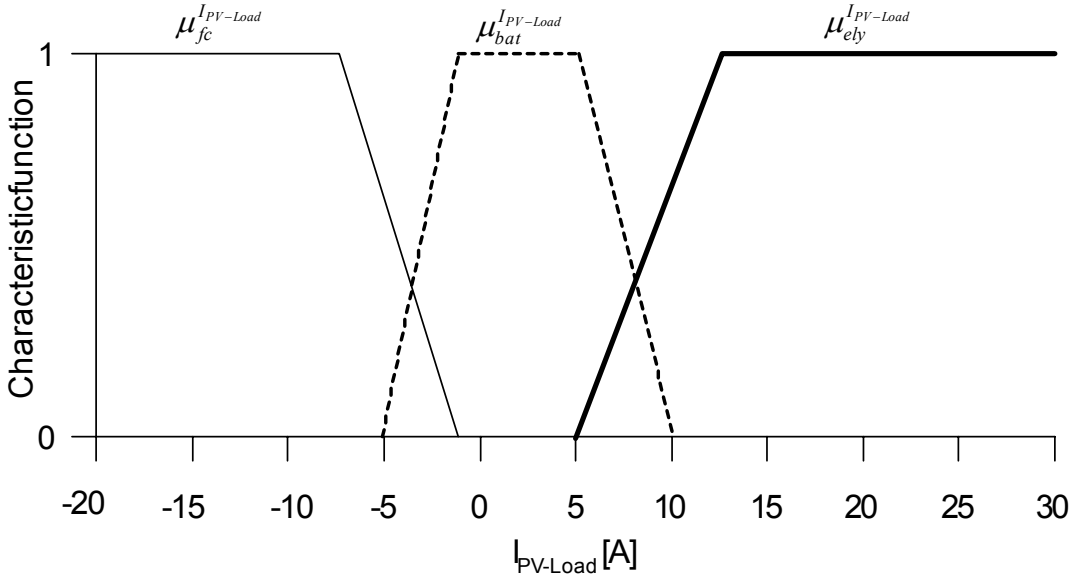

Figure 5.10 Input membership functions with $I_{PV\text{-}Load}$ as argument.

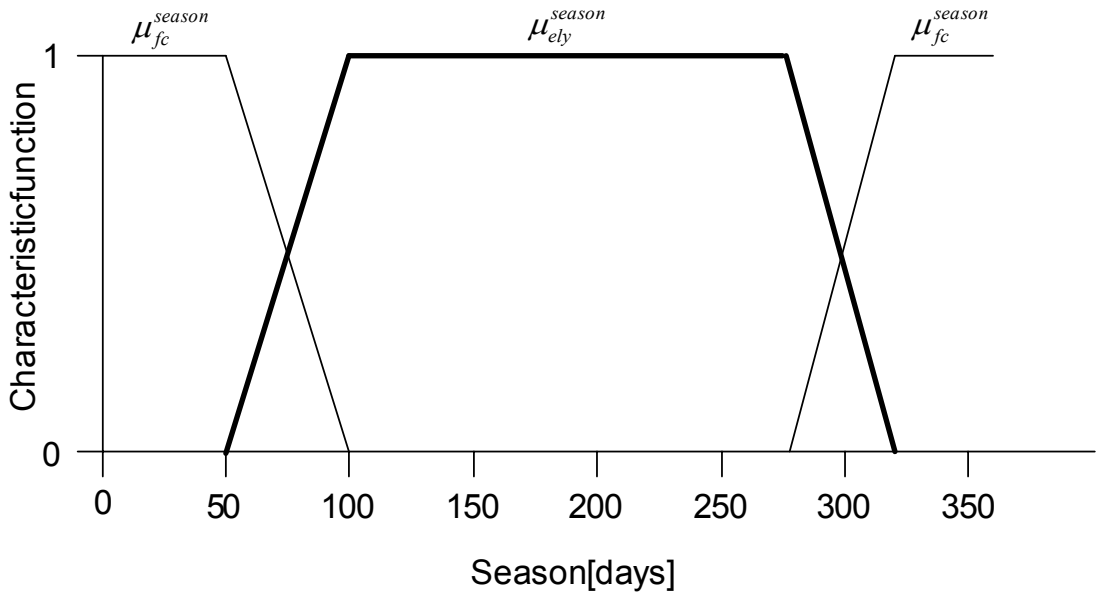

Figure 5.11 Input membership functions with *Season* as argument.

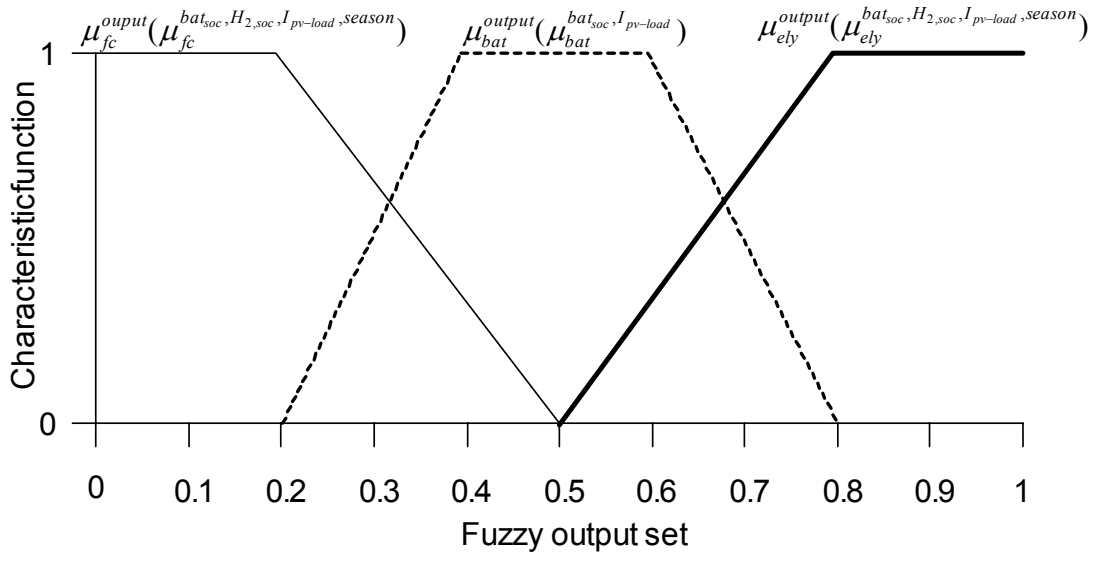

Figure 5.12 Output membership functions that are to be modified by the input membership functions presented in Figures 5.8 – 5.11 (see Appendix B and Appendix C).

The output membership functions shown in Figure 5.12 accept their inputs via the ordinates. However, before going into a detailed description of the mapping between the input/output membership functions a presentation of the three selected "If-Then" rules for the HSAPS fuzzy controller is required:

Rule #1: IF $\mu_{bat}^{bat_{soc}}$ OR $\mu_{bat}^{I_{pv-load}}$ THEN

$$\mu_{bat}^{output} = \text{Max}\{\ \mu_{bat}^{bat_{soc}}, \mu_{bat}^{I_{pv-load}}\ \}$$

Rule #2: IF $\mu_{fc}^{bat_{soc}}$ AND $\mu_{fc}^{H_{2,soc}}$ AND $\mu_{fc}^{I_{pv-load}}$ AND μ_{fc}^{season} THEN

$$\mu_{fc}^{output} = \text{Min}\{\ \mu_{fc}^{bat_{soc}}, \mu_{fc}^{H_{2,soc}}, \mu_{fc}^{I_{pv-load}}, \mu_{fc}^{season}\ \}$$

Rule #3: IF $\mu_{ely}^{bat_{soc}}$ AND $\mu_{ely}^{H_{2,soc}}$ AND $\mu_{ely}^{I_{pv-load}}$ AND μ_{ely}^{season} THEN

$$\mu_{ely}^{output} = \text{Min}\{\ \mu_{ely}^{bat_{soc}}, \mu_{ely}^{H_{2,soc}}, \mu_{ely}^{I_{pv-load}}, \mu_{ely}^{season}\ \}$$

Rule #1 says that, if one or both of the two membership functions that favour hydrogen balance register values larger than zero, then the maximum value of these two functions must be used to determine the specific area.

Rule #2 says that, if all of the membership functions that favour hydrogen discharging register values larger than zero, then the minimum value is used to determine the specific area. The reason for using the minimum value in this case is to ensure that ALL the four input system parameters favour fuel cell operation, reducing unnecessary fuel cell start-ups.

Rule #3 says that, if all of the membership functions that favour hydrogen charging register values larger than zero, then the minimum value is used to determine the specific area. The reason to use the minimum value is the same as for Rule #2, except here the scope is to reduce unnecessary electrolyser start-ups.

The resulting specific areas from each of the three rules are then aggregated. Finally, the centre of gravity (CoG) [17] of the aggregated areas is used as the fuzzy controller output.

It is important to notice that the output membership functions for the fuzzy controller give specific areas as their outputs, where the size of the specific areas are dependent on whether the specific rule uses maximum or minimum values from the input membership functions. This effect is illustrated in Figure 5.13 where the fuzzy rules 1 – 3 are repeated graphically. Figure 5.13 shows a situation where the fuzzy controller is balanced towards hydrogen discharging (fuel cell operation). In the forthcoming, the three "If-Then"-rules will be referred to as Rule #1, Rule #2, and Rule #3.

The crisp output from the fuzzy controller gives a value on the interval [0,1] that represents the state-of-system for the HSAPS. However, the components in the HSAPS defined in this work still needs a binary signal in order to be switched ON/OFF. Thus, the final fuzzy controller output value works as an HSAPS energy level meter for where the lower levels indicates hydrogen discharging, mid levels indicates hydrogen balance, while higher levels indicates hydrogen charging.

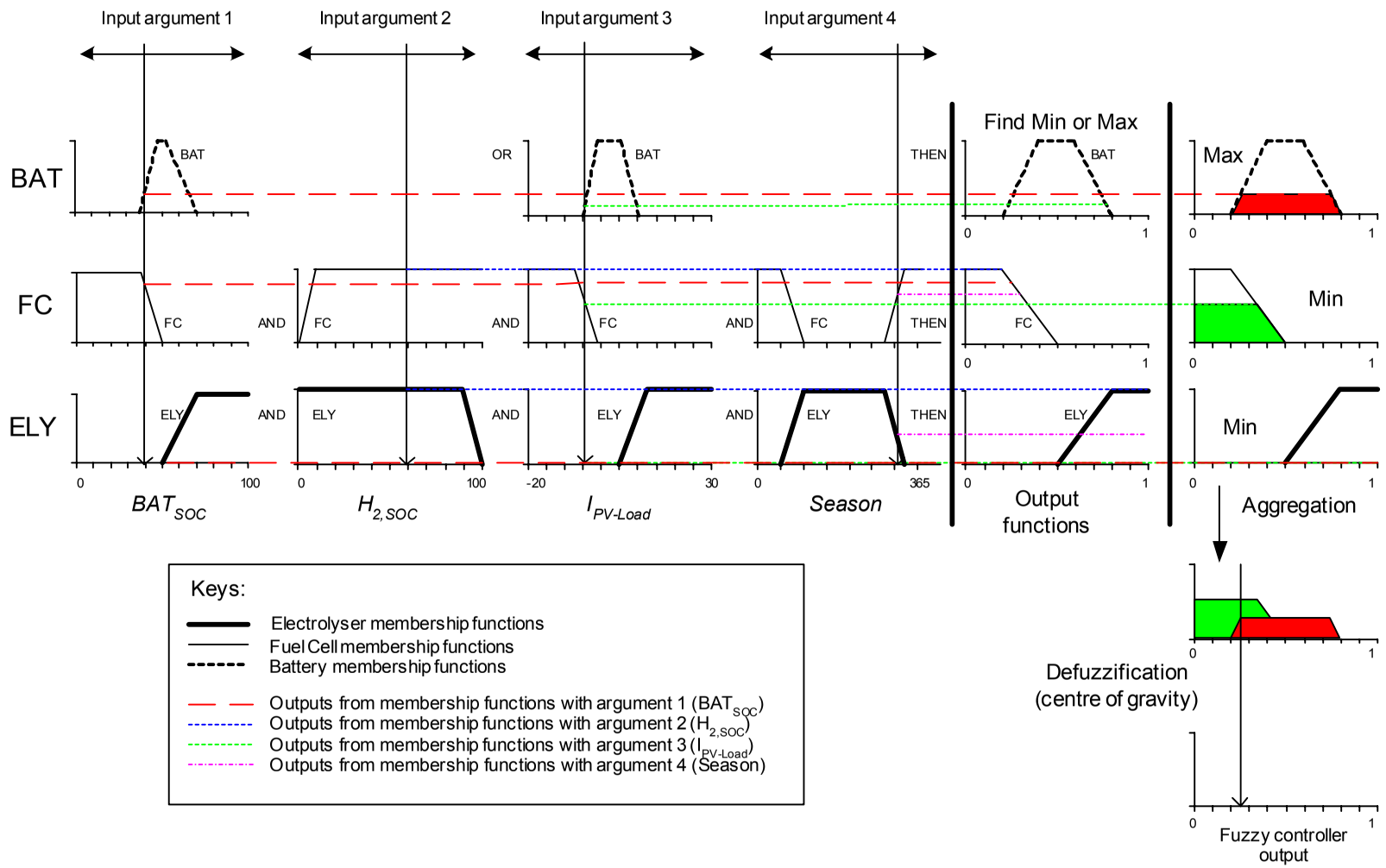

Figure 5.13 Graphical representation of the fuzzy controller operation used in this work. The example values for the system parameters make the fuzzy controller balance towards hydrogen discharge (fuel cell operation).

Figure 5.14 shows how the HSAPS is controlled in this simulation study by means of the fuzzy controller and two relays. Basically, this is the same solution as introduced for the battery five-step charge controller in Section 5.3.1, but the output from the fuzzy controller is more robust as all the selected important system parameters are weighted and balanced into a single output value. As for the five-step charge controller, the hysteresis-bands reduces unnecessary electrolyser and fuel cell start-ups and therefore introduce better system stability and possibly longer component lifetime.

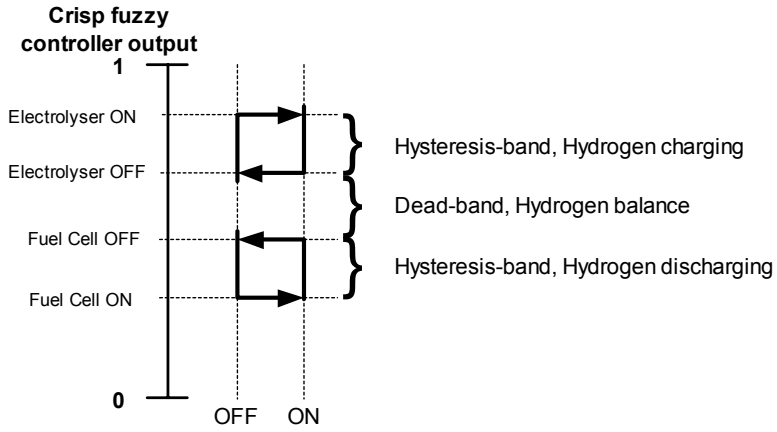

Figure 5.14 Fuzzy controller output combined with two relays, one for electrolyser operation and one for fuel cell operation, with the hysteresis-bands for the specific modes of operation for the HSAPS indicated.

5.4 Comparison of the three different HSAPS control strategies

In order to compare the three different control strategies described above, intensive computer simulations of a PV/H_2-energy system operated in stand-alone mode have been performed. For a thorough collection of key parameters for the different control strategies that have been identified and classified the reader is referred to Appendix D. It is of key importance that the control algorithms are practical to handle, i.e. avoiding implementation of control parameters with little impact on the controller-output, as too many control parameters result in a complicated controller that may even introduce instability into the system. The control algorithm must operate the HSAPS in a robust and stable manner, which often is more important than maximising the overall system efficiency, i.e. the quality of the power delivered to the customer must be within certain specifications. Unnecessary ON/OFF-switching and unnecessary operation is undesirable because it may introduce instability and possibly reduce component lifetime. Critical operating conditions must also be avoided, e.g., the electrolyser current is not allowed long-term operation above nominal value. Thus, the preferred system responses that are essential for optimal operation are:

- System robustness
- High energy efficiency
- Minimised fuel cell and electrolyser ON/OFF switching
- Minimised fuel cell and electrolyser runtime
- Avoiding critical operating conditions

5.4.1 Computer simulation setup

A total of six categories of computer simulations were run in this comparison study. The six categories of simulation runs may be characterised as follows:

Sim #1 Battery state-of-charge, five-step charge controller

Sim #2a Control Matrix where electrolyser is not switched ON if predicted power to the electrolyser is below 25 % of its rated power (400 W), Appendix E.

Sim #2b Control Matrix without the prediction parameter for electrolyser operation

Sim #3a Fuzzy controller

Sim #3b Fuzzy controller with higher power-balance parameter setting for electrolyser operation

Sim #3c Fuzzy controller with seasonal parameter only for electrolyser operation

All the simulations were executed with the empirical HSAPS Simulink models presented in Chapter 4. The empirical models were based on experimental data gathered from the laboratory HSAPS presented in Chapter 3. Thus, the size of the electrolyser and the fuel cell in these simulations were 1.7 kW and 0.5 kW, respectively. In order to match annual operation of a HSAPS, the size of the hydrogen storage and the size of the secondary battery simulated had to be enlarged compared to the size of the actual laboratory HSAPS.

The initial and common conditions for the simulations are as follows:

- Hourly solar radiation data measured in Oslo (60°N), Norway.
- Photovoltaic array with a peak power of 2 kW, generating a maximum energy supply of 1076 kWh. The photovoltaic array was coupled to the DC bus bar through a maximum power point tracker.
- The load was defined as a current sink operating within a voltage range of 35 – 50 V. The daily load-current profile utilised in the simulations is given in Figure 5.15, which is used for all the other days throughout the year, e.g., the electric current profile for a single household. The total energy required by the load can be seen to vary between 591.5 kWh/year and 594.2 kWh/year, Table 5.8. This is due to the voltage-variation applied to the load, depending on which of the components being used. More details about average power and operation hours are given in Table 5.8. The total load-current requirement was 14.24 kAh.
- The simulations started at the 1st of January at 00.00 hours with one-hour resolution.
- The initial BAT_{SOC} was 90 %. A 36 V lead-acid battery was chosen for reasons discussed in Section 3.3. The battery was capable to store 400 Ah. That is, the system simulated conducted an energy storage of 36 V · 400 Ah = 14.4 kWh, which agrees quite well with the minimum battery size found in Appendix F for an annual load requirement of 650 kWh/year.

- The initial $H_{2,SOC}$ was 48 %. The hydrogen storage was capable to hold a total volume of 148.2 Nm^3 H_2 which equals about 400 kWh (LHV). This is somewhat larger than the minimum hydrogen storage size found in Appendix F for an annual load requirement of 650 kWh/year. However, in these simulations the hydrogen storage is somewhat oversized in order to secure supply of power. According to Figure F.1 in Appendix F it is more cost effective to oversize the hydrogen storage (MH-storage) compared to oversize the batteries (lead-acid).

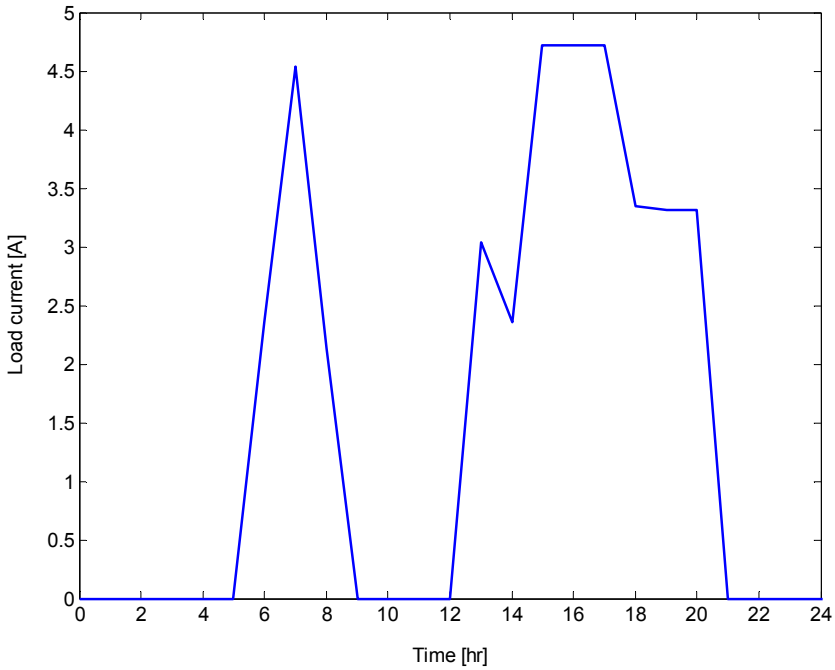

Figure 5.15 The load-current profile used for each day in the annual simulations, e.g., representative for a single household, though scaled in order to match the fuel cell installed in the HSAPS laboratory (Chapter 3). The load is defined to be a current sink able to accept a voltage range of 35 – 50 V.

5.4.2 System parameters and settings for control parameters in computer simulations

A detailed overview of the six system simulations is given in Table 5.5. One simulation was performed with the battery five-step charge controller. Two simulations were performed with the Control Matrix where one of the simulations was performed without the weather/load prediction parameter introduced in Section 5.3.2. Three simulations were undertaken with the fuzzy controller. Here, the first simulation was carried out with the membership functions given in Figures 5.8 – 5.12. In the second simulation, the membership function $\mu_{ely}^{I_{pv-load}}$ was altered, while in the third simulation the membership function μ_{ely}^{season} was altered and the membership function μ_{fc}^{season} was left out. Details on the alterations of the fuzzy membership function are given in Table 5.6 and Table 5.7.

In order to make the comparison between the different control strategies reasonable, no additional timer settings, e.g., day-time setting, for either the fuel cell or the electrolyser have been used. It is also of great importance that those control parameters that are common for the different control algorithms are equally set. Thus, no efforts have been put into optimisation of these control parameter settings.

Table 5.5 Parameters and settings for comparison of the three different control strategies given in Sections 5.3.1 – 5.3.3, with changed settings indicated with bold and shaded cell

System parameters →		BAT_{SOC} [%]				$H_{2,SOC}$ [%]				$I_{PV\text{-}Load}$ [A]				$Pred_{PV\text{-}Load}$ [W]	*Season* [Days]	
Control parameters →		$BAT_{ELY,ON}$	$\mu_{ely}^{bat_{soc}}$	$BAT_{FC,ON}$	$\mu_{fc}^{bat_{soc}}$	$H_{2,High}$	$\mu_{ely}^{H_{2,soc}}$	$H_{2,Low}$	$\mu_{fc}^{H_{2,soc}}$	$I_{Balance,+/-}$	$\mu_{ely}^{I_{pv\text{-}load}}$	$I_{Balance,+/-}$	$\mu_{fc}^{I_{pv-load}}$	$Pred_{ELY,ON/OFF}$	μ_{ely}^{season}	μ_{fc}^{season}
Control strategy ↓	**↓ Sim#**	Ely ON when BAT_{SOC}:		FC ON when BAT_{SOC}:		H_2 level defined as high when $H_{2,SOC}$:		H_2 level defined as low when $H_{2,SOC}$:		Ely ON when $I_{PV\text{-}Load}$:		FC ON when $I_{PV\text{-}Load}$:		Ely ON when:	Ely ON period:	FC ON periods:
BAT_{SOC} five-step controller	1	> 70	-	< 38	-	100	-	0	-	-	-	-	-	-	-	-
Control Matrix	2a	> 70	-	< 38	-	90	-	10	-	> 0		< 0		> 400	-	-
	2b	> 70	-	< 38	-	90	-	10	-	> 0		< 0		-	-	-
fuzzy controller	3a	-	> 50[1]	-	< 50[2]	-	90[3]	-	10[4]	-	> 5[5]	-	< -1[6]	-	75-300[7]	0-75 and 300-365[8]
	3b	-	> 50[1]	-	< 50[2]	-	90[3]	-	10[4]	-	**> 10**[9]	-	< -1[6]	-	75-300[7]	0-75 and 300-365[8]
	3c	-	> 50[1]	-	< 50[2]	-	90[3]	-	10[4]	-	*> 10*[9]	-	< -1[6]	-	**90-275**[10]	-

(1) Membership function given in Table C.3 in Appendix C, (2) Membership function given in Table C.1 in Appendix C
(3) Membership function given in Table C.5 in Appendix C, (4) Membership function given in Table C.4 in Appendix C
(5) Membership function given in Table C.8 in Appendix C, (6) Membership function given in Table C.6 in Appendix C
(7) Membership function given in Table C.10 in Appendix C, (8) Membership function given in Table C.9 in Appendix C
(9) The altered membership function for the electrolyser operation is given in Table 5.6, (10) The altered membership function is given in Table 5.7

System parameter: BAT_{SOC}

The system parameter BAT_{SOC} was implemented in all the three control strategies, thus the settings (the control parameters) for switching the electrolyser and the fuel cell ON were kept at the same level independent of the control strategy tested. The chosen ON settings were based on when the fuzzy membership function gave a 100 % ON signal, which was at BAT_{SOC} > 70 % for electrolyser operation and at BAT_{SOC} < 38 % for fuel cell operation. The reason why the ON-triggers for the electrolyser and the fuel cell operation were set at 50 % for the fuzzy controller in Table 5.5 was that this is where the transient regions in the membership functions starts/ends with OFF (0 %) as outputs; see Figure 5.8 in Section 5.3.3 and Table C.1 and Table C.3 in Appendix C.

The electrolyser and fuel cell OFF set-points implemented in the relays used in the battery five-step charge controller are not shown in Table 5.5. No relay operations based on the BAT_{SOC} parameter for the electrolyser or the fuel cell ON/OFF-switching were applied to the Control Matrix or the fuzzy controller. However, relay operations for electrolyser/fuel cell ON/OFF-switching were implemented on the fuzzy controller output value according to Figure 5.14. In this case, the settings for the fuzzy controller relays were set to: Electrolyser ON = 0.70, Electrolyser OFF = 0.55, Fuel Cell ON = 0.38 and Fuel Cell OFF = 0.45 (these values are not shown in Table 5.5). These ON set-points were simply chosen based on the settings for the BAT_{SOC} system parameter given above. The dead-band between the OFF-settings is important in order to avoid unnecessary ON/OFF-switching of the electrolyser and the fuel cell.

System parameter: $H_{2\ SOC}$

As will be shown later, the maximum $H_{2,SOC}$ was occasionally above the $H_{2,High}$ set-point during the simulations. In Section 5.3.2 several actions during this condition were suggested. The topic is further investigated in Chapter 7 where H_2 gas purification or compression work is prioritised when $H_{2,SOC}$ is high. In this case-study, however, no specific actions were performed during high $H_{2,SOC}$. Furthermore, the special case where $H_{2,SOC}$ decreases below $H_{2,Low}$ did not occur during the simulations. Thus, the influence of $H_{2,SOC}$ has not been a subject in this study.

System parameter: $I_{PV\text{-}Load}$

The system parameter $I_{PV\text{-}Load}$ was only implemented in the Control Matrix and the fuzzy controller (Section 5.3.2 and Section 5.3.3, respectively). The transient region for the membership function $\mu_{ely}^{I_{pv-load}}$ was however moved 5 A to the right with respect to the initial membership function given in Figure 5.10 in order to run the electrolyser at a higher power density. This parameter alteration is given in Table 5.6 and investigated in Sim #3b, Table 5.5.

System parameter: $Pred_{PV\text{-}Load}$

The system parameter $Pred_{PV\text{-}Load}$ was implemented only in the Control Matrix strategy. Comparing two simulations with and without the prediction parameter is interesting because it indicates the potential by having "perfect" weather and load forecast. Simulations with and without the prediction parameter were investigated in Sim #2a and Sim #2b, respectively, Table 5.5.

System parameter: Season

The system parameter *Season* was only implemented in the fuzzy controller. In Sim #3a, the *Season* parameter restricted the electrolyser and the fuel cell runtime, while in Sim #3c only the electrolyser runtime was restricted, Table 5.5. In addition, the seasonal period for the electrolyser runtime in Sim #3c was shortened with about 40 days. The altered fuzzy membership function for the hydrogen charge mode, which was investigated in Sim #3c (Table 5.5), is given in Table 5.7.

Table 5.6 Altered membership function for hydrogen charge mode with $I_{PV\text{-}Load}$ as input parameter in Sim #3b, the transition area is moved 5 A higher compared to the function shown in Figure 5.10 and listed in Table A5.8.

Region of $I_{PV\text{-}Load}$	**Output from $\mu_{ely}^{I_{pv\text{-}load}}$**
-20 A $\leq I_{PV\text{-}Load} \leq$ 10 A	0
10 A $< I_{PV\text{-}Load} <$ 18 A	($I_{PV\text{-}Load}$ - 10)/8
18 A $\leq I_{PV\text{-}Load} \leq$ 30 A	1

Table 5.7 Altered membership function for hydrogen charge mode with *Season* as input parameter in Sim #3c. The seasonal period for the electrolyser runtime was made shorter compared to the function listed in Figure 5.11 and given in Table C.10.

Region of *Season*	**Output from μ_{ely}^{season}**
day 0 $\leq$ *Season* $\leq$ day 90	0
day 90 $<$ *Season* $<$ day 130	(*Season* – 90)/40
day 130 $\leq$ *Season* $\leq$ day 230	1
day 230 $<$ *Season* $<$ day 270	(-*Season* + 270)/40
day 270 $\leq$ *Season* $\leq$ day 365	0

5.4.3 Results and discussion

The results of the six simulations are given in Table 5.8. The first impression when investigating Table 5.8 is that the different control strategies and their individual parameter settings had greater influence on the electrolyser than on the other components. This was however expected since electrolyser-operation has a greater extent of freedom as its only goal in this system configuration was to produce enough hydrogen prior to the winter season. E.g., if it was expected to be a short period with some excess power on the DC bus bar, and the battery was about fully charged, the electrolyser would have been restricted from starting up due to the $Pred_{PV\text{-}Load}$ in the Control Matrix or by the lower electrolyser current-limit in $\mu_{ely}^{I_{pv-load}}$ implemented in the fuzzy controller. Thus, avoiding unnecessary electrolyser start-up when only a small amount of hydrogen would have been produced. Very short periods of electrolyser operation, including the worst-case scenario of start-up of a cold electrolyser-stack, might even cause net energy losses due to the electrolyser control system energy requirements. The fuel cell, however, has less freedom because it *has* to be switched ON if BAT_{SOC} is low at the same time as the solar insolation is too low to cover the load requirement alone.

Table 5.8 Results from comparison of the three different control strategies where **1**, **2,** and **3** referrers to the battery five-step charge controller, Control Matrix, and fuzzy control strategies, respectively. The specific parameter settings for the individual simulation numbers are given in Table 5.5.

Simulation number	1	2a	2b	3a	3b	3c
PV energy [kWh]	1076.0	1076.0	1076.0	1076.0	1076.0	1076.0
PV runtime [hr]	2580.0	2580.0	2580.0	2580.0	2580.0	2580.0
PV average power [W]	417.1	417.1	417.1	417.1	417.1	417.1
PV ON/OFF [-]	417.0	417.0	417.0	417.0	417.0	417.0
PV average runtime [hr]	6.2	6.2	6.2	6.2	6.2	6.2
Load energy [kWh]	594.2	592.7	591.5	591.9	591.9	593.4
Load runtime [hr]	4016.0	4016.0	4016.0	4016.0	4016.0	4016.0
Load average power [W]	148.0	147.6	147.3	147.4	147.4	147.8
Load ON/OFF [-]	730.0	730.0	730.0	730.0	730.0	730.0
Load average runtime [hr]	5.5	5.5	5.5	5.5	5.5	5.5
ELY energy [kWh]	487.1	471.4	486.7	469.4	437.9	432.5
ELY runtime [hr]	1137.0	768.4	1119.0	725.7	574.5	563.9
ELY ON/OFF [-]	261.0	140.0	245.0	164.0	160.0	157.0
ELY average runtime [hr]	4.4	5.5	4.6	4.4	3.6	3.6
ELY average power [W]	428.4	613.5	434.9	646.8	762.2	767.0
FC energy [kWh]	153.7	151.9	150.8	150.9	150.9	153.8
FC runtime [hr]	849.7	838.4	818.3	795.8	795.8	815.2
FC ON/OFF [-]	177.0	189.0	198.0	189.0	189.0	195.0
FC average runtime [hr]	4.8	4.4	4.1	4.2	4.2	4.2
FC average power [W]	180.9	181.2	184.3	189.6	189.6	188.7
Net energy battery [kWh]	64.3	63.5	63.1	64.1	64.1	62.8
Battery charged energy [kWh]	292.0	292.1	292.3	293.5	293.5	290.8
Battery discharged energy [kWh]	-227.8	-228.6	-229.2	-229.5	-229.5	-228.0
Charge runtime [hr]	653.9	653.9	654.1	655.3	655.3	652.1
Discharge runtime [hr]	2275.0	2287.0	2307.0	2329.0	2329.0	2310.0
Average charge power [W]	446.6	446.7	446.9	447.9	447.9	445.9
Average discharge power [W]	100.1	100.0	99.3	98.5	98.5	98.7
Initial battery SOC [%]	90.0	90.0	90.0	90.0	90.0	90.0
Final battery SOC [%]	46.0	38.0	34.0	42.0	42.0	42.0
Average battery SOC [%]	72.9	71.4	70.9	73.1	73.1	73.9
Maximum battery SOC [%]	100.0	100.0	100.0	100.0	100.0	100.0
Minimum battery SOC [%]	38.0	38.0	33.8	29.1	29.1	40.9
Initial hydrogen SOC [%]	48.0	48.0	48.0	48.0	48.0	48.0
Final hydrogen SOC [%]	59.0	57.0	60.0	57.0	52.0	50.0
Average hydrogen SOC [%]	63.6	62.3	63.8	62.5	59.9	58.3
Maximum hydrogen SOC [%]	98.7	95.8	98.7	96.6	91.4	89.6
Minimum hydrogen SOC [%]	27.2	27.2	27.3	27.8	27.8	26.8
Excess energy [kWh]	64.2	80.3	64.3	76.5	111.1	119.8
System efficiency [%]	65.6	66.4	65.7	66.6	68.3	68.7

PV=photovoltaic array, ELY=electrolyser, FC=fuel cell, SOC=state-of-charge

Codes simulation numbers:

- **1 = Battery SOC, five-step charge controller**
- **2a = Control Matrix, electrolyser is not switched on if predicted power to electrolyser is below 400 W**
- **2b = Control Matrix without the prediction parameter for electrolyser operation**
- **3a = Fuzzy controller**
- **3b = Fuzzy controller with higher power-balance parameter for electrolyser operation**
- **3c = Fuzzy controller with seasonal parameter only for electrolyser operation**

Evaluation of electrolyser performance in simulation number 1, 2a, and 3a

The prediction parameter, $Pred_{PV\text{-}Load}$, implemented in the Control Matrix algorithm in Sim #2a prevented undesirable electrolyser start-ups if the solar insolation was predicted to be low within the next two hours, even though if $I_{PV\text{-}Load}$ happened to be positive. This feature reduced the number of electrolyser start-ups with 46.4 % and the

electrolyser runtime with 32.4 % compared to the five-step charge controller in Sim #1, while the total electrical energy converted by the electrolyser was lowered by only 3.2 % compared to Sim #1. At the same time, the average electrolyser power consumption increased with 43.2 % going from 428.4 W in Sim #1 to 613.5 W in Sim #2a.

$I_{PV\text{-}Load}$, which was implemented in the Control Matrix, was restricted to only two binary values; namely 1 when $I_{PV\text{-}Load}$ was positive and 0 when $I_{PV\text{-}Load}$ was zero or negative. These two values were used to control both the electrolyser and the fuel cell operation. The three fuzzy membership functions (one for each of the three fuzzy sets *ELY*, *BAT*, and *FC*), which used $I_{PV\text{-}Load}$ as their input, made the HSAPS more flexible because the three functions had their own settings for each of the system operation modes. Individual settings each for the electrolyser and the fuel cell could of course be introduced to the Control Matrix, but that would increase the number of system states from 36 to 54. One can argue that 54 states are though not many. However, it has been seen of great importance to keep the number of states as low as possible as too many states might introduce instabilities that can be hard to debug in a large matrix.

From the membership function for the electrolyser shown in Figure 5.10, it can be seen that the electrolyser is not allowed to operate below $I_{PV\text{-}Load}$ = 5 A. Due to this restriction, the fuzzy controller in Sim #3a reduced the electrolyser start-ups with 36.2 % and the electrolyser runtime with 37.2 %, respectively, compared to Sim #1. Compared to Sim #1 the total electrical energy converted by the electrolyser was only reduced by 3.6 %. That was about the same as for the Control Matrix in Sim #2a. Since the hydrogen production and consumption was about the same in Sim #3a as in Sim #1 and Sim #2a, the final $H_{2,SOC}$ for Sim #2a and Sim #3a are only 2 % lower compared to the control strategy used in Sim #1. At the same time, the average electrolyser power increased by 51.0 % going from 428.4 W in Sim #1 to 646.8 W in Sim #3a.

Evaluation of electrolyser performance in simulation number 2b and 3b

The prediction parameter, $Pred_{PV\text{-}Load}$, was removed from the Control Matrix in Sim #2b, which drastically increased the number of electrolyser start-ups and operating hours. This indicates that the parameter $I_{PV\text{-}Load}$ implemented in the Control Matrix (Section 5.3.2) had limited influence on the electrolyser performance. The results for the electrolyser were practically the same in Sim #1 and Sim #2b. Thus, it can be concluded that the settings for $I_{PV\text{-}Load}$ in the Control Matrix was too coarse, and a more precise setting for electrolyser/fuel cell ON/OFF-switching is needed. The effect of such precise settings will be demonstrated with $I_{PV\text{-}Load}$ in the fuzzy controller in Sim #3b.

The adjusted membership function, $\mu_{ely}^{I_{pv-load}}$, given in Table 5.6 and used in Sim #3b, clearly showed that the individual setting for the electrolyser operation strongly influenced the results when compared with Sim #3a. The electrolyser runtime decreased with about 150 hours and the start-ups decreased with only 4, indicating a decrease in the average electrolyser runtime. However, the average electrolyser power increased to 762.2 W, which is 17.8 % higher than in Sim #3a and 77.9 % higher than in Sim #1. Due to the restricted electrolyser runtime (Sim #3c), the total electrical energy converted by the electrolyser was 11.2 % lower compared to Sim #1. Still, the

resulting final $H_{2\ SOC}$ of 50 % was 2 % above the initial $H_{2,SOC}$, which represents a well-designed and proportioned HSAPS as the hydrogen storage did not have to be unnecessary large. Also, the electrolyser runtime and ON/OFF-switching were strongly reduced in order to preserve the guaranteed electrolyser efficiency. If the PEM electrolyser cells were assumed to have a guaranteed efficiency for about 3000 hours, the electrolyser-stack in Sim #1 would operate with the guaranteed efficiency for only 2.6 years, while the stack in Sim #3b would operate with the guaranteed efficiency for 5.2 years.

Evaluation of electrolyser and fuel cell performance in simulation number 3c
Reduction of the electrolyser season with 20 days in the spring and 20 days in the autumn (Sim #3c) did not affect the electrolyser behaviour significantly compared to the results in Sim #3b.

Regarding the fuel cell, from Figure 5.16 it can be seen that the seasonal restricted fuel cell runtime in Sim #3b caused the BAT_{SOC} to go as low as 29.8 % at day 73 and 29.1 % at day 282. Then, after removing the fuzzy membership function (μ_{fc}^{season}) for seasonal fuel cell runtime in Sim #3c, the number of days for fuel cell operation increased, which naturally resulted in a higher fuel cell runtime.

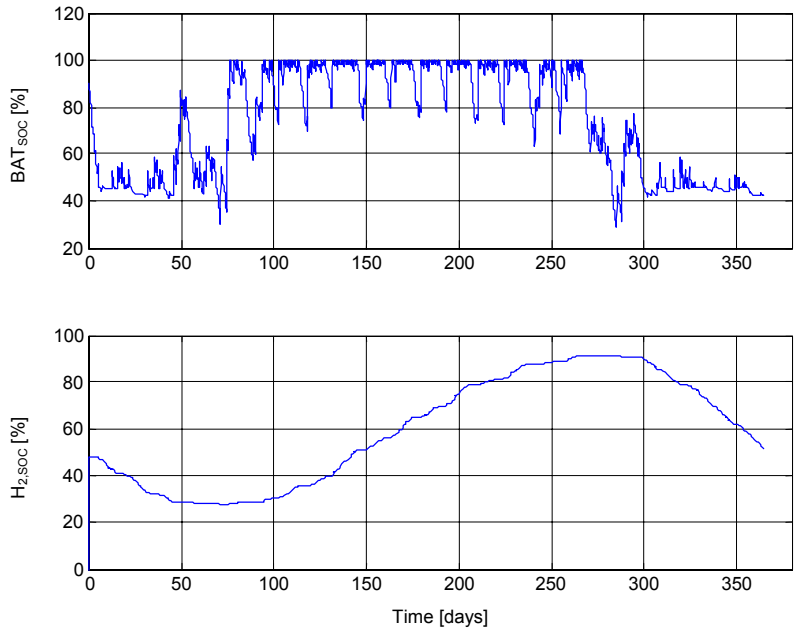

Figure 5.16 Battery- and hydrogen state-of-charge in Sim #3b

However, from Figure 5.17, the rather small increase in fuel cell runtime of about 20 hours in Sim #3c resulted in a minimum BAT_{SOC} of 40.9 % at day 282, which is higher than any of the minimum values found in the other simulations, Table 5.8. With the corresponding $H_{2,SOC}$ for Sim #3b given in Figure 5.16, there should be no reason for deep discharge of the battery when the all-time minimum $H_{2,SOC}$ was found to be as high as 27.8 %. However, if the amount of hydrogen was to decrease below the lower $H_{2,SOC}$ control limit (implemented in both the fuzzy controller and the Control Matrix), the fuel cell operation should be relaxed in order to save hydrogen. To save hydrogen and allow a deeper discharge of the battery can be justified because then the HSAPS is operated at a higher energy efficiency during critical periods of low $H_{2,SOC}$.

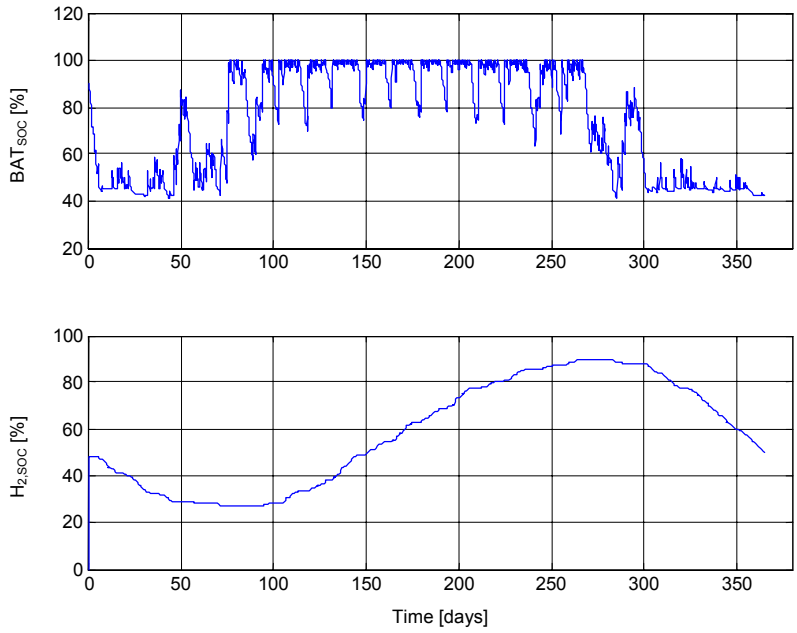

Figure 5.17 Battery- and hydrogen state-of-charge in Sim #3c

Summary of the results for the electrolyser

The results for the electrolyser are summarised in Figure 5.18 and Figure 5.19. It may be seen from Figure 5.18 that the average operating time (runtime) increases when going from the battery five-step controller to the Control Matrix. This is due to the prediction parameter for the electrolyser.

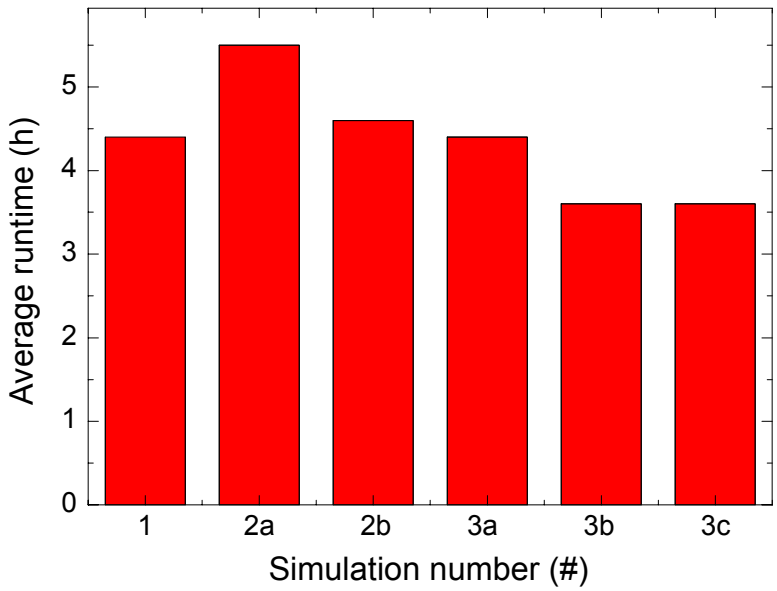

Figure 5.18 Average electrolyser runtime in the six categories of simulation runs.

At the same time it is seen from Figure 5.19 that the total runtime and the number of ON/OFF-switching of the electrolyser decreases, while the average power consumption of the electrolyser increases. In Sim #2b, where the prediction parameter is removed, the same characteristics as the five-step controller in Sim #1 is found, showing the importance of this parameter in the Control Matrix type control. In Sim #3a, Sim #3b and Sim #3c the fuzzy control is improved through adjusting the

parameters. The average power increases and the number of ON/OFF-switching is kept low. It may also be seen that the average power and the number of ON/OFF-switching can be further improved in the fuzzy control scheme by adjusting the system parameters for the electrolyser. The average runtime, however, decreases when adjusting the electrolyser operation parameters, but this is merely a result of the electrolyser being operated at a higher power level on average.

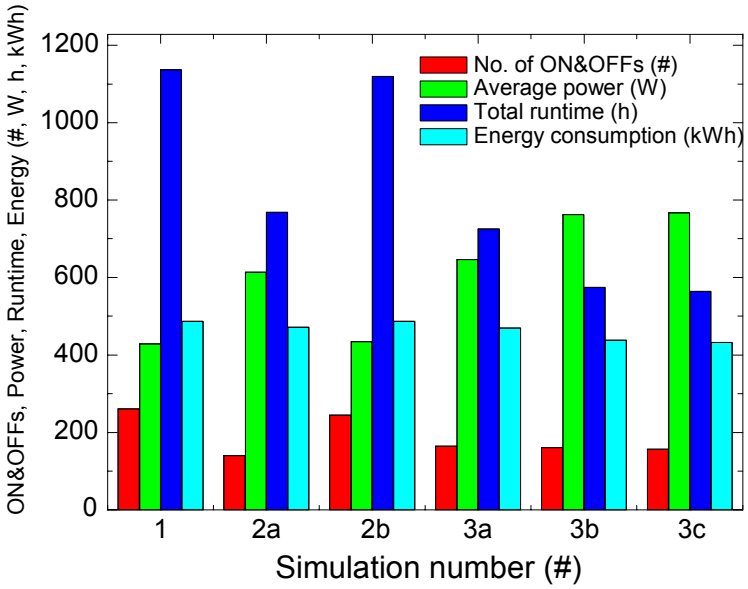

Figure 5.19 Electrolyser operation success parameters for the six simulation runs.

The overall fuel cell performance

Only small deviation in the fuel cell operation has been registered throughout the six simulations. The average electrical energy generated by the fuel cell was 152 kWh with a standard deviation of only 1.41 kWh. The best indication of the moderate fuel cell deviation within the different control strategies are however the low deviation in runtime and ON/OFF-switching, 5.4 % and 7.6 %, respectively. The same estimation for the deviation in electrolyser runtime and ON/OFF-switching was found to be 62.8 % and 54.7 %, respectively. The parameters in Sim #2b, Sim #3b, and Sim #3c were however altered with the electrolyser in mind, but as mentioned earlier, the fuel cell operation is truly dependent on the load profile and the actual size of the battery. Thus, reduction of the fuel cell runtime in pursue for minimum wear on the fuel cell stack is limited when considering changes of the parameter settings in a control algorithm. The ON/OFF-switching of the fuel cell can be reduced with timer settings and/or load prediction in order to prevent fuel cell shutdown during short periods of no-load requirements. However, even when the fuel cell is running in idling mode (only supplying power to its internal control system), it will increase the total fuel cell runtime.

Battery operation

The most important results concerning the battery operation are the minimum BAT_{SOC} and the average BAT_{SOC}. These values should be as high as possible for preservation of battery durability. It has already been shown that the lowest BAT_{SOC} was found in Sim #3a and Sim #3b with the membership function for seasonal fuel cell operation implemented in the fuzzy controller. On the other hand, the highest minimum BAT_{SOC} among all the simulations was accomplished in Sim #3c, using the fuzzy controller

without the seasonal fuel cell membership function, and with a minimal decrease in the final $H_{2,SOC}$. The reason for the higher minimum BAT_{SOC} and the higher average BAT_{SOC} in Sim #3c (compared to Sim #1, Sim #2a, and Sim #2b) is due to the transition region in the membership function for the fuel cell operation with BAT_{SOC} as input ($\mu_{fc}^{bat_{soc}}$). The transition area allows the fuel cell to start before BAT_{SOC} has decreased down to $BAT_{FC,ON}$ (38.0 %). At BAT_{SOC} = 38.0 %, the fuel cell ON signal from this parameter changes straight from 0 to 1 in the five-step charge controller and the Control Matrix, while the fuzzy controller already below BAT_{SOC} = 50 % indicates that it might be advantageous to switch the fuel cell ON, depending on the weights of the other parameters.

The flexibility of the fuzzy controller

The $BAT_{FC,ON}$ -settings in the five-step charge controller and the Control Matrix could have been optimised, but still, these control limits would be implemented without any flexibility. The main advance with the fuzzy controller is that it represents a dynamic and flexible solution as its final control output is balanced based on all the membership functions outputs with the system parameters as inputs. This flexibility can be illustrated by using the fuel cell operation as an example; by using the fuzzy controller presented in this work (without the seasonal fuel cell operation membership function) and assuming $H_{2,SOC}$ is somewhere between 10 % and 100 %, there exists a continuous set of combinations with the output from the two fuel cell membership functions with BAT_{SOC} ($\mu_{fc}^{bat_{soc}}$) and $I_{PV\text{-}Load}$ ($\mu_{fc}^{I_{pv-load}}$) as input arguments for which the final output from the fuzzy controller is 0.38 (fuel cell start-up). The transient regions for the two parameters where the fuzzy controller output is constant equal to 0.38 are found to be when:

BAT_{SOC} = [38.0 %, 45.5 %] and when
$I_{PV\text{-}Load}$ = [-10.0 A, -2.7 A]

Thus in this case, the two combinations at the boundaries for the transient regions that can start the fuel cell are:

$\{BAT_{SOC} = 38.0\ \%, I_{PV\text{-}Load} = -2.7\ A\}$ and
$\{BAT_{SOC} = 45.5\ \%, I_{PV\text{-}Load} = -10.0\ A\}$

To underline this, the combination $\{BAT_{SOC} = 37.0\ \%, I_{PV\text{-}Load} = -2.7\ A\}$ would also start the fuel cell, but the combination $\{BAT_{SOC} = 39.0\ \%, I_{PV\text{-}Load} = -2.7\ A\}$ would not. Likewise, the combination $\{BAT_{SOC} = 38.0\ \%, I_{PV\text{-}Load} = -3.0\ A\}$ would start the fuel cell but $\{BAT_{SOC} = 38.0\ \%, I_{PV\text{-}Load} = -2.0\ A\}$ would not. Explaining this with words; the fuel cell is switched ON if BAT_{SOC} is quite low and battery discharge current is slightly high, the fuel cell is also switched ON if BAT_{SOC} is slightly low and the battery discharge current is quite high.

Excess energy and system efficiency

Less electrical energy converted in the electrolyser means more excess energy in other parts of the system, which in turn may lower the overall energy conversion efficiency unless the excess energy can be used for hydrogen treatment like compression work and/or purification of the hydrogen gas. The overall system efficiency (Table 5.8) was defined based on that all excess energy could be utilised in the system. In a real-world

system, some of the excess power is too low for any practical applications. However, in the case of relative comparison of different control strategies, this definition for excess energy can be justified. Practical utilisation of excess energy in the HSAPS is investigated further in Chapter 7.

5.5 Conclusions

The battery five-step charge controller in Sim #1 was compared with the Control Matrix and the fuzzy controller in Sim #2 and Sim #3, respectively. The simulations clearly showed that the additional system parameters implemented in the Control Matrix and the fuzzy controller improved the HSAPS performance, especially for the electrolyser. The electrolyser operation can be relaxed as its main goal is to produce the needed amount of hydrogen before the winter season, i.e., the electrolyser does not have to be switched ON if the battery is fully charged and there is some excess power on the DC bus bar (dump loads must be installed), compared to the fuel cell which *has* to be switched ON if BAT_{SOC} is low at the same time as the solar insolation is too low to cover the load requirement alone. Even if the power requirements are very low, the fuel cell must be switched ON when the battery is deeply discharged. Only modest deviations were found within the fuel cell operations comparing all six simulations (Table 5.8).

The prediction parameter ($Pred_{PV\text{-}Load}$) implemented in the Control Matrix in Sim #2a achieved the lowest number of electrolyser start-ups and the highest average electrolyser runtime. But, when the prediction parameter was removed from the Control Matrix (Sim #2b), the resulting electrolyser operation was about the same as for the battery five-step charge controller (Sim #1), proving that the coarse system current balance parameter ($I_{PV\text{-}Load}$) implemented in the Control Matrix had little effect on the HSAPS performance.

The membership functions in the fuzzy controller added more flexibility to the ON/OFF-switching of the components compared to the battery five-step charge controller and the Control Matrix. Especially, $I_{PV\text{-}Load}$ and BAT_{SOC} proved to be important system parameters in the fuzzy controller. The results of the chosen system parameters implemented in the fuzzy controller were comparable to the results of the Control Matrix (Sim #2a) that used the prediction parameter $Pred_{PV\text{-}Load}$.

The Control Matrix represents a rigid and robust control algorithm that is very easy to implement as long as the number of control parameters is kept low (maximum 5 – 6 parameters). Large Control Matrixes might be hard to maintain and tune. However, this control algorithm can be very suitable for initial testing of a system, either a model or a real world system.

The fuzzy controller was found to be both flexible and rather easy to implement into the HSAPS model. Because of its flexibility, this control algorithm could be useful for further tuning and optimisation of HSAPS for commercial use. The main differences between the battery five-step controller, Control Matrix, and the fuzzy controller are summarised in Table 5.9.

Table 5.9 Evaluation of the three different controller schemes
(- = low, 0 = medium and + high)

Control Strategy	Ease of implementation	Flexibility	Stability
Battery five-step controller	+	-	-
Control Matrix	+	0	+
Fuzzy Controller	0	+	+

References

1. B.S.Blanchard and W.J.Fabrycky, *System Engineering and Analysis*. 1990, New Jersey: Prentince-Hall, Inc.
2. E.D.Sontag, *Mathematical Control Theory: Deterministic Finite Dimensional Systems*. Text in applied mathematics. Vol. 6. 1990, New York: Springer.
3. C.G.Cassandras, S.Lafortune, and G.J.Olsder, *Introduction to the modeling, control and optimization of discrete event systems*. 1995, Delft University of Technology: Delft, Netherlands.
4. V.Schaft and J.M.Schumacher, *An introduction to Hybrid Dynamical Systems*. Lectures Notes in Control and Information Science. Vol. 251. 2000, London: Springer-Verlag.
5. P.Philips, *Modelling, Control and Fault Detection of Discretely-Observed Systems*. 2001, PhD Thesis, Technische Universiteit Eindhoven, 2001: Eindhoven.
6. H.Barthels, et al., *Phoebus-Jülich:an Autonomous energy supply system comprising Photovoltaics, Electrolytic Hydrogen, Fuel Cell.* J. Hydrogen Energy, 1997. **23**(4): p. 295-301.
7. Ø.Ulleberg, *Stand-Alone power systems for the future: Optimal design, operation & control of solar-hydrogen energy system*. 1998, PhD Thesis, NTNU, Norges teknisk-naturvitenskapelige universitet: Trondheim. p. 210.
8. J.P.Vanhanen, *Dissertation for the degree of Doctor of Technology On the performance of improvements of small-scale photovoltaic hydrogen energy systems*. 1996: Espoo, Finland.
9. S.Galli, et al., *Stand Alone Photovoltaic Hydrogen Energy System, SAPHYS.* 1997, ENEA, IFE, KFA.
10. J.Eriksen, *Experimental Design of a Data Acquisition and Control System for a Small-Scale PV-H_2 System*, in *Faculty of Mathematics and Natural Sciences*. 2003, PhD Thesis, University of Oslo.
11. K.Agbossou, et al., *Renewable systems based on hydrogen for remote applications.* Journal of Power Sources, 2001. **96**: p. 168-172.
12. K.Voss, et al., *The Self-sufficient Solar House in Freiburg- Results of 3 years of operation.* Solar Energy, 1996. **58**: p. 17-23.
13. P.S.Kauranen, P.D.Lund, and J.P.Vanhanen, *Development of a Self-Sufficient Solar Hydrogen Energy System.* International Journal of Hydrogen Energy, 1994. **19**(1): p. 99-106.
14. Ø.Ulleberg, *The importance of control strategies in PV-hydrogen systems.* Solar Energy, 2003. **76**(1-3): p. 323-329.
15. L.A.Zadeh, *Fuzzy Sets*. Information and Control. Vol. 8. 1965.
16. C.Lee, *Fuzzy Logic in Control Systems: Fuzzy Logic Controller-Part II.* IEEE transactions on systems, man, and cybernetics, 1990. **20**(2): p. 419-432.
17. D.Driankov, H.Hellendoorn, and M.Reinfrank, *An Introduction to Fuzzy Control*. 1996: Springer.

6. Real-time and seasonal test of the laboratory HSAPS

To test a system in real-time throughout a whole year is of course time consuming and calls for larger energy storages to defend a minimum electrolyser- and fuel cell power level of about 100 – 200 W. If the power level is smaller, it might be difficult to achieve reasonable energy efficiency results due to rather large amounts of energy required by the components' control system (valves, flow controllers etc.) relative to the actual conversion energy. Another factor that may be of importance at low power levels is the measurement errors. Also, energy system demonstration projects should have practical and reasonable loads connected. It is important to distinguish between power and energy requiring loads. A constant load would be an example of an energy-requiring load while a typical dwelling would be an example of a combination of both power and energy requiring load.

6.1 Preparations for real-time testing

To investigate the performance of the laboratory HSAPS, it is convenient to cycle the system based on the actual hydrogen storage size. A data set consisting of solar energy profiles for seven days was chosen. The sequence of the days in the solar profile was combined in the SIMULINK model to approach a relative seasonal behaviour during a week, in the forthcoming also denoted as the *test-week*. The laboratory HSAPS was configured as sketched in Figure 6.1 throughout the test-week, where the power supply and the electronic load emulated the lead-acid battery.

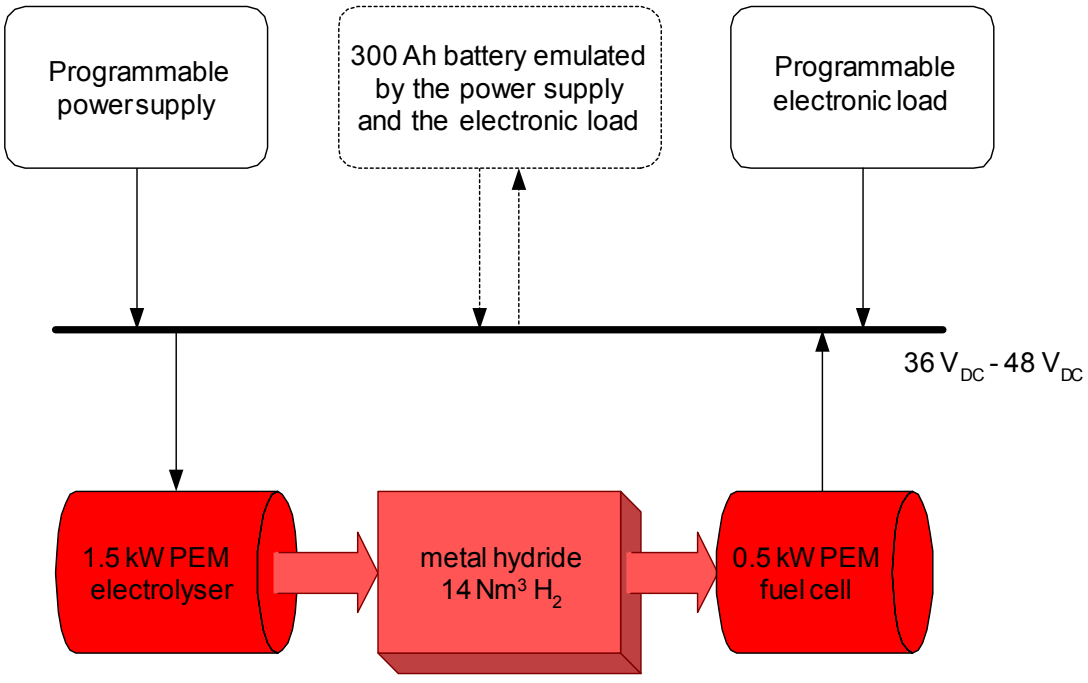

Figure 6.1 Schematic of the laboratory HSAPS used during the test-week.

6.1.1 Solar profile

The solar data was measured with a time resolution of 2 minutes at Kjeller during July and August 2000. The complete solar energy profile chosen for the week is shown in Figure 6.2.

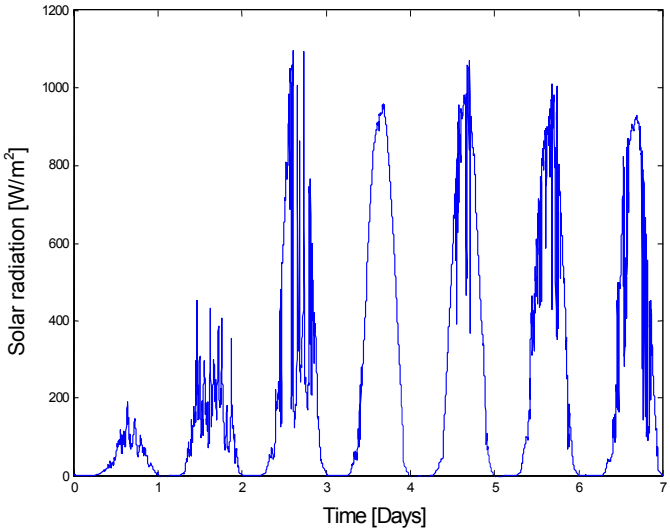

Figure 6.2 Solar energy profiles for seven different days combined for seasonal behaviour related to the laboratory hydrogen storage size. The measured data has a time resolution of 2 minutes and interpolated in order to update the laboratory HSAPS every minute. The data series start at 00:00 hours.

The two first days are representative for winter days with general low solar energy, while the third day is a typical varying cloudy day. The last four days represent summer days with good insolation, though last two days have some fluctuations. Anyhow, the fluctuations are interesting as a parameter that represents disturbances to the system. The measured solar data was used as input to the SIMULINK model where it was processed and interpolated, being able to update the laboratory HSAPS every minute.

6.1.2 Load profile

The load current profile had a quite regular behaviour representing a combination of both power- and energy demanding load. During the winter period, a constant base load was added to the second and third day. Figure 6.3 shows the load, as current requirement for the seven-day period.

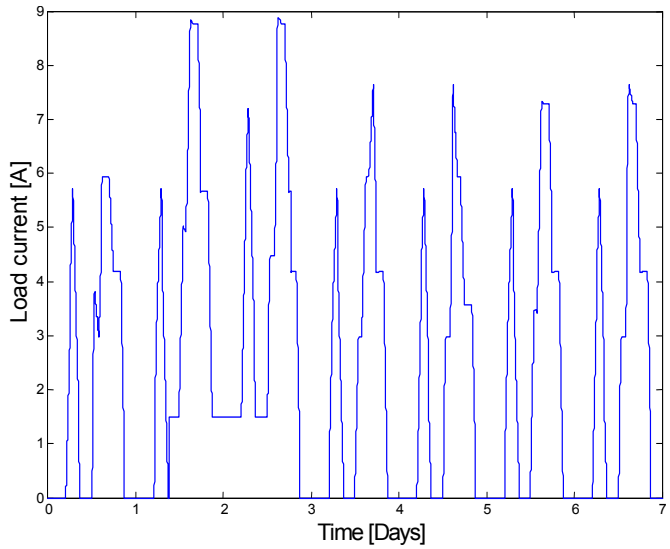

Figure 6.3 The load profile represented by the load current requirement, starting at 00:00 hours.

The chosen load current profile was used as the second dataset input to the SIMULINK model. The load is defined as a low voltage DC application with a special current requirement, which is able to work at "any" voltage levels responded from the HSAPS. A DC/DC converter is neither simulated nor installed between the HSAPS and the DC load.

6.1.3 The PV array and load power profiles

The power from the PV array through a maximum power point tracker (MPPT) and the power required by the load are shown in Figure 6.4 for the simulated system.

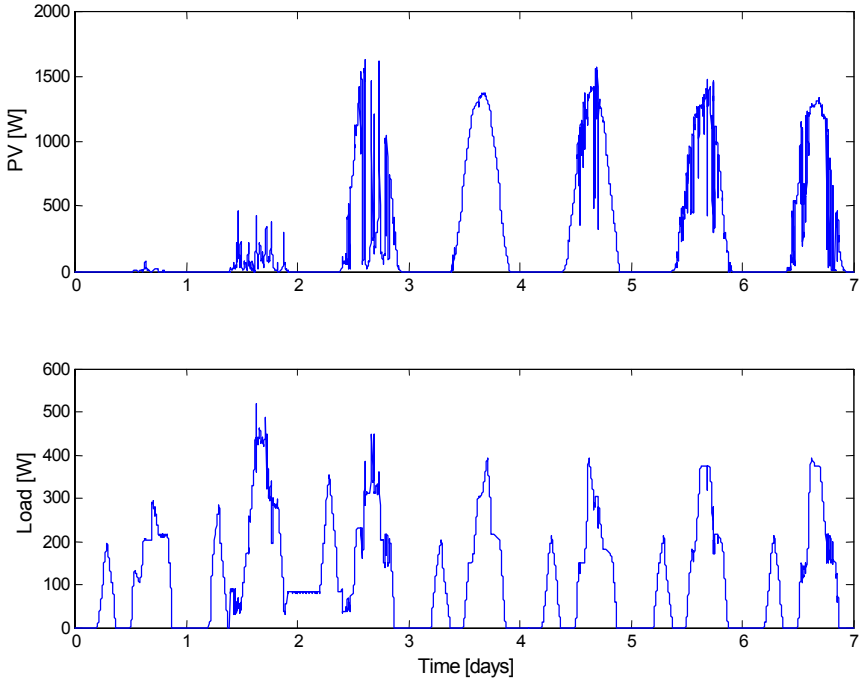

Figure 6.4 The simulated PV array- (above) and load power (below) resulting from the data sets used in this experiment.

The chosen PV array size has a peak power of 1.5 kW, which is about the nominal power input for the electrolyser. With the additional load power requirement in mind, the PV array should be scaled up to match parallel operation of the electrolyser and the load, but it was decided to ensure electrolyser operation within specifications because this was the first long-term experiment. Besides, optimal PV array size was not in focus in this work.

6.1.4 Emulation of a lead-acid battery in the laboratory HSAPS

A 36 $V_{nominal}$ 300 Ah battery was simulated as hardware (emulated) by the power supply and the electronic load. The simulated battery voltage and current used for battery emulation in the laboratory HSAPS are shown in Figure 6.5. The simulated battery discharging current profile was added to the simulated PV array's current profile comprising a dataset with current values used as input to the power supply. The simulated battery discharging/charging voltage was included in a voltage profile, which displayed the highest voltage available at any time either from the battery or from the PV panel. This voltage profile was used as input to the power supply. The simulated battery charging current was added to the load current, giving the dataset of current values fed to the electronic load.

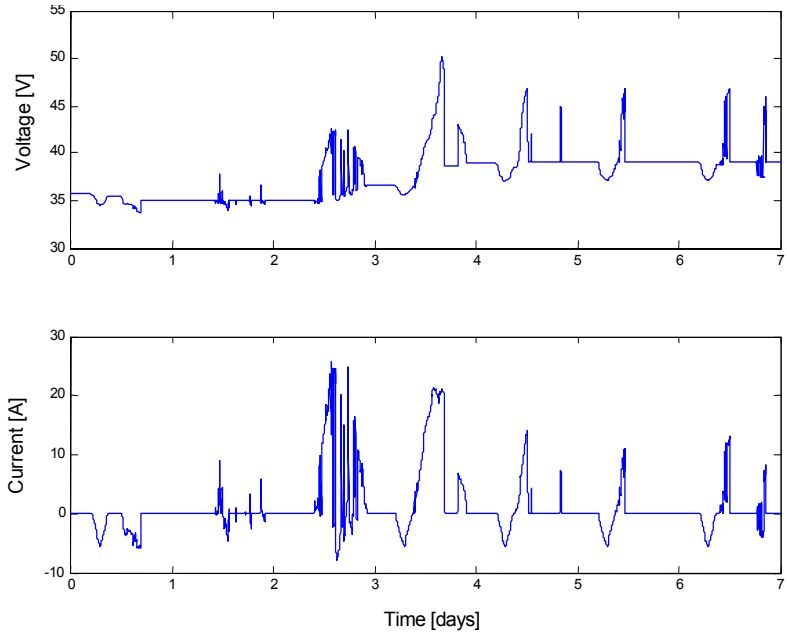

Figure 6.5 The simulated battery voltage (above) and current profiles (below) used as inputs to the laboratory HSAPS. Negative current discharges while positive current charges the battery.

6.1.5 Initial settings for the real-time / seasonal experiment

The initial hydrogen state-of-charge of the 14 m^3 (32 kWh) MH-storage was 52 %, while the initial battery state-of-charge for the 300 Ah (11 kWh) emulated lead-acid battery was set to 50 %. The Control Matrix with weather forecast (Section 5.6) was chosen as the HSAPS control strategy used for the energy management with these parameter settings:

$BAT_{ELY,ON}$ = 95 %, $BAT_{FC,ON}$ = 40 %, $Pred_{PV\text{-}Load}$ = 400 W, $H_{2,High}$ = 90 %, and $H_{2,Low}$ = 10 %.

6.1.6 Extraction of vital data for evaluation of the laboratory HSAPS

After the test-week was ended, the laboratory HSAPS performance was evaluated by extracting vital measured data from the DACS (Section 3.3) to data files (text files) with one-second time-resolution. The data files with the measured results extracted from the DACS for each of the components were:

- Electrolyser
  - Stack-voltage
  - Stack-current
  - Stack-temperature
  - Electrolyser pressure (after the purification unit)

- Fuel Cell
  - Stack-voltage
  - Stack-current
  - Stack-temperature
  - Fuel Cell pressure (in front of the fuel cell pressure regulator valve)

- Metal hydride unit
    - Hydride Temperature
    - Ambient temperature
    - Metal hydride pressure
    - Hydrogen flow in
    - Hydrogen flow out

- Power supply (PV array + battery charge/discharge emulation)
    - Voltage (MAX{PV voltage, battery charge/discharge voltage})
    - Current (PV current + battery discharge current)

- Electronic Load (Load + battery charge emulation)
    - Voltage (Voltage response from the laboratory HSAPS)
    - Current (Load current + battery charge current)

The data files were loaded into the MATLAB workspace for graphical representation, but also for further analysing with a dynamic data reader developed in SIMULINK, Figure 6.6. The experimental power profiles for all the components were easily generated in the SIMULINK data reader by multiplying the voltage and current profiles. Further, the energy distribution in the laboratory HSAPS was found by integration of the calculated power profiles. The total amount of hydrogen in and out of the MH-storage was found by integration of the measured hydrogen flow data. All these values are of course available directly from the LabView environment, but the ability to easily investigate the energy flows and the hydrogen consumed/produced within certain intervals is advantageous.

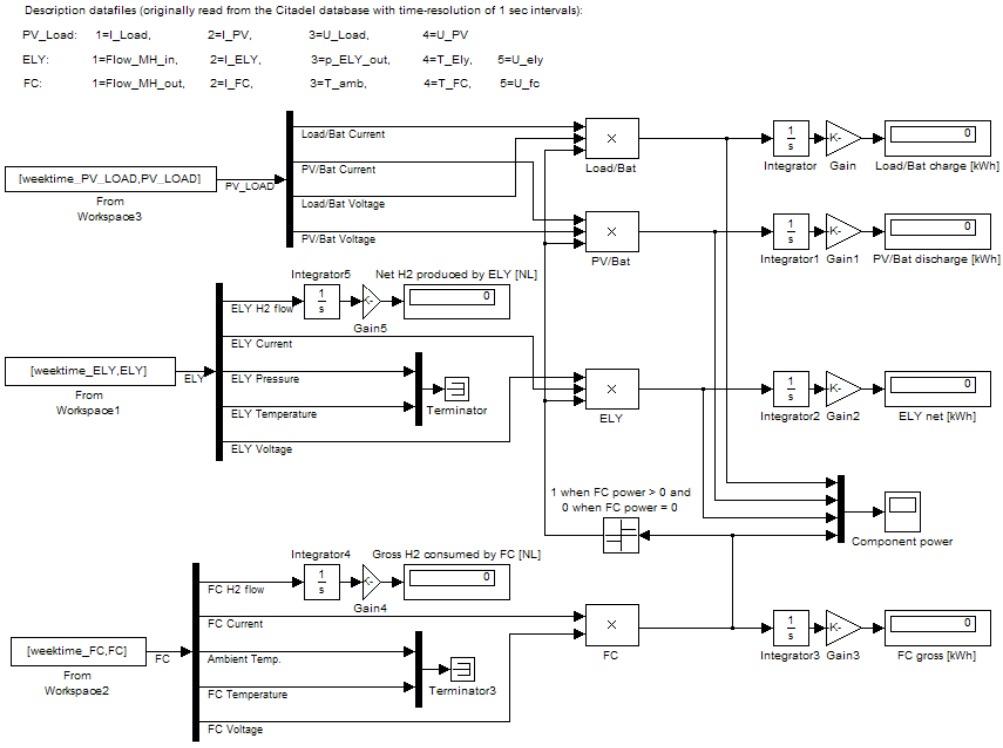

Figure 6.6 Experimental data reader developed in SIMULINK.

6.2 Results and discussion

6.2.1 Short and long-term energy storage state-of-charge: BAT_{SOC} and $H_{2,SOC}$

It is convenient to cycle the hydrogen storage to get practical operation experience and reliable energy efficiency results at least with some days at continuous operation. The emulated BAT_{SOC} and the experimental $H_{2,SOC}$ are shown in Figure 6.7.

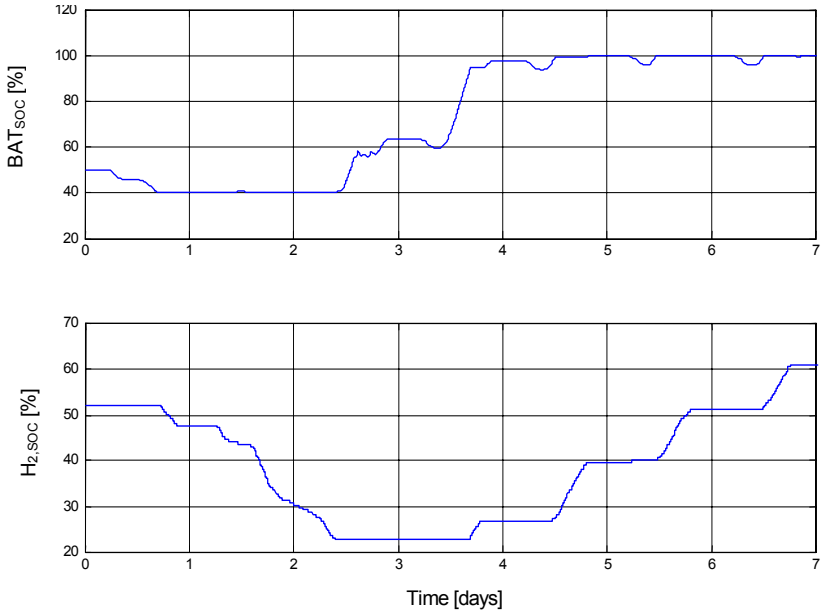

Figure 6.7 Emulated BAT_{SOC} (above) and $H_{2,SOC}$ (below).

The $H_{2,SOC}$ profile in Figure 6.7 is a half cycle instead of a full cycle, but the half cycle should be sufficient for reliable investigation of the hydrogen-loop roundtrip efficiency and performance. Thus, two main advantages are identified: Approach to a seasonal behaviour within few days where each of the days offers real-time operation of the laboratory HSAPS with measured weather data.

By observing Figure 6.7, with days as the unit time-scale, the hydrogen storage is discharged as soon as BAT_{SOC} descends to lower limit ($BAT_{FC,ON}$ = 40 %) and charged when the BAT_{SOC} reaches the higher limit ($BAT_{ELY,ON}$ = 95 %). Even though the Control Matrix uses four different parameters for energy management, it is obvious that the battery strongly influences the operation of the system. The additional parameters such as excess solar power in the system and weather forecast, operates within minutes/hours, thus, their influence are not clearly evident in Figure 6.7. However, from the discussion in Chapter 5 they have proven to reduce unnecessary start-ups and operation, though with focus on the electrolyser. The $H_{2,SOC}$ parameter only operates at the upper (90 %) and lower (10 %) boundary lines of the hydrogen storage. Because $H_{2,SOC}$ operated within 23 % and 61 %, this parameter stayed inactive for the whole test-week.

The hydrogen storage in the laboratory has a rather small capacity compared to a commercial storage system for operation throughout a whole year. While the emulated battery capacity is reasonable for a commercial system within this power range, the energy capacity in the hydrogen storage is only about three times larger than the energy capacity of the battery. Simulations indicate that the energy capacity

in the hydrogen storage would be about twenty times larger than the battery's energy capacity in a commercial system (Appendix F).

6.2.2 Input and output power profiles in the HSAPS during the test-week

The measured power profiles from the power supply and the electronic load are shown in Figure 6.8. The power supply emulates the PV array in addition to the battery discharging dynamics, while the electronic load emulates the load profile in addition to the battery charging dynamics. Figure 6.8 is comparable to the simulated results for the PV array, the load profile and the battery in Figure 6.4 and Figure 6.5.

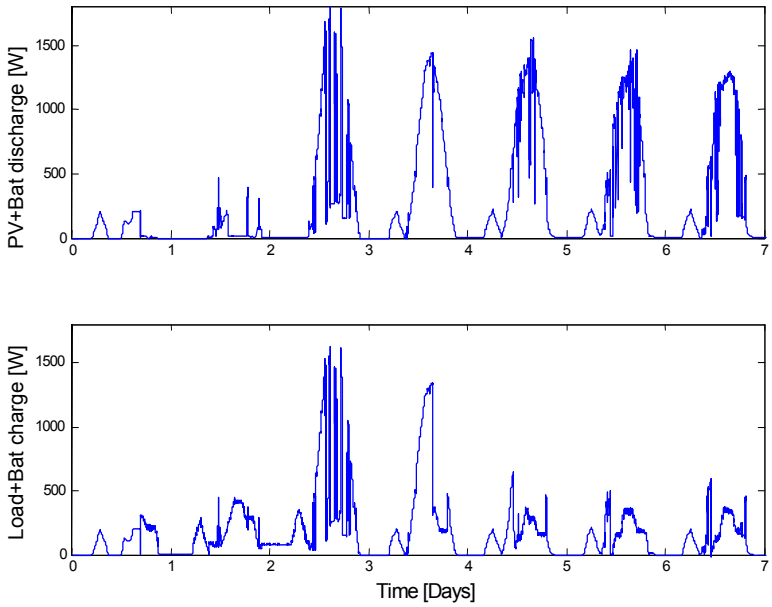

Figure 6.8 Power measured out of the power supply (PV array and battery discharge emulation) (above) and power measured consumed by the electronic load (Load and battery charge emulation) (below).

As expected, the load voltage was found to vary between 35 V and 50 V, where the lowest voltage is due to battery discharge and the highest voltage is the PV array voltage. Advantageous cooperation possibilities with electrolyser/battery charging and fuel cell/battery charging operations with a 42 V lead-acid battery were discussed in Section 3.2.7. Another benefit with an increase in battery voltage to 42 V is that the voltage range from the HSAPS sensed by the load would be narrower. But, the voltage range would still be quite wide, even for low voltage DC components, thus a commercial system should at least have some power conditioning between the system and the load. In this context, it should be mentioned that the automobile industry has chosen 42 V batteries as a standard.

6.2.3 Fuel cell and metal hydride

Figure 6.9 shows the fuel cell and MH-storage behaviours that were measured during the test-week, lasting from about 0.7 day to 2.5 day. Table 6.1 shows the main fuel cell results that are to be discussed in this section.

It can be seen from Figure 6.9 that $H_{2,SOC}$ decreases from initially 52 % down to about 23 % during the three first days with very little or no solar insolation at all, characterised as the "winter period". The total amount of hydrogen discharged amounts to 3288 NL (10.8 kWh, HHV) while the total amount of electric energy

delivered by the fuel cell is 5.2 kWh, thus a specific hydrogen consumption of 640 NL per kWh electric energy available for work. Furthermore, the fuel cell generated 3.6 kWh heat and the fuel cell control system required 1.4 kWh. As elaborated in Section 3.2.5, H_2 purging requires about 4 NL H_2/min for about 3 seconds with two minutes intervals, no matter how much power is drawn from the stack. About 178 NL (5 %) of the total amount of hydrogen consumed by the fuel cell was lost due to hydrogen purging, equal to an energy loss of approximately 0.6 kWh (HHV). The total energy distribution within the fuel cell is shown in Figure 6.10 based on hydrogen higher heating value.

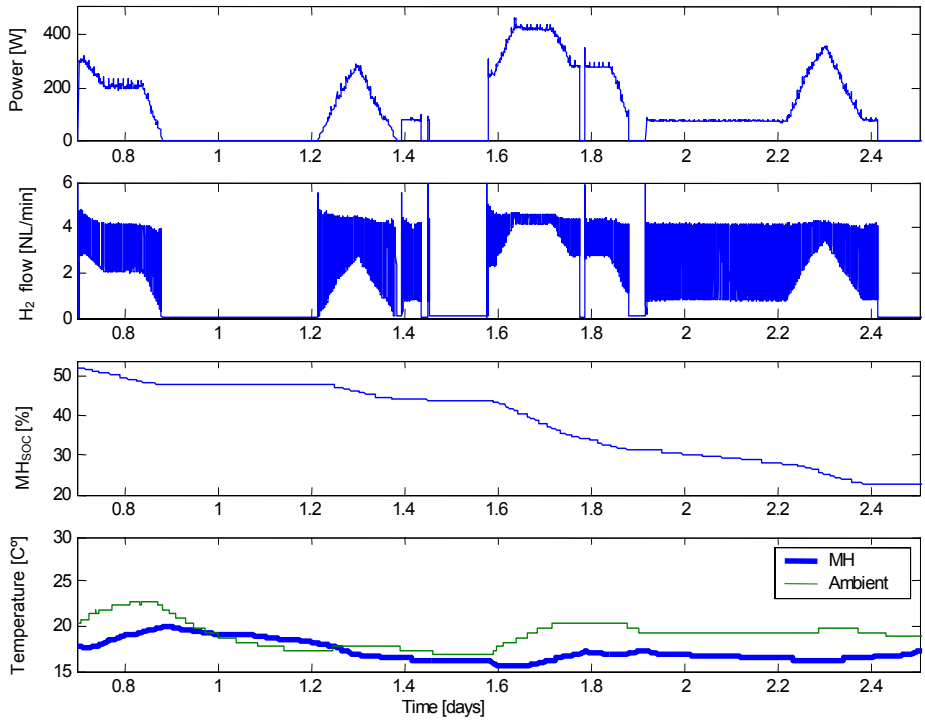

Figure 6.9 Fuel cell power and MH-storage characteristics. The endothermic hydrogen desorption consumes heat in the metal hydride. But there is no severe decrease in the hydride temperature since some of the heat produced by the fuel cell is supplied to the MH-storage through the air driven by the fuel cell cooling fans.

Table 6.1 Fuel cell performance data during the week-test

Fuel cell energy available for work [kWh]	5.2
Energy required by controller [kWh]	1.4
Fuel cell operation time [hr]	28.0
Fuel cell on/off [-]	7
Fuel cell average operation time [hr]	4.0
Fuel cell average power [W]	184.7
Gross Hydrogen consumed [NL]	3288
Hydrogen loss due to purging [NL]	178

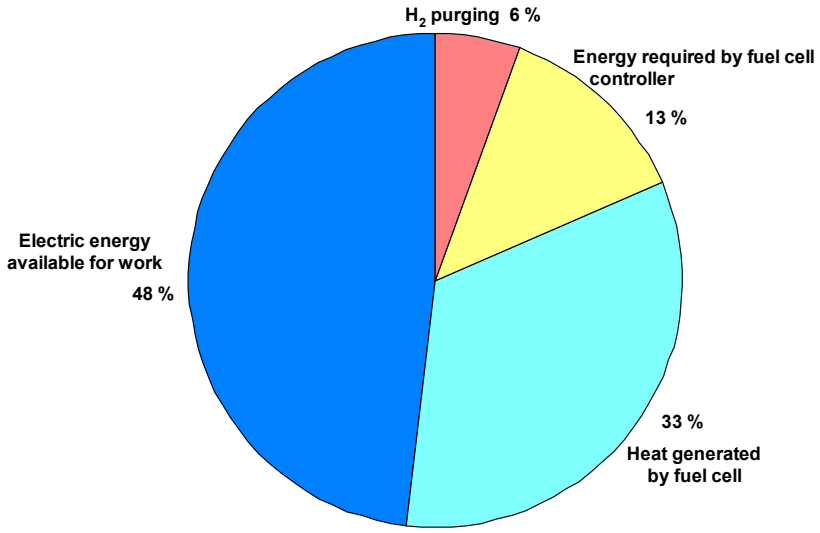

Figure 6.10 Energy distributions in the fuel cell during the test-week based on higher heating value (HHV) for H_2.

The fuel cell has four short start-ups during the second day. This occurs because the PV array is able to cover the load 100 %. Independently of the duration of these periods, the HSAPS energy management decides to shut off the fuel cell whenever there is enough direct solar power that can cover the load. In order to minimise stress on the electrodes, it is favourable to reduce number of fuel cell start-ups. To reduce the number of fuel cell *shutdowns* for short periods of time, a timer could be adjusted to ensure that the fuel cell is idling for a preset time after it normally would have been shut off. Idle means simply to disconnect the fuel cell electrically from the system, hydrogen and power to the fuel cell control system are still supplied. A suitable timer setting in this case would be an hour, or by a load prediction routine if available. Load prediction would be easy to interpret, as the load profile is quite regular. The number of full fuel cell shutdowns within the test-week could have been reduced from seven to three with the fuel cell *shutdown* timer implemented.

Due to the insufficient thermal properties in the MH-storage during desorption (Section 3.2.6), it was decided to set up a cardboard channel between the fuel cell and the MH-storage enabling the fuel cell to heat the MH-storage with heated air. This is a simple method for heat transfer control, but the fuel cell is able to balance or even increase the hydride temperature. The metal hydride temperature profile in Figure 6.9 truly shows this behaviour, when the fuel cell operates at approximately 200 W it clearly increases the hydride temperature. The average fuel cell power was estimated to 184.7 W (Table 6.1), thus enabling enough heat supply to the MH-storage. The measured ambient temperature in the laboratory ventilation compartment containing the HSAPS was also clearly influenced by the fuel cell operation.

The lowest depth of metal hydride discharge (23 %) was above the $H_{2,Low}$ limit of 10 %. The hydrogen flow rate required by the fuel cell in this experiment was low (maximum 4 NL/min) compared to the critical flow rates discussed in Section 3.2.6. The average fuel cell operation time shown in Table 6.1 is of lesser credibility as a fuel cell OFF timer could easily increase the average operation time to 9-14 hours.

Normally, an air-cooled fuel cell will not be able to supply enough heat to a metal hydride. This is due to the fact that a metal hydride unit in a real-world system will be quite large compared to the fuel cell. These parameters depend of course on the system configuration and type of load. For future commercial HSAPS with metal hydride units it is generally recommended to use a liquid heat exchange system for better heat exchange control, thus better control of the true $H_{2,SOC}$ in the metal hydride.

There were no fuel cell start-up failures during the test-week. Furthermore, no loss of load due to unexpected failures was registered during the 28 hours of fuel cell operation. Anyhow, at each fuel cell start-up there was expected five minutes loss of load due to the two minutes mandatory fuel cell start-up time (Section 3.2.5) in addition to three more minutes programmed into the LabView fuel cell start-up subroutine. The tree additional minutes was implemented to ensure full humidification of the fuel cell membranes. The resulting five minutes loss of load for a fuel cell start-up is shown in Figure 6.11.

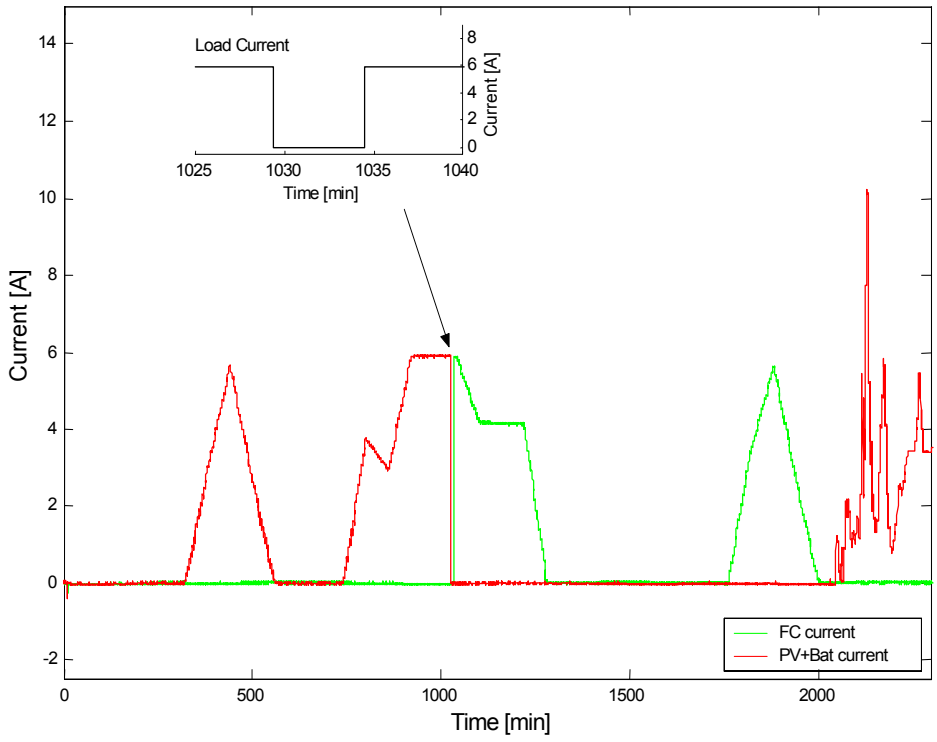

Figure 6.11 Loss of load due to the five minutes of fuel cell start-up time. The load must be covered with the battery during this period, but implementation of this feature was not prioritised in this experiment as the power supply and the electronic load emulated the battery operation.

The five minutes loss of load at fuel cell start-up could easily be implemented into the SIMULINK model ensuring battery emulation during these five minutes. However, the battery operation was not in focus in this study, thus, it was decided to disregard these five minutes with loss of load, which in this experiment would be nothing else than supplying electric power directly from the power supply to the electronic load. Besides, the five minutes fuel cell start-up time had no practical influence on the overall system results.

6.2.4 Electrolyser and metal hydride

The electrolyser and MH-storage performance within the test-week are presented in Figure 6.12. Because the electrolyser only operated for the last part of the week, only the last 3.5 days are shown. The electrolyser power had some fluctuations because of the fluctuations in the solar radiation profile shown in Figure 6.2, except for the fourth day in the test-week. Still, $H_{2,SOC}$ increased steadily each day and eventually stopped at 62 %. Then the final $H_{2,SOC}$ exceeded the initial $H_{2,SOC}$ at 52 % (Figure 6.9) with about 10 %, which ensured a reasonable half cycling of the hydrogen storage. The total hydrogen-loop efficiency will be examined in Section 6.2.5.

The hydride temperature shown in Figure 6.12 never reach any equilibrium due to the fact that the electrolyser is driven by a PV array and thus its operation time is limited by the natural daily solar behaviour. Maximum hydride temperature was found to be about 30 °C. Because no severe hydride temperatures were reached during the hydrogen charging periods, there were nor any high pressure build-ups in the MH-storage. The metal hydride pressure can be seen to start at 3 bars where it increases to about 6 – 7 bars during hydrogen charging and settles back to about 4 – 5 bars in equilibrium during the night. As noticed for the fuel cell, the ambient temperature is also influenced by the electrolyser operation, but can be seen to be kept within 19 – 23 °C. As long as the MH-storage is operated within a storage range between about 10 – 90 %, the air heat-convective MH-storage and the electrolyser powered by a PV array have proven to work satisfactory together at ambient temperature of about 20 °C.

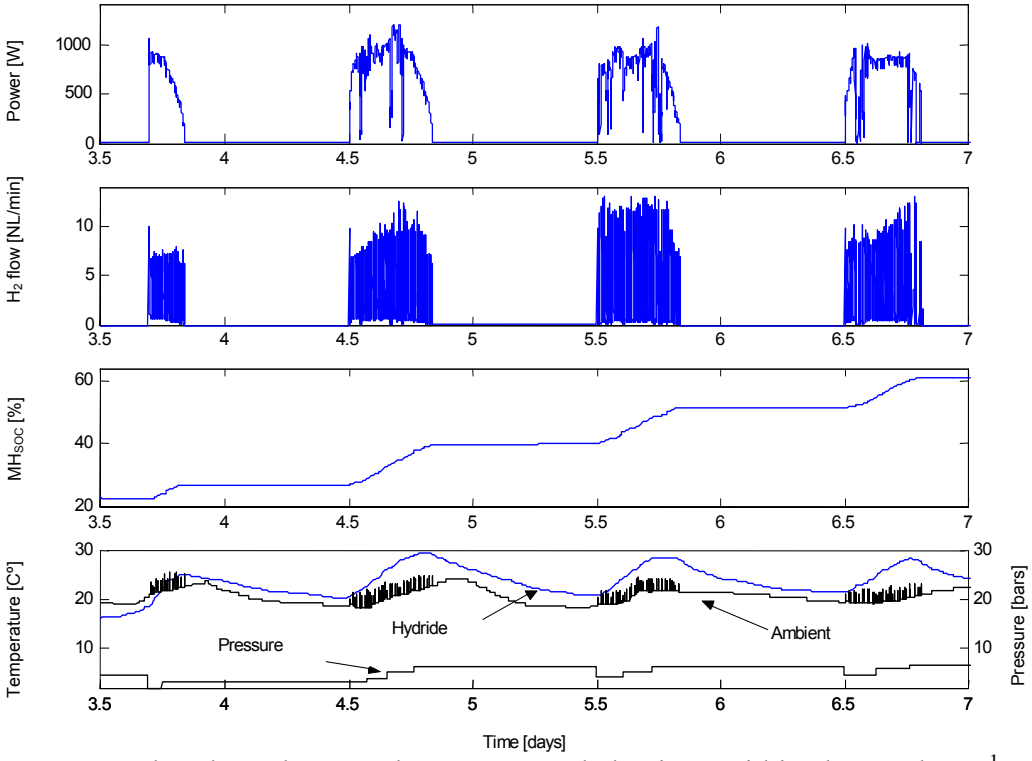

Figure 6.12 The electrolyser and MH-storage behaviour within the week-test[1]. The hydrogen flow rate from the electrolyser can be seen to be highly pulsating as the electrolyser maintains its internal pressure at about 16 bars.

[1] The heating device controlled by a thermostat for the catalytic oxygen remover when electrolyser is operating influences the measured ambient temperature.

Figure 6.13 shows a magnification of the measured hydrogen pulses from the electrolyser and the estimated hydrogen production during a cloudy period. The measured hydrogen flow-pulses of 10 – 12 NL/min at high solar insolation are reduced to minimum 6 NL/min at low solar insolation. Due to the specific valve characteristic and the criteria to keep the electrolyser pressure constant at 16 bars, further reduction in current results in longer time-intervals between the hydrogen flow-pulses from the electrolyser.

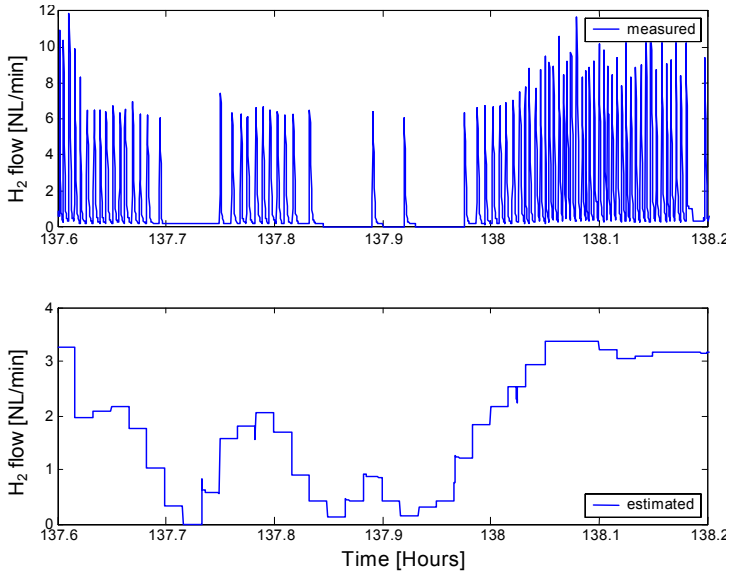

Figure 6.13 Measured and estimated hydrogen flow rate into the MH-storage.

The electrolyser experienced some intermediate shutdowns during the seventh (last) day of the test-week, shown in Figure 6.14. The electrolyser current profile in Figure 6.14 reveals that there were some fluctuations in the beginning of the day where the electrolyser current was barely above zero, just about to shut down the electrolyser if the balance between the PV array current and the load current happened to be negative. But in the last part of solar radiation period the negative power balance between the PV array and the load (the $I_{PV\text{-}Load}$ parameter from Section 5.6) caused the Control Matrix to shut off the electrolyser four times in a period of 1½ hour, though reminding of the small PV array chosen in this test.

The estimated and measured hydrogen flow rate during the four shutdowns the seventh day is shown in Figure 6.15. The accumulated difference between the estimated and measured hydrogen flow rate represents the hydrogen loss due to the pressure release (hydrogen and oxygen venting) at electrolyser shutdown. The short abrupt in the electrolyser operation at 118.7 hours and 120.0 hours are shorter than three minutes, thus, the electrolyser did not vent out the product gasses. But, the two electrolyser shutdowns at 119.2 hours and 119.6 hours both lasted for about 15 minutes and caused the electrolyser to release pressure. From Figure 6.15 it can be seen that the hydrogen loss accumulates during electrolyser start-up when the internal pressure builds up to 15 bars, no hydrogen is measured into the MH-storage and a difference occurs between the measured and the estimated hydrogen flow rate. The hydrogen loss is a fact when the accumulated difference doesn't return to zero during shutdown, meaning that the remaining hydrogen inside the electrolyser has been vented out of the system. The hydrogen loss amounted to 9 NL for each full

electrolyser shutdown. An appropriate control strategy (Chapter 5) would result in about 150 electrolyser ON/OFF-switching operations per year, giving a hydrogen venting loss of 150 · 9 NL ~ 1350 NL. This is though a relative small loss, it would be fuel-supply for a fuel cell running at 350 W for only 6 hours per year. If a cheap low pressure steel container was installed to collect the vented hydrogen, it could on the other side be valued as a backup fuel supply for emergency.

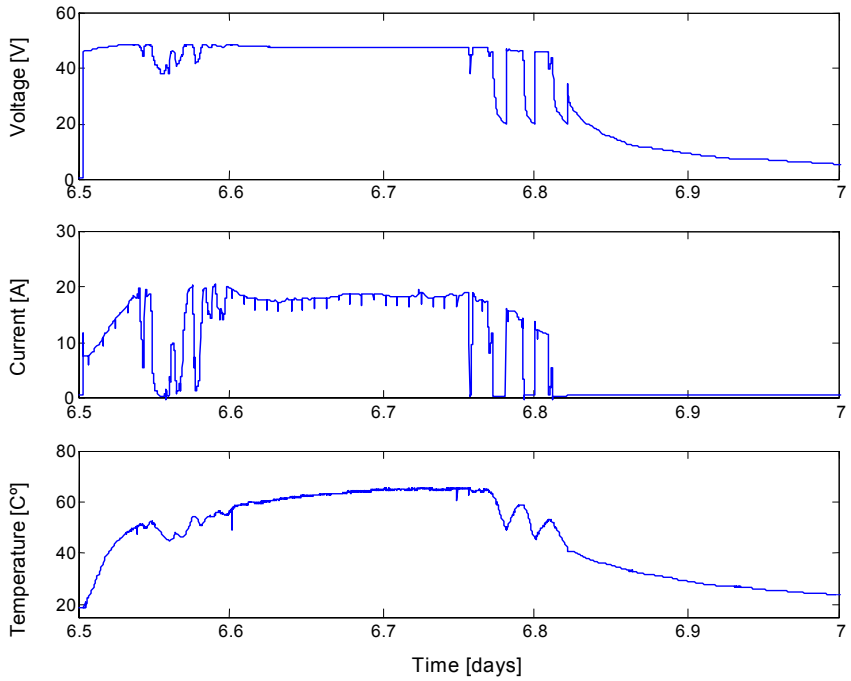

Figure 6.14 Measured electrolyser stack voltage, stack current and stack temperature during the last day in the test-week containing highly fluctuating solar insolation.

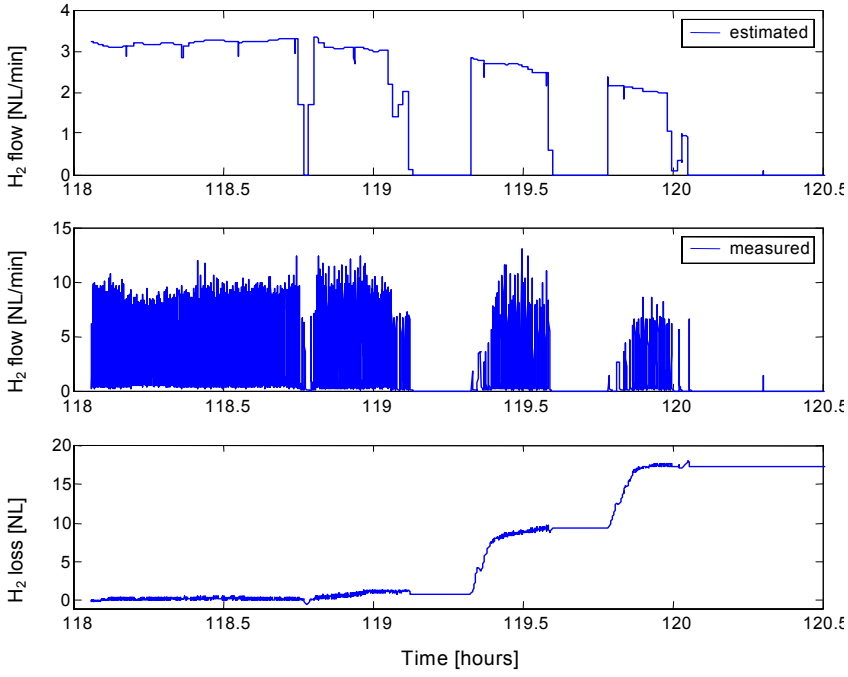

Figure 6.15 Measured hydrogen flow rate to the MH-storage and the estimated hydrogen flow rate based on the Faraday efficiency and the measured electrolyser stack-current. The accumulated difference represents the hydrogen loss during electrolyser shutdown.

Electrolyser performance data for the test-week are given in Table 6.2. From Figure 6.15, the electrolyser should have longer standby operation after the initial shutdown signal. The electrolyser standby mode should at least be an hour, and not three minutes as used in this experiment. Then the total electrolyser ON/OFF-switching operations would be reduced to four start-ups.

The laboratory electrolyser control system uses energy from the grid, but its energy consumption has been measured and added to the total electrolyser energy balance in order to reflect a real-world system. The specific energy consumption for the electrolyser stack was 4.5 kWh/m^3. However, when all losses included, the specific energy consumption for the electrolyser was 5.3 kWh/m^3. There is an additional specific energy consumption of 0.4 kWh/m^3 required by the hydrogen purification unit, giving a total of 5.7 kWh/m^3. The specific energy consumption for regeneration of the hydrogen purification unit is elaborated in Chapter 7. The energy distribution within the electrolyser at the end of the test-week based on the results from Table 6.2 is shown in Figure 6.16.

Table 6.2 Electrolyser performance data during the test-week

Electrolyser gross energy [kWh]	22.3
Electrolyser stack energy (net) [kWh]	19.4
Energy required by controller [kWh]	2.1
Energy required by purification unit [kWh]	1.7
Energy loss in cables/switches [kWh]	0.8
Heat generated in stack [kWh]	7.1
Net Hydrogen to storage [NL]	4237
Gross Hydrogen produced [NL]	4291
Electrolyser operation time [hr]	26.3
Electrolyser on/off [-]	8
Electrolyser average operation time [hr]	3.3
Electrolyser stack average power [W]	738.4

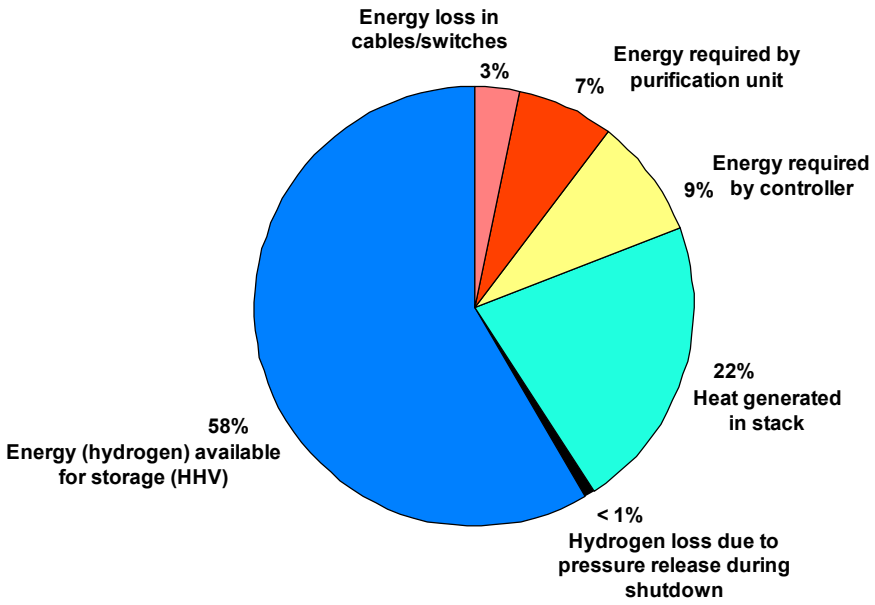

Figure 6.16 The energy distribution for the electrolyser within the test-week based higher heating value (HHV) for H_2.

6.2.5 The hydrogen-loop performance

The hydrogen-loop energy efficiency was evaluated with the specific hydrogen consumption found for the fuel cell and the specific energy input found for the electrolyser. The specific hydrogen consumption for the fuel cell is converted to electric energy available per Nm^3 hydrogen fed to the fuel cell, and in the forthcoming mentioned as the *specific energy output*. By using the specific energy input for the electrolyser and the specific energy output for the fuel cell, there is no confusion whether the hydrogen higher- or lower heating value is used, as the calculated hydrogen-loop efficiency is based on the same unit volume hydrogen produced and consumed. Furthermore, the hydrogen-loop energy efficiency solely based on the electrolyser and fuel cell stack was compared with the real operational energy efficiency. Hydrogen-loop efficiency calculated on per stack basis includes only the energy losses in the electrolyser and the fuel cell *stack*, which in the forthcoming will be denoted as the hydrogen-loop *stack-only* efficiency. Calculation of the real operational hydrogen-loop energy efficiency includes energy utilised by the electrolyser and the fuel cell control system in addition to the energy needed for hydrogen purification and the energy losses in the electrolyser and fuel cell stack. This will in the forthcoming be denoted as the hydrogen-loop *real-operational* efficiency.

For convenience, the specific energy input for the electrolyser and the specific energy output for the fuel cell are given in Table 6.3. Values for calculation of both the stack-only and real-operational hydrogen-loop efficiency are given. The fuel cell specific energy output for calculation of the stack-only efficiency is found by adding the measured energy required by the fuel cell controller to the net electrical energy available from the stack, in addition to the assumption that the purged hydrogen was collected and reused or that the stack was operated dead-ended. Compression work would be required to increase the purged hydrogen up to at least 2 bars if the purged hydrogen was to be reused in the fuel cell. The other values in Table 6.3 were found in Section 6.2.3 and Section 6.2.4.

Table 6.3 The specific energy input for the electrolyser and the specific energy output for the fuel cell used for calculation of the stack-only and the real-operational hydrogen-loop energy efficiency during the test-week

Type of hydrogen-loop energy efficiency	Specific energy output for FC	Specific energy input for ELY	hydrogen-loop energy efficiency
stack-only	2.1 $kWh_{el,\ out}/m^3\ H_2$	4.5 $kWh_{el,\ in}/m^3\ H_2$	**46.7 %**
real-operational	1.6 $kWh_{el,\ out}/m^3\ H_2$	5.7 $kWh_{el,\ in}/m^3\ H_2$	**28.1 %**

FC = fuel cell
ELY = electrolyser

The difference between the stack-only and the real-operational hydrogen-loop efficiency is quite large. It is important to compare the stack-only and the real-operational efficiencies to evaluate the potential of the hydrogen subsystem. The real-operational hydrogen-loop efficiency can be further increased with better energy efficient solutions regarding the components control systems, as they are not optimized for being a real stand-alone component. Furthermore, the hydrogen-loop efficiency will increase with larger systems as the energy required by the components control system do not increase as much as the energy converted through the stacks. Real-operational energy efficiencies for the hydrogen-loop with and without hydrogen

treatment, and fuel cell/electrolyser power at low or nominal level are compared to the results from the test-week in order to evaluate the potential of the laboratory HSAPS. Estimated hydrogen-loop energy efficiencies for these scenarios in addition to result for a similar system from the literature are given in Table 6.4.

Table 6.4 Real-operational hydrogen-loop efficiencies for the laboratory HSAPS with different system configuration and operation scenarios compared to the test-week setup

Scenario #	System configuration compared to laboratory HSAPS	FC and ELY power level compared to test-week	real-operational efficiency
1	*No H_2 purification or compression work (using low pressure H_2 tank)*	*Same as during test-week*	**30.2 %**
2	*Same as during test-week*	*At nominal power level*	**36.3 %**
3	*No H_2 purification or compression work (using low pressure H_2 tank)*	*At nominal power level*	**39.4 %**
Ref. [1]	*Same as during test-week*	*Approximately at nominal power level*	**25 %**

FC = fuel cell
ELY = electrolyser
MH = metal hydride

The real-operational specific electrolyser energy input could be reduced from 5.7 kWh/m^3 to 5.3 kWh/m^3 if there were no need for high purity hydrogen or compression work, resulting in a hydrogen-loop efficiency of 30.2 % (Scenario #1). Table 6.1 and Table 6.2 reveal that the average fuel cell power is 36 % of the nominal power while the average electrolyser power is about half the nominal level. The real-operational hydrogen-loop efficiency would be 36.3 % if the electrolyser and the fuel cell were to be operated at their respective nominal levels of 1.5 kW and 0.5 kW (Scenario #2). The benefit of operating the small-scale electrolyser and fuel cell at nominal power level will be discussed in detail in Section 6.2.6 and 6.2.7. Furthermore, the real-operational hydrogen-loop efficiency in this case would be 39.4 % if a low pressure steel vessel could be used, requiring no additional compression work and the hydrogen purity could be relaxed (Scenario #3). The oxygen has to be removed from the produced hydrogen, but the required energy is small compared to the energy used for regeneration of the desiccant that absorbs water from the hydrogen. Kauranen et al. [1] found the hydrogen-loop real-operational efficiency to be 25 % for a similar small-scale system consisting of an 800 W alkaline electrolyser and a 500 W phosphoric acid fuel cell, where the preheating of stack and high hydrogen flow-by during purging caused a high energy loss.

6.2.6 Minimum fuel cell power output

It is beneficial to achieve a high average conversion power in order to maximize the components energy efficiency. The electrolyser operation can be optimized and tuned in the high-level control strategy with time and power level settings in addition to possible changes of the PV array size. But the fuel cell operation is less direct controllable in the high-level control strategy since the fuel cell power level is dependent on the load. A possible way to control the fuel cell power (from the high-

level control strategy) is to let the fuel cell charge the battery at nominal power level for maximum fuel cell energy efficiency. Figure 6.17 shows the minimum fuel cell power level, of about 180 W, for which it is more energy efficient for the hydrogen-loop to let the fuel cell supply only the load directly. If the fuel cell power level is lower than 180 W, it is more energy efficient for the hydrogen-loop to allow the fuel cell to operate at higher power levels supplying the load *and* charge the lead-acid battery (Appendix G). The hydrogen-loop real-operational energy efficiency multiplied by the lead-acid battery efficiency of 80 % is based on the specific electrolyser energy input of 5.3 kWh/m^3. The resulting minimum fuel cell power level of about 180 W found in Figure 6.17 is independent of the actual specific electrolyser energy input, as the curves would simply be shifted upwards or downwards in parallel.

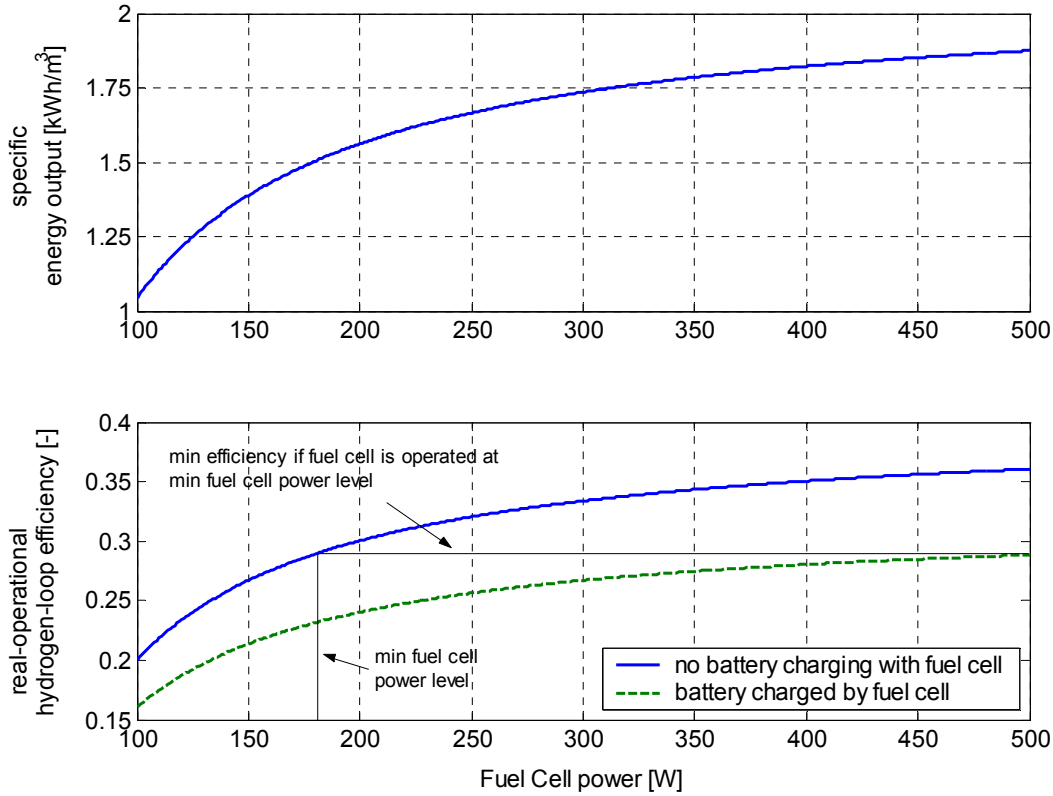

Figure 6.17 Specific energy output for the 500 W fuel cell and the hydrogen-loop efficiency revealing the minimum fuel cell stack power of 180 W beneath where it is more energy efficient for the hydrogen-loop to let the fuel cell operate at higher power rates and charge the battery *and* supply the load.

6.2.7 Minimum electrolyser power input

The minimum power level for the PEM electrolyser has also been identified and is presented in Figure 6.18. If the power from the PV array into the electrolyser is 240 W or less, meaning specific electrolyser energy input of 6.5 kWh/m^3 or higher, the hydrogen-loop energy efficiency could be higher if the electrolyser were operated at nominal power (1.5 kW) with the aid of the battery. On the other hand, unnecessary battery discharge, depending on the depth of discharge, may shorten the battery lifetime. The electrolyser should be electrically disconnected from the common bus bar when the PV array power input is lower than 240 W and reside in a standby modus. E.g. if the electrolyser was set in standby modus and the standby timer

(Section 6.2.4) was set to one hour before full shutdown and the PV array excess power was about 240 W during that hour, the amount of energy consumed by the electrolyser controller would be 0.08 kWh (80 W · 1 hr) while the energy supplied to the battery would be 0.16 kWh (160 W · 1 hr). This would result in a total energy storage (battery and hydrogen) efficiency of 0.16 · 0.8 / 0.24 · 100 % = 53 %, which is larger than the maximum energy efficiency available for the hydrogen-loop. The reason why this is not applicable for the fuel cell/battery operation is that the battery is not allowed to be further discharged, because low BAT_{SOC} indicates fuel cell start-up. The low load power requirement can also prevail for longer periods, while low excess PV array power for longer periods simply indicates that the electrolyser should be switched OFF.

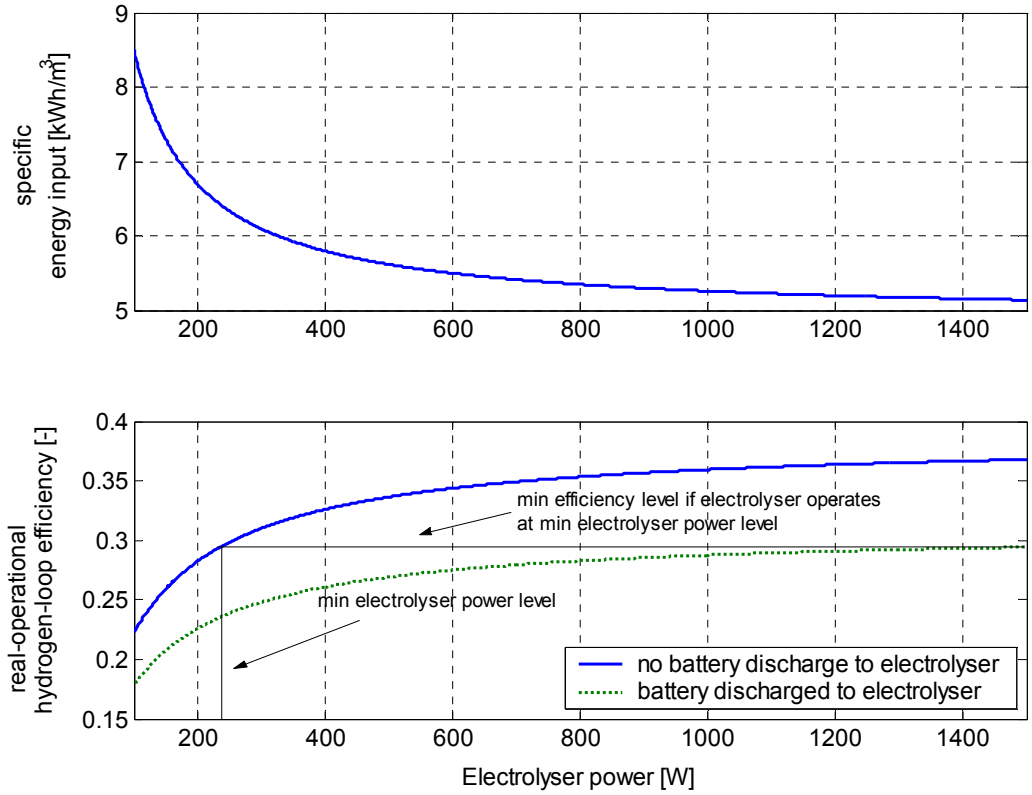

Figure 6.18 Electrolyser specific energy input and the minimum electrolyser power beneath where it is more energy efficient to operate the electrolyser with the aid from the battery.

Anyhow, the average power input to the electrolyser was 738 W + 80 W = 818 W, which is far higher than the critical minimum electrolyser input of 240 W. From Figure 6.18, there is not so much to gain in the real-operational hydrogen-loop energy efficiency if the average electrolyser power input was raised to 1500 W as it would if the fuel cell average power output was raised to 500 W (Figure 6.17). Besides, with the system configuration used in this work, it would not be possible to discharge the battery to the electrolyser in a direct electric connection because the electrolyser voltage of 48 V is too high to be operated by a 36 V battery.

6.3 Summary; Energy distribution within the laboratory HSAPS

The energy flow and energy distribution within the laboratory HSAPS is summarised in Figure 6.19 and Table 6.5. A total amount of 39.7 kWh was available from the PV array/MPPT. Some 1.2 kWh solar energy was unused (excess energy not available for either battery charging or hydrogen production), thus the PV array had a conversion efficiency of [38.5 / 39.7] ·100 % = 97 % relative to the possible energy output.

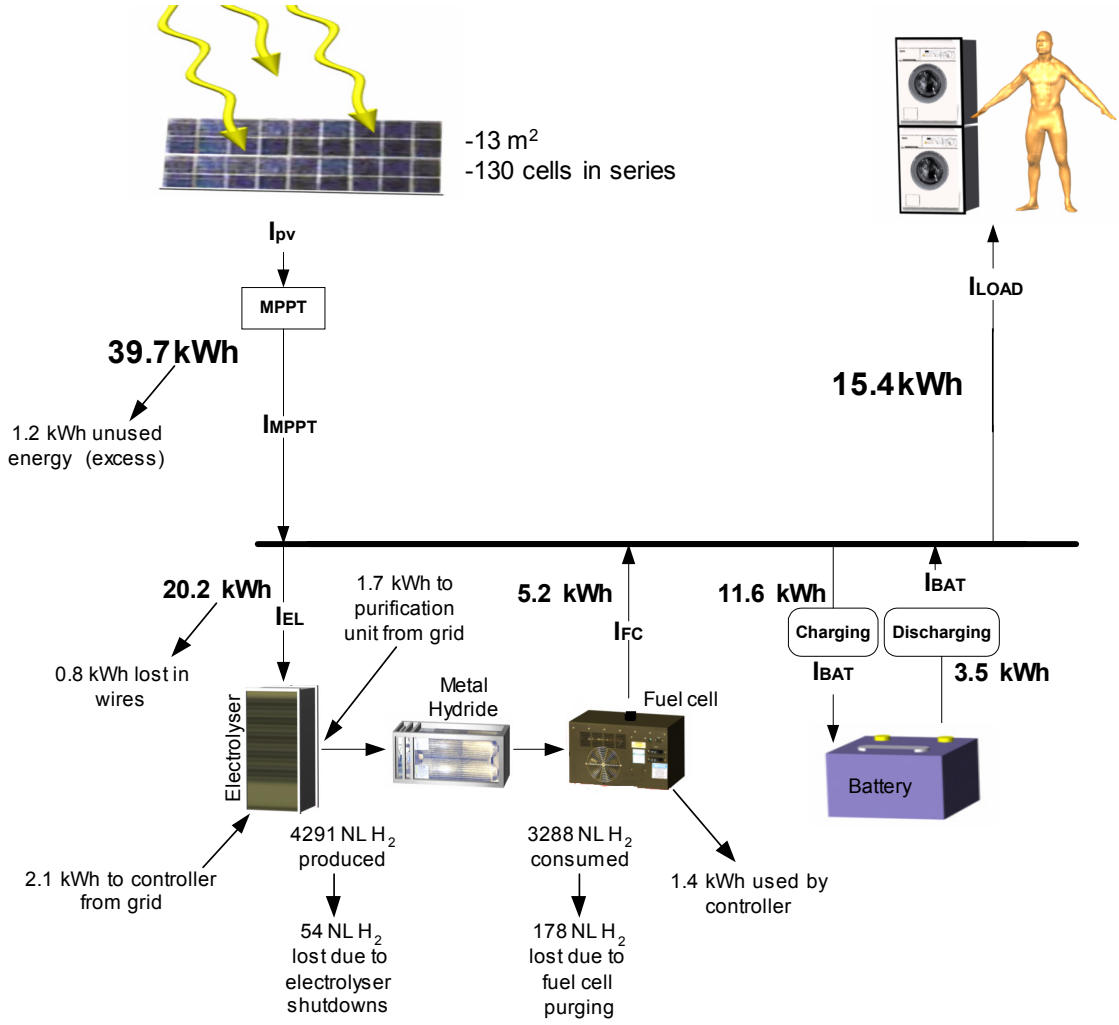

Figure 6.19 Electric energy distribution within the total laboratory HSAPS. (Figure made by Bård A. *Melk Design*)

20.2 kWh from the power supply was directed to the electrolyser where 0.8 kWh was lost due to voltage drop through the wires and switches. The additional energy required by the electrolyser controller (2.1 kWh) and the energy required by the hydrogen purification unit (1.7 kWh) was supplied from the grid. The electrolyser stack-only energy efficiency was 73.2 % with respect to HHV (60.9 % LHV), which agrees with result in Section 3.3.1. The real-operational energy efficiency was 59.6 % with respect to HHV (49.2 % LHV).

5.2 kWh was supplied from the fuel cell directly to the load (the fuel cell was not charging the battery in this experiment). The fuel cell stack solely supplied the

1.4 kWh electric energy required by the fuel cell controller. The fuel cell stack-only energy efficiency was 60.6 % with respect to HHV (72.5 % LHV) and the real-operational energy efficiency was 47.7 % with respect to HHV (57.4 % LHV), which agrees with result in Section 3.3.2.

Table 6.5 Electric energy distribution within the laboratory HSAPS during the test-week

Component	Gross Energy [kWh]	Energy loss [kWh]	Net Energy [kWh]
PV array + MPPT	+ 39.7	1.2 [(1)]	+ 38.5
ELY stack	- 20.2	0.8 [(2)]	- 19.4
FC stack	+ 6.6	negligible	+ 6.6
FC control system[(3)]	- 1.4	negligible	- 1.4
BAT charging	- 11.6	negligible	- 11.6
BAT discharging	+ 3.5	negligible	+ 3.5
Load	- 15.4	incl. in total load	- 15.4
Energy balance	**+ 1.2**	**-**	**+ 0.8**
ELY control system[(4)]	2.1	negligible	2.1
H_2 purification system[(4)]	1.7	negligible	1.7

ELY = electrolyser, FC = fuel cell, BAT = battery
[(1)]Excess electric energy not available for either battery charging or hydrogen production
[(2)]Electric energy lost through wires and switches
[(3)]Electric energy supplied by the fuel cell stack
[(4)]Electric energy supplied by the grid

The hydrogen-loop energy efficiency calculated with the real-operational energy efficiencies for the electrolyser and fuel cell found above is:

$$\eta_{electrolyser(HHV)} \cdot \eta_{fuel\ cell(HHV)} = 0.596 \cdot 0.477 \cdot 100\% = \underline{28.4\%} \qquad (6.6)$$

The efficiency estimated in Equation 6.6 deviates with about 1% from the efficiency found from the specific energy input/output based on per unit standard volume H_2 produced and consumed. The average of the real-operational hydrogen-loop energy efficiency given in Table 6.3 and Equation 6.6 is then 28.3 %.

The hydrogen-loop energy efficiency calculated with the stack-only energy efficiencies for the electrolyser and fuel cell found above is:

$$\eta_{electrolyser(HHV)} \cdot \eta_{fuel\ cell(HHV)} = 0.732 \cdot 0.606 \cdot 100\% = \underline{44.4\%} \qquad (6.7)$$

The efficiency estimated in Equation 6.7 deviates with about 5 % from the efficiency found from the specific energy input/output based on per unit standard volume H_2 produced and consumed. The average of the stack-only hydrogen-loop energy efficiency given in Table 6.3 and Equation 6.7 is then 45.5 %.

The total HSAPS (excluding the PV array/MPPT efficiency) real-operational energy efficiency throughout the test-week was found to be:

$$\frac{\left(kWh_{Hydrogen\text{-}loop} \cdot \eta_{real\text{-}operational\ Hydrogen\text{-}loop\ efficiency}\right) + \left(kWh_{battery} \cdot \eta_{battery\ round\text{-}trip\ efficiency}\right) + kWh_{directly\ to\ load}}{kWh_{PV\ array/MPPT}} =$$

$$\frac{\left(\left(20.2 + 2.1 + 1.7\right) \cdot 0.283\right) + \left(11.6 \cdot 0.80\right) + 6.3}{39.7 + 2.1 + 1.7} \cdot 100\% = \underline{51.4\%} \qquad (6.8)$$

where

$kWh_{hydrogen\text{-}loop}$ = total energy supplied to the hydrogen-loop which includes the electrolyser stack, the electrolyser control system, and the H_2 purification system

$\eta_{real\text{-}operational\ hydrogen\text{-}loop\ efficiency}$ = the average real-operational hydrogen-loop efficiency

$kWh_{battery}$ = total energy supplied to the lead-acid battery

$\eta_{battery\ round\text{-}trip\ efficiency}$ = battery energy efficiency (80 %)

$kWh_{directly\ to\ load}$ = the amount of PV array/MPPT energy supplied directly to the load (15.4 – 11.6 – 3.5 = $\underline{6.3}$) kWh

$kWh_{PV\ array/MPPT}$ = total amount of energy available from the PV array/MPPT (including the energy from the grid supplying the electrolyser controller and the H_2 purification system)

A summary of the energy efficiencies in the laboratory HSAPS during the test-week are given in Table 6.6.

Table 6.6 Summary of the energy efficiencies in the laboratory HSAPS

Components / subsystem	stack-only efficiency [%]	real-operational efficiency [%]
Electrolyser	73.2 (HHV)	59.6 (HHV)
Fuel cell	60.6 (HHV)	47.7 (HHV)
hydrogen-loop[(1)]	45.5 %	28.3 %
Total HSAPS	-	53.5 %

[(1)]The average hydrogen-loop energy efficiency based on Table 6.3, and Equation 6.6 and Equation 6.7.

6.4 Conclusions

The hydrogen storage round-trip energy efficiency for the small-scale HSAPS during the test-week was found to be 28.1%. This number could be higher, especially if the average fuel cell power of 184 W had been closer to the nominal power of 500 W. The average fuel cell power output can be raised by allowing the fuel cell charge the battery in parallel to coverage of the load. The hydrogen-loop energy efficiency, or strictly speaking, the hydrogen-loop/battery energy efficiency was estimated to be raised to 30.1% if the fuel cell had been allowed to supply the load power requirement of about 130 W in parallel with charging the battery at about 320 W in addition to the mandatory fuel cell controller requirement of 50 W, which would add up to the nominal fuel cell power level of 500 W. It is encouraging that the hydrogen-loop energy efficiency for the laboratory HSAPS can reach 36.3% with the fuel cell and

electrolyser running at nominal power, indicating that larger HSAPS installations can operate with this energy efficiency even at partial loads and at low and fluctuating solar insolation. Further, the energy hydrogen-loop efficiency for the laboratory HSAPS could reach 39.4% if both the fuel cell and the electrolyser were operated at nominal power and if a larger low pressure container was used as hydrogen storage or that the energy needed for hydrogen purification could be 100% supplied by excess energy in the system. During the test-week, 1.2 kWh was registered as excess energy while the amount of energy required by the hydrogen purification unit was 1.7 kWh, thus a little shortage. The amount of excess energy can in reality be even lower as the actual excess power level in periods might be to low to do usable work. Anyhow, the possibility to use excess energy also increases the total utilisation efficiency for a general power system. The possibility to use excess energy in order to cover the hydrogen treatment energy requirement for a HSAPS is examined in Chapter 7.

The rather high PV array/MPPT energy utilisation efficiency of 97 % implies that the PV array should be scaled up, and as can be seen from the electrolyser power profile in Figure 6.12, the electrolyser power is seldom above 1 kW. But as stated earlier, finding the actual PV size was not in focus in this experiment. The focus was directed towards the hydrogen-loop efficiency and the practical operation of the hydrogen subsystem, especially during low and fluctuating solar insolation periods. Anyways, for a small-scale HSAPS, the importance of a PV array that can both supply the load and the electrolyser preferably at nominal power has been identified. Excess energy can be used for hydrogen treatment energy requirement.

The total system energy efficiency of 54 % is to some extent dependent on the control strategy but is closely related to the specific load profile and the actual location of the HSAPS with the specific renewable energy profile, which have been investigated by [2].

No failures or instabilities were registered during the test-week, thus the laboratory HSAPS promised good reliability and stability. On the other hand, allowing the fuel cell to charge the battery could introduce instability as discussed in section 3. Because the five minutes of fuel cell start-up time was not accounted for regarding the emulated lead-acid battery, the HSAPS caused 35 minutes of loss of load during the test-week. The electrolyser was 100 % available throughout the whole test-week. Though, a few minutes loss of load is much more critical than some minutes with loss of hydrogen production.

References

1. P.S.Kauranen, P.D.Lund, and J.P.Vanhanen, *Development of a Self-Sufficient Solar Hydrogen Energy System.* International Journal of Hydrogen Energy, 1994. **19**(1): p. 99-106.
2. J.P.Vanhanen and P.D.Lund. *Guidelines for sizing PV and storage components of self-sufficient solar hydrogen systems*. in *13th European Photovoltaic Solar Energy Conference and Exhibition*. 1995. Nice, France.

7. Comparison of metal hydride vs. pressurised steel vessel as long-term energy storage for small-scale HSAPS

Chapter 7 was originally presented as a paper in the 1st European Hydrogen Energy Conference, 2 – 5 September 2003, Grenoble, France [1].

With a view to use hydrogen as an energy carrier in stationary and mobile applications, hydrogen may be stored in several ways. However, practical, safe and economical storage of hydrogen is one of the major challenges for the introducing of the hydrogen society; especially for mobile applications due to both gravimetric and volumetric specifications that have to be met. Cost, volume, weight, lifetime and kinetics are important factors that should influence the decision maker. Different storage methods are listed in Table 7.1.

Table 7.1 List of different hydrogen storage methods

Technology	Pressure [Bar]	Temperature [°C]	Wt %	Density [g/L]
Medium pressure steel containers	200	20	100	18
Medium pressure composite containers	250	20	100	22
High pressure composite containers	700	20	100	30
Liquid Hydrogen storage	1	-250	100	70
Low temperature metal hydride	1 – 30	20 – 100	1.5 – 1.8	~ 95
High temperature metal hydride	1 – 30	250 – 400	3.5 – 7.6	~ 95
Alanates	1 – 200	20 – 170	4.0 – 5.6	30
Organic hydrides	10 – 100	300 – 400	5.0 – 7.0	85

In this chapter, two viable methods for hydrogen storage in a small-scale HSAPS are to be compared:

Alternative 1 - a medium pressure hydrogen steel container at 110 bars charged with a two-stage reciprocating compressor

Alternative 2 - a low-temperature metal hydride, which is charged directly by the electrolyser at 16 bars without additional compression work

The evaluation of the two different methods for hydrogen storage is based on three main parameters:

- *specific energy consumption*
- *performance/system-integration*
- *economics*

Computer models of the HSAPS are utilised in order to determine the specific energy consumed by the two different methods for hydrogen storage. The performance/system integration for the metal hydride is based on both simulations and operational experience from the HSAPS laboratory. A pressurised steel vessel was not implemented into the HSAPS laboratory, however, it was considered to be a well-known and mature technology compared to metal hydrides. Thus, the performance/system integration for the pressurised steel vessel was based on the simulations (models presented in Chapter 4) and information gathered from the literature. The economics was based on present and estimated future costs (10 years perspective).

A metal hydride unit vs. a pressurised vessel

A metal hydride unit offers high volumetric energy density, which is of great importance for small-scale stationary HSAPS where gravimetric energy density is of lesser concern. Use of low temperature metal hydrides comprises safe storage solutions because the low hydrogen pressures needed (10 – 15 bars). To be technically feasible in this energy system however, the thermal characteristic of the metal hydride must prevent excessive pressure build-up during hydrogen absorption and excessive pressure drop during hydrogen desorption. Pure and dry hydrogen should be applied to preserve maximum metal hydride lifetime, preferably > 99.999 % quality. The dryer operates as a passive filter under normal operation, but consumes electricity and gas product during regeneration.

A steel vessel with the same volumetric density as the metal hydride unit discussed in this study requires about 110 bars, dictating need for a compressor. In addition to the energy consumed during operation, the compressor needs maintenance on mechanically moving parts. However, hydrogen purity > 99.9 % is sufficient for this type of storage technology. By analyzing the energy balance throughout annual simulations together with operating costs/purchase costs and practical operation, this chapter gives a decision basis for the choice of long-term energy storage in a small-scale HSAPS.

7.1 System layout

Figure 7.1 shows a schematic of the HSAPS with the two methods for hydrogen storage compared and discussed in this chapter.

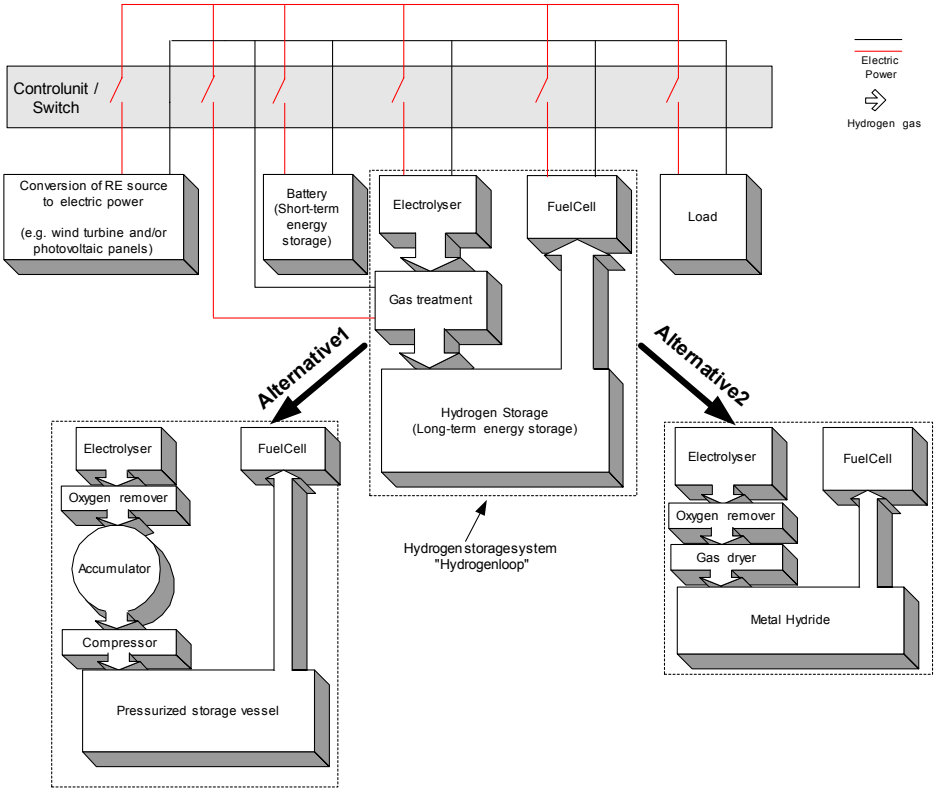

Figure 7.1 Schematic of an HSAPS where two alternatives for hydrogen long-term energy storage are shown. Alternative 1 is usage of a pressurized steel vessel with compressor and Alternative 2 is metal hydride with dryer equipment.

Alternative 1 shows the medium pressurised vessel while Alternative 2 shows the metal hydride as a method for hydrogen storage in a small-scale HSAPS. Alternative 2 is the very same configuration as in the laboratory HSAPS test-facility used in this thesis, the reader is referred to Chapter 3 for details. The Control Matrix proposed in Section 5.6 is used as high-level energy management for the HSAPS in this simulation study.

7.2 Simulations

The computer models used in this chapter are presented in Chapter 4. The renewable energy source is solar radiation and the load could e.g. represent electric power profile for a dwelling. The simulations are based on hourly solar radiation data measured at The University of Oslo. The PV array model is sized to 2 kW_{peak}, which results in an energy output of 939.7 kWh/year. The load, PV array, battery and fuel cell power profiles are shown for 3.January – 7.January in Figure 7.2. The total load is 581.9 kWh/year and the average load is 143 W.

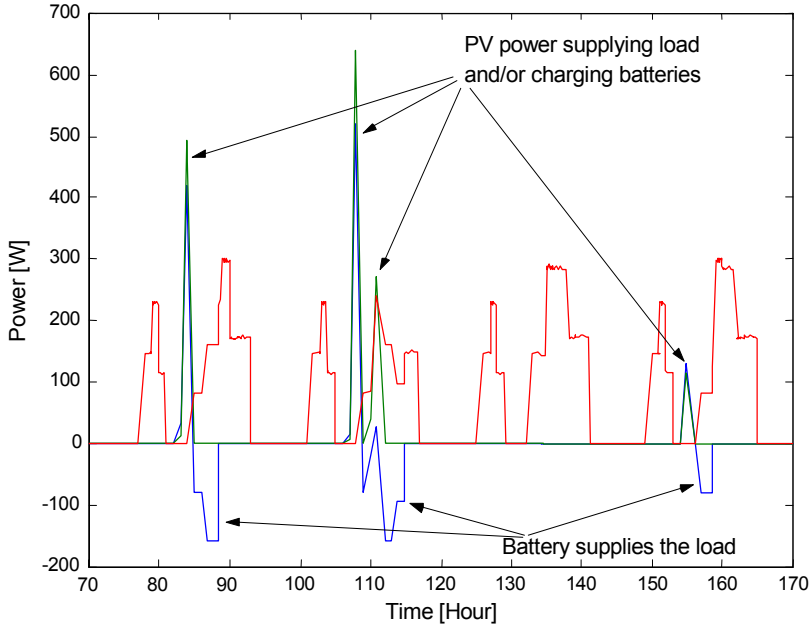

Figure 7.2 Power profiles for the load, PV panel, battery and fuel cell between 3.January –7.January. The red curve (with no arrow explanation) is the fuel cell supplying the load.

The simulated hydrogen storage size is 270 kWh (8.1 kg H_2 at LHV) and the capacity of the simulated lead-acid battery is 540 Ah (25.9 kWh at a constant voltage of 48 V). The annual simulation starts at 00.00 hours the 1st of January. One-hour time steps are used, initial setting for the hydrogen storage state-of-charge is 47 %, and initial setting for the battery state-of-charge is 40 %.

7.3 Results and Discussion

7.3.1 Evaluation of pressurized steel vessel with compressor

Pressurized steel vessels/cylinders for storage of hydrogen are commercially available and are used to both store and transport hydrogen today. The main advantage is the ease of use and cost, approximately 40 $/$Nm^3$ [2]. Fuel cells are sensitive to

contaminations, meaning traditional low-cost (5.000-10.000 $ [3, 4]) reciprocating compressors without proper filter function catching oil mist and/or piston/piston-ring particles downstream should be avoided. Unfortunately all compressors have sliding seals between high and low pressure zones, which always leak to some extent. In reciprocating compressors the usual leakage path are through the piston rings and valves, which do not seal perfectly against reversible flow [5], thus typical volumetric efficiency is 95 %. A more appropriate compressor for fuel cell grade hydrogen is a diaphragm compressor (30.000 –150.000 $ [3, 4]) which separates the piston and cylinder from the product gas with a metallic diaphragm, the hydrogen leakage for such a compressor has been reported down to 0.1 % (Palm Desert, Schatz Energy Research Centre [6]). The efficiency of compressors is 50 – 80 % with respect to adiabatic work. However, safety is a critical issue concerning pressurized gas, especially in the transport applications. Cyclic use of the hydrogen storage units stresses valves, fittings, etc. under pressurized conditions.

The simulated system configuration for pressurized steel vessel includes a 0.1 m^3 steel accumulator tank installed between the 16 bars electrolyser and the two stage reciprocating compressor (Figure 7.1). This configuration is usually used to level out the pulsating hydrogen flow from the electrolyser to prevent wear on compressor and pulsation losses. But this configuration also allows the compressor to run more independently with respect to electrolyser operation. It may run sporadic and for shorter periods of time and achieve more advantageous use of any excess energy. The size of the main steel vessel without compressor would have been 6.2 m^3 at 16 bars. It is beneficial to fit a small-scale stationary power system into standard size containers in order to ease transport, installation and possible re-location. In order to reduce the hydrogen storage volume, a compressor must be introduced. At 110 bars, a 0.9 m^3 vessel is the minimum size for which a two-stage compressor manages to fully charge it with 100 Nm^3 of hydrogen gas. The compressor is switched ON when the pressure in the accumulator reaches 16 bars and switched OFF when the pressure fall below 1 bar. Total annual electrolyser operating time is 649 hours, but with the accumulator installed the operating time of a 200 W compressor is only 98 hrs distributed on 49 start-ups. Even with as low as 3000 hrs expected compressor lifetime, the compressor would last about 30 years in this system.

For a compressor with 80 % isentropic efficiency the total electric energy consumption is 7.57 kWh/year transferring a total of 89.1 m^3 hydrogen gas from low pressure to high pressure. The specific energy consumption for this modelled compressor is then 0.1 kWh/m^3. This is in accordance with specific energy consumption of 0.1 –0.13 kWh/m^3 for real reciprocating compressors used for hydrogen, reported in the literature [7, 8].

Excess energy in system (*after* electrolyser, battery and load) is 13.9 kWh/year, which exceeds the isentropic compressor energy requirement. However, only 0.5 kWh of the excess energy coincides with the compressor energy demand when only the pressure level in the accumulator controls the compressor. A smaller compressor or a larger accumulator vessel could be installed to optimize the match between compressor operation and excess energy. However, a smaller compressor would lead to a larger power mismatch with respect to excess power (average 200 – 250 W). It would also increase compressor operating hours and need for maintenance and, hence, decrease

the lifetime of the compressor. A larger accumulator vessel would be unacceptably large to give the system ability to "wait" until enough excess power is available.
A viable solution to this optimization problem is to tune the Control Matrix (Section 5.3.2) for priority to use excess energy to run the compressor. This means that the Control Matrix only allows the compressor to be switched ON when the HSAPS is in one of the *states of system* which indicates available excess energy, high battery state-of-charge, and high hydrogen state-of-charge. A minimum excess power-limit prevents the compressor to be switched ON at low excess power, which is useful in order to reduce number of unnecessary compressor start-ups. In this case, the minimum excess power limit should be about 300 W reflecting the rated compressor power.

Analysing the Control Matrix, Figure 5.5 and Figure 5.6 in Section 5.3.2 can identify the favourable states of system. It is advantageous to run the compressor at high battery state-of-charge (H_1) that suggests $\mathbf{C_1}$, $\mathbf{C_2}$ and $\mathbf{C_3}$ from Figure 5.5. However, $\mathbf{C_3}$ should be excluded because it contains four *states of system* with low hydrogen state-of-charge (L_2) in the main vessel. These states do not need compressor work because the electrolyser pressure is high enough to charge the main vessel directly. Furthermore, from Figure 5.6, it is advisable to run the compressor when $I_{PV\text{-}Load} = 1$. The compressor should therefore be activated at the following *states of system*: 3, 4, 7 and 8.

Table 7.2 shows the simulation results after comparing system performance with three different settings of the control strategy for the compressor. In *simrun1* the compressor is only activated by the accumulator vessel; turned on at 16 bars and turned off at 1 bar. In *simrun2* all the available excess energy can be used to switch the compressor on in addition to the accumulator strategy given in *simrun1*. In *simrun3* a minimum power limit of > 300 W is required of excess power in *states of system* number 3, 4, 7 and 8 in sub control matrixes $\mathbf{C_1}$ and $\mathbf{C_2}$ before it allows the compressor to be switched ON (Figure 5.6). The control strategy in *simrun1* is also activated in *simrun3*.

Table 7.2 Comparison of different settings in the control strategy for operation of the hydrogen compressor (settings for simulation is explained in text)

Simulation run number	simrun1	simrun2	simrun3
Compressor total usage [Hours]	98.6	98.6	99.6
Total compressor ON/OFF-switching [-]	46	129	61
Time compressor served by excess power [Hour]	3.6	24.6	13.0
Compressor ON/OFF-switching due to excess power [-]	3	95	23
Total energy consumed by the compressor [kWh]	7.57	8.26	7.77

The minimum number of ON/OFF-switches for the compressor occurs in *simrun1*. The maximum number of ON/OFF-switches for the compressor occurs in *simrun2*, which is expected because of the "liberal" control strategy. Although decreased compressor ON/OFF-switching increases lifetime, the ability to use more of the excess energy and free more energy to battery charging, load serving and/or hydrogen production is a technical and economic benefit for the system. Thus *simrun3* gives the best result, allowing for an increase in usage of excess energy with a moderate increase in compressor ON/OFF-switching compared to *simrun1*. The total compressor operation time is approximately the same for all simulations because

approximately the same amounts of hydrogen have to be processed by the compressor.

7.3.2 Evaluation of metal hydride with dryer

Compared to pressurized vessels, metal hydrides have a potential for being safer. This is mainly due to lower storage pressures (~10 – 30 bars) and the fact that hydrogen leakage caused by fracture will be controlled due to the temperature fall upon fast discharge. The metal hydride market is not yet established and the prices today still contain a large portion of R&D costs. Small- to medium sized storage units (from litres to several tens m^3) are available on a pre-commercial / prototype basis. In 2001 prices for m^3-sized metal hydride storage units was ~700 \$/Nm^3. A price analysis based on estimated production and material costs, estimated the costs for metal hydride storage unit in 2015 to be ~200 \$/Nm^3 [4]. The specific price for the laboratory dryer is 71 \$/Nm^3.

Since the electrolyser working pressure is high enough to charge the metal hydride, there is no need for additional compression work. Electrolyser pressure in HSAPS applications has been reported up to 120 bars for an alkaline electrolyser [9] and up to 420 bars for a PEM electrolyser [10], but normally the maximum electrolyser pressure does not exceed 30 bars. This is more than enough to charge the metal hydride. An increase in the electrolyser pressure gives a relatively small increase in the reversible voltage, about 30 mV per cell per decade of pressure, which would increase power consumption with about 1 – 2 %. The electrical efficiency of alkaline electrolysers have been reported to increase at increased pressure, because the increased pressure leads to smaller product gas bubbles surrounding the electrodes. Thus, the ohmic resistance decreases between the electrolyte and the electrodes [11].

The physical occupation of the metal hydride including the mandatory hydrogen gas purification unit is about 40 % of the pressurised steel vessel system presented in Section 7.3.1. The purification unit installed in the HSAPS laboratory demands 1.8 kW for 6 hrs during regeneration of one fully saturated column. The specific energy consumption is then 1.8 kW*6 hr / 84 Nm^3 = 0.13 kWh/Nm^3. This is in very good agreement with data found in the literature [7] for a smaller system (60 – 200 W). The regenerator gas used with the laboratory dryer is N_2. For a stand-alone system located out in the field the only regeneration gas available is the dry hydrogen from the long-term energy storage. If hydrogen is used as regeneration gas, about 8 % of the annual hydrogen production is consumed [6, 7]. A cooling device that chills the hydrogen gas to ~20°C and removes the majority of water before the desiccant absorbs the remaining water has been reported (Palm Desert, Schatz Energy Research Centre [6]). The hydrogen consumed during regeneration can be reduced to about 1 %.

The capacity of the dryer is quite large, with a compact volume of 0.013 m^3 and 6 kg desiccant. A column can dry 84 Nm^3 hydrogen saturated with water at 40°C, which is about the same as the total annual hydrogen productions in these simulations. Because of the large dryer capacity, regeneration of the wet desiccant can preferably take place whenever there is excess power in the system. But unfortunately thermal systems are often subject to slow start-up due to the nature of heat transfer. In this system simulation at least 200 W must be supplied to a heater element for at least 30 minutes in order to heat the heater element, the regeneration gas, the desiccant and finally the

water to about 90°C before water starts evaporating and can be carried out of system by the regeneration gas. Energy must be supplied from either the short or long-term energy storage in order to fulfil the regeneration. The final water level in dryer, where only excess energy is used for regeneration, is shown in Figure 7.3. *State of system* 3, 4, 7, 8 and a minimum excess power limit of 200 W are favourable conditions for dryer regeneration with the same arguments for compressor usage given in Section 7.3.1. The possibility to avoid unnecessary start-ups of dryer regeneration prevents unnecessary use of regeneration gas. The argument for not running dryer regeneration when hydrogen state-of-charge is low (L_2) is because the hydrogen storage is normally at its minimum late winter/early spring (when solar energy is used) when there is little chance for excess energy, besides only minor hydrogen production have taken place at this time of year so there should be unnecessary to regenerate the dryer at this point.

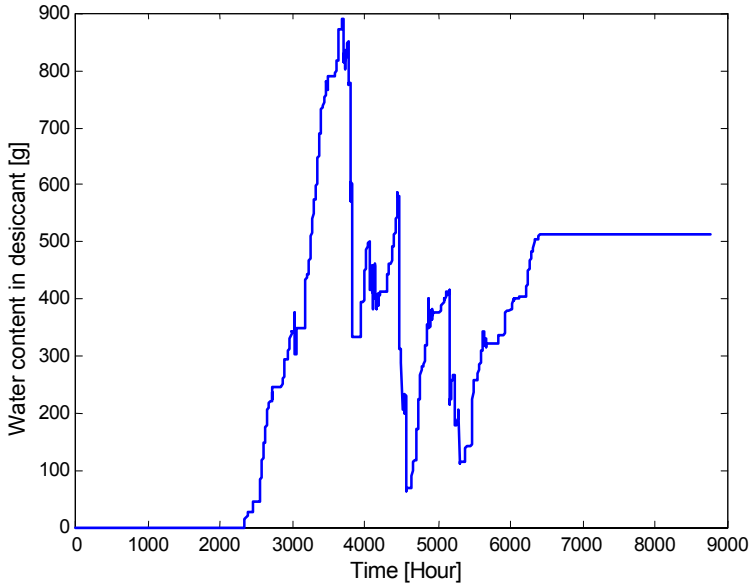

Figure 7.3 Water content in desiccant, if regenerated solely with excess energy. Capacity is 2.5 kg H_2O.

7.3.3 Comparison of pressurised steel vessel and metal hydride

The specific energy consumption for the dryer is 0.13 kWh/Nm^3 in addition to 8 % of the total hydrogen production used as regeneration gas. The final specific energy consumption for the dryer is then 0.4 kWh/Nm^3 based on hydrogen LHV and an electrolyser energy efficiency of 80 %. The specific energy consumption for the compressor is 0.10 kWh/Nm^3 in addition to 5 % hydrogen leakage. The final specific energy consumption for the compressor is then 0.27 kWh/Nm^3 based on hydrogen LHV and an electrolyser energy efficiency of 80 %. With total hydrogen production of 88 Nm^3 the total energy consumption for the dryer is 35.2 kWh and 23.8 kWh for the compressor. A cooling device installed to chill the hydrogen to ~20°C before the hydrogen is fluxed through the dryer would decrease the total energy consumption of the metal hydride to 14.4 kWh. This number would be larger if an electric pump were needed to transport possible cooling water. But, replacing the reciprocating compressor with a diaphragm compressor with hydrogen leakage down to 0.1 % would on the other hand give a specific energy consumption of 9.0 kWh.

Compared to the compressor, the dryer can utilise more of the excess energy as shown in Figure 7.4. The dryer utilizes 67 % of the total excess energy available, which covers 81 % of the total energy required by the dryer regeneration. The compressor utilizes 12 % of the total excess energy available, which covers 21 % of the total energy required by the compressor. This indicates that the dryer is able to utilize excess energy better than the compressor. On the other hand, if the load consumption increases with 5 % (to 618 kWh/year, average load 154 W), a reduction to 54 % of dryer energy served by excess energy is realized. A reduction to 17 % of compressor energy served by excess energy is only a moderate change. The sensitivity analysis thus shows that the dryer designed to supply most of its energy requirements from excess energy should be treated with care in systems were the load can vary significantly from year to year. Such systems should, on the other hand, always be oversized to some extent.

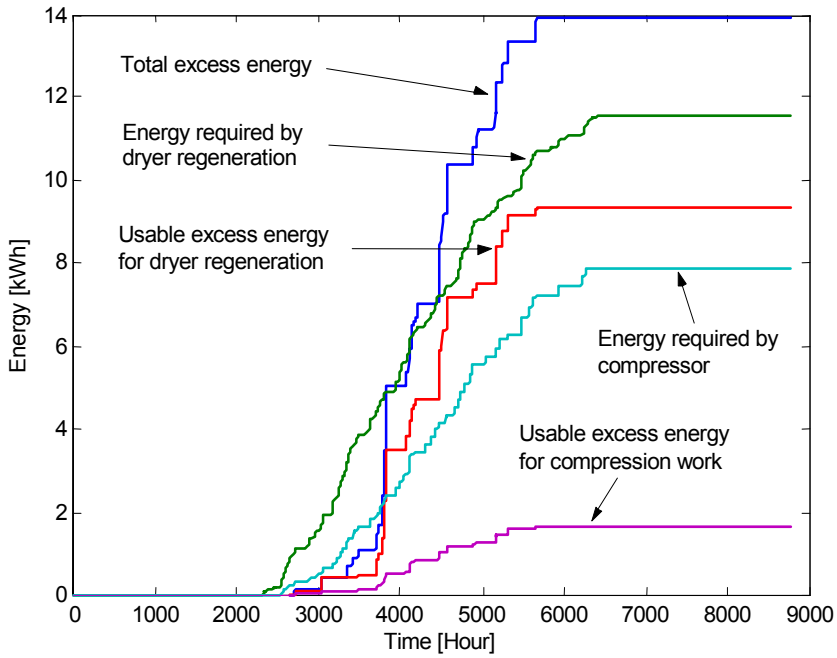

Figure 7.4 Excess energy in system available for running the hydrogen compressor in Alternative 1 and for regeneration of the desiccant in the hydrogen dryer in Alternative 2.

From the control strategy point of view, the pressurised vessel is preferred because it is much easier to estimate the $H_{2,SOC}$. When the ambient temperature is known the pressure in the vessel translates directly to $H_{2,SOC}$. The PCT curves must be used in order to estimate $H_{2,SOC}$ for the metal hydride. Over time, the estimation of $H_{2,SOC}$ from PCT curves will deviate from true $H_{2,SOC}$ due to repetitive cycles of the metal hydride. Heat must also be supplied to the metal hydride during discharging unless the pressure will decrease and $H_{2,SOC}$ will literally be measured as 0 % even though the true $H_{2,SOC}$ could be e.g. 50 %. Heat must on the other hand be removed during charging or the $H_{2,SOC}$ would wrongly be reported as 100 % caused by the pressure build-up.

With an interest rate of 7 % and component lifetime of 20 years, the *present worth* (PW) for a hydrogen subsystem comprising of a pressurized steel vessel with a classic reciprocating compressor is calculated to be approximately 2.400 – 3.700 $\$_{PW}$

including compressor and vessel maintenance (2 % of initial cost). The present worth with a diaphragm compressor is approximately 9.300 $\$_{PW}$. With the same assumptions for interest rate and lifetime used for Alternative 1, the present worth for the metal hydride hydrogen subsystem with the estimated future metal hydride price and dryer, will be approximately 5.800 $\$_{PW}$, while the actual 2002 price would be 16.600 $\$_{PW}$. Maintenance for the dryer and metal hydride is also included (1 % of initial cost).

7.4 Conclusion

Two alternatives for hydrogen storage in a small-scale stand-alone power system have been investigated. Alternative 1 was pressurized steel vessel with compressor and Alternative 2 was metal hydride with gas dryer. The main parameters have been: energy consumption, performance/system integration and economics. The metal hydride represents a safe storage method due to the low pressure (16 bars) in addition to a compact design (about 10 % of the volume represented by the pressurized vessel). But a vessel pressure of 110 bars is moderate compared to commercial storage pressures of > 200 bars. The pressurized vessel storage volume of about 1 m^3 is still small enough to be mounted in portable small-scale energy systems. The dryer utilized excess system energy better than the compressor but the rather low energy consumption and ease of operation favours the pressurized vessel. With present prices (2003) the pressurized vessel with diaphragm compressor is about half the price of the metal hydride system. But with the estimated future price for metal hydrides the price will be about the same for the two different alternatives. The pressurized steel vessel with a diaphragm compressor was at the present found to be the most proper hydrogen storage for the small-scale system used in this work. A suggestion for future work would be to investigate solar thermal energy as cooling source and the possibility to use vacuum to dry the desiccant and improve the drying process for the metal hydride.

References

1. H.Miland R.J.Aaberg R.Glöckner G.Hagen. *A Comparison of Metal Hydride vs. Pressurised Steel Vessel as Long-term Energy Storage for Small-scale Hydrogen stand-alone power system (HSAPS)*. in *1st European Hydrogen Energy Conference*. 2003. CO2/142 in proceedings. Grenoble, France.
2. A.de Groot, F.W.A.Tillemans, and K.Brandwagt, *An analysis of different options for energy systems in residential districts*. 2001, ECN, Netherlands.
3. M.Bracht and A.de Groot, *Final Report of Subtask C: Design Evaluation and System Comparison Guidelines*. 2001, IEA.
4. *Internal IFE Report, IFE/KR/F-2003/020*. 2003.
5. P.C.Hanlon, *Compressor Handbook*. 2001, New York: McGraw-Hill.
6. T.Schucan, *Case studies of integrated Hydrogen Energy Systems*. 2001, IEA.
7. P. Hollmuller, et al., *Evaluation of a 5 kW photovoltaic hydrogen production and storage installation for a residential home in Switzerland.* Int.J.Hydrogen Energy, 2000. **25**: p. 97-109.
8. S.Galli and M.Stefanoni, *Development of a Solar-Hydrogen Cycle in Italy.* J. Hydrogen Energy, 1997. **22**(5): p. 453-458.
9. H.Barthels, et al., *Phoebus-Jülich:an Autonomous energy supply system comprising Photovoltaics, Electrolytic Hydrogen, Fuel Cell.* J. Hydrogen Energy, 1997. **23**(4): p. 295-301.

10. W.Smith, *The role of fuel cells in energy storage.* J. Power Sources, 2000. **86**: p. 74-83.
11. J.Thonstad, *FAG 53541 Elektrolyseprosesser, NTNU*. 1998, Trondheim: Tapir.

8. Load control of a wind-hydrogen stand-alone power system

This chapter is a paper submitted for publication in *The International Journal of Hydrogen Energy*.

LOAD CONTROL OF A WIND-HYDROGEN STAND-ALONE POWER SYSTEM

Harald Miland[2], **Ronny Glöckner**
Institute of Energy Technology (IFE), P.O. Box 40, 2027 Kjeller, Norway

Phil Taylor
Econnect, 19 Haugh Lane Ind Est, Hexham NE46 3PU, UK

Rolf Jarle Aaberg
Statkraft SF, PB 200 Lilleaker, 0216 Oslo, Norway

Georg Hagen
Department of Materials Technology, NTNU, 7491 Trondheim, Norway

Abstract

A new generation of load controllers enable stand-alone power systems to use one or many standard (grid-connected) wind turbines. The controllers use fuzzy logic software algorithms. The strategy is to use the control loads to balance the flow of active power in the system and hence control system frequency. The dynamic supply of reactive power by a synchronous compensator maintains the system voltage within the limits specified in EN50160. The resistive controller loads produce a certain amount of heat that is exchanged down to the end user (hot water). It was decided to investigate the implementation of a hydrogen subsystem into the stand-alone power system that can work in parallel with the Distributed Intelligent Load Controller (DILC). The hydrogen subsystem can then function as energy storage on long-term basis and an active load controller on short-term basis.

Keywords: Hydrogen; Electrolyser; Fuel cell; Wind turbine; Load control; Fuzzy logic

1 Introduction

A stand-alone power system (SAPS) is defined as a system that supplies electricity without being connected to a main grid. These types of systems are often located on islands and in remote parts of the world where power generation on-site is favourable because grid connection is either technically and/or economically demanding. The electric power input can be generated from e.g. diesel, natural gas or preferably, in terms of environmental impact, from renewable energy sources such as wind-, hydro- and direct solar energy. A load connected to a large and stiff grid senses its power source as an "unlimited" and robust source, whereas a load connected to a SAPS can experience fluctuations in voltage (AC and DC systems) and frequency (AC systems). Econnect Ltd has developed a new generation of Distributed Intelligent Load Controller (DILC) to enable SAPS to use one or many standard (grid-connected) wind turbines. Econnect has modelled, designed, built and tested a wind-diesel SAPS with a 20 kW wind turbine. The resistive loads used by the DILC produce a certain amount of heat that is usable for e.g. water heating. It has been suggested to introduce a hydrogen subsystem comprising of an electrolyser, hydrogen storage and a fuel cell into the SAPS (in the forthcoming entitled as HSAPS). The benefit by doing this is two fold; first, the electrolyser can convert excess wind power into hydrogen (energy storage) whereas the fuel cell can re-introduce the energy into the system during deficit wind power with respect to the end user; secondly, the electrolyser can also contribute as a resistive load controller. Particular focus will be given to the interaction between the electrolyser and the three-phase AC system.

[2] Corresponding author. Fax: +47 63 81 29 05. E-mail address: haraldm@ife.no

2 System of reference and simulation models

The simulation work presented in this paper is based on a 20 kW wind-diesel SAPS, where the diesel engine and tank have been replaced by a fuel cell and an electrolyser. Hence, the virtual wind-HSAPS has been set up. The models are all developed in Matlab/Simulink with access to the Fuzzy logic toolbox and Simulink's Power Systems Blockset [1]. A schematic of the wind-HSAPS is shown in Figure 1. The stand-alone system contains a 20 kW wind turbine, a 40 kVA synchronous compensator, a 10 kVA power factor correction capacitor, a 6 kW fuel cell, an 8 kW_{DC}, 48 V electrolyser, a total of 30 kW resistive loads implemented in the DILC, 6 kW base load and a H_2 storage.

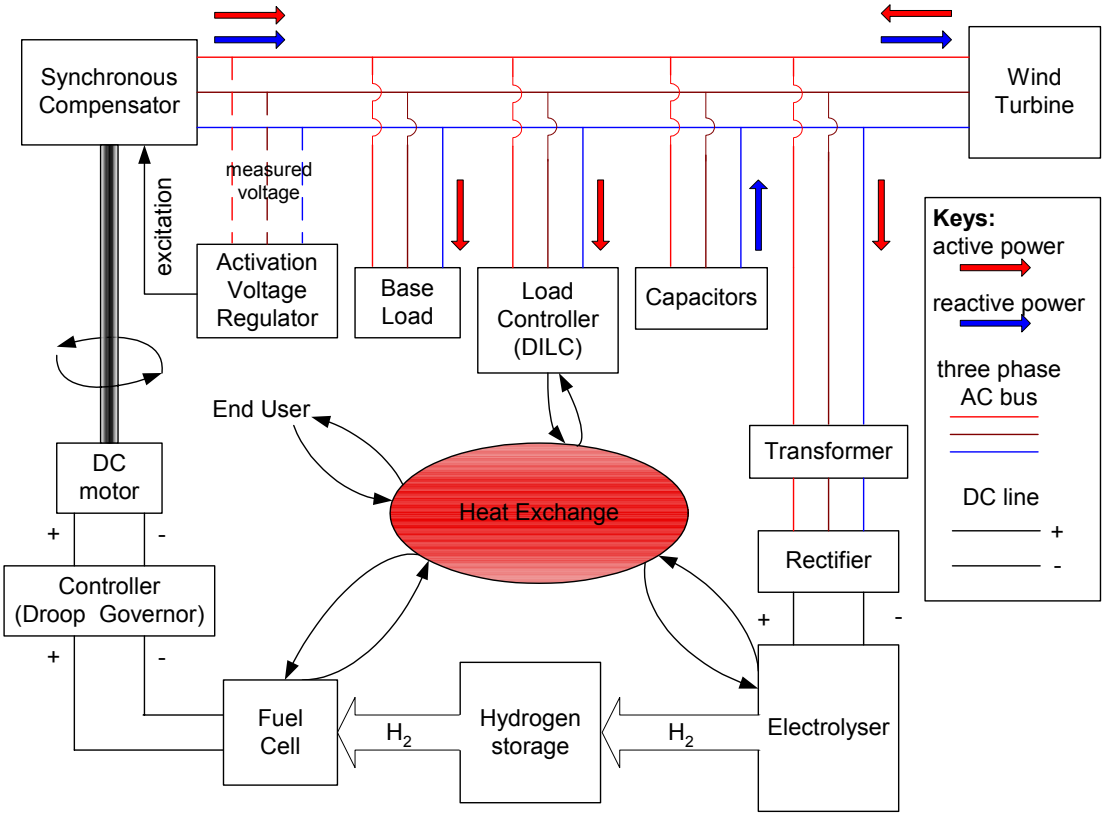

Figure 1 Schematic of the wind-HSAPS used in this simulation work.

The heat generated by the DILC can, along with hot water for the end user, also be exchanged with the cooling water flow of the fuel cell and the electrolyser in order to minimise wear and reduce start-up time. The HSAPS is connected to a three-phase AC bus at a nominal voltage of 230 V_{rms} (rms = root mean square). Since the electrolyser runs on DC power, it needs power electronics at the connection point with the AC bus as indicated in Figure 1.

2.1 Wind turbine

A Gazelle wind turbine is modelled in two sections, the aerodynamic performance and the generator.

Aerodynamic model
The aerodynamic torque applied to the generator by the wind turbine is calculated from the rotor speed and the wind speed, based on a generalised relationship between torque coefficient and tip speed ratio. For each time step in the Simulink model, torque is calculated as follows:

$$tip\ speed\ ratio = \frac{rotor\ radius \cdot rotor\ \ rotational\ speed}{wind\ \ speed} \tag{2.1}$$

Simulink finds the corresponding torque coefficient *Cq* from the calculated tip speed ratio (from a lookup table) and calculates:

$$torque = Cq \cdot 0.5 \cdot air\ density \cdot windspeed^3 \cdot \pi \cdot rotor\ radius^3 \tag{2.2}$$

The use of tip speed ratio and torque coefficient is valid only for fixed pitch wind turbines like the Gazelle, but within this constraint it allows the wind turbine's torque to be estimated at rotational speeds other than the design speed without employing a two-dimensional lookup table.

Wind turbine generator model
The aerodynamic torque is applied to an asynchronous machine predefined block from the Power Systems Blockset library of Matlab [2]. The asynchronous machine block can operate in either generating or motoring mode. The mode of operation is dictated by the sign of the mechanical torque (positive for motoring and negative for generating). The electrical part of the machine was represented by a standard fourth-order state-space model [3] and the mechanical part by a second-order system. All stator and rotor quantities were in the rotor reference frame. The mechanical system is represented by:

$$\frac{d\omega_r}{dt} = \frac{1}{2H}(T_e - F\omega_r - T_m) \tag{2.3}$$

Where H is the inertia constant, ω_r is the rotor angular velocity, F is the combined rotor and load viscous friction, T_e is the electromagnetic torque and T_m is the shaft mechanical torque.

The electrical inputs are the three stator-voltages, the electrical outputs are the three electrical connections of the rotor which are directly connected together. The remaining input is the mechanical torque at the machine's shaft. The model did not include a representation of the effects of stator and rotor iron saturation.

2.2 Power factor correction capacitor (PFC)
The wind turbine power factor correction capacitor (PFC) is a Capacitor block element from the Power Systems Blockset library [1].

2.3 Synchronous compensator (SC)
The synchronous compensator (SC) comprises two major components, the synchronous machine and the automatic voltage regulator (AVR).

Synchronous machine
The model employs the Simplified Synchronous Machine bloc from the Power Systems Blockset library [2]. The simplified model is sufficient for the purposes of the simulation, which focuses on the entire system rather than the detailed performance of each individual component. The Simplified Synchronous Machine block models both the electrical and mechanical characteristics of a synchronous machine. The electrical system for each phase consists of a voltage source in series with the armature resistance (Ra) and synchronous reactance (Xs), as shown in Figure 2 [4].

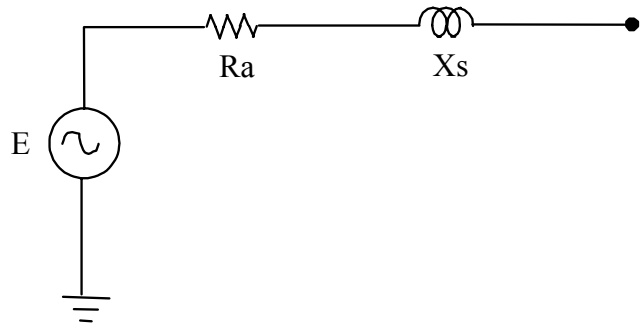

Figure 2 Simplified synchronous machine equivalent circuit. E is voltage source, Ra is the armature resistance and Xs is the synchronous reactance.

The Simplified Synchronous Machine block implements the mechanical system described by:

$$\Delta\omega(t) = \frac{1}{2H}\int_0^t (T_m - T_e)dt - K_d\Delta\omega \qquad (2.4)$$

Note, in this case the model computes a deviation, $\Delta\omega$, with respect to the speed of operation, and not the absolute speed itself. H is the inertia constant, T_m is the mechanical torque, T_e the electromagnetic torque and K_d is the damping factor.

The first input of the Simplified Synchronous Machine block is mechanical power. The second is the field excitation input that determines the amplitude of the internal voltage. The output voltage, frequency and power are available as outputs.

Automatic voltage regulator (AVR)
The automatic voltage regulator (AVR) model attached to the synchronous machine for voltage regulation consists of a proportional controller. The AVR model monitors all three phase-voltages and uses a mean rms value as its input voltage and the output is the exciter signal to the synchronous machine.

2.4 Distributed Intelligent Load Controller (DILC)

The total effect of the DILC is 30 kW. This comfortably exceeds the maximum power produced by the wind turbine even in the strongest winds. Each phase has four 1 kW and three 2 kW switchable resistive loads, each with its own fuzzy controller. In a real installation the DILC would control available distributed dump loads such as water heaters. The DILC acts to try and maintain the system frequency at 50 Hz, or at least within the specified limits. The DILC was implemented using the MATLAB Fuzzy Toolbox library [5]. This permits easy integration of the controller into the Simulink simulations.

2.5 Base Load (BL)

It is assumed that SAPS will have some essential loads that are not deferrable. Past work [6, 7] suggests that uncontrolled loads should not exceed 20 – 33 % of the wind turbine's rated power.

2.6 Electrolyser stack and the electrolyser power electronics

Electrolyser stack

In general electrochemical cells operate at low voltage. Even when they are connected in series in typical industrial applications, the total voltage across the stack would normally not exceed 50 – 100 V_{dc} [8]. The current, however, can range up to several hundreds of amperes depending on the actual size of each cell. Because of the rather low voltage of the current electrolyser (48 V_{dc}) compared to the AC system (230 $V_{rms,line}$), a transformer has been implemented in the model in order to step down the AC voltage before it enters the rectifier.

The electrolyser is modelled as a series of unit cells forming the stack. Figure 3 shows an equivalent circuit of a unit cell used in this work. The stack contains 26 cells, which gives a nominal stack voltage of 48 V_{DC}. A 26 cells stack configuration is chosen in order to verify the results from the empirical electrolyser model with a 26 cells, 48 V, 2 kW PEM (Polymer Electrolyte Membrane) electrolyser installed in the laboratories of IFE. Experimental values for the equivalent circuit capacitance and resistance are found from E. Rasten [9]. The PEM laboratory electrolyser has a maximum operation voltage of 52 V and a minimum operation voltage of 43 V. By using a nominal current density of 0.6 A/cm^2, a cell area is required by the model in order to determine the total current flow and thus the power. Assuming that the initial cell temperature is at the nominal operating temperature, the results for this model are in good agreement with the experimental data from the 2 kW PEM electrolyser. The electrolyser model has no thermal transient included, therefore the assumption for this model is preheating of the electrolyser stack (about 80°C) by the DILC as indicated in Figure 1.

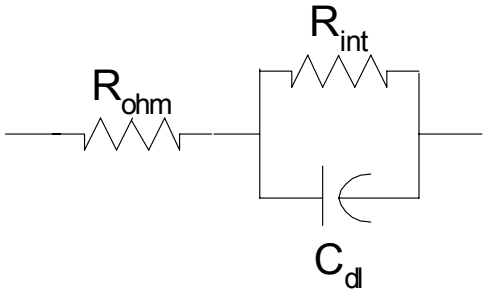

Figure 3 Equivalent circuit of an electrochemical unit cell where R_{ohm} is the ohmic resistance in the electrolyte, R_{int} is the charge transfer resistance between the electrolyte and the electrodes and C_{dl} is the charge due to the double layer present at the electrode surface.

Transformer and rectifier

Component models for the transformer and rectifier is imported directly from the Simulink Power Systems Blockset, and connected between the three-phase AC system and the electrolyser model as shown in Figure 4.

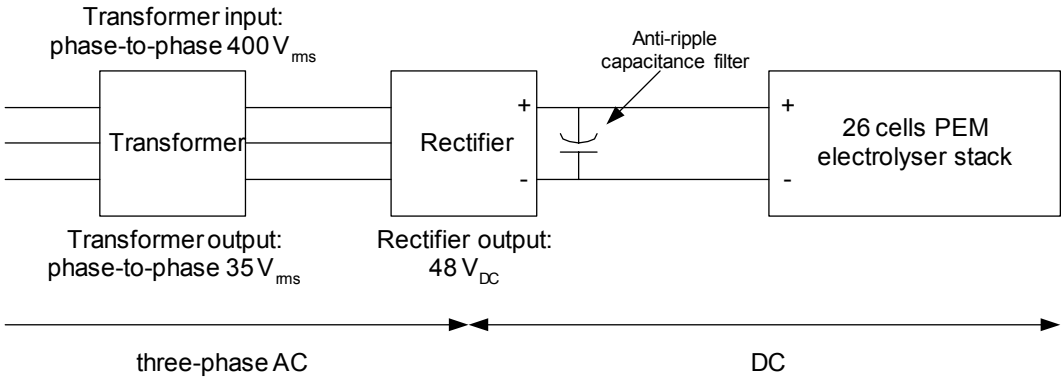

Figure 4 Electrolyser connected to the three-phase AC bus by a transformer and a rectifier.

The first windings of the 10 kVA rated transformer is modelled with 400 V_{rms} phase-to-phase as input from the wind turbine whereas the second windings phase to phase voltage output is calculated on the basis of the desired mean rectifier voltage output (the electrolyser voltage) [8]:

$$V_{dc,electrolyser} = 2 \cdot \frac{3\sqrt{2}}{2\pi} V_{ph-ph(rms),transformer,out} \tag{2.5}$$

$V_{dc,electrolyser}$ is the nominal electrolyser DC voltage at 48 V and $V_{ph\text{-}ph\ (rms),transformer,out}$ is the output voltage (second windings) of the transformer. Rearranging Equation 2.1 and solving for the transformer voltage output, we get:

$$V_{ph-ph(rms),transformer,out} = \frac{\pi}{3\sqrt{2}} V_{dc,electrolyser} = \frac{\pi}{3\sqrt{2}} \cdot 48 = \underline{35\, V_{rms}} \tag{2.6}$$

Standard values for internal resistance and leakage inductance, 0.004 and 0.02 pu respectively in addition to magnetization resistance (Rm) and reactance (Lm), both 200 pu, have been accounted for in the model.

The rectifier shown in Figure 4 is based on the Universal Bridge component model from the SimPower Blockset. Six diodes, each with 0.8 V forward voltages, act as power switches according to the diagram in Figure 5. The electrolyser operation can, however, not be regulated with this setup, when switched ON it will constantly draw 8.7 kW_{AC}.

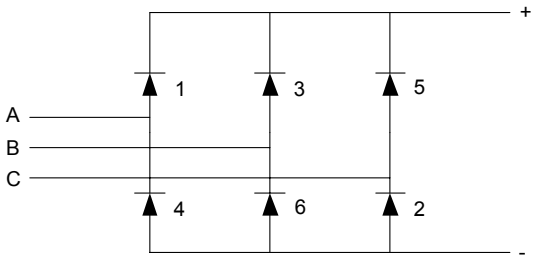

Figure 5 Schematic of the Universal bridge component model acting as a rectifier. Simple diodes are used as power switches.

A capacitive filter has been implemented in the system model as well to prevent deviation of more than 1 % ripple voltage for the electrolyser. This ensures a rather smooth and constant electrolyser-voltage well within the limit of 43 V – 52 V. The size of the capacitive filter has been calculated from [10]:

$$C_{filter} = \frac{V_{dc,electrolyser} \Big/ V_{1\%ripple}}{3 \cdot f \cdot R_{electrolyser}} = \frac{48V_{dc} \Big/ 0.48V_{dc}}{3 \cdot 50Hz \cdot 0.26ohm} = \underline{2.6F} \qquad (2.7)$$

Where C_{filter} is the capacitive filter connected in parallel with the electrolyser stack as indicated in Figure 3. $V_{1\%ripple}$ is the allowable 1 % ripple voltage calculated on the basis of the nominal electrolyser voltage of 48 V_{dc}. f is the system frequency multiplied by number of phases and $R_{electrolyser}$ is the total resistance in the electrolyser stack.

2.6 Fuel Cell

During low wind speed some mechanical work must be applied to the SC in order to keep up the system frequency. This is regulated by a simple droop relationship between system frequency and mechanical power needed by the SC as indicated in Figure 6. A diesel engine is usually installed to provide the mechanical work, but a fuel cell running a DC motor has been considered in this specific case study. When the system frequency drops below 48 Hz, the fuel cell output power is increased linearly until the system frequency is stabilized at minimum 47 Hz. The fuel cell could also help to start the wind turbine. This is not included in this work as steady state operation is assumed.

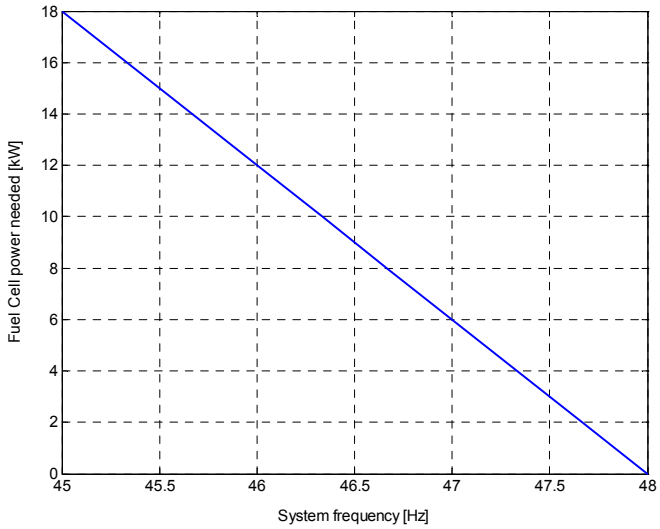

Figure 6 The droop governor relationship, the fuel cell power needed is regulated according to the system frequency. In this work, a fuel cell power output of at least 6 kW is needed to serve the base load.

No specific model has been implemented for the fuel cell in this preliminary study other than using the droop relationship in Figure 6 to calculate the required fuel cell output power. The linear equation for Figure 6 is:

$$Fuel\ Cell\ power = \left(48 - \frac{f}{0.02}\right) \cdot P_{\max,FC} \qquad (2.8)$$

where f is the system frequency given in per unit [pu] (pu = per unit, i.e.,50 Hz = 1 pu) and $P_{max,FC}$ is the maximum fuel cell power given in watts [W]. A 6 kW fuel cell was chosen in order to meet the base load requirement. The fuel cell output power is then converted to the corresponding hydrogen flow needed. The corresponding hydrogen flow rate is calculated based on the lower hydrogen heating value (33.3 kWh/kg H_2) and assumption of fuel cell energy efficiency of 50 %.

2.7 Hydrogen subsystem ON/OFF controller

The electrolyser and fuel cell operation in the system frequency range are shown in Figure 7. The electrolyser controller measures the system frequency and switches the electrolyser ON at the upper frequency limit (ELY_{ON}) and switches the electrolyser OFF at the lower limit (ELY_{OFF}). The fuel cell is switched ON when the system frequency drops down to the lower limit ($FC_{ON/OFF}$). The electrolyser experience additional stress during start-up/shut-down due to possible large deviation from its nominal operation design point. High frequency ON/OFF switching will cause an extra decrease in electrolyser performance and lifetime. Therefore a timer that insures at least 2 hour continuous electrolyser operation is implemented.

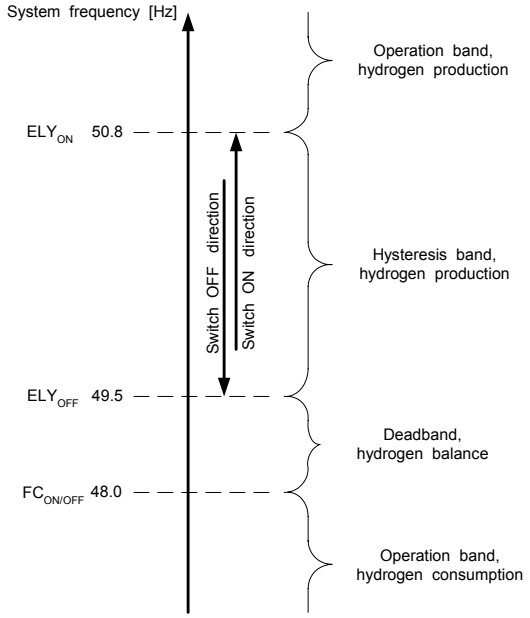

Figure 7 Electrolyser and fuel cell operation controlled by system frequency.

3 Results and discussion

Evaluation criteria

The simulation model provides indications about the systems power quality. The most important aspects of power quality are voltage control and system frequency stability. Because of the large computational CPU and memory requirement of the system model, the results will be based on 15 – 40 seconds time-spans.

The European standard BSEN50160 [11] requires that a non-interconnected (i.e. stand-alone) system should achieve the following:

- 50 Hz ± 2 % (i.e. 49 – 51 Hz) for 95 % of week; ± 15 % (i.e. 42.5-57.5 Hz) for 100 % of week
- 230 V ± 10 % (i.e. 207 – 253 V) for 95 % of week
- over 1 week, 95 % of the 10 minute rms values of negative phase sequence component shall be within 0 to 2 %, of positive phase sequence component ("in some areas … unbalanced up to about 3 % at three-phase supply terminals")

The aim of this study is to compare the power quality of the wind-HSAPS with the power quality of the datum wind-SAPS. In other words, would the end-user notice any difference in the power quality if a hydrogen subsystem had been implemented? Due to use of power electronics, the quality of the power supplied to the electrolyser and the characteristic of the power required from the fuel cell are also of interest regarding the component lifetime. Important criteria for evaluation of the hydrogen subsystem are:

- Monitoring the electrolyser's and the fuel cell's voltage/current levels and ripple voltage/current due to power conditioning. However, the focus in this work will be upon the power quality supplied to the electrolyser.
- Monitoring the ON/OFF switching of the fuel cell and electrolyser. Evaluation of the hydrogen subsystem's control strategy.

The power quality of the wind-HSAPS will mainly be investigated by performing a sensitivity test by altering two parameters; (1) changing the wind speed, and (2) either the hydrogen subsystem, in this case only represented by the electrolyser, is implemented or not. A total of four simulation test runs are carried out.

Overview of simulation test runs

Table 1 shows the scheme for the sensitivity test of the wind-HSAPS model. The wind speed is either a constant value or a set of measured data. A constant wind speed is of course unrealistic, but it is convenient to introduce minimal disturbances to the wind-HSAPS model when investigating the influence of the electrolyser. Two data sets containing wind speed data with mean values of 10 m/s and 12 m/s are used to evaluate the electrolyser operation under more realistic conditions. 10 m/s and 12 m/s are defined as mid and high wind speeds in this case, respectively. The chosen size of the electrolyser stack is 8 kW_{DC}, which produces hydrogen at a rate of about 30 NL/min that is about half the hydrogen flow rate consumed by the fuel cell running at peak power of 6 kW_{DC}. However, it will be showed that the average annual fuel cell power output for a measured wind speed data set is approximately 4 kW_{DC}, thus the hydrogen flow rate produced and consumed is about the same.

Test run#1 and Test run#2 are used to evaluate the system response when an electrolyser is implemented. Important computations are the average system voltage transients and the system frequency transients on the AC bus. In addition, Test run#2 is used to evaluate the ripple voltage/current from the rectifier to the electrolyser.

Test run#3 and Test run#4 are utilised for investigation of the hydrogen subsystem ON/OFF controller performance with measured wind speed data. Further more, Test run#3 is also used for evaluations of the AC bus power quality when an electrolyser is implemented during fluctuating wind speed, in addition to evaluation of the corresponding DC power supplied to the electrolyser.

Table 1 Overview of the four simulation test runs.

Test run #	**Wind speed**	**Electrolyser size [kW_{DC}]**
1	Constant 12 m/s	No electrolyser
2		8
3	Wind data, mean 12 m/s	
4	Wind data, mean 10 m/s	

Test run#1

Figure 8 shows the mean voltage of all the three phases (rms value) for the datum wind-SAPS at a constant wind speed of 12 m/s. The mean value is 227 V with a deviation of only ± 2 %, which is well within the specification.

The mean system frequency is 50.2 Hz, varying between 48.5 Hz and 51.5 Hz as showed in Figure 9. A number of simulation runs were performed in order to check the reproducibility. The standard deviation was found to vary between 0.8 Hz and 1.1 Hz, resulting in a frequency deviation between ± 3 – 4 %, somewhat outside the limit of ± 2 %, but well within the limit of ± 15 %. Due to high wind speed and the rather low base load level (6 kW_{AC}), the DILC has to fill a large gap between wind turbine's power output and load demand as shown for the active power flow in Figure 10. The reactive power flows in the system are also shown in Figure 10 (lower part) to illustrate the balance between the SC and the PFC that supplies the wind turbine with the required reactive power.

Figure 9 shows the ON/OFF switching of the resistive loads regulated by the fuzzy logic controllers implemented in the DILC. As seen from the system frequency in Figure 9, the DILC are not able to completely level out the frequency fluctuations but ensures the frequency to stay within the limit. More dynamic operation of the DILC is possible by tuning the fuzzy controller for higher sensitivity, but this increases the computational-time drastically during simulations. Previous work has, however, shown better frequency control with well-optimized load controllers [12]. The reason for the fluctuation in the system, even with constant load and constant wind speed, is because of the mechanical inertia in the wind turbine and the SC, in addition to an initial mismatch between the active power for the base load and the wind turbine output. The mechanical inertia in the system makes the DILC overshoot the frequency during regulation because the DILC's fuzzy controllers are not optimized. Optimisation of the DILC's fuzzy controllers is however not a subject in this work.

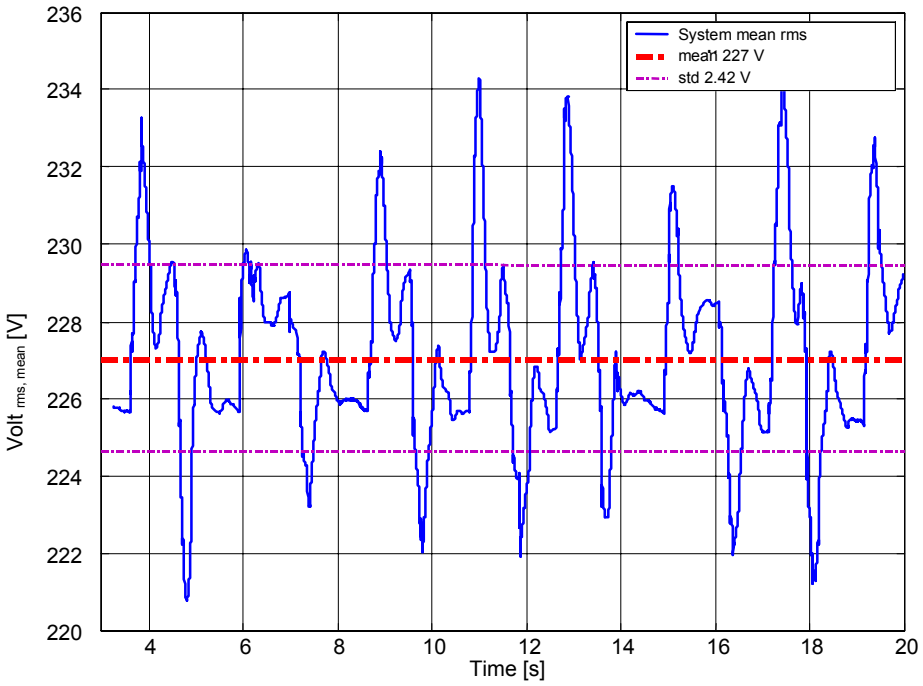

Figure 8 Mean rms voltage for a system without electrolyser at constant wind speed of 12 m/s.

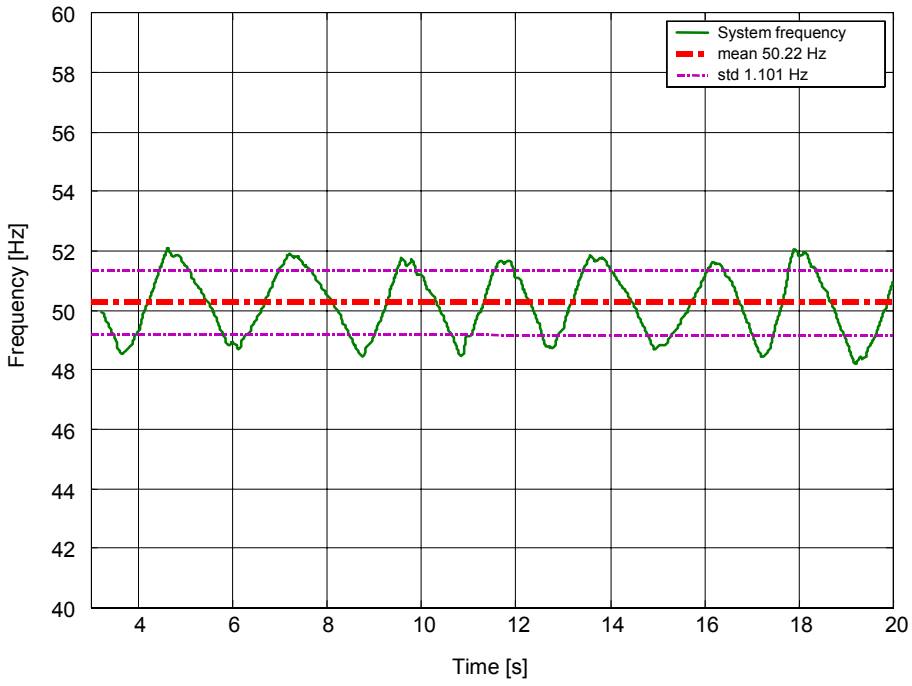

Figure 9 Frequency for a system without electrolyser at constant wind speed of 12 m/s.

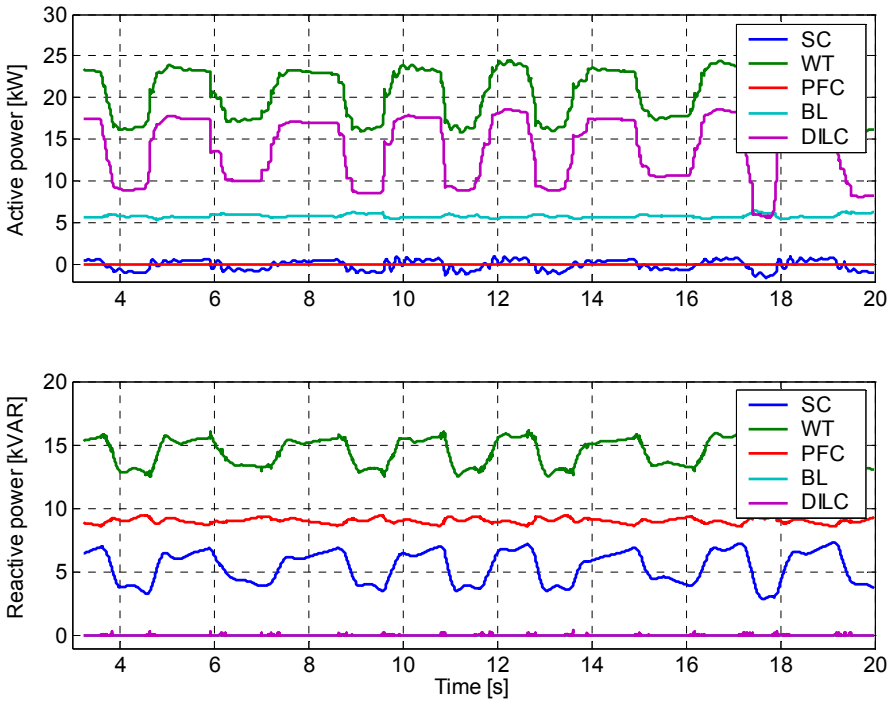

Figure 10 Active and reactive power in a system without electrolyser. SC=synchronous compensator, WT=wind turbine, PFC=power factor correction capacitor, BL=base load, and DILC=control load.

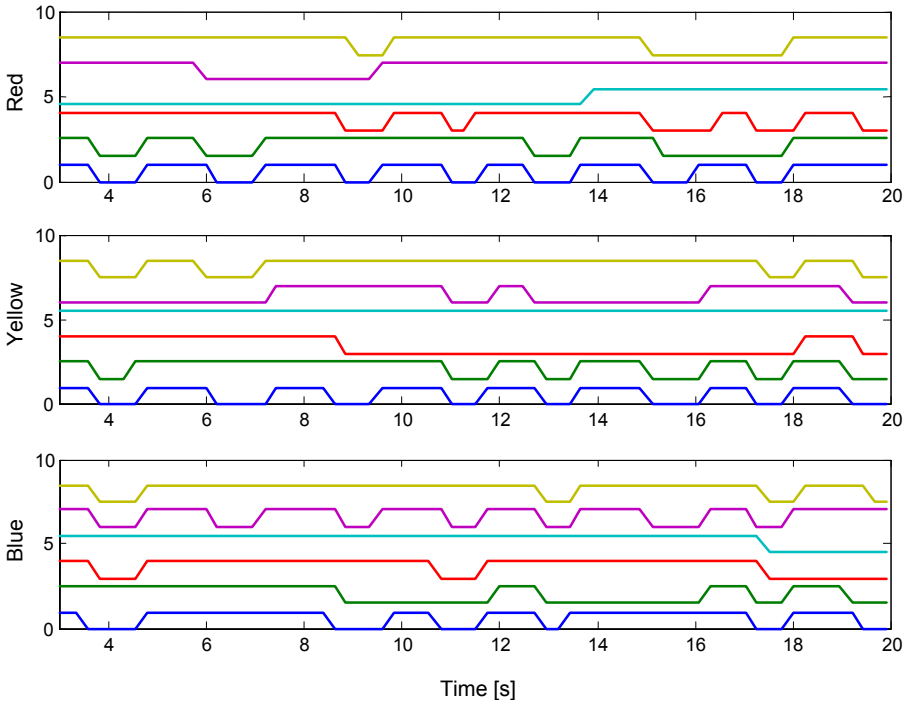

Figure 11 Resistive loads implemented in the DILC are switched on and off. There are six resistive loads on each phase as indicated.

Test run#2

Figure 12 – 17 show the system and component behaviour with an 8 kW_{DC} electrolyser connected at a constant wind speed of 12 m/s. The controller switches on the electrolyser after 4.5 seconds. The AVR shows good regulation, as the average voltage is 226 V with a standard deviation of 2.5 V, which is well within the limits as shown in Figure 12. Compared to the system without an electrolyser, the mean system frequency shown in Figure 13 is lowered by approximately 0.4 Hz to 49.8 Hz. The standard deviation is 0.8 Hz, which is reproducible unlike the case found in Test run#1. An interesting aspect here is that the electrolyser helps the DILC stabilize the system frequency by increasing the total amount of constant load during high wind speed, thus reducing the level of power mismatch between wind turbine and load (base load + electrolyser) as shown in Figure 14. The electrolyser is in this case acting as a coarse load controller, while the DILC acts as a fine-tuning load controller. Figure 14 also shows that the active power to the electrolyser is constant at 8.7 kW_{AC}, while the reactive power to the electrolyser is about 1 kVAR due to the rectifier.

Figure 15 shows the unregulated operation of the electrolyser at constant 8.0 kW_{DC}, indicating that the transformer and the rectifier are modelled with a total efficiency of about 92 %. Figure 15 also shows that there is no need for backup power, because the frequency does not go below the lower limit of 48.0 Hz. The electrolyser voltage and current are given in Figure 16, showing that the power electronics and the anti ripple capacitance filter are working properly. The DILC ON/OFF switching showed in Figure 17 is less frequent compared to the DILC operation in the datum wind-SAPS shown in Figure 13.

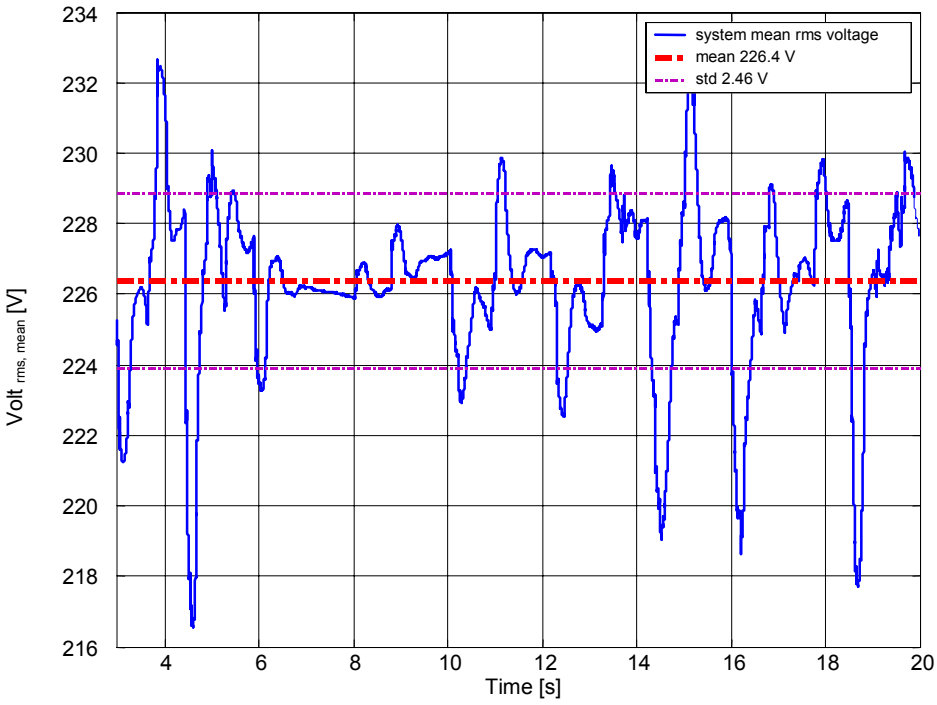

Figure 12 Mean rms voltage for a system with an 8 kW_{DC} electrolyser at constant wind speed of 12 m/s.

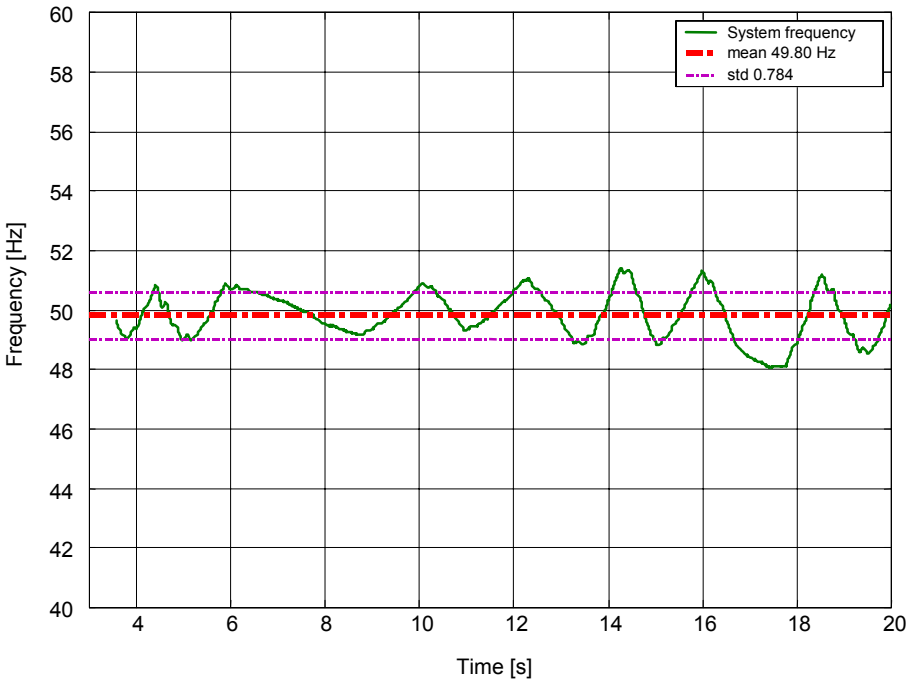

Figure 13 Frequency for a system with 8 kW_{DC} electrolyser at constant wind speed of 12 m/s.

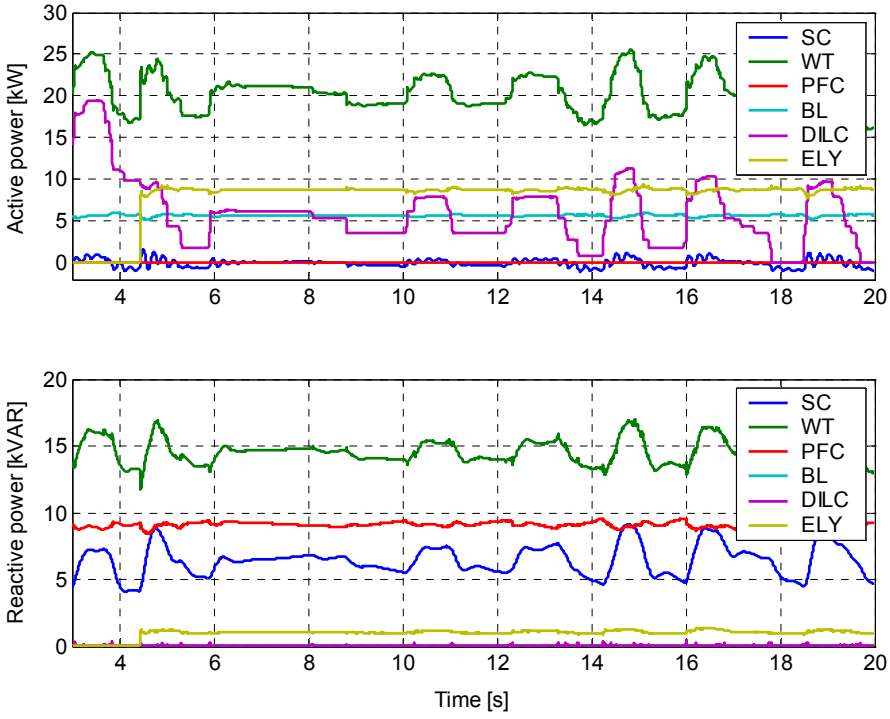

Figure 14 Active and reactive power in a system with an 8 kW_{DC} electrolyser connected. SC=synchronous compensator, WT=wind turbine, PFC=power factor correction capacitor, BL=base load, DILC=control load, and ELY=electrolyser.

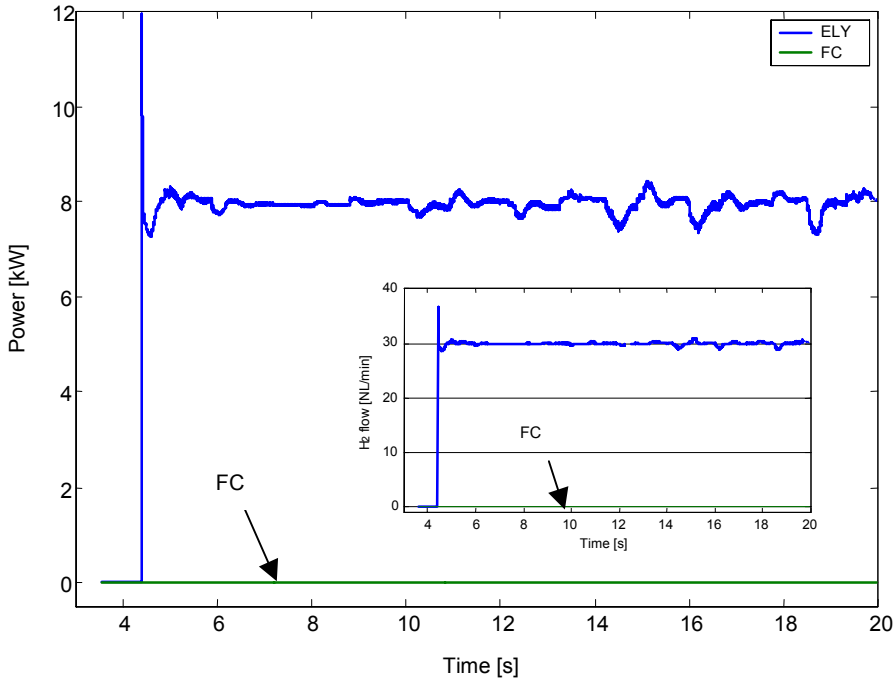

Figure 15 DC power supplied to electrolyser. As indicated there is no need for fuel cell start-up (green line). The corresponding hydrogen flow is also shown. ELY=electrolyser, and FC=fuel cell.

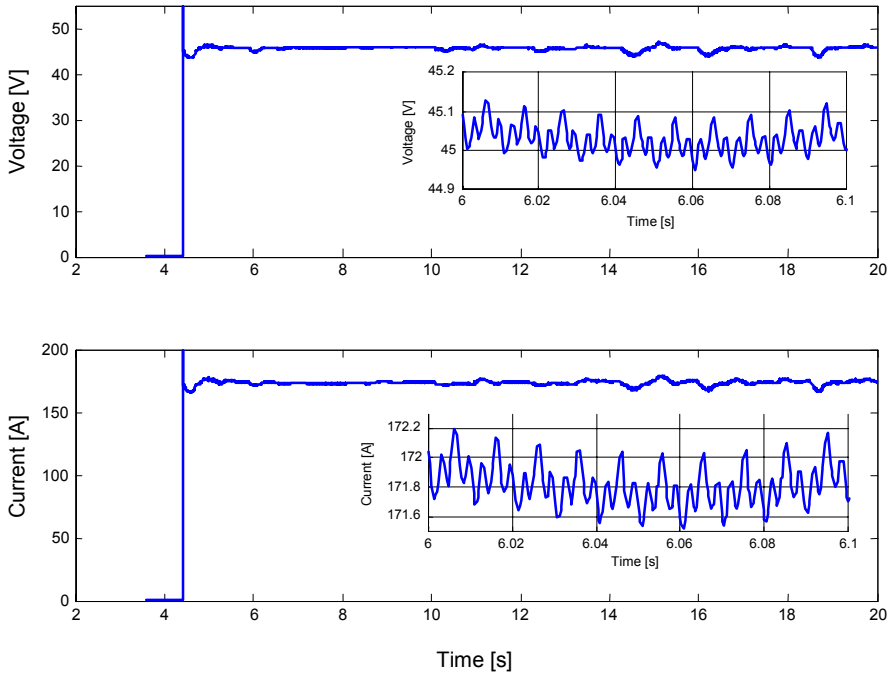

Figure 16 Rather smooth electrolyser DC voltage and current proving the benefit of the anti ripple filtering.

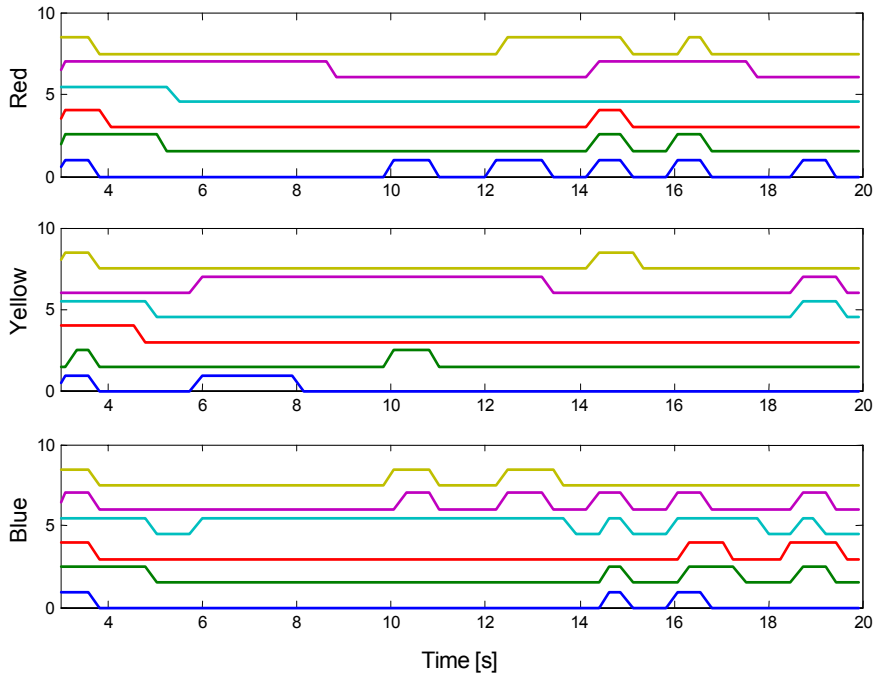

Figure 17 Resistive loads implemented in the DILC are switched on and off for a system with an 8 kW_{DC} electrolyser. There are six resistive controllers on each phase.

Test run#3

A data set of wind speed varying between about 10.5 m/s and 13 m/s measured at the northeast coast of England is shown in Figure 18. The data set is used as input to the wind-HSAPS model in this test run and the electrolyser is switched ON after 5.2 seconds.

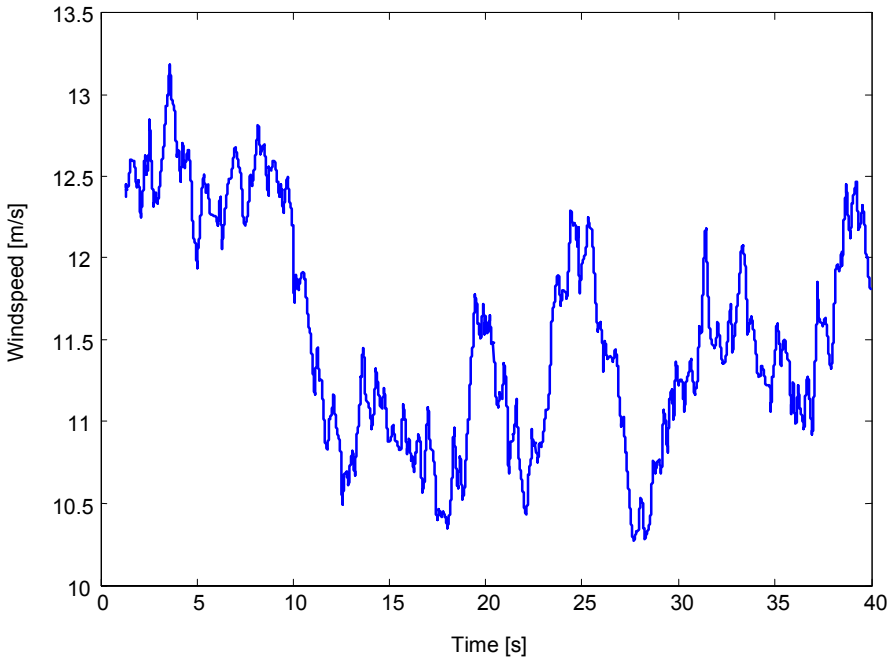

Figure 18 Measured wind speed data with mean wind speed 11.5 m/s.

Figure 19 shows the system rms voltages for all three phases. The voltage control can be seen to be good, varying between 215 – 233 V at an average of 226.6 V, which is well within the limits. The worst imbalance between two phase-voltages was found to be about 7 V after 7 seconds, a deviation of 3 % of nominal voltage, which is within the limit.

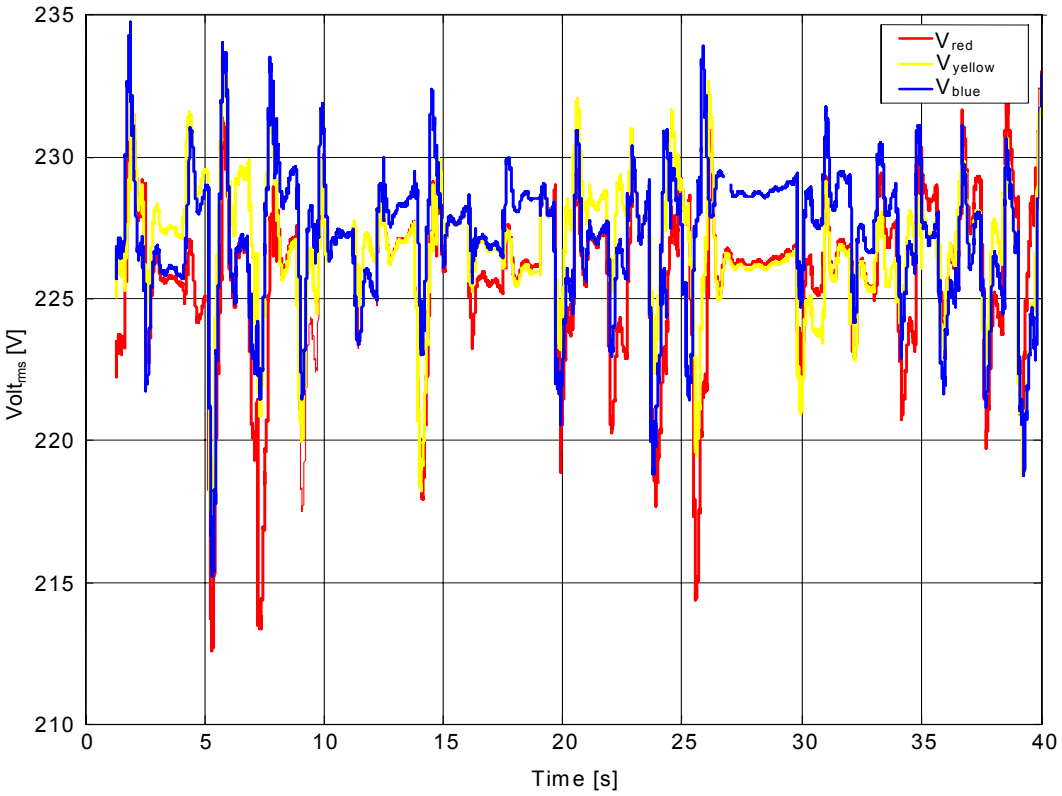

Figure 19 System rms voltages for each of the three phases with 11 m/s wind data as input.

The system frequency can be seen in Figure 20 to vary between 48.1 Hz and 51.4 Hz at an average of 49.9 Hz with standard deviation 0.8 Hz that is reproducible. The electrolyser DC power, voltage and current are shown in Figure 21. The simulated electrolyser voltage is within the allowable voltage operation range of ± 10 %, where the upper voltage limit is most critical. This voltage deviation must not be confused with the ripple voltage level of maximum 1 % as discussed in Test run#2.

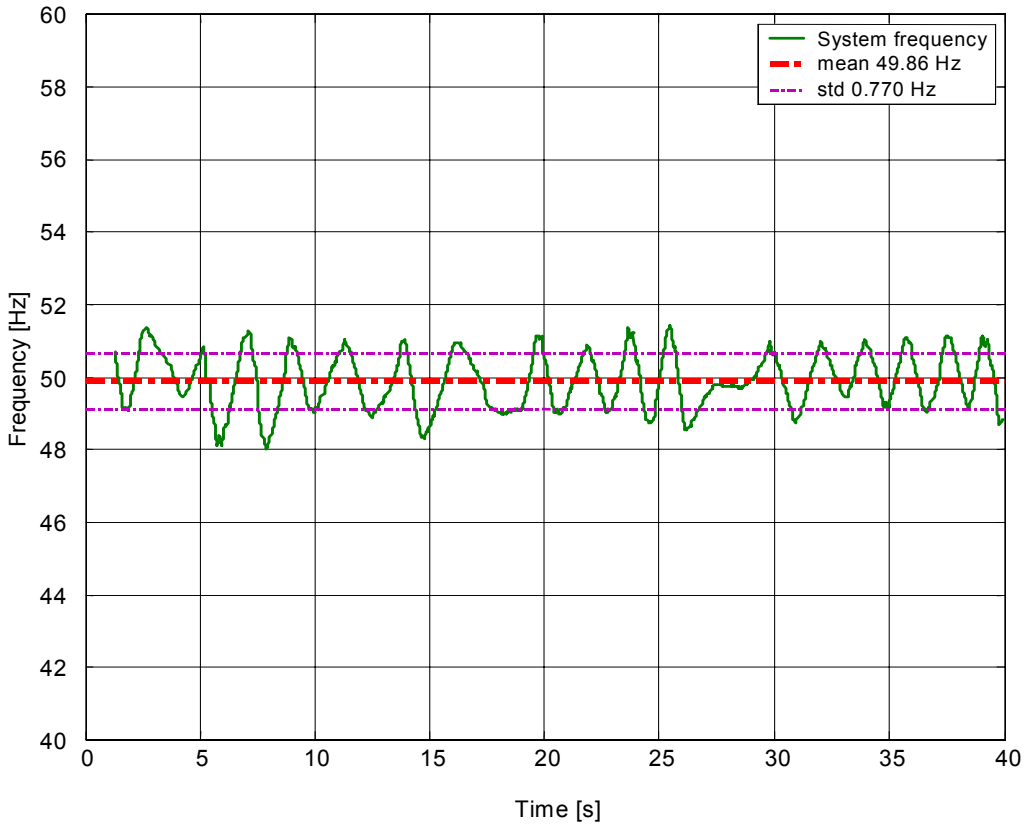

Figure 20 Frequency for a system with 8 kW_{DC} electrolyser and 11 – 12 m/s wind data as input.

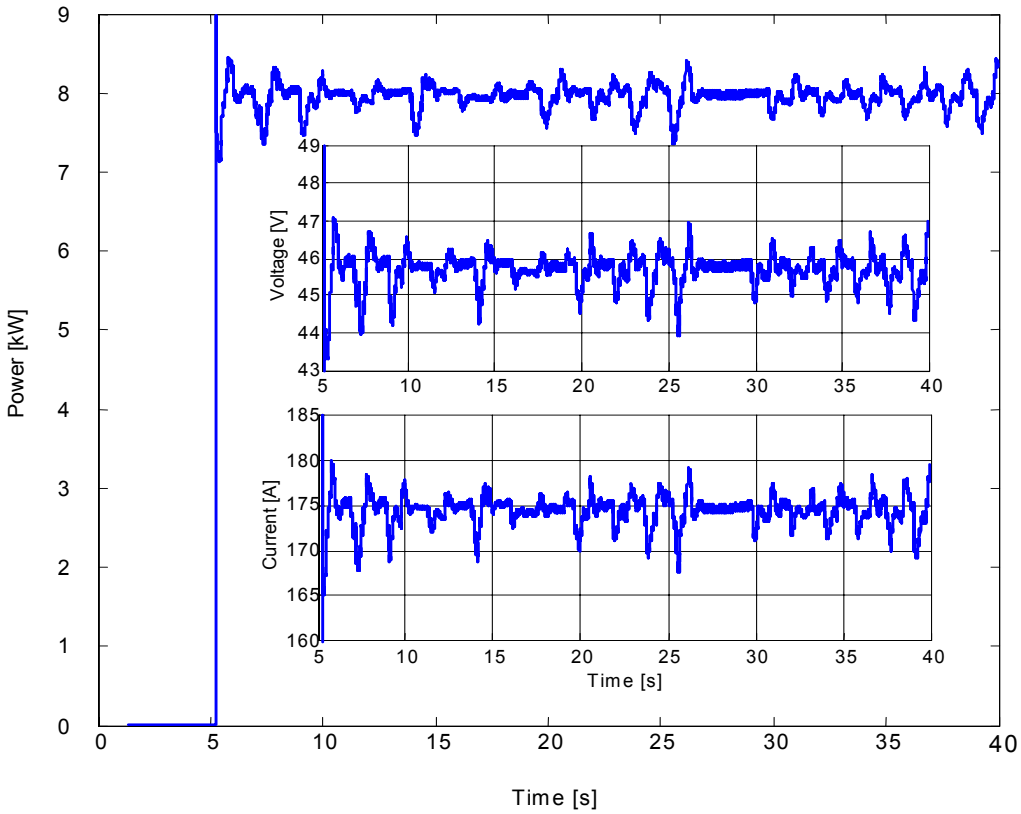

Figure 21 Electrolyser DC power, voltage and current characteristics. The voltage deviation of about 10 % must not be confused with the ripple voltage earlier set at maximum of 1 %.

Test run#4

The results from Test run#1 – 3 imply that an unregulated electrolyser, operated at a constant power level that is about half the peak power of the wind turbine, can be used as an active load controller during high wind speeds where only the system frequency is used as ON/OFF parameter for the electrolyser. In Test run#4 the hydrogen subsystem ON/OFF controller will be evaluated with lower wind speed.

Figure 22 shows the data set of lower wind speed varying between about 7.5 m/s and 10.5 m/s. From Figure 23, which shows the hydrogen flow generated and consumed by the electrolyser and the fuel cell respectively, it can be seen that the electrolyser starts even at lower wind speeds. Once the electrolyser is started it will run for at least two hours to avoid rapid ON/OFF switching according to the hydrogen subsystem ON/OFF controller given in Section 2.7. The timer and the unregulated operation of the electrolyser cause the fuel cell to start-up, as indirectly shown by the hydrogen flow required by the fuel cell in Figure 23. Continuously parallel operation of the fuel cell and the electrolyser is nothing else than an expensive dump load where little net hydrogen is accumulated. This cause unnecessary wears on hydrogen components and must be avoided. Another timer is added to the hydrogen subsystem ON/OFF controller that switches OFF the electrolyser if both the electrolyser and the fuel cell have been operated continuously in parallel for more than ten seconds, but it is not a robust solution regarding minimal ON/OFF switching of the electrolyser and the fuel cell.

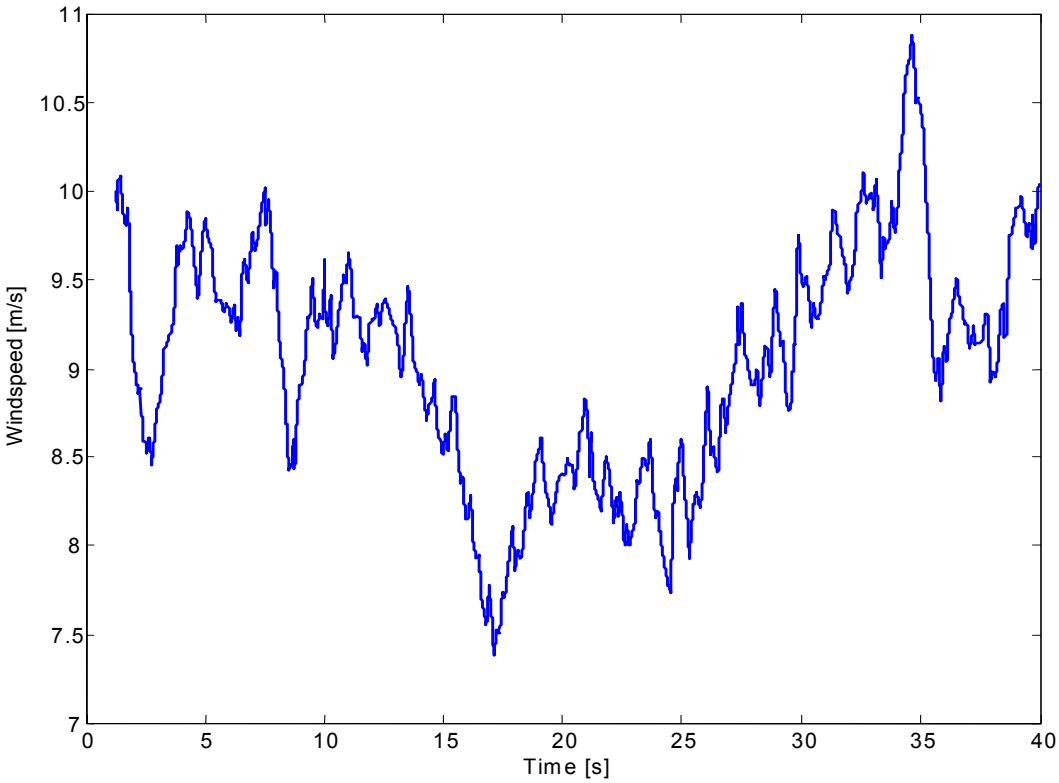

Figure 22 Measured wind speed used in the simulation defined as lower wind speeds.

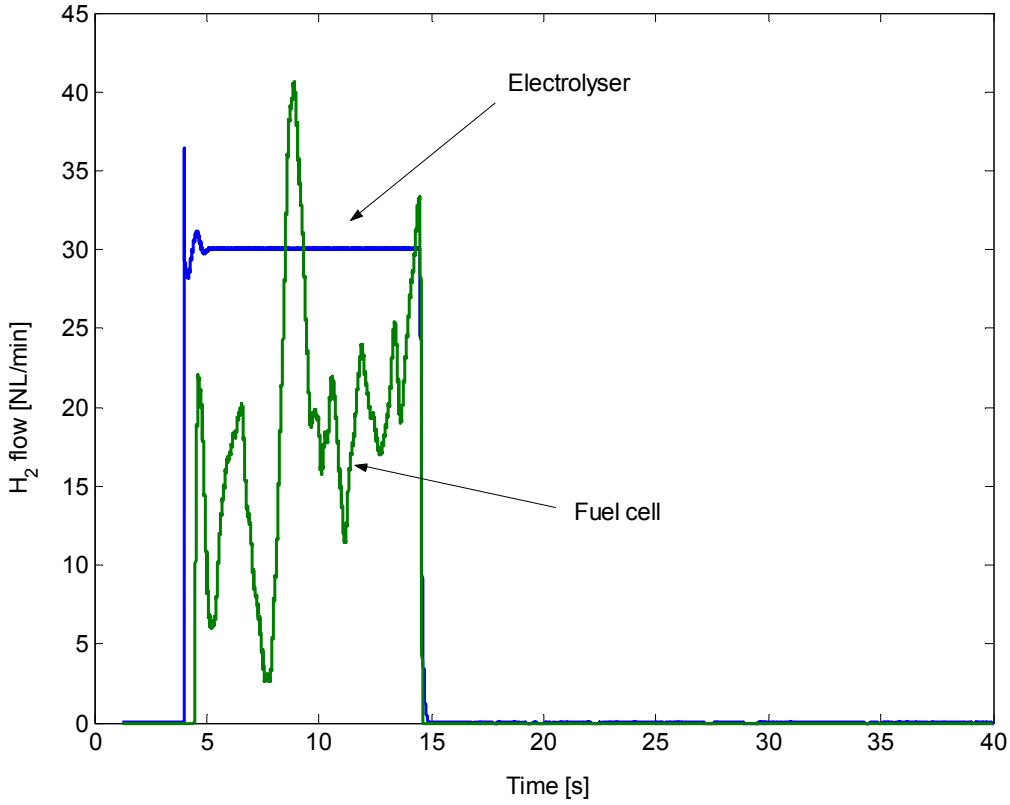

Figure 23 Hydrogen production (blue) and consumption (green) by electrolyser and fuel cell respectively.

Sizing of the H_2-storage and heat distribution based on annual simulation

A simple Simulink model study based on annual power flow through the wind-HSAPS has been conducted. The 20 kW wind turbine is modelled by using a look-up table, which interpolates the correlation between wind speed and wind turbine power output. The base load is fixed at 6 kW while the 8.0 kW (8.7 kW_{AC}) electrolyser is switched ON when the wind turbine power exceeds 14.7 kW (load + electrolyser). Negative power in the system is simply defined as power supplied by the fuel cell. A 600 kWh hydrogen storage (~200 Nm^3 H_2) matches this system setup quite well.

The hydrogen state-of-charge throughout the year is given in Figure 24. Maximum and minimum state of charge is 90 % and 20 % respectively. When the final hydrogen state-of-charge is about the same as the initial state-of-charge, it indicates that the chosen sizes of the electrolyser, the fuel cell, and the hydrogen storage are reasonable. If the hydrogen storage was a 200 bars compressed steel vessel, it would occupy about 1 m^3 with a weight of some few hundreds kilos including the compressor. A metal hydride with the benefit of low pressure operation, and assuming commercially available low-temperature hydride of the AB_5 or AB_2 type (1.5 wt% H_2 in alloy) would have a mass of about 1400 – 1800 kg. The metal hydride physical volume would be in the same range as the pressure vessel. The input wind speed data with time resolution of 15 minutes is also given in Figure 24. The mean power outputs and inputs along with operation hours and system energy balance are given in Table 2.

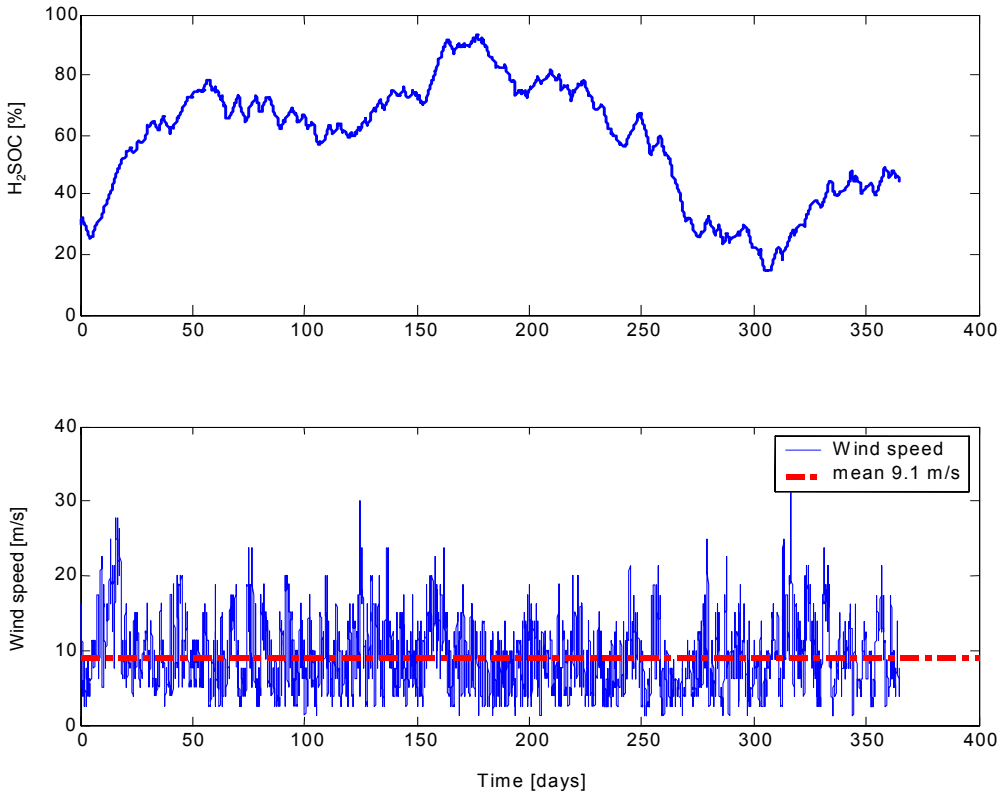

Figure 24 Annual hydrogen state-of-charge and wind speed for a wind-HSAPS.

Table 2 Energy balance, operation hours and mean power (based on component operation time) for the wind-HSAPS

Component	Energy [kWh]	Operation time [hr]	Power [kW_{mean}]	Heat generation [kWh]
Wind turbine	112400	8708	12.9	0
Electrolyser	32890	3781	8.7	6530
Load controllers (DILCs)	38680	5693	6.8	38680
Base load	52560	8760	6	0
Fuel cell	11710	3067	3.8	12550

The fuel cell- and electrolyser operation times are 3000 and 3800 hours, respectively. This is within and quite close to the commonly guarantied PEM cell lifetime warranty. In a real system, shifting the frequency settings and letting the DILC work more can reduce the electrolyser operation time. No frequency regulation is available in this simple annual system model. The electric energy share of a total of 83 280 kWh between the DILC, the fuel cell and the electrolyser shown in Figure 25 indicates that the DILC and the electrolyser equally share the excess energy. The fuel cell covers the deficit wind turbine energy, which is about 1/6 of the excess energy.

Another interesting parameter in this annual simulation study is the distribution of the generated heat. The components that generate heat in this wind-HSAPS are the DILC, the electrolyser, and the fuel cell. The heat generated in the electrochemical components is the difference between the thermo-neutral cell voltage and the actual cell voltage multiplied by number of cells in the stack and the total stack current. The mean heat (based on 8760 hrs operation) generated by the combination of the DILC and the hydrogen subsystem is 6.6 kW compared to 4.4 kW if the heat generated by

the hydrogen subsystem were excluded. It can be seen from Figure 25 that the electrolyser and the fuel cell contribute with about 33 % of the total heat production of 57 760 kWh. With a constant heat demand of 6.6 kW, matching the annual mean heat generated, Figure 26 shows the water temperature profile for a heat distribution/buffer system. Even with the constant heat load, the heat buffer is never below 50°C. It is assumed that there are no heat losses in the system except for in the water storage tank. The storage tank containing about 50 m^3 heated water is encapsulated with a standard isolation material with a specific heat transfer value of 0.036 Wm/K. The resulting total thermal resistance with 0.2 m isolation is $(1/ (0.036/0.2))_{isolation}$ K/W + 0.17_{air} K/W = 5.7 K/W. The heat capacitance of the steel tank and tubes is neglected compared to the heat capacitance of the water, with specific heat capacity of 4.2 kJ/kg-K.

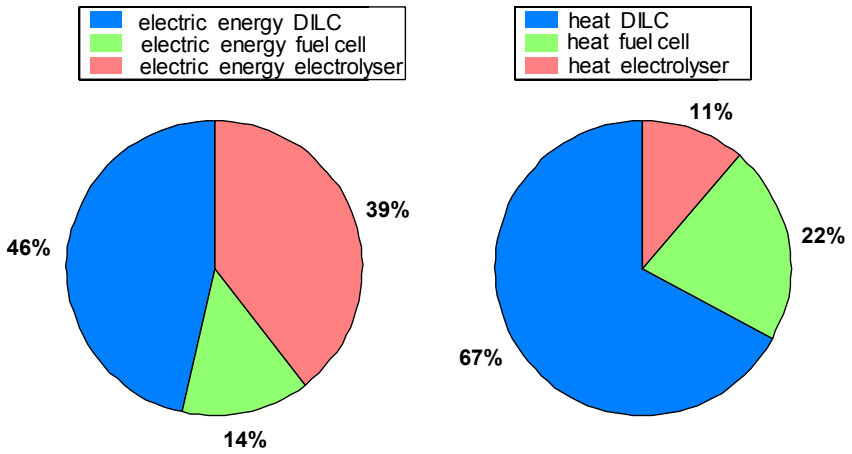

Figure 25 Distribution of electric energy and heating energy between the DILC, fuel cell and the electrolyser.

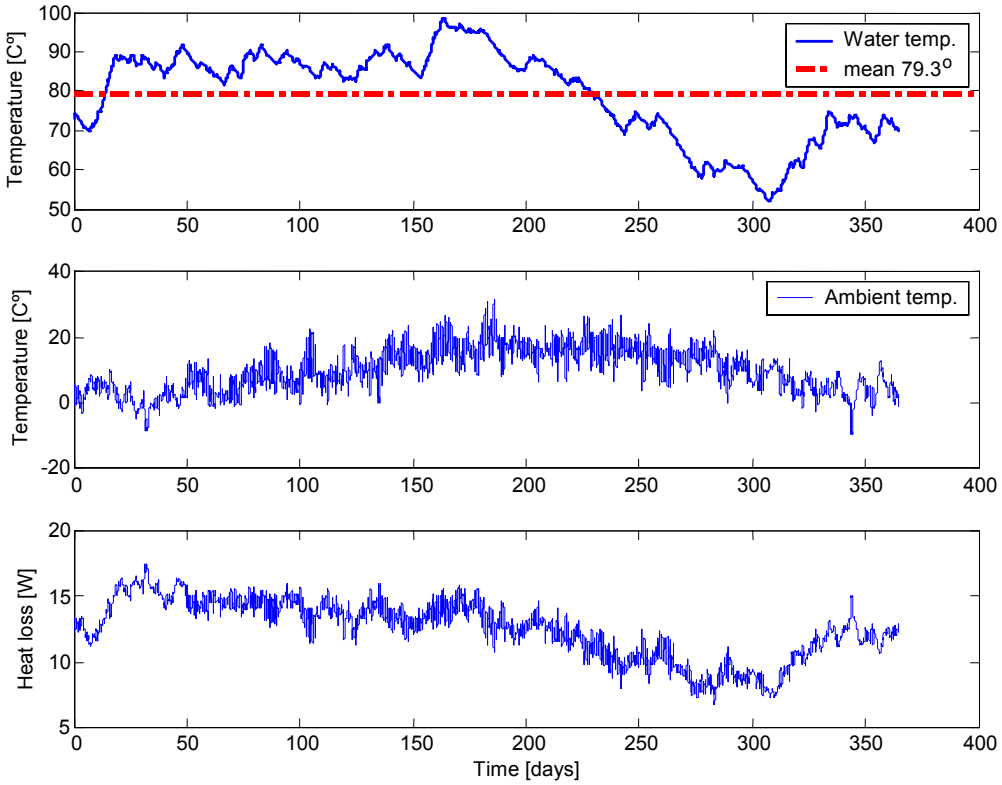

Figure 26 Distributed heating water temperature, ambient temperature and the heat loss in the isolated water tank.

4 Recommendations

At lower wind speeds the sole use of the system frequency as an ON/OFF parameter seems to be too sensitive for regulation of the hydrogen subsystem. One simple solution could be to reduce the electrolyser stack, but then again, the advantage of the energy storage concept might become minimal because a too small amount of hydrogen produced would be of lesser practical interest. Another more promising solution would be to utilise e.g. a fuzzy ON/OFF controller that would take into consideration the system frequency, the frequency derivative, the average measured wind speed e.g. for the last hour, and any possible wind speed forecast. And when the electrolyser is switched ON, the electrolyser current should preferably be regulated according to the actual excess wind turbine power in the system. Similar work has been done by [13] where the electrolyser power follows the wind power.

Further recommendations would be to investigate the option where the fuel cell is connected to the three-phase system with power electronics as suggested in Figure 27, and not through the DC machine and the mechanical shaft spinning the synchronous compensator as indicated in Figure 1. Preliminary investigations indicate that the energy efficiency through the DC motor and the synchronous compensator would be about 82 –85 %, compared to an energy efficiency of about 90 – 93 % through the power electronics. It should also be mentioned that the mechanical system suffers from mechanical wear and maintenance. But a step-up DC/DC converter might be necessary in order to ensure satisfactory voltage level for proper operation of the inverter [14]. This could reduce the energy efficiency to about 86 – 89 %. However, the energy efficiency for the power electronics has potential for further improvements, especially when the semiconductor technology will be based on silicon carbide in the near future [8].

Based on simulation work done for a grid-connected fuel cell [15], a switching control signal for the fuel cell inverter can be generated through a PID-type controller to adjust the phase difference between the voltage of the system bus and the voltage of the inverter. It then supplies more or less active power to the system bus, compensating for the change in system loading thus regulating the system frequency. Also, a control signal proportional to the voltage-change can activate the angle controller through another PID-type controller. Then an appropriate switching signal is generated to modulate the amplitude of the inverter output voltage in relation to the system bus voltage, thus implementing reactive power and regulating the system voltage. On the other hand, since the synchronous compensator (SC) regulates the system voltage more or less throughout the whole year, using a fuel cell would not be rational for the time being because of the relative short manufacturer lifetime warranty (~3000 hrs). However, the fuel cell would be suitable for regulating the active power and thus the frequency during low wind speed and peaks in load requirements. The fuel cell in the simulation study done by [15] was found to stabilize the grid at sudden perturbations. Because a SAPS is more vulnerable to perturbations compared to a “stiffer” grid, it is important to investigate if the fuel cell and its controller are robust enough for SAPS.

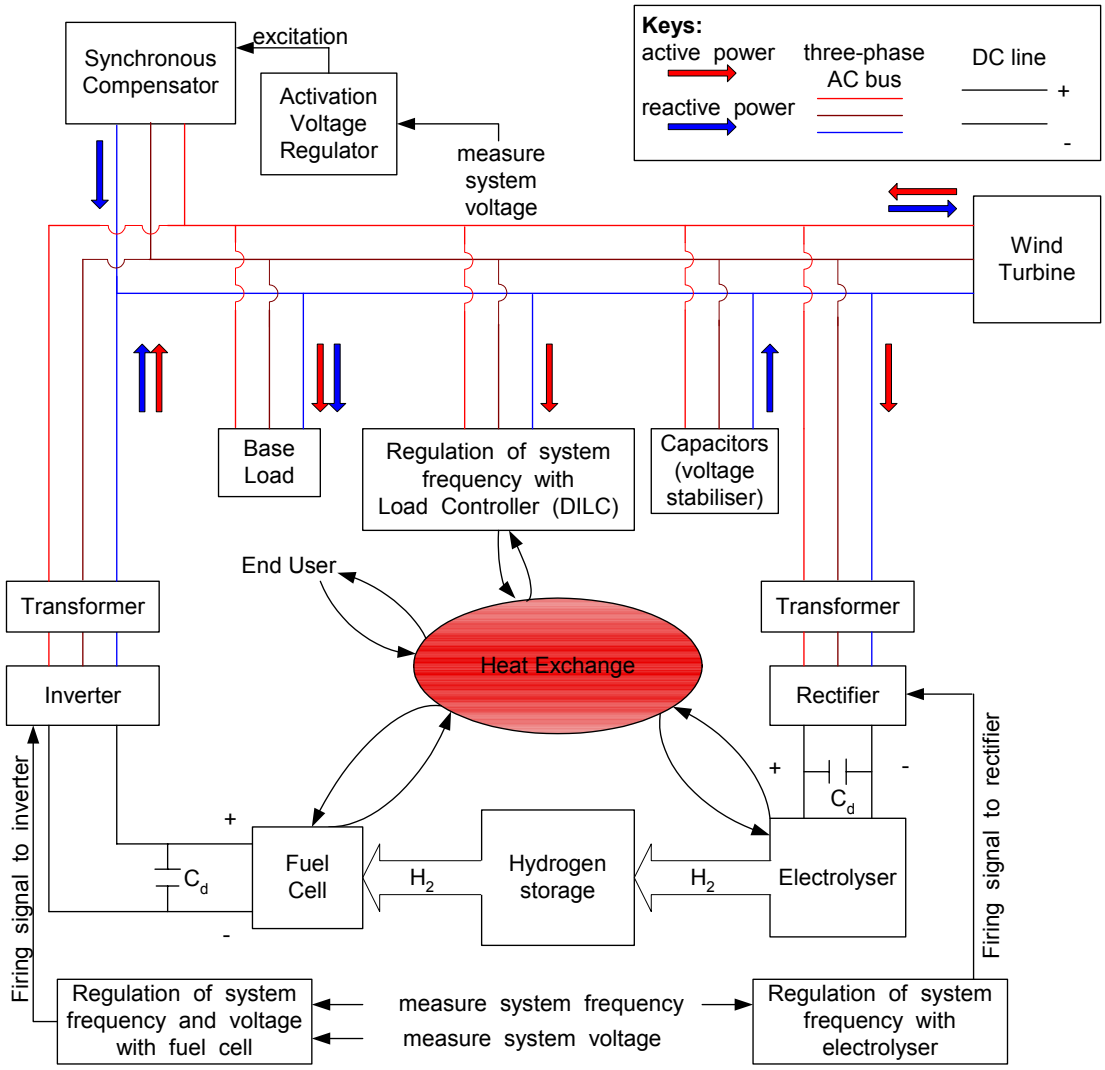

Figure 27 Wind-HSAPS with fuel cell connected to the system through power electronics, not through the DC motor and the mechanical shaft as indicated in Figure 1.

5 Conclusions

These preliminary test results are encouraging, regarding the use of an electrolyser both as a flexible power sink and a hydrogen production unit in order to store renewable energy as hydrogen for re-electrification during deficits in wind power or peaks in demand. Following integration of an electrolyser into the wind-HSAPS, the system power quality, mainly the frequency and voltage, have not been found to differ significantly from the wind-SAPS without the electrolyser. In fact the system frequency has been observed to be more stable when the electrolyser operates in parallel with the Distributed Intelligent Load Controller (DILC), especially during periods of high excess energy in the system.

It is on the other hand clear that the electrolyser needs more parameters in addition to the system frequency for proper ON/OFF switching of the electrolyser (this would also be the case for the fuel cell). Average wind speeds for e.g. the last hour, wind speed forecast, and the derivative of the system frequency has been suggested as additional parameters for the electrolyser ON/OFF switching, thereby reducing the

risk for electrolyser start-up at lower wind speeds. Apart from the actual on/off switching, it has been suggested to control the electrolyser operation to "shave" off the actual excess wind power in order to avoid unnecessary fuel cell start-ups for stabilising of system frequency when an unregulated electrolyser would draw too much power from the wind turbine.

The heat generated by the DILC, which can be used as a heat source for the end user, seems promising for keeping the fuel cell- and electrolyser stack (low temperature PEM or alkaline technology) temperature within the nominal operating temperature, thus minimizing start-up transients. Once the electrochemical components have started up they can also contribute to the total heat generation. The fuel cell is particularly important in this regard as it can provide heat during deficits in wind power or peaks in demand.

Acknowledgements
The Norwegian Research Council has financially supported this work.

References

1. www.mathworks.com.
2. The Math Works Inc., *Matlab Power System User's Guide Ver1*. 1999.
3. P.C.Krause, O.Wasynczuk, and S.D.Sudhoff, *Analysis of Electrical Machinery*. IEEE Power Systems Engineering Series. 1995.
4. P.Kundur, *Power System Stability and Control*. Power System Engineering Series. 1994, New York: McGraw-Hill.
5. The Math Works Inc., *Matlab Fuzzy Logic Toolbox User's Guide Ver2*. 1998.
6. W.M.Somerville. *Fair Isle renewed*. in *British Wind Energy Association Conference*. 1999.
7. I.Ba-maung, I.A.Irvine, and S.McDonald, *Maximising the penetration of wind generated electricity into a weak distribution network on a remote Scottish island by employing demand side load management control using radio telemetry.* ScottishPower Technology.
8. C.W.Lander, *Power Electronics*. 3 ed. 1993, London: McGraw-Hill.
9. E.Rasten, *Electrocatalysis in Water Electrolysis with Solid Polymer Electrolyte*, in *Department of Materials Technology*. 2001, PhD.Thesis, Norwegian University of Science and Technology (NTNU): Trondheim, Norway.
10. R.J.Smith, *Electronics Circuits and Devices*. 1987, New York: Wiley.
11. European Standard EN50160, *Voltage characteristics of electricity supplied by public distribution systems*. CENELEC, November 1994. p. 18-19.
12. P.Taylor, *Doctoral Thesis "Distributed Intelligent Load Control of Autonomous Renewable Energy Systems"*. 2001, UMIST and Econnect, UK.
13. F.Menzl, M.Wenske, and J.Lehmann. *Windmill-electrolyser-system for a hydrogen based energy supply*. *European Wind Energy Conference*. 1999. Nice, France.
14. Department of Energy/National Energy Technology Laboratory, *Fuel Cell Handbook*. 2002.
15. K.Ro and S.Rahman, *Control of grid-connected fuel cell plants for enhancement of power system stability.* Renewable energy, 2003. **28**: p. 397-407.

9. Conclusions and Recommendations

Three different control strategies for high-level operation of a Hydrogen stand-alone power system (HSAPS) were compared in Chapter 5. The comparison was carried out with the aid of semi empirical computer models generated from the experimental data measured in the hydrogen system laboratory. The traditional *battery five-step charger* was compared to two different control strategies proposed in this thesis for a HSAPS: *(1)* the *Control Matrix*, and *(2)* the *fuzzy controller*.

The Control Matrix represents a rigid and robust control algorithm that is very easy to implement as long as the number of control parameters is kept low (maximum 5 – 6 parameters). Large Control Matrixes might be hard to maintain and tune. However, this control algorithm can be very suitable for initial testing of a system, either a model or a real world system. The fuzzy controller was found to be both flexible and rather easy to implement into the HSAPS model. Because of its flexibility, this control algorithm could be useful for further tuning and optimisation of HSAPS for commercial use.

The hydrogen storage round-trip energy efficiency for the small-scale HSAPS during the laboratory test-week was found to be 28.1 %, reported on in Chapter 6. This number could be higher, especially if the average fuel cell power of 184 W had been closer to the nominal power of 500 W. It is encouraging that the hydrogen-loop energy efficiency for the laboratory HSAPS can reach 36.3 % with the fuel cell and electrolyser running at nominal power, indicating that larger HSAPS installations can operate with this energy efficiency even at partial loads and at low and fluctuating solar/wind energy input. Further, the energy hydrogen-loop efficiency for the laboratory HSAPS could reach 39.4 % if both the fuel cell and the electrolyser were operated at nominal power and if a large low pressure container had been used as hydrogen storage (less hydrogen purification), or the energy needed for hydrogen purification could be 100 % supplied by excess energy in the system.

No failures or instabilities were registered during the test-week (Chapter 6), thus the laboratory HSAPS promised good reliability and stability. On the other hand, allowing the fuel cell to charge the battery could introduce instability as discussed in Section 3.3.4. The fuel cell needed about five minutes before the stack could be connected to the HSAPS bus bar. The electrolyser was 100 % available throughout the whole test-week. The operational experience with the H_2-components comprising the electrolyser, metal hydride, and fuel cell showed very good reliability and availability. Both the electrolyser and the fuel cell were equipped with local control systems for automatic operations. These integrated local control systems made it easy to implement a high-level energy management into the laboratory HSAPS.

Two alternatives for hydrogen storage in a small-scale HSAPS were investigated in Chapter 7. Alternative 1 was pressurized steel vessel with compressor and Alternative 2 was metal hydride with gas dryer. Even though the metal hydride represents a safe storage method due to the low pressure (16 bars), the pressurized steel vessel with a diaphragm compressor was at the present found to be the most proper hydrogen storage for the small-scale system used in this work. This conclusion was primarily based on the fact that it is easier to know the exact amount of hydrogen in a pressurised steel vessel system compared to a metal hydride system. Also, with

present prices (2003) the pressurized vessel with diaphragm compressor is about half the price of the metal hydride system. However, with the estimated future price for metal hydrides the price will be about the same for the two different alternatives.

The preliminary test results in Chapter 8 was encouraging, regarding the use of an electrolyser both as a flexible power sink and a hydrogen production unit in order to store renewable energy as hydrogen for re-electrification during deficits in wind power or peaks in demand. Following integration of an electrolyser into the wind-HSAPS, the system power quality, mainly the frequency and voltage, have not been found to differ significantly from the wind-SAPS without the electrolyser. In fact the system frequency has been observed to be more stable when the electrolyser operates in parallel with the Distributed Intelligent Load Controller (DILC), especially during periods of high excess energy in the system. The heat generated by the DILC, which can be used as a heat source for the end user, seems promising for keeping the fuel cell- and electrolyser stack (low temperature PEM or alkaline technology) temperature within the nominal operating temperature, thus minimizing start-up transients. Once the electrochemical components have started up they can also contribute to the total heat generation. The fuel cell is particularly important in this regard as it can provide heat during deficits in wind power or peaks in demand.

Recommendations for future work

The high-level energy management fuzzy controller can further be improved by introducing a self-tuning algorithm for optimal performance. The self-tuning algorithm could be based on a *neural network* algorithm. Furthermore, if power electronics were to be used between the electrolyser/fuel cell and the common bus bar, the crisp output from the fuzzy controller could be scaled and used as a reference signal to control the DC/DC (or DC/AC) converters. E.g. when the output from the fuzzy controller is at minimum, the fuel cell converter would operate the fuel cell at full capacity. This is similar to the high-level strategy used in the SAPHYS project (reference [9] in Chapter 1), except they used the battery state-of-charge as reference signal, which is not as reliable as the output from the fuzzy controller. Use of converters is anyhow recommended in order to regulate the voltage on the bus bar, especially the fuel cell voltage, which in this case could vary with 25 %. Furthermore, electrochemical components are subject to degradation, thus, changes in nominal voltage levels can be compensated by means of controlling the voltage with the converters.

The energy requirement for the purification process of hydrogen to be stored in metal hydrides has potential for improvement. A suggestion for future work would be to investigate solar thermal energy as cooling source for cooling down hydrogen from the electrolyser saturated with water, thus, a large amount of the water would condensate and removed before entered the dryer column. The possibility to use vacuum to regenerate the desiccant is also interesting in order to avoid use of dry hydrogen from the main hydrogen storage. The penalty by using vacuum pump is of course introduction of additional auxiliaries that need maintenance.

Heat transfer based on air convection in the metal hydride is not recommended, especially not for out-door installations. A controllable heat exchanger transferring heat from the fuel cell stack to the metal hydride during discharge should be used.

Appendix A

Table A.1 Electrical specification of the DC power supply (6684A,Agilent Technologies)

Parameter	Value	Unit
Voltage range	0–60	V
Current range	0–80	A
Maximum Power	4800	W
Transient response time	< 900	µs

Table A.2 Electrical specification of programmable electronic load (PLZ603W,Kikusui)

Parameter	Value	Unit
Voltage range	0–120	V
Current range	0–120	A
Maximum Power	600	W
Transient response time	±30 % of set value, ±15	µs

Table A.3 Technical data of the PEM electrolyser system (Fraunhofer ISE)

Peak power	1750 W
Nominal voltage	48 V
Maximum operating current	35 A
Number of cells	26
Active area per cell	57 cm^2
Operating pressure	15 bar
Operating temperature	75 °C
Hydrogen production	390 Nl/h H_2
Gas purity	0.01–0.3 % O_2 in H_2
Electrolyte	Nafion 117
Water for electrolysis	Max. conductivity 1µS/cm
Cooling medium	Water
Rack dimensions	0.60 × 0.50 × 1.80 m
Power supply	240 Vac / 16 A (peripheral devices and control)

Table A.4a Technical data of the hydrogen gas dryer (MG03, AquaGas)

Parameter	Value
Gas inlet flow rate	0.5 Nm^3/h
Water vapour content	Saturated at inlet temperature 2.55 ppm at 70 °C and 1 atm at outlet
Operating pressure	16 bar
Operating temperature	40 °C
Absorption period	168 hours effective time
Type of desiccant	Mol. Sieve MS512
Quantity of desiccant	6 kg / tower
Reactivation gas	Dry nitrogen
Reactivation gas flow rate	10 Nm^3/h
Reactivation gas pressure	0–1 bar
Reactivation gas temperature	150-200 °C
Regeneration with N_2	6 hours heating and 2 hours cooling
Supply voltage	230 V, 50 Hz, 1 ph
Power consumption	1.5 kW

Table A.4b Technical data of the oxygen trap and heater (Deoxon, Alltech Associates)

Parameter	Value
Oxygen content	0.01–0.03 % at inlet 2 ppm at outlet
Dimensions	60 mm diameter and 230 mm high
Power consumption (heater)	100–200 W (continuous during system operation)

Table A.5 Specification for the PEM fuel cell system (PS-P-500-1, H Power)

Parameter	Value/type
Rated power	500 W
Peak power	630 W at 15 A
Power density	0.1 W/cm^2 at 500 W
Operating voltage	46 V at 12 A
Open circuit voltage	65 V
Number of cells	64
Active electrode area per cell	78 cm^2
Membrane (electrolyte)	Nafion 1135
Typical efficiency	42 %
Operating pressure	0.34 bar (max. inlet pressure: 2.06 bar)
Operating temperature	0–40 °C
Fuel	Hydrogen (industrial grade or better)
Oxidant	Air (air pump powered by the FC-stack)
Coolant	Forced air (fans powered by the FC-stack)
Rack dimensions	0.22 × 0.47 × 0.29 m
Weight	16.1 kg

Table A.6 Technical specification of the MH-storage unit (4-SL 14 AR, HERA)

Parameter	Value/type
Nominal H_2-capacity	14 Nm^3
Hydride alloy	Hydralloy C10 (AB_2-type hydride)
Hydride alloy mass	85 kg
Total tank volume	25 l
Operating pressure	Approx. 3 bar at 20 °C
Maximum charging pressure	30 bar
Maximum operating temperature	60 °C
Required hydrogen quality	5N = 99.999% H_2
Construction material, tank	Stainless steel
Construction material, fins	Aluminium
System weight	Approx. 160 kg

Table A.7 Summary of alien substances in parts per million (ppm) H_2-molecules for various hydrogen qualities

Hydrogen quality	O_2	N_2	H_2O
Hydrogen 5.0 ($H_2 \geq 99.999\%$)	2	3	5
Hydrogen 3.0 ($H_2 \geq 99.9\%$)	50	500	100
Electrolytic hydrogen	1	0	5000

Table A.8 Technical data of the secondary battery (MK12-44, Kiel)

Parameter	Value	Unit	Comment
Nominal voltage	12	V	
Nominal capacity	44.0	Ah	20 hours
Maximum discharge current	200	A	5 seconds
Internal resistance	8	mΩ	20 °C
Charge voltage range	2.45 ± 0.05	V/cell	Cycle use, 20 °C
Maximum charging current	13.2	A	

Table A.9 Summary of the DACS I/O-capacity

Type	# of I/O	Comment
Analog input	16	Max. ±10 Vdc, 0–20 mA, 4–20 mA, ±20 mA
Discrete input	16	On: 15–30 Vdc, Off: -30–5 Vdc
RTD input	16	PT100, PT1000, 0–400 Ω, 0–4000 Ω
Thermocouple input	8	Types: J, K, T, N, R, S, E, B ±25 mV, ±50 mV, ±100 mV, -20–80 mV
Relay output	16	Max. 3 A at 250 Vac and 35 Vdc Single Pole Single Throw
High-speed analog input	16	200 kS/s, 16 bits, ±0.05 to ±10 Vdc
Digital I/O	8	5 V/TTL, two 24 bits counter/timers
Analog output	2	10 kS/s, 12 bits, ±10 Vdc
RS232-communication	2	Used for communication with the FieldPoint network module and the two mass flow meter/controllers
GPIB-communication	1	Used for communication with the electronic power supply and the electronic load

Appendix B

Fuzzy control theory

Fuzzy control is a method first introduced by L.A. Zadeh in 1965 [1]. The first practical use of fuzzy control occurred in the mid 70's. During the last decades the use of fuzzy control has increased strongly, especially by Japanese scientists and companies. Today, commercial equipment using fuzzy control is quite common, e.g., self-focusing cameras, water quality in washing machines, anti-locking brakes, and elevator control.

A fuzzy controller offers robust non-linear control. Conventional controllers can be very effective for a given application but their performance suffers greatly and can become unstable when subjected to external disturbances or substantial parameter changes. Fuzzy control systems, on the other hand, can be developed to cope with these disturbances and changes [2]. Fuzzy control can be suitable when the process is based on human experience which forms a set of rules that express how the system should be operated. This means that fuzzy controllers might be advantageous when no exact mathematic presentation of the system exists, which is the case for the overall high-level energy flow control of the HSAPS described in Section 5.4.

Fuzzy logic was developed in an attempt to allow the vagueness, uncertainty and imprecision of real world problems and human language to be described mathematically. Fuzzy logic is somehow the way the human brain works, which can be implemented in a machine that to a certain extent can perform like humans. Fuzzy logic must nevertheless not be confused with Artificial Intelligence (AI) where the goal for the machine is to perform exactly like humans.

Fuzzy control at a glance
The fuzzy logic analysis and control method is explained as follows, which is backed up by a diagram of the analysis/control routine shown in Figure B.1 [3]:

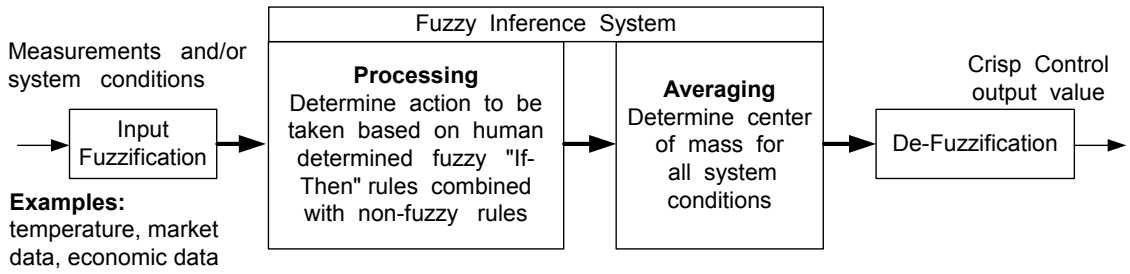

Figure B.1 The general fuzzy logic analysis/control routine.

1. Input fuzzification: Input of one, or more measurements or conditions from the system that is to be analysed and controlled.

2. Fuzzy inference system: Processing all of these inputs according to human based, fuzzy "if-then"-rules, which can be expressed in plain language words in combination with traditional non-fuzzy processing.

3. De-fuzzification: Averaging and weighting the resulting outputs from all the individual rules into one single output decision or signal that decides what to do or tell a controlled system what to do. This defuzzified controller output value is a precise crisp value.

In the theory of fuzzy regulation it is important to explain the term *fuzzy sets* which often is presented in the literature [4]. First, for clarity, the definition of a *classical set* is a group of objects of any kind, which mathematically can be explained as follows: letting A be a set, then $x \in A$ means that x is an element of the set A, while $x \notin A$ means that x is not an element of the set A. In other words, the set A is fully defined by the element it contains, referred to as a crisp set in the fuzzy set theory. So, the classical set, in this example represented by A, can be defined by listing all the elements it contains. Another way to define the classical set A is to introduce its characteristic function μ_A, thus defining A on the domain X:

$$\mu_A : X \rightarrow \{0,1\} \text{ is a characteristic function of the set } A \text{ for all } x \qquad \text{(B.1)}$$

Equation B.1 implies that $\mu_A(x) = 1$ when $x \in A$ and 0 when $x \notin A$.

Now, for any element u on a defined universe U, and with a fuzzy set F it is not necessary that either $u \in F$ or $u \notin F$. This generalisation states that for any crisp set C it is possible to define a characteristic function μ_C: $U \rightarrow \{0,1\}$. Fuzzy set theory then generalises the characteristic function, μ_C, to an extended membership function, μ_F, which holds for every $u \in U$, meaning a value from the unit interval [0,1] rather than the two-element set $\{0,1\}$. These extended membership functions is defined as the fuzzy sets. The membership function μ_F of a fuzzy set F can be written as:

$$\mu_F: U \rightarrow [0,1] \qquad \text{(B.2)}$$

where F is completely determined by the set of ordered pairs $F = \{(u, \mu_F(u))\}$, $u \in U$, and u has a degree of membership $\mu_F(u)$.

Input fuzzification

With the fuzzy set theory in mind, Figure B.1 can be explained in more detail. At the first stage, labelled input fuzzification, the degree of the input parameters to which they belong to the fuzzy sets is determined by using the membership functions. A membership function is a curve that maps the relation between the input universe and the membership output value between 0 and 1 (unity). An example could be the age of a person in a group of people, e.g. if the person is 74 years old the specific membership function might have an output of e.g. 0.83 which indicates a rather old person. If the fuzzy set in this case was called *Age*, the ordered pair in this specific condition would be $Age = \{(74, 0.83)\}$.

Fuzzy Inference System
The fuzzy inference is the process of mapping from a given input to an output using fuzzy logic. The "If-Then" rules represent the core of the chosen control strategy on the form:

IF (condition fuzzy set 1) AND/OR (condition fuzzy set 2) THEN (control output)

The controllers can be designed easily for single input single output (SISO) and for multiple input multiple output (MIMO) systems. The number of rules increases with the number of inputs and outputs.

The output from each rule, which is a new fuzzy set represented by a specific area, must be aggregated and then de-fuzzified in order to produce a crisp control output. Aggregation implies that all the output sets from the rule base are combined into a single set.

De-fuzzification
At last, the single aggregated output set is de-fuzzified into a single crisp control value. The most common method for de-fuzzification are the Centre of Gravity (CoG) and the Centre of Sums (CoS) method that returns the weighted average of all the elements in the aggregated output set. There are many de-fuzzification algorithms. Some of the most important ones are:

- Centre of Gravity (also denoted as Centre of Area)
- Centre of Sums
- First of Maxima
- Middle of Maxima
- Max Criterion
- Height de-fuzzification

Centre of Gravity (CoG) and Centre of Sums (CoS) will be explained in the following, for details about the other de-fuzzification methods the reader is referred to [5, 6] amongst others. Figure B.2 shows a graphical representation of both CoG and CoS.

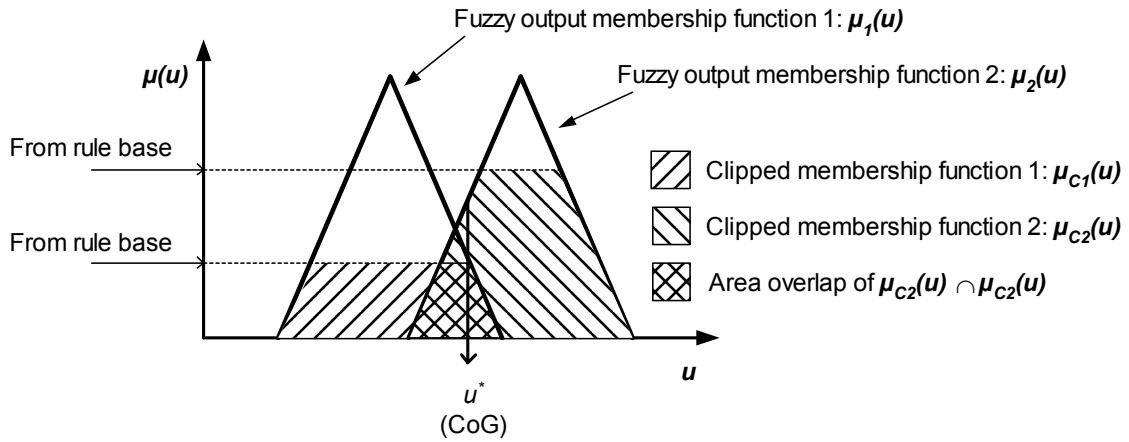

Figure B.2 Graphical representation of the Centre of Gravity and Centre of Sums methods for de-fuzzification

The modified output membership function of $\mu(u)$ is in general called the *clipped* $\mu(u)$ which are denoted as $\mu_{C1}(u)$ and $\mu_{C2}(u)$ in the example given in Figure B.2.

CoG calculates the centre of mass of the aggregated areas of the clipped output fuzzy membership functions:

$$u^* = \frac{\int u \cdot \mu(u) du}{\int \mu(u) du} = \frac{\int u \cdot \max(\mu_{C1}(u), \mu_{C2}(u)) du}{\int \max(\mu_{C1}(u), \mu_{C2}(u)) du} \quad \text{(continuous case)} \quad \text{(B.3)}$$

It can be seen from Equation B.3 that this de-fuzzification method does not reflect the overlapping area $\mu_{C1}(u) \cap \mu_{C2}(u)$, it only calculate this area once, thus, the actual area considered is $\mu_{C1}(u) \cup \mu_{C2}(u)$.

In the CoS method, the overlapping area are reflected twice when:

$$u^* = \frac{\int u \cdot \sum_{k=1}^{n} \mu_{C(k)}(u) du}{\int \sum_{k=1}^{n} \mu_{C(k)}(u) du} \quad \text{(continuous case)} \quad \text{(B.4)}$$

References

1. L.A.Zadeh, *Fuzzy Sets*. Information and Control. Vol. 8. 1965.
2. C.Lee, *Fuzzy Logic in Control Systems: Fuzzy Logic Controller-Part II.* IEEE transactions on systems, man, and cybernetics, 1990. **20**(2): p. 419-432.
3. T.Sowell, *Fuzzy Logic for "Just Plain Folks"*. 2003.
4. P.Taylor, *Doctoral Thesis "Distributed Intelligent Load Control of Autonomous Renewable Energy Systems"*. 2001, UMIST and Econnect, UK.
5. D.Driankov, H.Hellendoorn, and M.Reinfrank, *An Introduction to Fuzzy Control*. 1996: Springer.
6. R.Fullr, *Neural fuzzy systems*. Advances in Soft Computing Series. 2000, Berlin/Heidelberg: Springer.

Appendix C

Fuzzification of the system/control parameters

The fuzzy controller membership functions shown in Figure 5.8 have the following mathematical expressions given in Tables C.1 – C.3.

Table C.1 Mathematical expression for the hydrogen discharge membership functions shown in Figure 5.8

Region of BAT_{SOC} [%]	**Output from $\mu_{fc}^{bat_{soc}}$**
$BAT_{SOC} < 38$	1
$38 \leq BAT_{SOC} \leq 50$	$(-BAT_{SOC} + 50)/12$
$50 < BAT_{SOC}$	0

Table C.2 Mathematical expression for the hydrogen balance membership functions shown in Figure 5.8

Region of BAT_{SOC} [%]	**Output from $\mu_{bat}^{bat_{soc}}$**
$BAT_{SOC} < 38$	0
$38 \leq BAT_{SOC} \leq 48$	$(BAT_{SOC} - 38)/10$
$48 < BAT_{SOC} < 52$	1
$52 \leq BAT_{SOC} \leq 70$	$(-BAT_{SOC} - 70)/18$
$70 < BAT_{SOC}$	0

Table C.3 Mathematical expression for the hydrogen charge membership functions shown in Figure 5.8

Region of BAT_{SOC} [%]	**Output from $\mu_{ely}^{bat_{soc}}$**
$BAT_{SOC} < 50$	0
$50 \leq BAT_{SOC} \leq 70$	$(BAT_{SOC} - 50)/20$
$70 < BAT_{SOC}$	1

The fuzzy controller membership functions shown in Figure 5.9 have the following mathematical expressions given in Tables C.4 and C.5.

Table C.4 Mathematical expression for the hydrogen discharge membership functions shown in Figure 5.9

Region of $H_{2,SOC}$ [%]	**Output from $\mu_{fc}^{H_{2,soc}}$**
$0 \leq H_{2,SOC} < 10$	$(H_{2,SOC})/10$
$10 \leq H_{2,SOC} \leq 100$	1

Table C.5 Mathematical expression for the hydrogen charge membership functions shown in Figure 5.9

Region of $H_{2,SOC}$ [%]	**Output from $\mu_{ely}^{H_{2,soc}}$**
$0 \leq H_{2,SOC} \leq 90$	1
$90 < H_{2,SOC} \leq 100$	$(-H_{2,SOC} + 100)/10$

The fuzzy controller membership functions shown in Figure 5.10 have the following mathematical expressions given in Tables C.6 – C.8.

Table C.6 Mathematical expression for the hydrogen discharge membership functions shown in Figure 5.10

Region of $I_{PV\text{-}Load}$ [A]	**Output from $\mu_{fc}^{I_{pv\text{-}load}}$**
$I_{PV\text{-}Load} < -7$	1
$-7 \leq I_{PV\text{-}Load} \leq -1$	$(-I_{PV\text{-}Load} - 1)/6$
$-1 < I_{PV\text{-}Load}$	0

Table C.7 Mathematical expression for the hydrogen balance membership functions shown in Figure 5.10

Region of $I_{PV\text{-}Load}$ [A]	**Output from $\mu_{bat}^{I_{pv\text{-}load}}$**
$I_{PV\text{-}Load} \leq -5$	0
$-5 \leq I_{PV\text{-}Load} \leq -1$	$(I_{PV\text{-}Load} + 5)/4$
$-1 < I_{PV\text{-}Load} < 5$	1
$5 \leq I_{PV\text{-}Load} \leq 10$	$(-I_{PV\text{-}Load} + 10)/5$
$10 < I_{PV\text{-}Load}$	0

Table C.8 Mathematical expression for the hydrogen charge membership functions shown in Figure 5.10

Region of $I_{PV\text{-}Load}$ [A]	**Output from $\mu_{ely}^{I_{pv\text{-}load}}$**
$I_{PV\text{-}Load} < 5$ A	0
5 A $\leq I_{PV\text{-}Load} \leq 13$ A	$(I_{PV\text{-}Load} - 5)/8$
13 A $< I_{PV\text{-}Load}$	1

The fuzzy controller membership functions shown in Figure 5.11 have the following mathematical expressions given in Tables C.9 and C.10.

Table C.9 Mathematical expression for the hydrogen discharge membership functions shown in Figure 5.11

Region of *Season* [Days]	**Output from μ_{fc}^{season}**
$Season < 50$	1
$50 \leq Season \leq 100$	$(-Season + 100)/50$
$100 < Season < 270$	0
$270 \leq Season \leq 320$	$(Season - 270)/50$
$320 < Season$	1

Table C.10 Mathematical expression for the hydrogen charge membership functions shown in Figure 5.11

Region of *Season* [Days]	**Output from μ_{ely}^{season}**
$Season < 50$	0
$50 \leq Season \leq 100$	$(Season - 50)/50$
$100 < Season < 270$	1
$270 \leq Season \leq 320$	$(-Season + 320)/50$
$320 < Season$	0

De-fuzzification in order to produce a crisp controller output value

The fuzzy controller output membership functions shown in Figure 5.12 are different because they are modified (clipped) by the values from the input membership functions entered through the ordinate. Then, the areas for the modified output functions have to be calculated. While the fuzzification of the input system parameters have been shown in Figures 5.8 - 5.12 and given in Tables C.1 - C.10, the de-fuzzification of the output membership functions will be examined.

In the forthcoming, the inputs to the output membership functions will be denoted as $Max\{\mu_{bat}^{input}\}$ for μ_{bat}^{output}, $Min\{\mu_{fc}^{input}\}$ for μ_{fc}^{output}, and $Min\{\mu_{ely}^{input}\}$ for μ_{ely}^{output}, where *Min* and *Max* are according to the corresponding "If-Then"-rules given in Section 5.7 as:

1. IF $\mu_{bat}^{bat_{soc}}$ OR $\mu_{bat}^{I_{pv-load}}$ THEN
   $\text{Max}\{\mu_{bat}^{output}(\mu_{bat}^{bat_{soc}}, \mu_{bat}^{I_{pv-load}})\}$
2. IF $\mu_{fc}^{bat_{soc}}$ AND $\mu_{fc}^{H_{2,soc}}$ AND $\mu_{fc}^{I_{pv-load}}$ AND μ_{fc}^{season} THEN
   $\text{Min}\{\mu_{fc}^{output}(\mu_{fc}^{bat_{soc}}, \mu_{fc}^{H_{2,soc}}, \mu_{fc}^{I_{pv-load}}, \mu_{fc}^{season})\}$
3. IF $\mu_{ely}^{bat_{soc}}$ AND $\mu_{ely}^{H_{2,soc}}$ AND $\mu_{ely}^{I_{pv-load}}$ AND μ_{ely}^{season} THEN
   $\text{Min}\{\mu_{ely}^{output}(\mu_{ely}^{bat_{soc}}, \mu_{ely}^{H_{2,soc}}, \mu_{ely}^{I_{pv-load}}, \mu_{ely}^{season})\}$

Figure C.1 shows an operation condition that is to be de-fuzzified based on the Centre of Sums (CoS) method (Appendix B). The example shows a situation where the fuzzy controller signals that the fuel cell should be switched ON, or continue to run the fuel cell if it is already ON. Notice that no actions for the electrolyser have been registered.

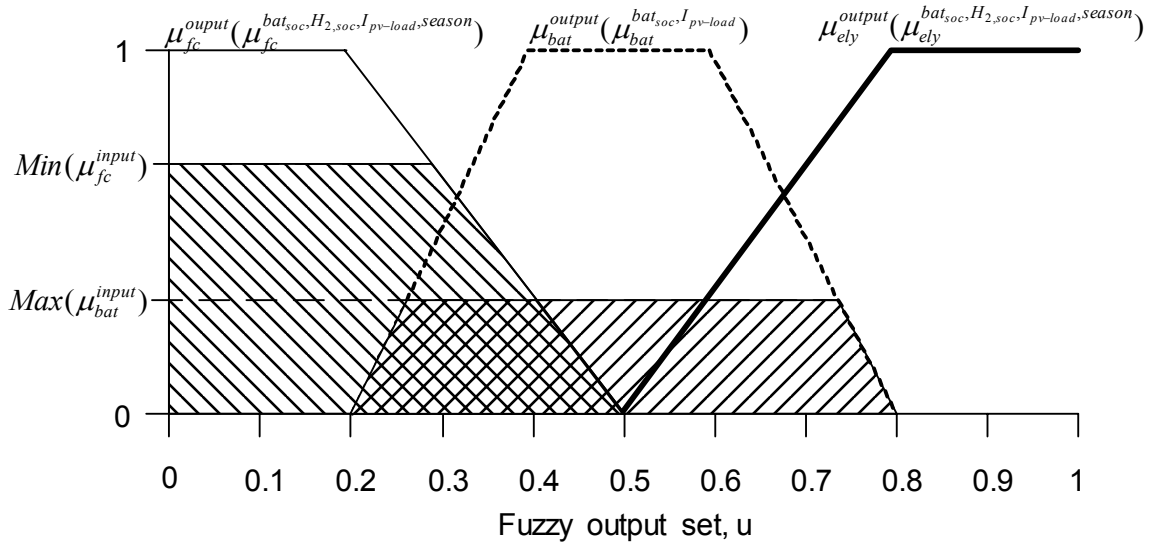

Figure C.1 De-fuzzification in order to produce a crisp output value.

The output membership functions modified by $Min(\mu_{fc}^{input})$ and $Max(\mu_{bat}^{input})$ are denoted $\mu_{Cfc}^{output}(u)$ and $\mu_{Cbat}^{output}(u)$ respectively, which are given by:

$$\mu_{Cfc}^{output}(u) = Min(Min(\mu_{fc}^{input}), \mu_{fc}^{output}(u)) \quad \text{(C.1)}$$

and

$$\mu_{Cbat}^{output}(u) = Min(Min(\mu_{bat}^{input}), \mu_{bat}^{output}(u)) \quad \text{(C.2)}$$

As recalled from Appendix B, the functions C.1 and C.2 are called the clipped output membership functions (denoted by the C in the subscript). The mathematical expressions for the fuzzy output membership functions used in this thesis are given in Table C.11, Table C.12 and Table C.13 for the fuel cell, battery, and the electrolyser respectively.

Table C.11 Mathematical expression for the output membership function for hydrogen discharge shown in Figure 5.12

Region of *u*	**Value of μ_{fc}^{output}**
u < 0.2	1
0.2 ≤ u ≤ 0.5	(0.5-u)/0.3
u > 0.5	0

Table C.12 Mathematical expression for the output membership function for hydrogen balance shown in Figure 5.12

Region of *u*	**Value of μ_{bat}^{output}**
u < 0.2	0
0.2 ≤ u < 0.4	(u-0.2)/0.2
0.4 ≤ u ≤ 0.6	1
0.6 < u ≤ 0.8	(0.8-u)/0.2
u > 0.8	0

Table C.13 Mathematical expression for the output membership function for hydrogen charge shown in Figure 5.12

Region of *u*	**Value of μ_{ely}^{output}**
u < 0.5	0
0.5 ≤ u ≤ 0.8	(u-0.5)/0.3
u > 0.8	1

The Centre of Sums is finally computed by:

$$CoS = \frac{\int u \cdot (\mu_{Cfc}^{output}(u) + \mu_{Cbat}^{output}(u))du}{\int (\mu_{Cfc}^{output}(u) + \mu_{Cbat}^{output}(u))du} \quad \text{(C.3)}$$

In this example, the crisp output from the fuzzy controller is calculated to be 0.26, thus, the fuel cell should be running.

Appendix D

Table D.1 Key parameters for the *battery five-step charge controller*, the *Control Matrix*, and the *fuzzy controller* explained in Chapter 5. All parameters are defined as *system parameters* and denoted with an *S*, *measured parameters* are denoted with a *M*, *derived parameters* (parameters that are predicted or not directly measured) are denoted with a *D*, parameters that includes a threshold setting are denoted with a *T*, and *control parameters* are denoted with a *C*.

Parameter	*S*	*M*	*D*	*T*	*C*	*BATcontroller specific*	*ControlMatrix specific*	*Fuzzycontroller specific*
Current	X	X						
Voltage	X	X						
Temperature	X	X						
Pressure	X	X						
H_2 flow	X	X						
BAT_{SOC}	X		X			X	X	X
$H_{2,SOC}$	X		X				X	X
$I_{PV\text{-}Load}$	X		X				X	X
$Pred_{PV\text{-}Load}$	X		X				X	
Season	X	X						X
$BAT_{ELY,ON}$	X			X	X	X	X	
$BAT_{ELY,OFF}$	X			X	X	X		
$BAT_{FC,ON}$	X			X	X	X	X	
$BAT_{FC,OFF}$	X			X	X	X		
$H_{2,High}$	X			X	X		X	
$H_{2,Low}$	X			X	X		X	
$I_{Balance,+/-}$	X			X	X		X	
$Pred_{ELY,ON/OFF}$	X			X	X		X	
$\mu_{ely}^{bat_{soc}}$	X			X	X			X
$\mu_{bat}^{bat_{soc}}$	X			X	X			X
$\mu_{fc}^{bat_{soc}}$	X			X	X			X
$\mu_{ely}^{H_{2,soc}}$	X			X	X			X
$\mu_{fc}^{H_{2,soc}}$	X			X	X			X
$\mu_{ely}^{I_{pv-load}}$	X			X	X			X
$\mu_{bat}^{I_{pv-load}}$	X			X	X			X
$\mu_{fc}^{I_{pv-load}}$	X			X	X			X
μ_{ely}^{season}	X			X	X			X
μ_{fc}^{season}	X			X	X			X
Time[(1)]	X	X				X	X	X

[(1)]The Time parameter is important in order to optimize the controllers. Thus, it is marked as specific for all the controllers even though it is not used in the specific comparison study in Chapter 5.

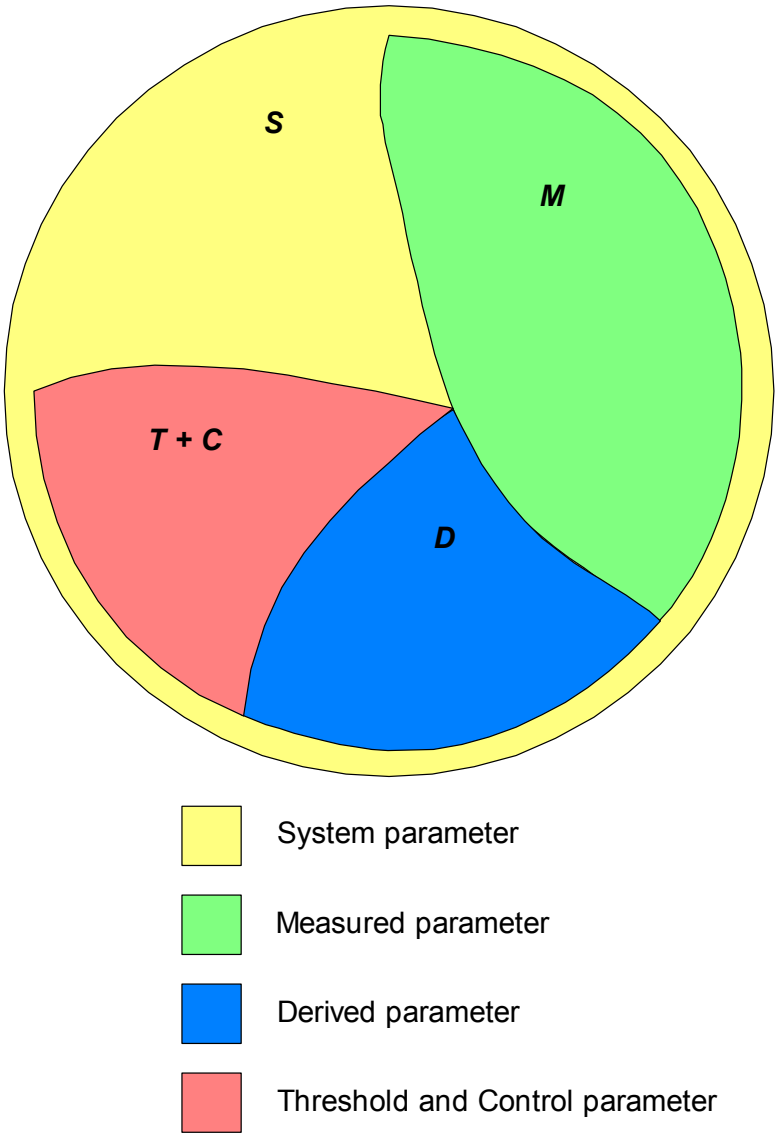

Figure D.1 Classification of system parameters identified in an HSAPS. The system parameters are listed in Table D.1.

Appendix E

The setting of the threshold in the control parameter $Pred_{ELY,ON/OFF}$ has been tuned through computer simulations by varying this value between 0 W – 1000 W. The computer simulation setup is the same as used in Section 5.4.1. The effect of varying this prediction parameter has been evaluated by plotting these electrolyser results:

- electrolyser ON&OFFs [-] (Figure E.1)
- electrolyser runtime [hr] (Figure E.2)
- electrolyser average power input [W] (Figure E.3)
- total energy consumed by electrolyser [kWh] (Figure E.4)
- excess energy in system (dumped energy from PV array) [kWh] (Figure E.5)
- final H_2 state-of-charge by the end of the year [%] (Figure E.6)

The results will now be plotted and discussed:

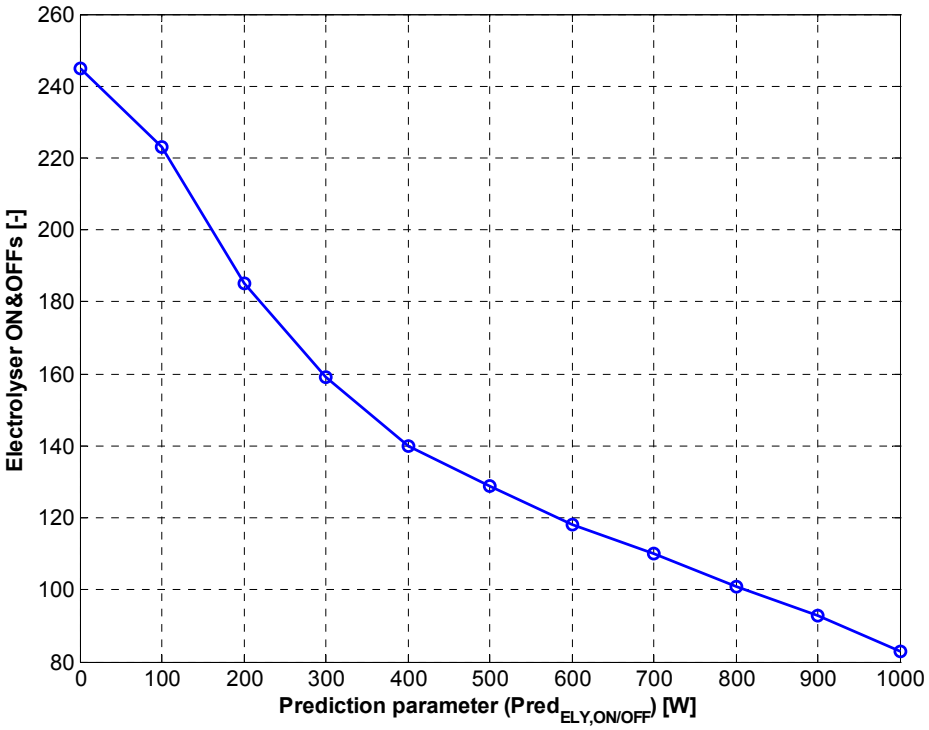

Figure E.1 Electrolyser ON&OFFs.

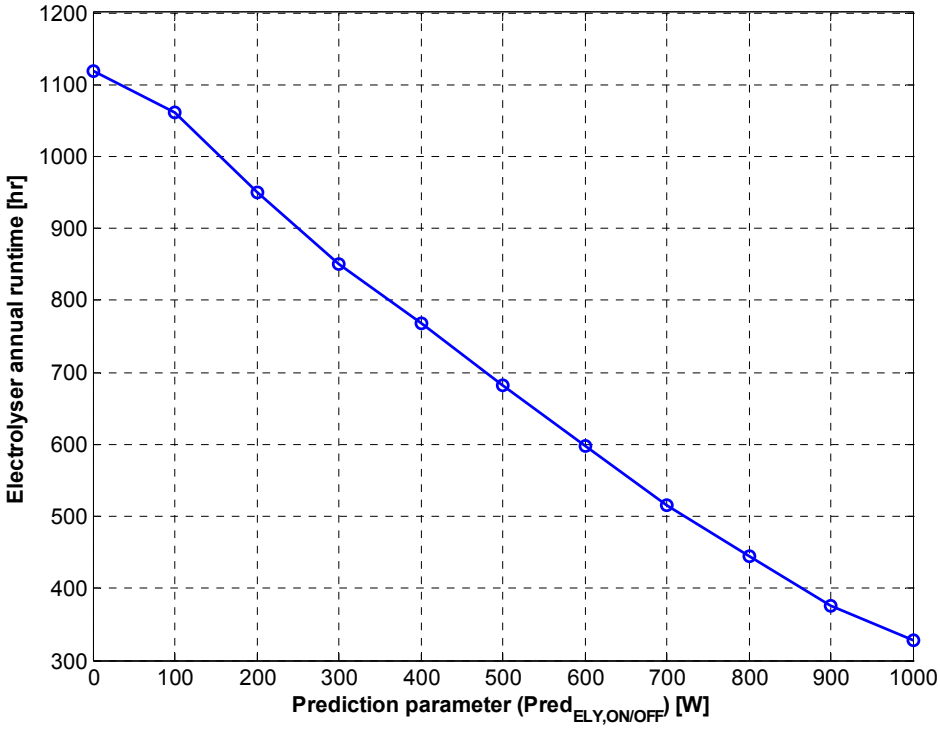

Figure E.2 Electrolyser annual runtime.

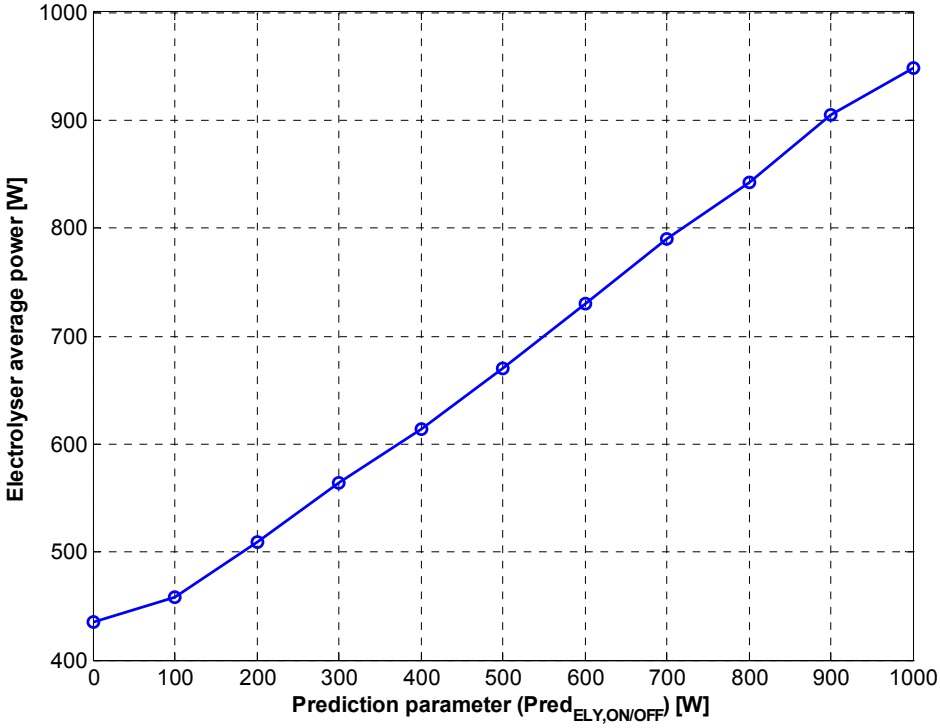

Figure E.3 Electrolyser average power.

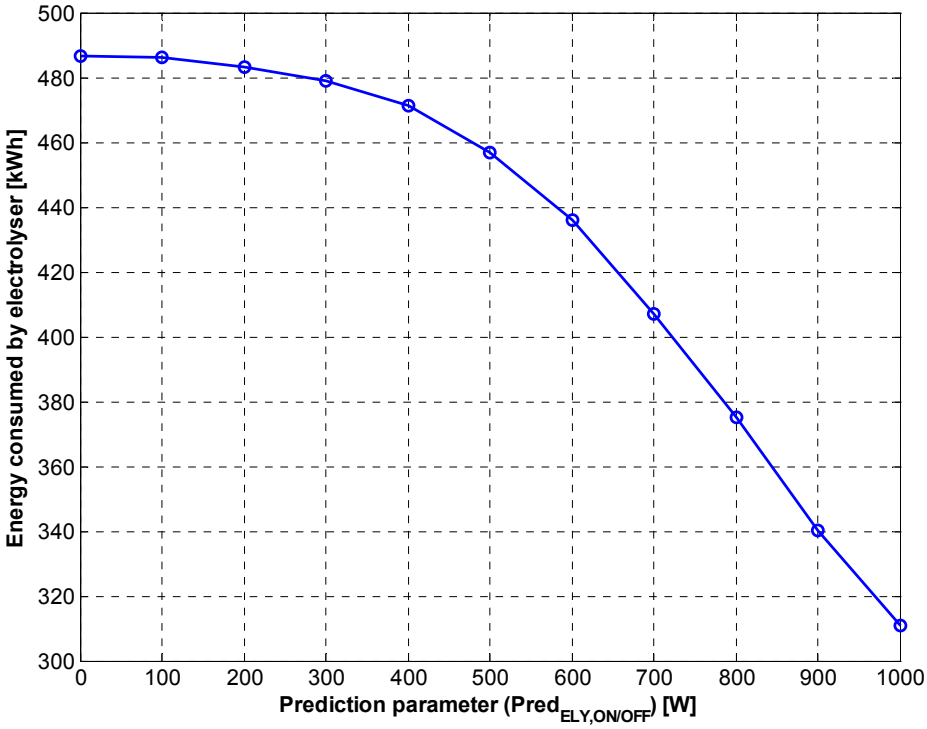

Figure E.4 Electric energy consumed by electrolyser.

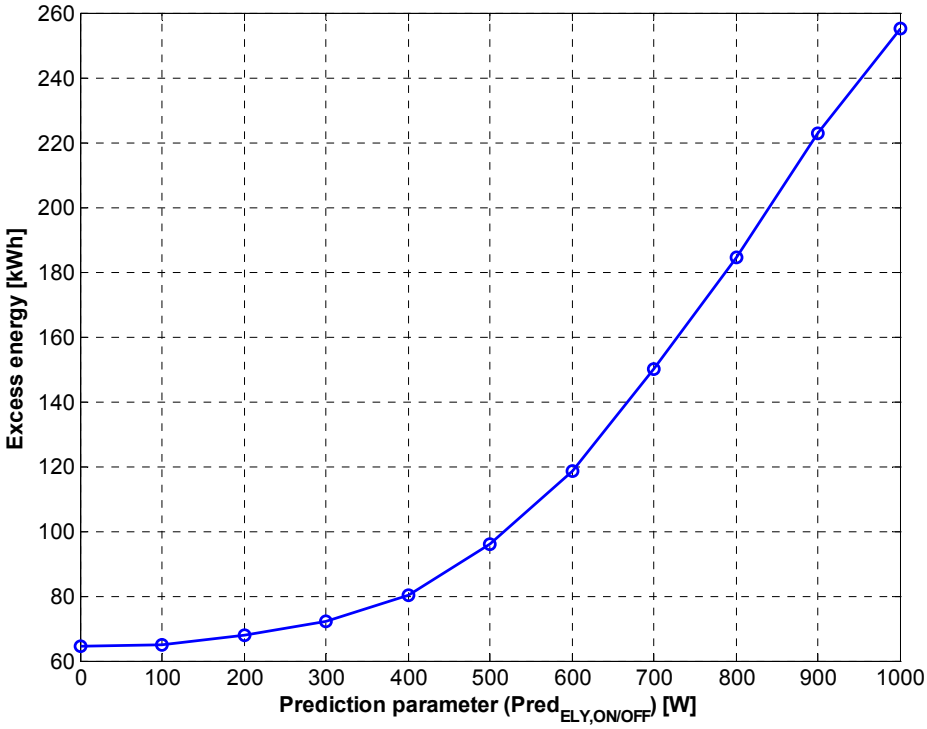

Figure E.5 Excess electric energy in HSAPS (dumped PV array energy).

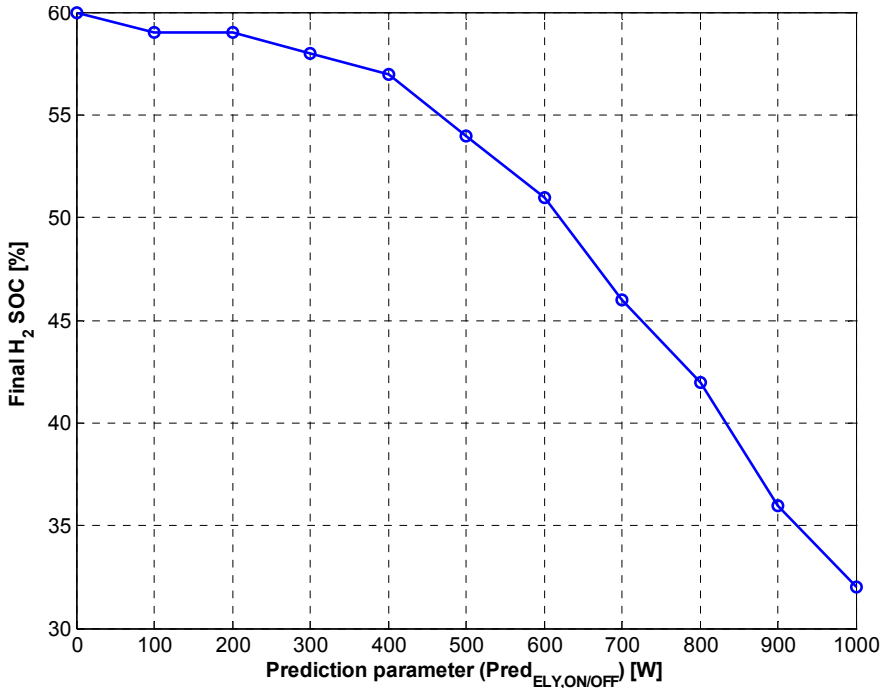

Figure E.6 Final hydrogen state-of-charge in hydrogen storage by the end of the year.

Discussion and conclusion

Investigation of Figure E.1 reveals there is a 42.9 % reduction in number of electrolyser ON&OFFs going from 0 W to 400 W as threshold for the control parameter, $Pred_{ELY,ON/OFF}$. Setting the threshold to 0 W is practically the same as removing the prediction parameter. Above 400 W the negative gradient for number of ON&OFFs is more flat. In going from 400 W to 800 W the reduction in number of ON&OFFs is not even half of what was gained in going from 0 W to 400 W.

Figure E.2 and Figure E.3 show more or less linear relationship between the prediction parameter and the electrolyser runtime and the prediction parameter and the average electrolyser power, respectively. Thus, these two figures gives no specific indication for setting of the threshold value in $Pred_{ELY,ON/OFF}$ in this simulation study.

It can be seen from Figure E.4 that the electric energy consumed by the electrolyser is only reduced by 3.1 % going from 0 W to 400 W as threshold for the prediction parameter, while going from 400 W to 800 W reduces the electric energy consumption with 20.7 %.

The noticeable increase in excess energy above prediction parameter equal to 400 W in Figure E.5 is directly related to the decrease in the electrolyser energy consumption shown in Figure E.4. The decrease in final H_2 state-of-charge shown in Figure E.6 is also a consequence of the decreasing electrolyser energy consumption, thus, a decrease in the total annual hydrogen production.

The conclusion from the sensitivity analysis in this appendix is that the threshold for the control parameter $Pred_{ELY,ON/OFF}$ should be set to 400 W because a change in the gradient was found at this value both in Figure E.1 and Figure E.4. By using this value, the number of electrolyser ON&OFFs is reduced by 42.9 % while the electrolyser energy consumption, thus the hydrogen production is only reduced by 3.1 %.

Appendix F

Techno- economical analysis of the interplay between short-term vs. long-term energy storage in a small-scale Hydrogen stand-alone power system (HSAPS) based on renewable energy

1. Introduction

The purpose with this appendix is to find a correlation between a lead-acid battery size and a metal hydride size in the system described in this thesis (Chapter 3). A specific annual load energy requirement must be satisfied (650 kWh/year). The economic and technologic results will be discussed. It must however be stressed that this is primarily a methodology study, the actual minimum cost found in this study is in the order 5 – 10 higher than the costs of energy found by others that have performed similar but more detailed life cycle analysis for such hydrogen energy systems [1]. Thus, the focus here is to investigate the trends rather than finding the true cost. This illustrates more a worst-case scenario as cost data for the electrolyser and the fuel cell is based on prototype costs.

2. Background for economic considerations

The main expense in the laboratory HSAPS was the advanced 1.7 kW PEM pressurized electrolyser with specific cost 53 000 $/kW. However, this was a prototype unit, thus, this price was not used in the calculations that follow. To justify the rather expensive hydrogen production unit, specific prices for low pressure PEM electrolysers are used; 30 000 $/kWh is used for PEM electrolyser under 5 kW and 20 000 $/kWh for each kW over 5 kW. This highly non-linear cost curve can of course be criticized, but it's interesting to include it into the calculation to investigate its effect on the total system cost. Still, the quite high PEM electrolyser costs used above reflects prototype systems more than actual near future market prices. Thus, it may also be worth mentioning that specific prices for commercial alkaline electrolysers is about 500 $/kW in MW scale and 500 – 2500 $/kW in the kW scale [2].

The 42 kWh (14Nm^3) metal hydride storage had a specific cost of 250 $/kWh. Future estimates (10 year perspective) indicates a MH specific cost of 200 $/$Nm^3$ for this type of hydrogen storage [3], this price is used in the calculations that follow.

For estimating the average price of PV modules, the "peak-watt" (W_{peak}) price is often used as a fixed economic parameter. In accordance with Kyocera catalogue and internet survey, the average price with life cycle cost of 20 year is estimated as 4.25 $/$W_{peak}$ [4]. The maximum power point tracker (MPPT), which finds the maximum power output of the PV panels, is estimated to a average price of about 660 $ [4]. The PV array has to be increased when the electrolyser size is increased. The PV array should also to some extent be oversized in order to ensure proper electrolyser operation. It's not enough to match PV array peak power (W_{peak}) to nominal electrolyser power, simply because the PV array is not always in the optimum position regarding the sun, there may also be clouds which interfere.

The cost of battery is significant, since the initial investment is high and has to be replaced several times (about every 5 years) during a PV system lifetime. Battery price is strongly dependent on its quality, Concorde lead-acid batteries is chosen for this work with a specific price of 3 $/Ah. Annual inflation rate in battery prices is considered to be f = 3 %, while the market discount rate is d = 6 % [4].

PEM fuel cells at present time are more *"off the shelf"* products than PEM electrolysers because the automobile companies accelerates the technology and production methods, but still specific cost is about 15 000 $/kW. The target price for automobile PEM fuel cell is 50 $/kW and 500 $/kW for stationary applications [5]. The specific price in this work is set to 10 000 $/kW which is neither to optimistic nor pessimistic according to prices as of today. Nevertheless the fuel cell is set to a constant size (500 W) because the load is constant, so, when the fuel cell is present the cost will be constant in the overall economic results.

Installation cost has been estimated to be 10 % of the initial cost [6], while the annual maintenance cost is estimated to be 2 % of the initial cost [7].

The initial cost is only one element in the overall economics of a system. Some type of economic assessment is required to determine which system from a number of choices will give the best value for money in the longer run. Life cycle costing (LCC) examines all the costs incurred over the lifetime of different systems, and compares them on an equal basis by converting all future cost into today's money. LCC is calculated by the sum of the present worth's (PW) of the different components in addition to installation and maintenance cost.

The PW factor of the replacement batteries after N years is given as $PW_{BAT} = ((1+f)/(1+d))^N$ [8].

The annuity factor ***a***, given as $1/(1-(1+r)^{-N})$, have interest rate r = 0.12 and time duration N = 20 years as inputs in this work and is used to find the PW of electrolyser, fuel cell, metal hydride, and MPPT. Little reliable LCC cost data exists for the hydrogen components, thus the factor **a** is just approximate and must be used with caution.

3. Matlab scripts

A cost function is programmed in Matlab, the main program *MH_BAT_CAP.m* and function *cap_cost_fcn.m* are given in the end of this appendix.

4. Results and discussion

The resulting correlation between battery and metal hydride to serve the specific load (650 kWh/year, peak power 350 W) chosen for the HSAPS is given in Figure F.1. The colour map indicates the LCC for the total system throughout 20 year lifetime for the ranges chosen for metal hydride [kWh] and battery capacity [Ah].

The results in Figure F.1 clearly shows that use of pure battery energy storage (7518 Ah) is about 175 % of the cost resulting from a pure hydrogen storage system (766.8 kWh), about 350 000 $ vs. about 200 000 $, respectively. 7 518 Ah, 48 V battery is 360.9 kWh, and with a battery discharge efficiency of maximum 90 %, the net energy amount delivered to load would be 360 kWh*0.9 = 324.8 kWh in a fully continuousdischarge. This is in good agreement with the capacity found for the pure hydrogen storage, with a fuel cell with fuel conversion efficiency of 42 %. With the fuel cell, the net energy amount delivered to load would be 766.8 kWh*0.42 = 322.0 kWh if the fuel cell where to run continuously and empty a fully charged metal hydride storage. The minimum system cost of about 65 000 $ appears to be at metal hydride size 250 – 260 kWh and battery size 200 – 400 Ah.

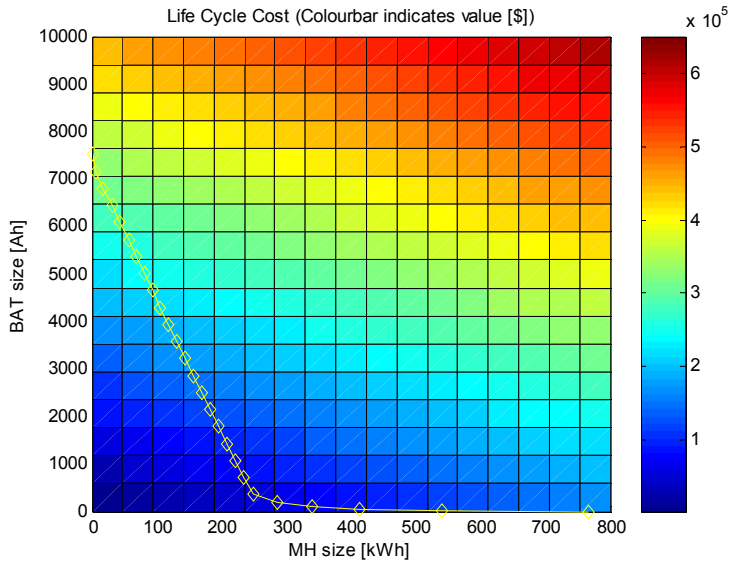

Figure F.1 Metal hydride and battery correlation plotted on a colour map indicating LCC system cost, 20 year lifetime.

Another interesting observation from Figure F.1 is that the metal hydride capacity is very sensitive to low battery size. When the battery size changes from 358 Ah down to zero the metal hydride size rises rapidly from 248.2 kWh to 766.8 kWh. Rising battery size from 358 Ah up to 7518 Ah gives a linear relation with the metal hydride size.

Figure F.2 is basically the same plot as Figure F.1, but the resulting LCC is shown in a 3-D surface plot.

Figure F.3 shows the system efficiency (green, right axis) plotted together with metal hydride and battery correlation (blue, left axis). As can be seen from Figure F.3, the efficiency is lowest for hydrogen dominant energy storage, a result that is expected since the hydrogen-loop has the lowest energy conversion efficiency, 30 –35 %. But, as more battery is used instead of hydrogen, the system efficiency increases because batteries have higher efficiency (about 80 % total energy efficiency). The efficiency curve descents from left to right in Figure F.3, but at metal hydride size of 250 kWh, there is a sudden drop in system efficiency caused by the large increase in hydrogen storage. This makes sense because the sudden increase in the hydrogen storage results in larger amounts of solar energy flowing through the hydrogen-loop, thus, a sudden decrease in overall system efficiency.

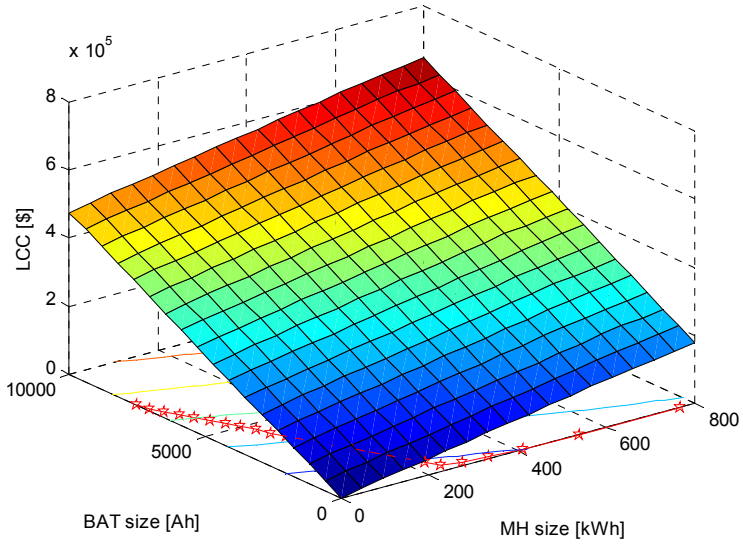

Figure F.2 Surface/contour plot of LCC for HSAPS, metal hydride/battery size correlation plotted as red stars in the XY-plane.

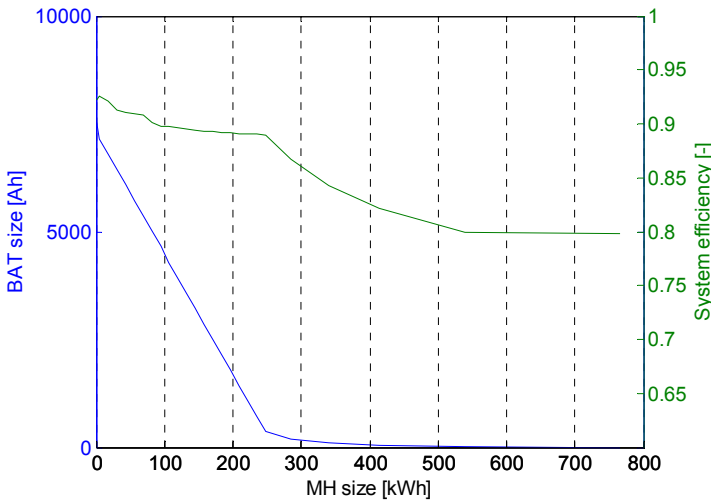

Figure F.3 System efficiency (the efficiency is in general high because all excess energy is defined available for work).

Equation 2.5 from Section 2.2.5 is used to calculate the overall system energy efficiency. The system efficiency used in this work consider the energy out of the PV panel as 100 %, thus the system boundary is set *behind* the PV panel.

Figure F.4 shows battery charge and discharge hours that are rather smooth along their capacity range compared to the fuel cell operation hours and ON/OFF-switching, which increases suddenly at metal hydride size larger than 250 kWh in Figure F.5.

The results from Figure F.4 and Figure F.5 indicate that the metal hydride size should be set at no value larger than 250 kWh and the corresponding battery size at no value lower than 350 Ah to reduce number of fuel cell ON/OFF-switching and operating hours which will shorten lifetime. This extra fuel cell maintenance and/or replacement cost is not included in the cost function and could be criticised, but since there is a lack of data on this economic issue in addition to that the fuel cell is "cheap" compared to the metal hydride storage and PEM electrolyser, it was not implemented in the cost function.

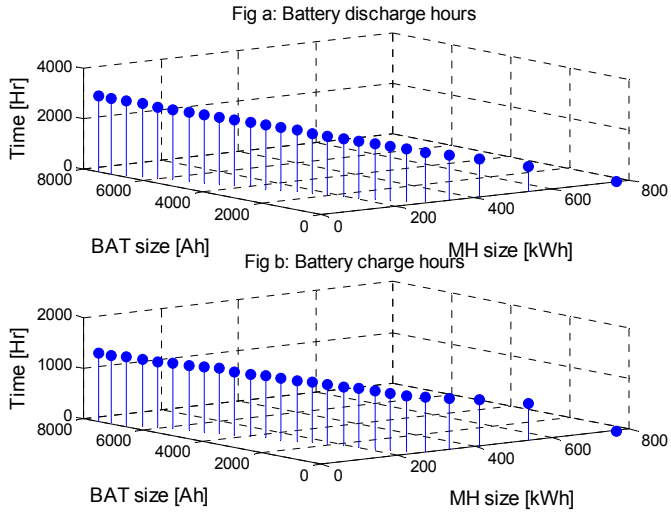

Figure F.4 Battery discharge hours (above) and battery charge hours (below).

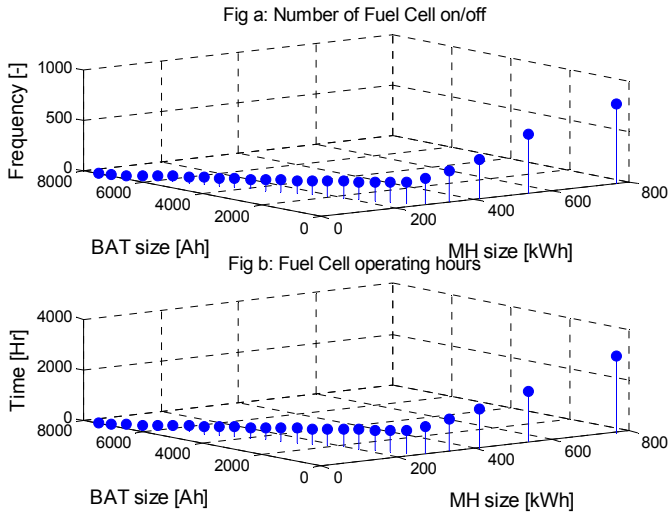

Figure F.5 Fuel Cell operation. Number of ON/OFF-switching (above), and operating hours (below).

5. Conclusion

A correlation between metal hydride storage as a hydrogen long-term energy storage vs. lead-acid battery as a short-term energy storage has been investigated for a Hydrogen Stand-Alone Power System (HSAPS) with a specific load requirement of 650 kWh/year. The optimum metal hydride storage size was found to be about 250 kWh and the corresponding battery size was found to be about 360 Ah. A 48V battery system contains 360 kWh*48 = 17.3 kWh energy which is about 17.3/250 = 7 % of the long-term energy storage.

These results are based on cost function programmed in Matlab and system performance simulated in and Simulink.

References

1. R.Glöckner, *Market Potential Analysis for Introduction of Hydrogen Energy Technology in Stand-Alone Power Systems. Final report, EU/ALTENER Programme. Contract No. 4.1030/Z/01-101/200*. 2004, Institute for Energy Technology, Kjeller, NO-2027, 2004.
2. A.de Groot, F.W.A.T., K.Brandwagt, *An analysis of different options for energy systems in residential districts*. 2001, ECN, Netherlands.
3. *Internal IFE Report, IFE/KR/F-2003/020*. 2003.
4. M.Dakkak, A.H., R.Muhida, Z.Kawasaki, *Operation strategy of residential centralized photovoltaic system in remote areas.* Renewable Energy, 2002. **28**: p. 997-1012.
5. W.Smith, *The role of fuel cells in energy storage.* J.Power Sources, 2000. **86**: p. 74-83.
6. P.Groumpos, G., Papageorgious, *An optimal sizing method for stand-alone-photovoltaic-power-system.* J.Solar Energy, 1987. **38**: p. 341-351.
7. M.Muselli, G.N., A.Louche, *Design of hybrid-photovoltaic power generation, with optimization of energy managament.* J.Solar Energy, 1999. **65**(3): p. 143-157.
8. R.Messenger, J.V., *Photovoltaic system engineering*. Boca Raton. 1999: CRC press.

Matlab scripts (m-files)

Main program file: *MH_BAT_CAP.m*

```
global PV_price ELYH_price ELYL_price FC_price FC_size MH_price BAT_price Cont_price f_BAT d_BAT N inst_pros maint_pros r MH_ELY_scale a a_BAT5 a_BAT10 a_BAT15 a_BAT20 a_BAT25

PV_price=4.25; %USD/Wpeak
ELYH_price=20; %USD/W
ELYL_price=30; %USD/W
FC_price=10; %USD/W
FC_size=500; %Rigid FC size in this work
MH_price=67; %USD/kWh
BAT_price=3*4; %USD/Ah, added with four because price related to 12V BAT, this system runs on 48 V
Cont_price=660; %USD/piece, power conditioning
f_BAT=0.03; % percent point, battery inflation rate
d_BAT=0.06; % percent point, battery market discount rate
inst_pros=0.1; %percent point, installation cost 10 % of initial cost
maint_pros=0.02; %percent point, maintenance cost 2 % of initial cost
MH_ELY_scale=7.14; %calculates the necesarry electrolyser size (in W) based on the metal hydride capacity (in kWh)

r=0.12; %Interest rate
N=20; %System lifetime in years

a=r/(1-(1+r)^-N); % annuity factor
a_BAT5=((1+f_BAT)/(1+d_BAT))^5; % annuity factor battery 5 years
a_BAT10=((1+f_BAT)/(1+d_BAT))^10; % annuity factor battery 10-15 years
a_BAT15=((1+f_BAT)/(1+d_BAT))^15; % annuity factor battery 15-20 years
a_BAT20=((1+f_BAT)/(1+d_BAT))^20; % annuity factor battery 20-25 years
a_BAT25=((1+f_BAT)/(1+d_BAT))^25; % annuity factor battery 25-30 years
```

```
MH_cap=linspace(0,800,18)'; %Range metal hydride capacity [kWh]
BAT_cap=linspace(0,10000,18)'; %Range battery capacity [Ah]

[X,Y]=meshgrid(MH_cap,BAT_cap); % Making a working matrix with vectors MH_cap and BAT_cap

A=MH_size; %MH size vs. BAT size correlation found in Simulink(read from workspace)
B=BAT_size; % --||--

cap_cost=cap_cost_fcn(X,Y); %Function call with matrixes X and Y as arguments

figure(5)
pcolor(MH_cap,BAT_cap,cap_cost)
title('Life Cycle Cost (Colourbar indicates value [$])')
xlabel('MH size [kWh]')
ylabel('BAT size [Ah]')
colorbar
hold on
plot(A,B,'y-d')
hold off

figure(6)
surfc(MH_cap,BAT_cap,cap_cost)
title('Life Cycle Cost')
xlabel('MH size [kWh]')
ylabel('BAT size [Ah]')
zlabel('LCC [$]')
hold on
plot(A,B,'r-p')
hold off

figure(7)
subplot (2,1,1)
stem3(MH_size,BAT_size,FCon_off,'fill')
title('Fig a: Number of Fuel Cell on/off')
xlabel('MH size [kWh]')
ylabel('BAT size [Ah]')
zlabel('Frequency [-]')
grid on

subplot (2,1,2)
stem3(MH_size,BAT_size,FChour,'fill')
title('Fig b: Fuel Cell operating hours')
xlabel('MH size [kWh]')
ylabel('BAT size [Ah]')
zlabel('Time [Hr]')
grid on

figure(8)
subplot (2,1,1)
stem3(MH_size,BAT_size,Bat_dch_hour,'fill')
title('Fig a: Battery discharge hours')
xlabel('MH size [kWh]')
ylabel('BAT size [Ah]')
zlabel('Time [Hr]')
grid on

subplot (2,1,2)
stem3(MH_size,BAT_size,Bat_ch_hour,'fill')
title('Fig b: Battery charge hours')
xlabel('MH size [kWh]')
ylabel('BAT size [Ah]')
zlabel('Time [Hr]')
grid on
```

Function file: *cap_cost_fcn.m*

```
function cap_cost=cap_cost_fcn(X,Y)

global PV_price ELYH_price ELYL_price FC_price FC_size MH_price BAT_price Cont_price f_BAT d_BAT N
inst_pros maint_pros r MH_ELY_scale a a_BAT5 a_BAT10 a_BAT15 a_BAT20 a_BAT25

%Calculation of Electrolyser size and price based on Metal Hydride size
```

```
cs=size(X); %Getting size of MH_cap vector
c=cs(1,1); %Getting number of coloumns for loop counting

for n=1:c
   MH=X(1,n); % Evaluate each and every MH size value in the MH_cap vector

   ELY_size_sc=MH*MH_ELY_scale; % ELY size calculation [W]

   if MH*MH_ELY_scale>=5000 %Specific ELY cost over 5kW=0.5USD/W, specific cost under 5kW is 2.5USD/W,
MH size is converted to ELY size with tha factor MH_ELY_scale
      % Electrolyser price at higher Electrolyser size
      ELY_price=ELYH_price;
      MH_dt=MH-MH_old; % Calculates the incremental MH size
      ELY_si=MH_dt*MH_ELY_scale; % Electrolyser size scaled based on MH size and a scaling factor
      ELY_init_tot1=ELY_init_old1+ELY_price*ELY_si; % Integrates price for ELY size over 5 kW
   else % Electrolyser price at lower Electrolyser size
      ELY_price=ELYL_price;
      ELY_si=MH*MH_ELY_scale; % Electrolyser size scaled based on MH size and a scaling factor
      ELY_init_tot2=ELY_price*ELY_si; % Integrates price for ELY size under 5 kW
      ELY_init_tot1=0;
   end
    ELY_init_tot(1:18,n)=ELY_init_tot1+ELY_init_tot2; %Making total initial cost matrix for the Electrolyser
    ELY_size(1:18,n)=ELY_size_sc; %Making Electrolyser size matrix
    MH_old=MH;
    ELY_init_old1=ELY_init_tot1;
 end

 %Calculation of FC cost, the size is set to constant 500W

 for i=1:c
    FC=X(1,i);
    if FC<=0 % No FC is needed if there is no hydrogen storage
       FC_s_price=0;
    else
       FC_s_price=FC_price;
    end
    FC_price_m(1:18,i)=FC_s_price*FC_size; % Making total FC price matrix
 end

%PV sizing to accommodate Hydrogen production

PV_size_MH=X*MH_ELY_scale; %[W]

%PV sizing to accommodate battery charging

PV_size_BAT=500+Y*0.3; %[W]

%Total PV size

PV_size=PV_size_MH+PV_size_BAT; %[W]

%Initial cost

PV_init=PV_size*PV_price;
ELY_init=ELY_init_tot;
FC_init=FC_price_m;
MH_init=X*MH_price;
BAT_init=Y*BAT_price;

Tot_init=PV_init+ELY_init+FC_init+MH_init+BAT_init+Cont_price;

Inst_cost=Tot_init*inst_pros;
Maint_cost=Tot_init*maint_pros*N;

%Present worth cost (PW), Life Cycle Cost (LCC)

PV_PW=PV_init;
ELY_PW=ELY_init*a;
FC_PW=FC_init*a;
MH_PW=MH_init*a;
BAT_PW=BAT_init; %Batteries the first five years
BAT_PW5=BAT_init*a_BAT5; %Batteries the next five years
BAT_PW10=BAT_init*a_BAT10; %Batteries from 10 to 15 years
BAT_PW15=BAT_init*a_BAT15; %Batteries from 15 to 20 years
Cont_PW=Cont_price*a;
```

```
% Final result, LCC, this result is returned from function back to main program
cap_cost=PV_PW+ELY_PW+MH_PW+BAT_PW+BAT_PW5+BAT_PW10+BAT_PW15+Inst_cost+Maint_cost+Cont_
PW;

figure(1)
surf(X,Y,PV_size)
title('PV panel size')
xlabel('MH size [kWh]')
ylabel('BAT size [Ah]')
zlabel('ELY size [W]')

figure(2)
surfc(X,Y,Tot_init)
title('Total initial cost')
xlabel('MH size [kWh]')
ylabel('BAT size [Ah]')
zlabel('Initial cost [$]')

figure(3)
surf(X,Y,Inst_cost)
title('Installation cost')
xlabel('MH size [kWh]')
ylabel('BAT size [Ah]')
zlabel('Inst. cost [$]')

figure(4)
surf(X,Y,Maint_cost)
title('Maintenance cost')
xlabel('MH size [kWh]')
ylabel('BAT size [Ah]')
zlabel('Maint. cost [$]')
```

Appendix G

What does it really mean that the hydrogen-loop efficiency actually increases with additional battery charging? This can be better understood with two different examples based on the amount of net energy (5.2 kWh) required from the fuel cell during the test-week:

In these examples the load power requirement is set to constant 130 W, and the total load energy requirement is set to 5.2 kWh. This means that the fuel cell stack must produce minimum about 180 W which includes the power to the fuel cell controller of approximately 50 W. From Figure 6.17 it can be seen that the fuel cell is operated in the critical efficiency region at 180 W, questioning if the fuel cell should start charging the battery or not depending on whether the load requirement start to decrease or increase. In both cases the electrolyser is assumed to have a specific energy input of 5.3 kWh/m^3 as found from the test-week (without the energy required by the hydrogen purification unit).

Example 1: Estimation of hydrogen-loop efficiency with no battery charging.

Duration of fuel cell operation to cover load energy requirement of 5.2 kWh at 0.13 kW:

$$\frac{5.2kWh}{0.13kW} = \underline{40hr} \qquad \text{(G.1)}$$

Energy required by fuel cell controller:

$$0.05kW \cdot 40hr = \underline{2kWh} \qquad \text{(G.2)}$$

The hydrogen-loop efficiency of 28.3 % without battery charging can be found directly from Figure 6.17 with fuel cell power at 180 W, which is in good agreement with the hydrogen-loop efficiency found from the test-week were the fuel cell average power was estimated to about 185 W.

Example 2: Estimation of hydrogen-loop efficiency where the fuel cell is allowed to charge the battery while it covers the load. The fuel cell is assumed to run constant at nominal power, 500 W.

With a constant load power of 130 W and a battery efficiency of 80 %, iteration result in a fuel cell operation time of 12.2 hr where the fuel cell energy directly to the load and to the battery is balanced as followed:

$$\frac{4.52kWh_{from\ FC\ to\ BAT}}{0.37kW_{FC\ power\ available\ for\ BAT\ charge}} = \underline{12.2hr} = \frac{1.59kWh_{direct\ to\ load}}{0.13kW_{power\ required\ by\ load}} \qquad \text{(G.3)}$$

1.59 kWh is fed directly to the load and 4.52 kWh of the fuel cell energy is fed to the battery, which is further discharged to the load for 4.52 kWh · 0.80 / 0.13 kW = 27.81 hr, thus the load is supplied with 5.2 kWh at 130 W for (27.8 + 12.2) hr = 40 hr which

is the same found in example one but at an hydrogen-loop/battery energy efficiency of:

$$\eta_{H_2-loop} \cdot \eta_{FC/BAT/LOAD} = 0.36 \cdot \frac{(4.52 \cdot 0.8 + 1.59)kWh}{(4.52 + 1.59)kWh} = 0.36 \cdot 0.85 \cdot 100\% = \underline{30.1\%} \quad \text{(G.4)}$$

The η_{H_2-loop} is the hydrogen-loop energy efficiency found from Figure 6.17 with fuel cell power at 500 W and $\eta_{FC/BAT/LOAD}$ is the energy efficiency from the fuel cell to the load partly via the battery. Equation F.4 shows that the total hydrogen-loop/battery energy efficiency is about 2 % higher than for the hydrogen-loop operation without the use of battery. This difference will be even larger as the fuel cell stack power further decrease below 180 W. The calculated efficiency in Equation F.4 is larger than the efficiency found from the hydrogen-loop/battery efficiency curve found with fuel cell power at 180 W in Figure 6.17 because this efficiency curve is based on worst case where all energy from the fuel cell is passed through the battery and eventually to the load.

The main reason for the improved energy efficiency is as already stressed above, the lesser energy required by fuel cell controller due to the shorter fuel cell operation time:

$$0.05kW \cdot 12.2hr = \underline{0.61kWh} \quad \text{(G.5)}$$

which is less than one third of the fuel cell controller energy required in example one.

Another factor that favours battery charging with the fuel cell when reasonable is the fact that the battery is usually at the minimum state-of-charge allowable when the HSAPS energy management decides to switch on the fuel cell, so additional battery charging at low battery state-of-charge would be beneficial regarding battery lifetime.